HOMOGENEOUS AND IMMOBILIZED NICKEL CATALYSTS AND MOBILITY STUDIES OF METALLOCENES ADSORBED ON HIGH SURFACE AREA MATERIALS

A Dissertation

by

KYLE JAMES CLUFF

Submitted to the Office of Graduate and Professional Studies of
Texas A&M University
in partial fulfillment of the requirements for the degree of

DOCTOR OF PHILOSOPHY

Chair of Committee,	Janet Bluemel
Committee Members,	Marcetta Darensbourg
	Emile Schweikert
	Joseph Ross
Head of Department,	Francois Gabbai

May 2016

Major Subject: Chemistry

ABSTRACT

This thesis will explore two different facets of the quest for superior immobilized catalysts: (**1**) cyclotrimerization of acetylenes with nickel catalysts and (**2**) solid-state NMR studies of the adsorption and subsequent mobility of organometallic solids on silica gel and other relevant surfaces.

The cyclotrimerization of acetylenes has a wide range of applications and can be catalyzed by inexpensive immobilized nickel complexes. However, the selectivity of these catalysts changes over time, and the activity declines. In this study, tridentate ligands are employed to reduce leaching and decomposition.

The chelate nickel complexes incorporating tridentate phosphine ligands $(CO)Ni[(PPh_2CH_2)_3CMe]$ (**2**), $(CO)Ni[(PPh_2CH_2CH_2)_3SiMe]$ (**6**), and $Ph_3PNi[(PPh_2CH_2CH_2)_3SiMe]$ (**7**), as well as the bidentate complex $(CO)_2Ni[(PPh_2CH_2)_2CMeCH_2PPh_2]$ (**3**) and the heterobimetallic complex $(CO)_2Ni[(PPh_2CH_2)_2CMeCH_2Ph_2PAuCl]$ (**4**) have been synthesized and characterized in solution and in the solid state. While complexes **2**-**4** displayed low catalytic activity, complex **7** led to 100% conversion of the substrate within four hours and was highly selective throughout the catalytic reaction.

Various metallocenes have been adsorbed on high surface area materials including mesoporous silica, carbon nanotubes and activated carbon. The adsorption progresses quickly onto a favorable support, even when the solids contact each other without a solvent, and is practically complete within two hours. Its progress is monitored

by ^{1}H, ^{13}C, and ^{2}H solid-state NMR spectroscopy. The transition from the crystal lattice to the surface species that are highly mobile is proven by strongly reduced chemical shift anisotropies and diminished dipolar interactions. All solid-state NMR spectra indicate that the transition from a monolayer to the crystalline state is abrupt, and no multiple layers form on the surfaces. A correlation between surface coverage and ^{2}H residual linewidths has been established. Besides a hydrophobic dry silica surface, wet and TMS-capped silica have been used as supports. The ^{2}H MAS spectra of surface-adsorbed ferrocene-d_2 prove that the motion of the metallocenes on the surfaces is fast and nearly isotropic, as in solution. Consequently, it is demonstrated that ^{1}H and ^{13}C NMR spectra of adsorbed ferrocene can be recorded using a conventional liquids NMR instrument. Additionally, it is possible to visually monitor the adsorption and translational mobility of ferrocene and other metallocenes in large pieces of silica gel.

ACKNOWLEDGEMENTS

Thank you Dr. Janet Bluemel for the countless hours of help and guidance throughout these last 5 years. You have spared neither time, nor effort to teach me and to help me develop the skills I need. It has been a pleasure to work with you and I could not ask for a better advisor.

Thanks also to my committee members, Dr. Marcetta Darensbourg, Dr. Emile Schweikert, and Dr. Joseph Ross for attending my seminars and for the helpful questions and suggestions.

I would like to especially acknowledge Dr. Vladimir Bakhmoutov for constantly helping me with the solid-state NMR instrument. I could not have done it without your help and teachings and I appreciate your patience and effort on my behalf. I likewise thank Mr. Steven Silber, Dr. Greg Wylie, and Dr. Howard Williams for their help with NMR experiments and instrumentation.

I also sincerely thank Dr. Nattamai Bhuvanesh, for the many excellent and sometimes difficult X-ray crystal structures.

I am indebted to the Bluemel group members for their help. Thank you for listening to all my talks so many times, and for the many helpful ideas. I would like to especially thank Johannes for training me on the Avance 400 and for the many other helpful hints, and Jackie for showing me a lot of things on the solid-state NMR as well.

I would also like to especially thank Jordon and Darcy who worked with me as undergraduates and who really did a great job. Thank you for all your help, and I hope you enjoyed the semester as much as I did.

Finally, thank you to parents, grandparents and other family members for teaching me the importance of education and encouraging me to follow my interests and pursue a career that I enjoy. Most of all, thank you Angela for your patience and encouragement these last five years. I could not have done it without you!

TABLE OF CONTENTS

Page

LIST OF FIGURES

Page

LIST OF SCHEMES

Page

LIST OF TABLES

CHAPTER I

INTRODUCTION

The utopian chemical process would take abundant, low-cost, renewable inputs and convert them at ambient pressure and temperature and with perfect selectivity to highly desirable products without producing any toxic waste. This ideal may not be achievable in every case, but the application of the proper catalyst can realize some fraction of these goals. Widespread efforts are afoot to discover and optimize the catalysts we need.

Immobilized catalysts have many potential benefits including recyclability and reduced metal contamination of products. The main difficulty that is encountered with immobilized catalysts is leaching, whereby the metal catalyst detaches from the support material. Leaching reduces the recyclability of the catalyst and leads to metal contamination of the products.

The first goal of the work presented in this thesis is to prevent catalyst leaching and decomposition by using tridentate phosphine ligands to firmly coordinate the metal complex. The next chapter will focus on the catalysis, using both homogeneous and immobilized nickel complexes to accomplish the cyclotrimerization of phenylacetylene. The decomposition of nickel catalysts to form nanoparticles will be discussed, and the reactivity of these nanoparticles as catalysts will be briefly investigated.

The final chapters of this work will delve into the mobilities of organometallic complexes on surfaces. These important studies are relevant to understanding the

mechanism of nanoparticle formation on surfaces, as well as to the deliberate formation of supported nanoparticle catalysts and perhaps even single atom catalysts.

CHAPTER II

COMPLEXES WITH TRIPODAL PHOSPHINE LIGANDS*

INTRODUCTION

Immobilized Catalysts

A central focus of the Bluemel group research is to immobilize homogeneous catalysts on silica gel to facilitate the separation of the catalyst from the reaction mixture. This easy separation will ideally lead to reduced metal contamination of the product as well as recyclability of the catalyst.[1] Leaching of the metal species is the bane of immobilized catalysts, but well chosen linkers can improve the lifetime of immobilized catalysts. Examples of successful immobilized catalysts include rhodium hydrogenation catalysts,[2] Pd(0)/Cu(I) Sonogashira systems for C-C cross-coupling reactions,[3] and nickel catalysts for acetylene cyclotrimerization[4] and hydrophosphonation.[5]

Benefits of Tripodal Phosphine Ligands

The Bluemel group has previously applied mono- and bidentate phosphine linkers to the immobilization of nickel catalysts. While some of these catalysts are very active and recyclable, they do display symptoms of nanoparticle formation.[6] The group

* Reproduced with permission from "Monometallic Ni(0) and Heterobimetallic Ni(0)/Au(I) Complexes of Tripodal Phosphine Ligands – Characterization in Solution and in the Solid State and Catalysis" Cluff, K. J.; Bhuvanesh, N.; Blümel, J. *Chem. - Eur. J.* **2015**, *21*, 10138-10148. Copyright Wiley-VCH Verlag GmbH & Co. KGaA.

has also observed that immobilized molecular rhodium hydrogenation catalysts eventually form nanoparticles,[2a,2b] but that these are also very active catalysts. In the case of nickel, however, it is desirable to avoid nanoparticle formation since it leads to less selective catalysts. Metal complexes linked to the surface via multidentate linkers[3a,4a] have more favorable recycling characteristics than those which employ only monodentate linkers. The Bluemel group has also shown with *in situ* HRMAS NMR that catalysts are retained better by linkers with higher coordinating strengths.[3a,3b]

Tripodal phosphine ligands (tripods), with strong tridentate coordination of the Ni^0 metal center were employed in this work to prevent nanoparticle formation on the premise that if bidentate linkers reduce leaching somewhat, a tridentate linker may stop leaching and nanoparticle formation altogether.

Tripod ligands are also expected to reduce agglomeration by shielding the metal center from other complexes, thus impeding nanoparticle formation, but still allowing substrate access. As shown in Figure 2.1, tripod ligands shield the metal center from interaction with the reactive oxide support and from interaction with neighboring catalysts with the "fence" of phenyl groups surrounding the metal. This is very important since it was noted in earlier work[6a] that the immobilized nickel catalysts had much longer lifetimes when they were dilute on the surface. With a protective ligand, like the tripod ligands shown in Figure 2.1, higher catalyst loadings might be possible without sacrificing recyclability. This is a key benefit because it reduces the catalyst bulk, and thus makes it more attractive for industry.

Furthermore, the sterics of these complexes preclude the formation of double layers of linkers[3a,4c] which have been shown to facilitate metal leaching.

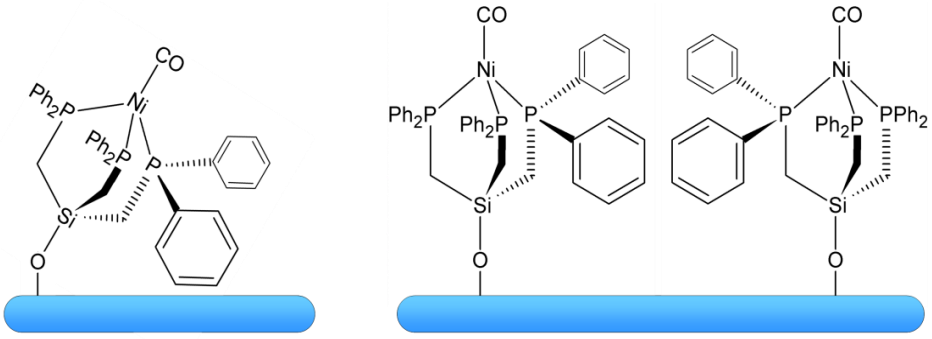

Figure 2.1 Immobilized nickel tripod complexes which are shielded from interactions with the support surface and neighbors.

RESULTS AND DISCUSSION

Synthesis and Characterization of Ni(CO)Triphos (2)

Although immobilizable versions of tripod ligands incorporating ethoxysilane groups[7] or phosphonium salts[2b] can easily be synthesized, for the sake of solubility and the ease of handling without having to prevent cross-linking, the original tripodal phosphine ligands **1** and **5** with methyl groups and carbon or silicon as center atoms have been applied here.

The nickel tripod complex **2** was prepared as a yellow crystalline powder in good yield by the reaction of **1** with $Ni(CO)_2(PPh_3)_2$ in toluene at 90 °C (Scheme 2.01). **2** may

also be obtained by heating complex **3** either in solution or in the dry state (*vide infra*). An alternative route, albeit less convenient, is to form the bidentate Ni(II) complex by reaction of the tripod ligand **1** with either $NiCl_2$ or $NiCl_2(py)_4$ and then reducing with Zn powder while CO is bubbled through the solution.

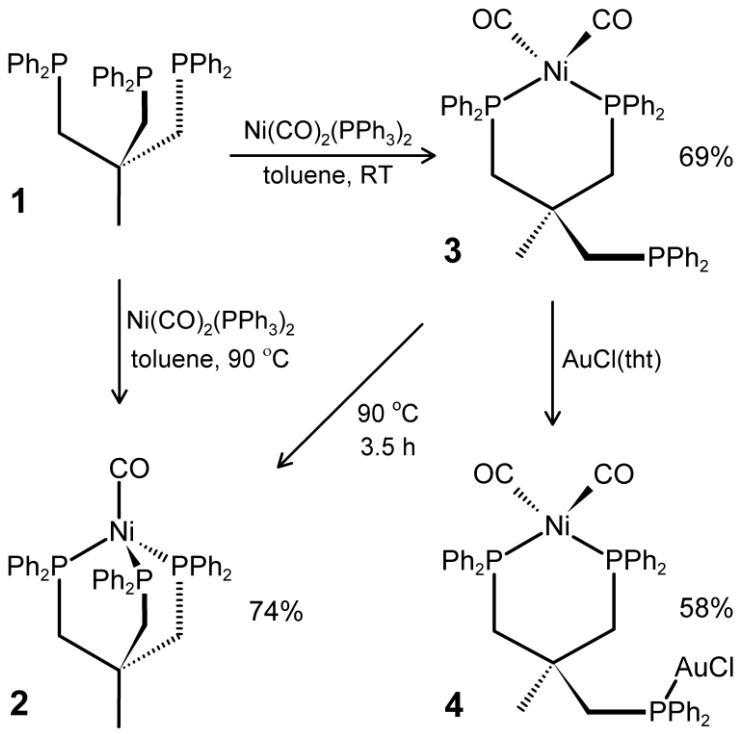

Scheme 2.1 The synthesis of nickel complexes **2-3** and nickel/gold complex **4**.

A single equivalent of PPh_3 is produced by the reaction and easily washed away with pentane, since **2** is insoluble in pentane. Although oligomers and polymers could theoretically form, in practice, this has not been observed, even when the reaction is performed under concentrated conditions, most likely because the ligand exchange takes

place very quickly. Ligand **1** is relatively stable in air as a solid, and is prevented from oxidizing during the reaction by rigorous Schlenk techniques. Although **2** may be weighed and handled in air briefly, it decomposes, turning green, if exposed to air for long periods of time. The ^{31}P NMR spectrum of **2** shows a clean singlet as expected from the symmetry of the molecule (Figure 2.2).

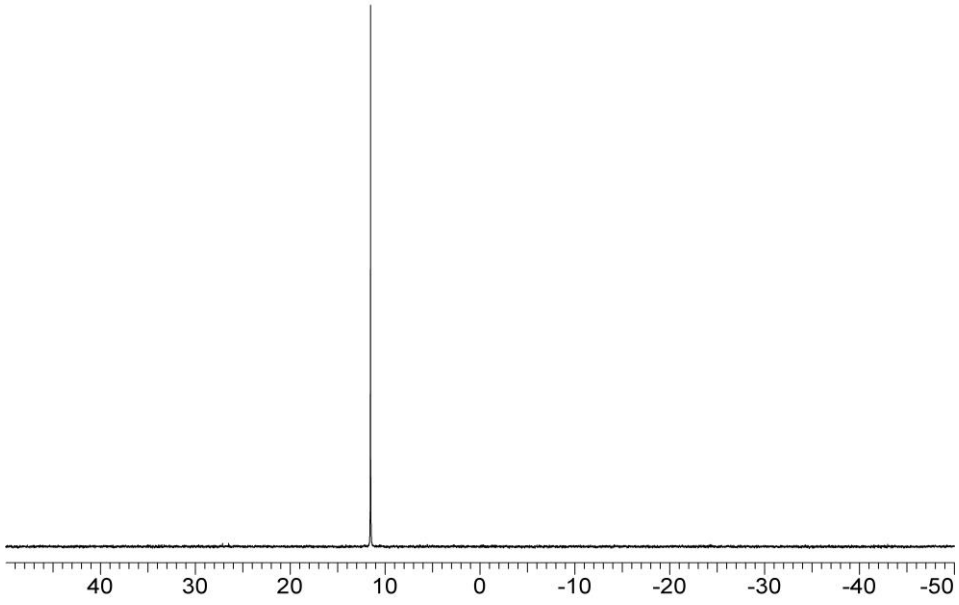

Figure 2.2 ^{31}P NMR of complex **2** in C_6D_6.

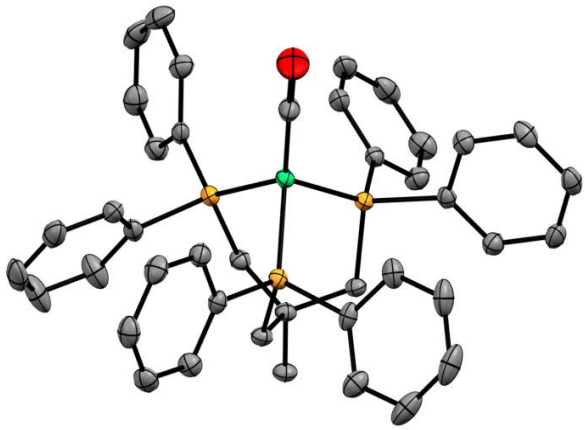

Figure 2.3 Single crystal X-ray structure of **2**. Thermal ellipsoids are shown at the 50% probability level. Hydrogen atoms are omitted for clarity.

The X-ray structure of **2** (Figure 2.3) shows that the nickel center is tetrahedrally coordinated by the phosphines of the tripod ligand and a single CO group. The Ni-P bond lengths are nearly identical with 2.182/2.181/2.186 Å and are mainly determined by the steric demands of the ligand. The P-Ni-P angles (92.45/93.91/95.95°) are all smaller than the expected tetrahedral angle, probably due to steric constraints.

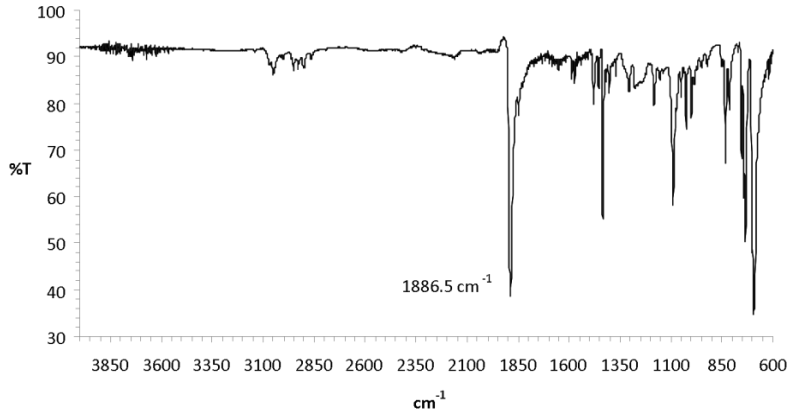

Figure 2.4 IR spectrum of **2**.

The IR stretching band of the carbonyl group is found at 1886.5 cm^{-1}, which indicates strong π-backbonding interactions with the metal. This strong bond makes it very difficult for the substrate to find an open site, and the catalytic activity of this compound suffers as a result.

Synthesis and Characterization of $Ni(CO)_2$Triphos (3)

Complex **3** is synthesized as shown in Scheme 2.01, by exchanging the two PPh_3 ligands of $Ni(CO)_2(PPh_3)_2$ with two of the alkyldiphenyl phosphine arms of **1** to give a white powder. Both CO ligands remain coordinated to nickel if the reaction is carried out at room temperature. The reaction proceeds very cleanly, giving a pure product after several washes with pentane. The ^{31}P NMR spectrum (Figure 2.5) shows a clean doublet and triplet with a $^4J(^{31}P\text{-}^{31}P)$ coupling constant of 2.2 Hz. While 100% conversion of **3** to **2** is fast at high temperatures (Figure 2.6), the conversion is much slower at room temperature, with less than 10% conversion even after 20 days (Figure 2.7). This

compound is reasonably stable at room temperature, but for long term storage lower temperatures are best. The purity of **3** is readily apparent in the color which is pure white but turns yellow as **2** is formed.

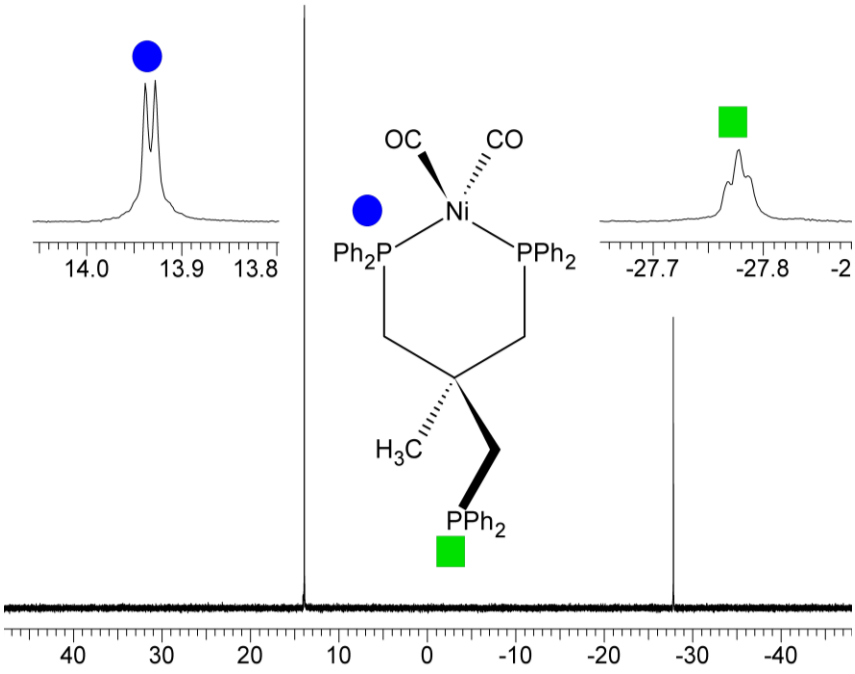

Figure 2.5 ^{31}P NMR spectrum of **3**.

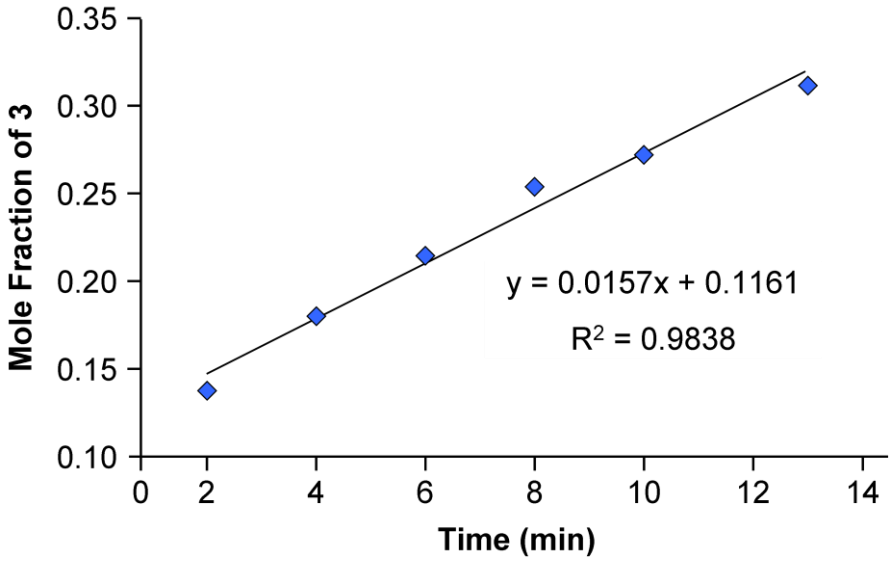

Figure 2.6 Plot showing the conversion of **2** to **3** at 90 °C.

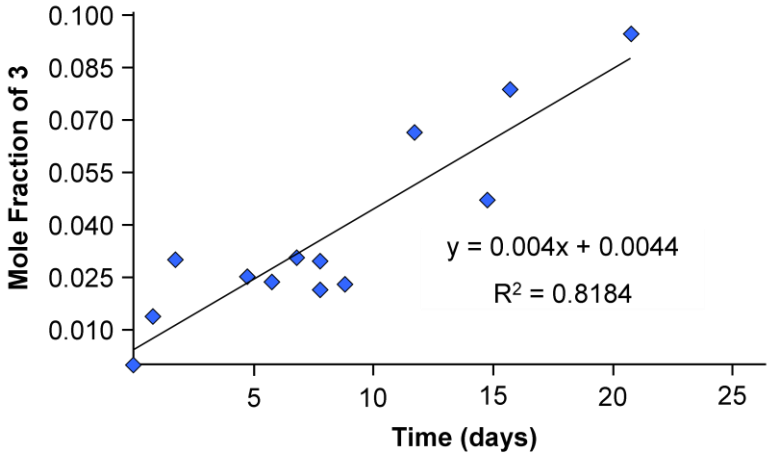

Figure 2.7 Plot showing the conversion of **2** to **3** over time at room temperature.

The assignment of some of the ^{1}H and ^{13}C NMR signals required 2-dimensional methods. $H3_{anti}$ and $H3_{syn}$ (Figure 2.8) are diastereotopic, and thus have different chemical shifts, and they couple with each other. Both proton resonances are seen to

correlate with a single carbon resonance in the ^{1}H-^{13}C COSY spectrum (Figure 2.8). The two signals are assigned via the NOESY spectrum (Figure 2.9) where $H3_{anti}$ shows a correlation with the methyl protons H1, while $H3_{syn}$, being further away, gives only a very weak cross-peak.

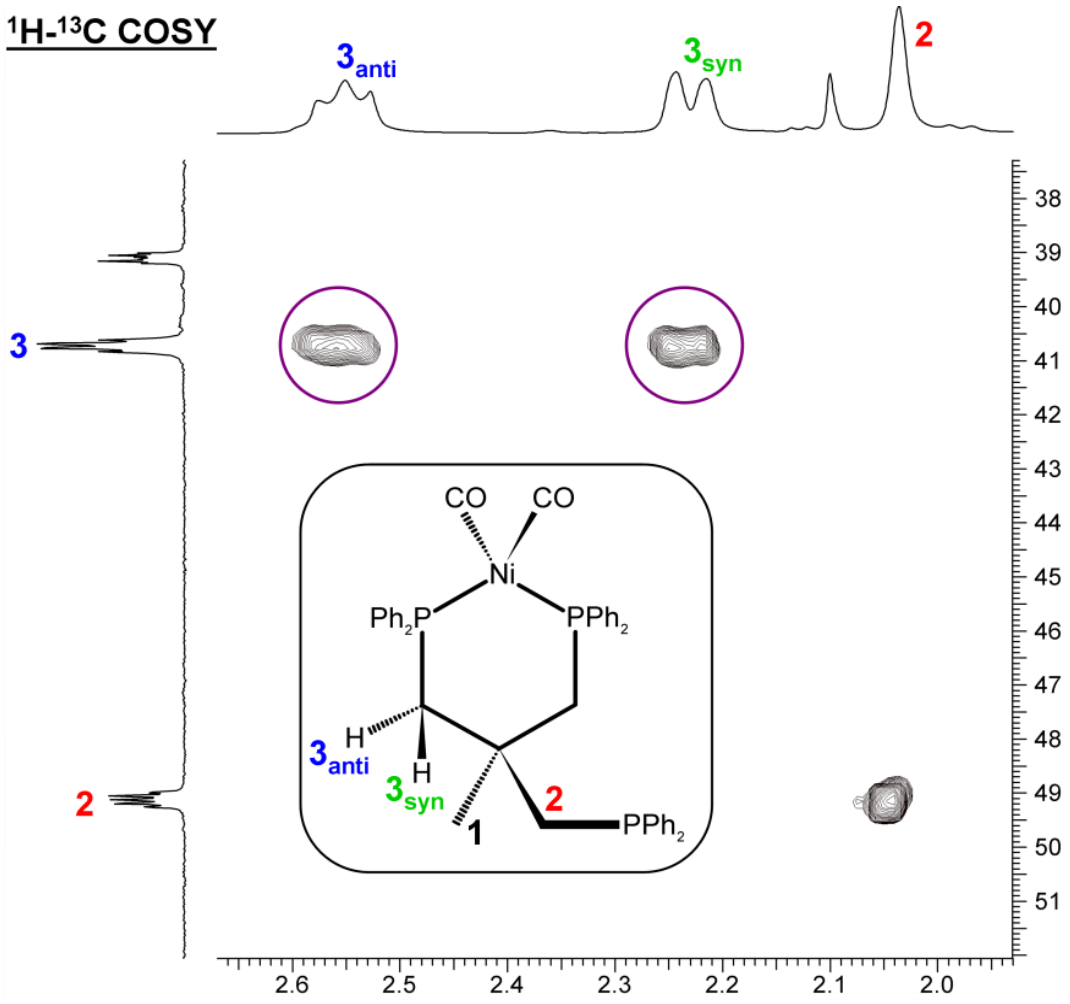

Figure 2.8 ^{1}H-^{13}C COSY spectrum of complex **3**.

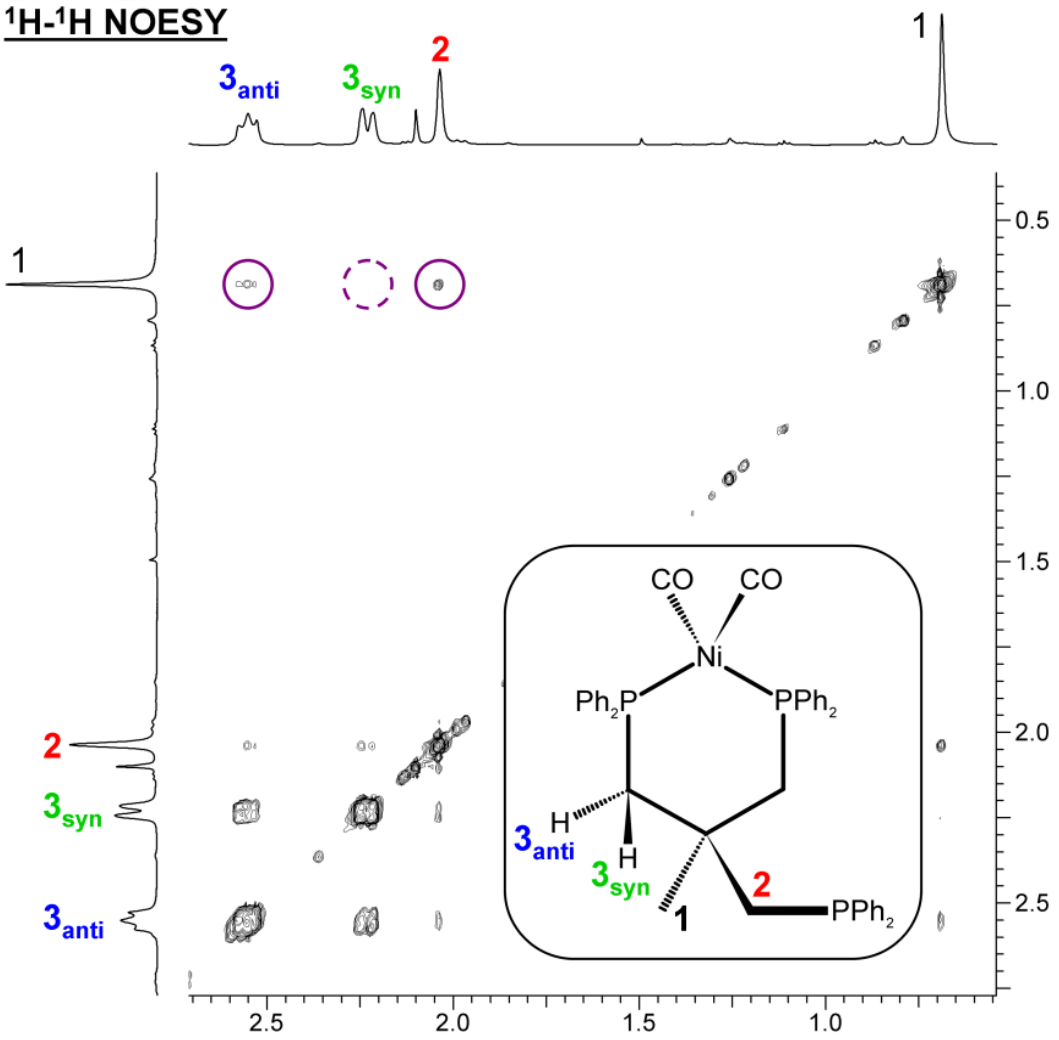

Figure 2.9 ^{1}H-^{1}H NOESY NMR spectrum of complex **3** in C_6D_6.

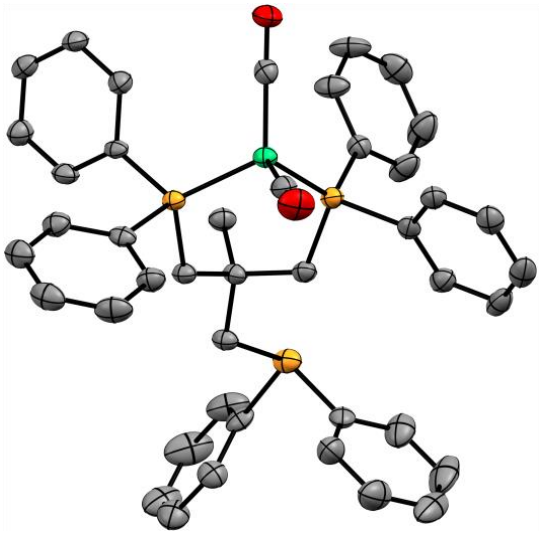

Figure 2.10 Single crystal X-ray structure of **3**. Thermal ellipsoids are shown at the 50% probability level. Hydrogen atoms are omitted for clarity.

The X-ray structure of **3** proves that only two phosphine groups of the tripodal ligand are coordinated to the nickel center. The third phosphine group remains uncoordinated (Figure 2.10), although the orientation of its lone pair seems to predestine it for replacing one of the two CO groups. The relative stability of **3** might be due to steric constraints of the tripodal ligand and thus hindrance of the attack of the phosphine at the metal center in the direction of the syn-positioned CO group. Furthermore, the chair conformation of the six-membered ring incorporating the nickel atom, which is best seen in Figure 2.11, has to change into a less favorable boat conformation for coordinating the third phosphine group.

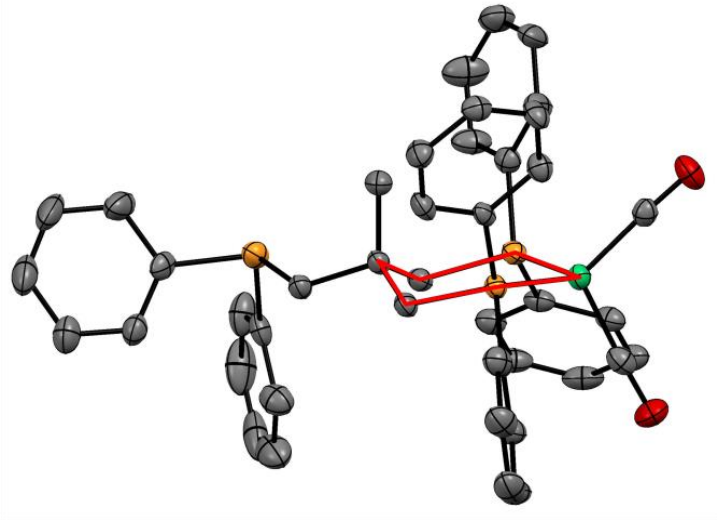

Figure 2.11 Single crystal X-ray structure of **3** with the chair structure highlighted in red. Thermal ellipsoids are shown at the 50% probability level. Hydrogen atoms are omitted for clarity.

Two CO stretching absorptions are observed in the IR spectrum as expected (Figure 2.12). They are both at higher frequencies than the stretching band observed for **2** (Figure 2.4). This is in accord with the consideration that the electron density available for back-bonding is now shared between two CO groups and so neither bond is attenuated to a great extent. This weaker bonding of CO is additionally manifested by the fact that CO leaves slowly over time, even at room temperature (Figure 2.7) and quickly if the sample is heated (Figure 2.6).

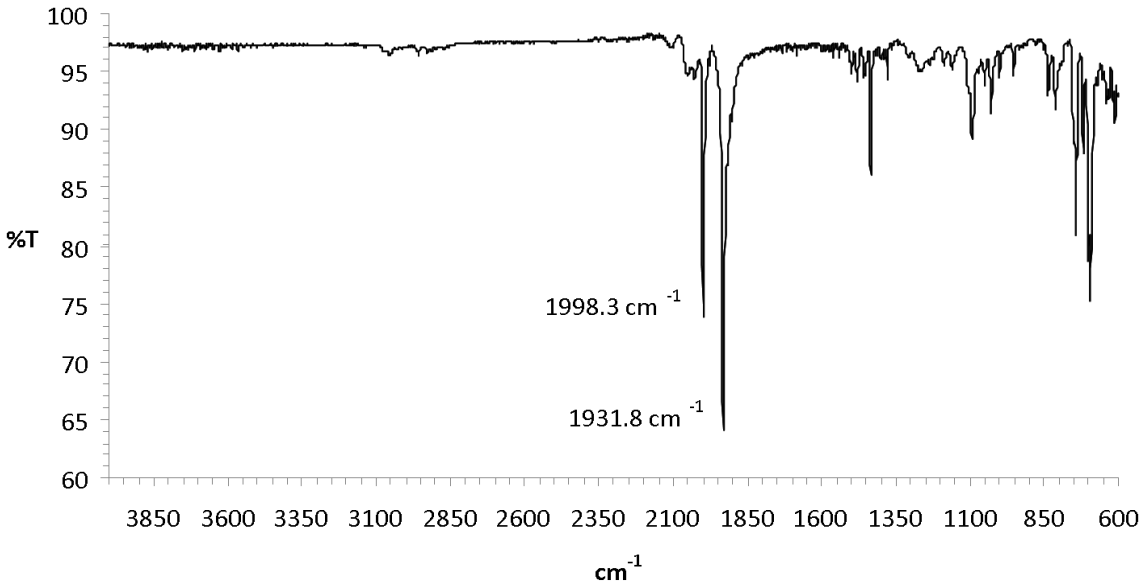

Figure 2.12 IR spectrum of complex **3**.

Synthesis and Characterization of Ni(CO)$_2$TriphosAuCl (4)

The most exciting feature of **3** is the possibility to coordinate an additional metal atom by the free phosphine "arm". Preliminary efforts applying ClAuPPh$_3$ as the gold source resulted in a situation where PPh$_3$ and the free phosphine arm competed for Au, leading to a rapid dynamic equilibrium. It proved impossible to remove the PPh$_3$ by washing with pentane. Depending on the exact amount of PPh$_3$, different chemical shifts were observed for the phosphine coordinating to gold in the ^{31}P NMR spectra (Figure 2.13). For example, the signal for Ph$_3$P-Au moves upfield as additional PPh$_3$ is added until there is such an excess that each molecule of PPh$_3$ spends so little time coordinated to gold that the chemical shift almost matches that of pure PPh$_3$. Similarly, the signal arising from a tripod arm coordinating to gold also steadily shifts upfield as it is increasingly outcompeted for gold by the excess of PPh$_3$ until each free tripod arm

coordinates gold so briefly, on average, that the chemical shift matches that of the free phosphine.

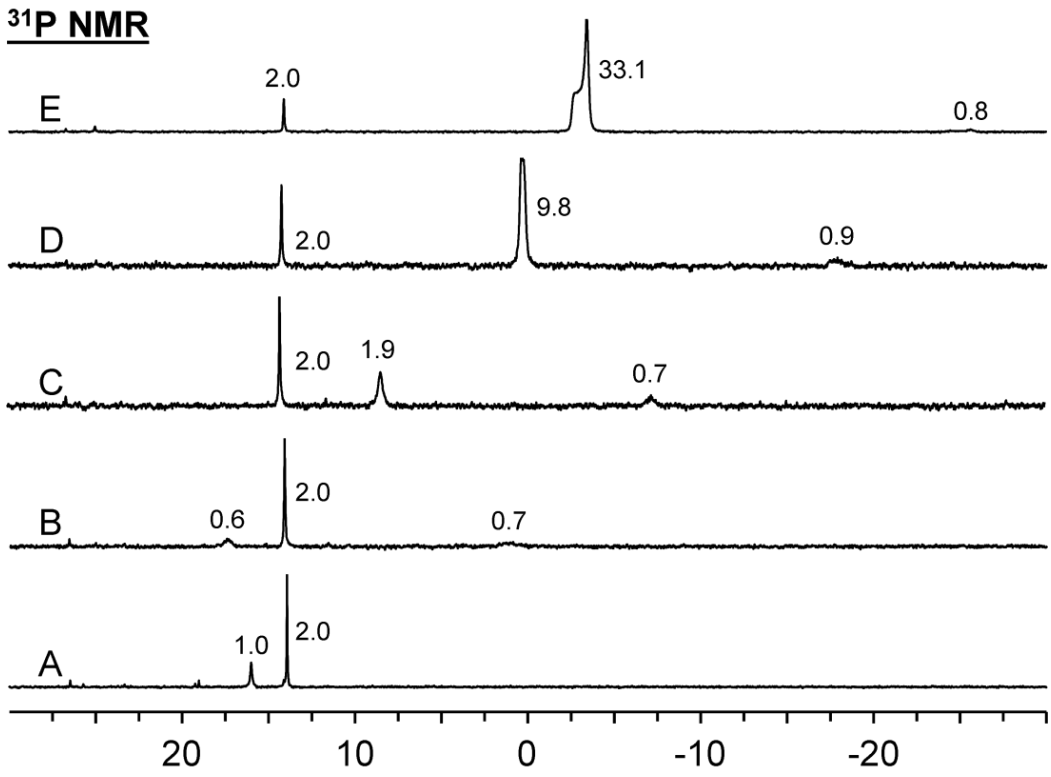

Figure 2.13 ^{31}P NMR (in C_6D_6) spectra of $Ni(CO)_2$TriphosAuCl (A) synthesized via ClAu(tht); (B to E) increasing amounts (not precisely measured) of PPh_3 added to the NMR tube. Relative signal intensities for all signals are given in the spectra.

4

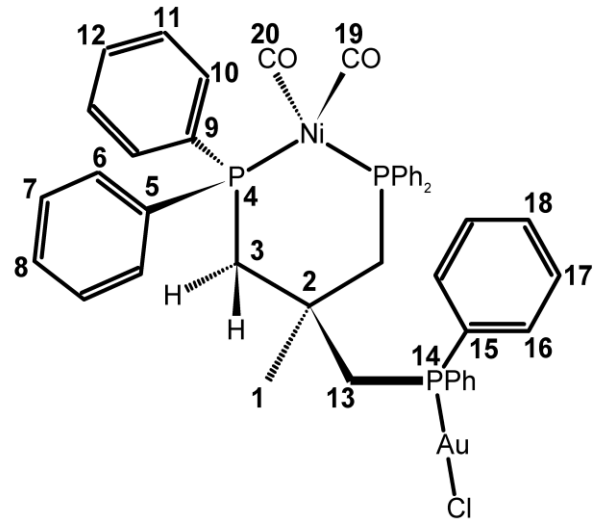

Figure 2.14 Numbering of complex **4** used for NMR assignments.

Although the peak for P14 (Figure 2.14) was always too broad to observe the triplet brought about by the $^{4}J(^{31}P\text{-}^{31}P)$ coupling, a 1.7 Hz coupling is visible on the signal for P4, resulting in a doublet. Variable temperature experiments helped to identify the signals seen in the ^{31}P NMR spectra (Figure 2.15).

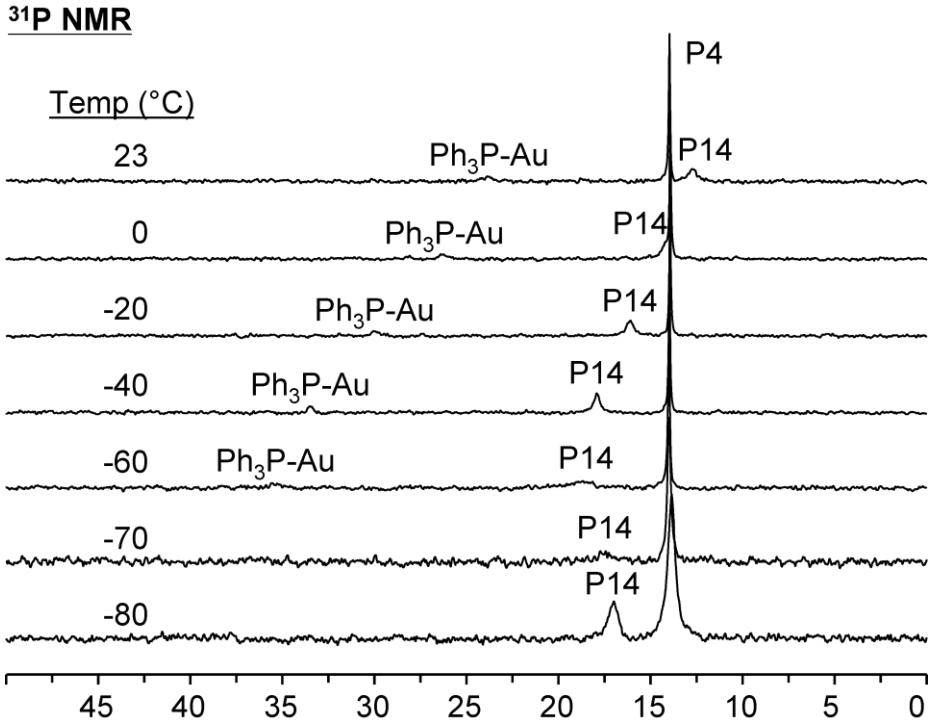

Figure 2.15 Variable temperature ^{31}P NMR spectra (acetone-d_6) of **4** with PPh_3 contamination. See Figure 2.14 for assignment of P14 and P4.

As the temperature is lowered, signal B, which corresponds to PPh_3 in equilibrium with $ClAuPPh_3$, shifts downfield and approaches the chemical shift of undisturbed $ClAuPPh_3$. This signal also seems to lose intensity at lower temperatures, probably because the alkyldiphenylphosphine-Au complex is more thermodynamically stable than the triarylphosphine-Au complex. Signal A, which is assignable to P14 in equilibrium with P of the free tripod arm, shifts, at very low temperatures, to the position of the undisturbed tripod-Au complex. Unlike signal B, A grows in intensity at lower temperatures because it corresponds to the thermodynamically favored product. Based on these results, it may be possible to remove the PPh_3 by cooling a toluene/pentane

solution slowly until the desired product precipitates and then removing the supernatant while still cold. It is much easier, however, to simply repeat the synthesis using a different gold precursor, ClAu(tht). The PPh_3-free precursor yields much simpler results and the ^{31}P NMR spectrum (Figure 2.16) very closely resembled the -80 °C spectrum in Figure 2.15. All further syntheses were conducted using ClAu(tht) and proceeded in a straightforward manner, without any of the complicating factors of fluxional behavior or ligand exchange.

Complex **4** is the simplest nickel/gold heterobimetallic complex known so far, and it is the only one in which nickel has a (0) oxidation state.[8] Heterobimetallic complexes are difficult to synthesize selectively,[9] but they are of phenomenological and also practical importance because they might display synergistic effects in catalysis. Heterobimetallic complexes may also have the potential to provide metal atom assemblies as preconditioned systems for the formation of nanoparticles with a well-defined stoichiometry of metal atoms. Such nanoparticles or clusters are very rare in the literature.[10]

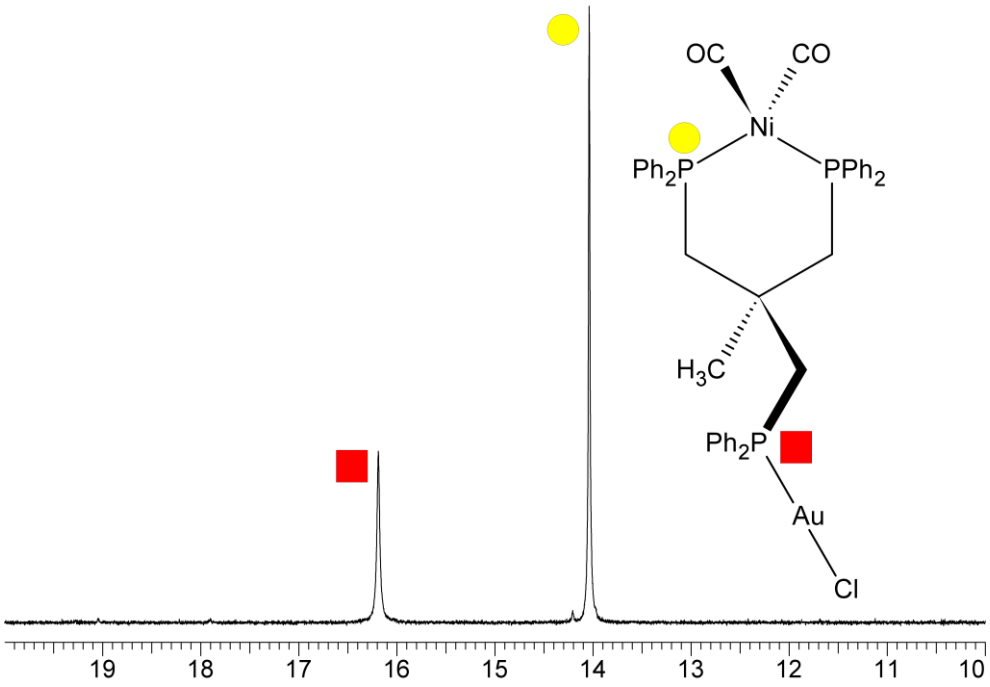

Figure 2.16 ^{31}P NMR spectrum of complex **4** in C_6D_6.

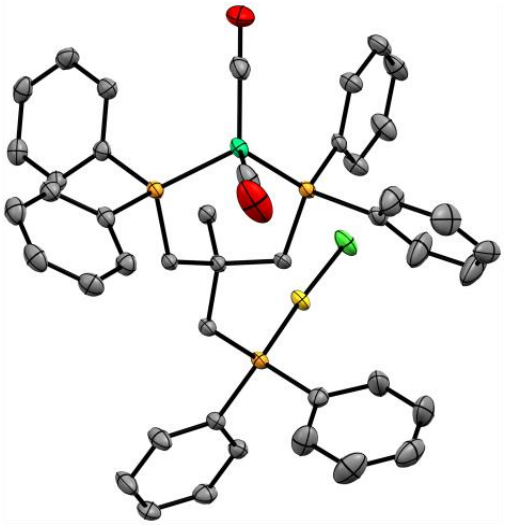

Figure 2.17 Single crystal X-ray structure of **4**. Thermal ellipsoids are shown at the 50% probability level. Hydrogen atoms are omitted for clarity.

The X-ray structure of the heterobimetallic complex **4** differs only slightly from the one of **3**, except for the additional presence of the AuCl moiety (Figure 2.17). As with complex **3**, a chair conformation of the six-membered ring incorporating the nickel atom is observed. Taking into account that the AuCl moiety is pointing towards the nickel center, with a rather short Ni···Au distance of 7.085 Å, the stability of the compound is even more astonishing. Probably the steric constraints discussed for **3** above play a major role in **4** as well.

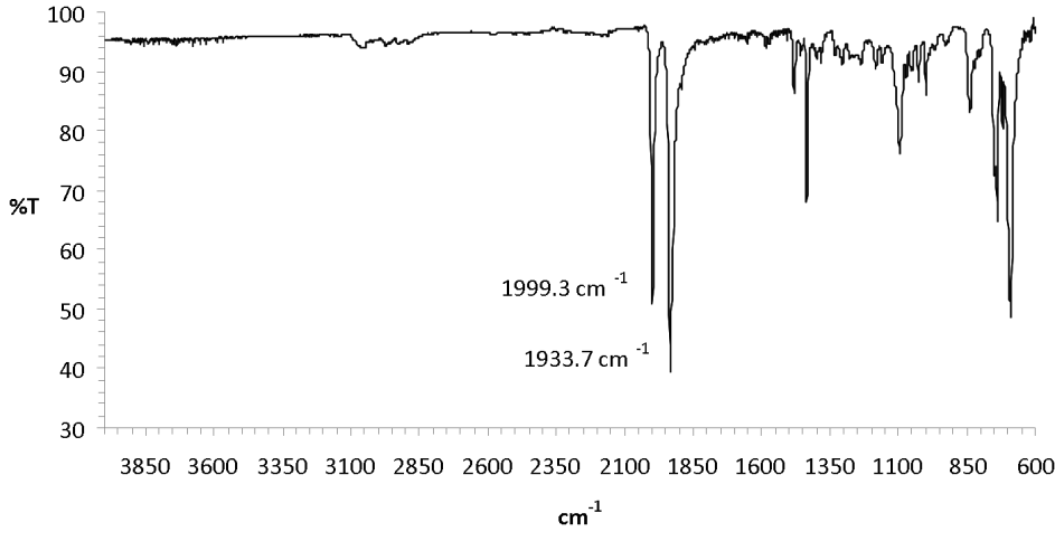

Figure 2.18 IR spectrum of complex **4**.

The IR spectrum of **4** (Figure 2.18) is also very similar to that of **3**, however, there is a clear difference in the ^{13}C NMR spectra in the region of the carbonyl resonances. Although the two signals are separated by almost 3 ppm (Figure 2.19-A) in the case of complex **3**, they are separated by only 0.25 ppm (Figure 2.19-C) in the

spectrum of complex **4**. Interestingly, an intermediate case arises when complex **4** is contaminated by PPh_3 (Figure 2.19-B). This is an unexpected result since **4** would be expected to have slower fluxional behavior than **3**, and thus the widest separation of the signals. On the other hand, **3** whose uncoordinated phosphine arm is poised to quickly trade with either coordinated arm, might be more likely, because of this potential motional averaging of the two carbonyl positions, to have closely spaced carbonyl resonances. Since this is clearly not the case, the chemical shift differences must arise from purely electronic factors.

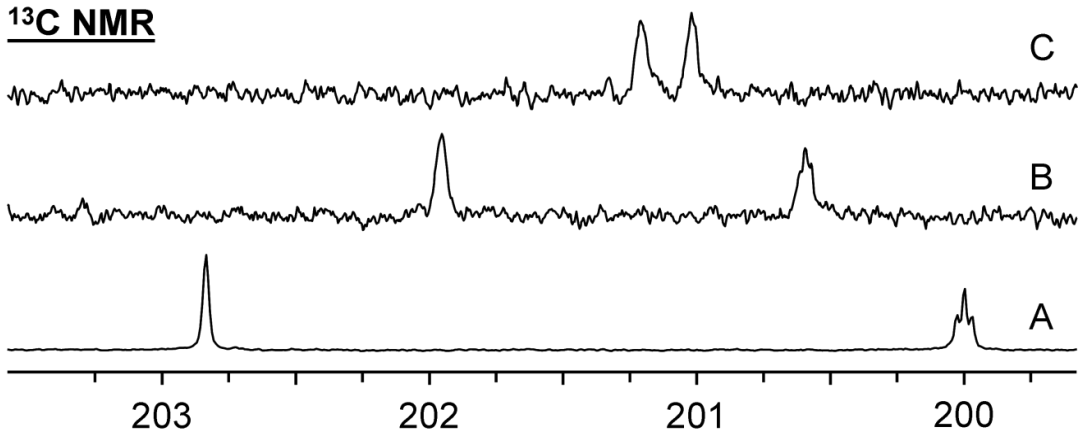

Figure 2.19 ^{13}C NMR spectra of **3** (A), **4** with PPh_3 contamination (B), and clean **4** (C).

The methylene proton signals in the ^{1}H NMR spectrum of **4** are shown in Figure 2.20 with different ^{31}P frequencies selectively decoupled. The upfield signal belongs to H13 (Refer to Figure 2.14 for numbering) because it couples very strongly to the Au-coordinating phosphine (P14) and collapses to a singlet when P14 is selectively

irradiated. As with complex **3**, the protons bound to C3 are diastereotopic and give different signals. The selective ^{31}P decoupling experiments show that one of these diastereotopic protons couples more strongly to P14 than the other. This difference arises because of the dihedral angles, which, according to the Karplus curve, predict that $H3_{anti}$ couples more strongly to P14 than $H3_{syn}$. This slight difference in the coupling characteristics can be used for the signal assignment.

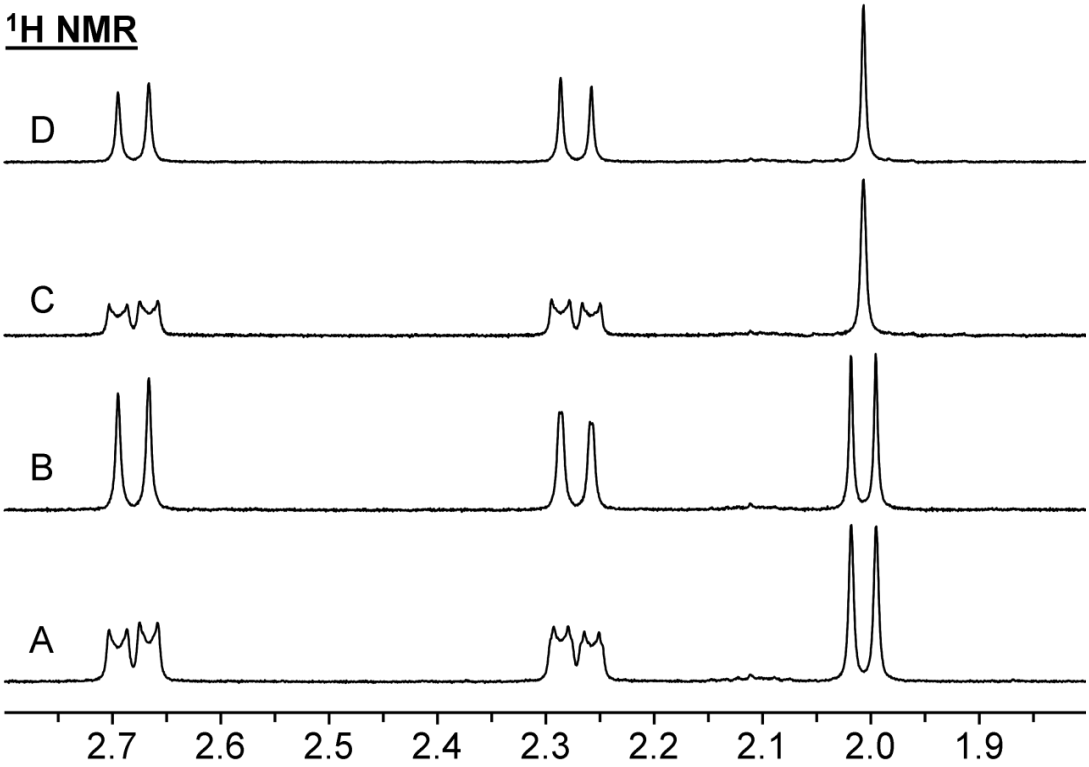

Figure 2.20 ^{1}H NMR spectra of **4**, alkyl region. A: no ^{31}P decoupling; B: selective decoupling on the P-Ni resonance; C: decoupling on the P-Au resonance; D: decoupling on both phosphorus resonances.

This signal assignment is confirmed by 2-dimensional methods. In the NOESY NMR spectrum (Figure 2.21) $H3_{anti}$, which is much closer to the methyl group (H1) shows a strong cross-peak with (H1) while a much weaker peak is observed for $H3_{syn}$. A similar difference in coupling is observed for complex **3**.

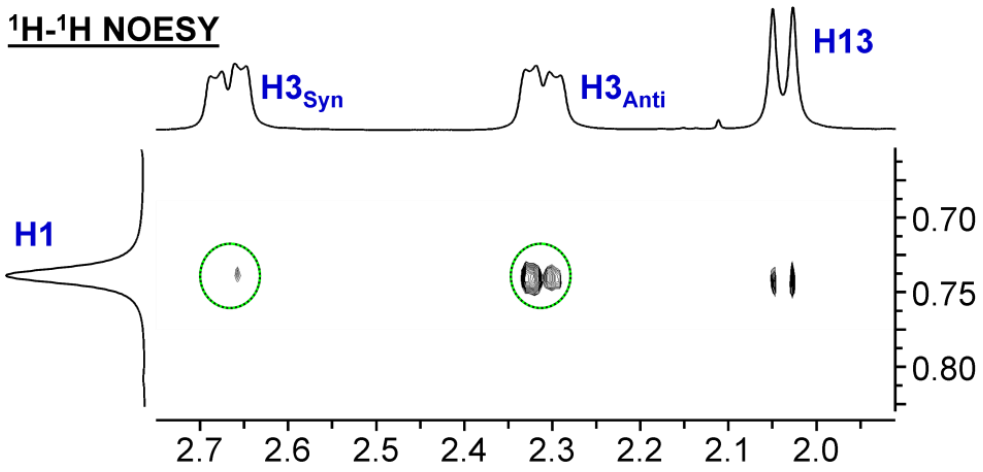

Figure 2.21 ^{1}H-^{1}H NOESY spectrum of complex **4**, alkyl region.

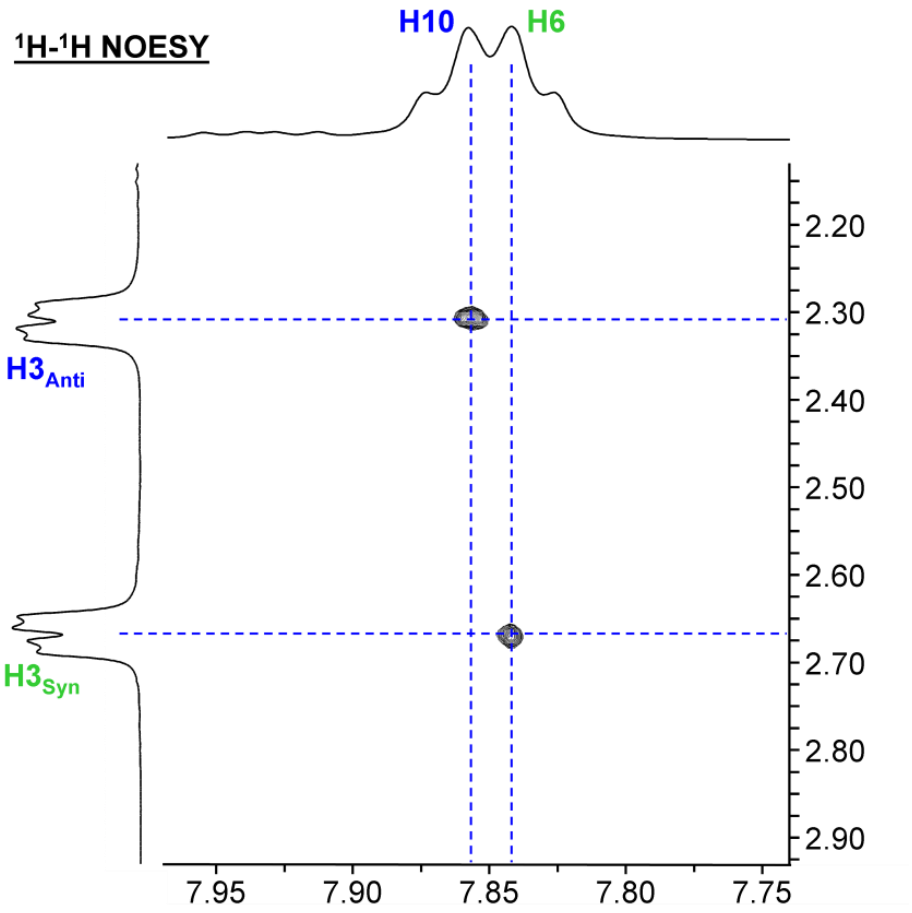

Figure 2.22 ^{1}H-^{1}H NOESY spectrum of complex **4**, aryl region.

Once the assignment is known for $H3_{anti}$ and $H3_{syn}$, the NOESY spectrum also differentiates H10 from H6 (Figure 2.22), because the backward facing phenyl rings interact with the backward facing protons and vice versa. C10 and C6 can then be assigned via the HSQC spectrum (Figure 2.23).

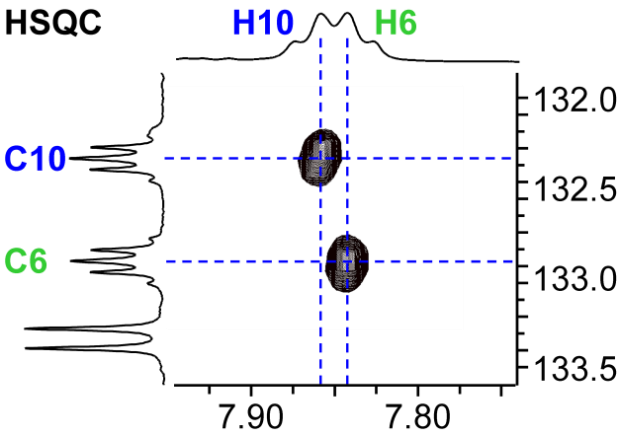

Figure 2.23 ^{13}C-^{1}H COSY of complex **4**, aryl region.

Synthesis of Ni(CO)[PMe(CH$_2$PPh$_2$)$_3$][OTf]

Ni(CO)[PMe(CH$_2$PPh$_2$)$_3$]$^+$[OTf]$^-$ was synthesized in the same way as **2**, save that the phosphonium centered tripod (Figure 2.24) was used in place of **1**. The ^{31}P NMR spectrum is shown in Figure 2.24. Although the desired product features prominently in the spectrum, there are also several byproducts, probably a mixture of various phosphine oxides and/or oligomeric products between 20 and 30 ppm. These could probably be avoided by the use of cleaner starting materials, and by running the reaction under much more dilute conditions. This complex has not been fully characterized because **2** was an ineffective catalyst and it was expected that this similar complex would also be relatively inactive with respect to acetylene cyclotrimerization.

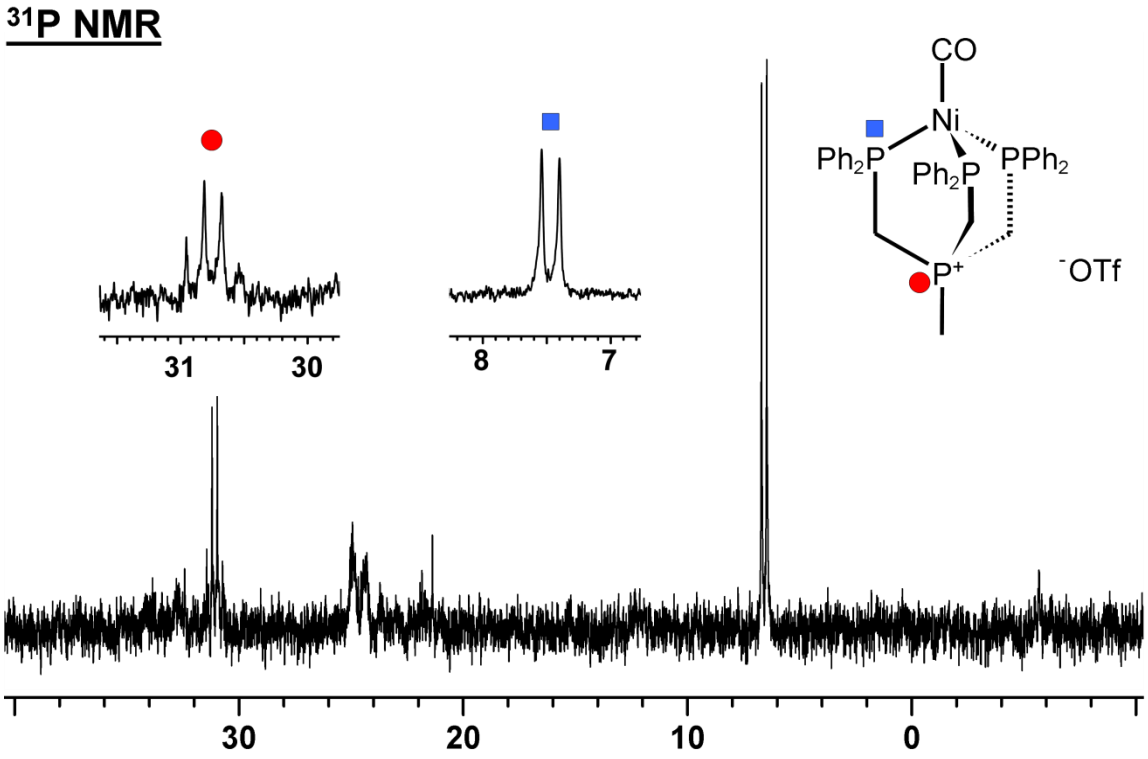

Figure 2.24 ^{31}P NMR spectrum of Ni(CO)[PMe(CH$_2$PPh$_2$)$_3$]$^+$[OTf]$^-$.

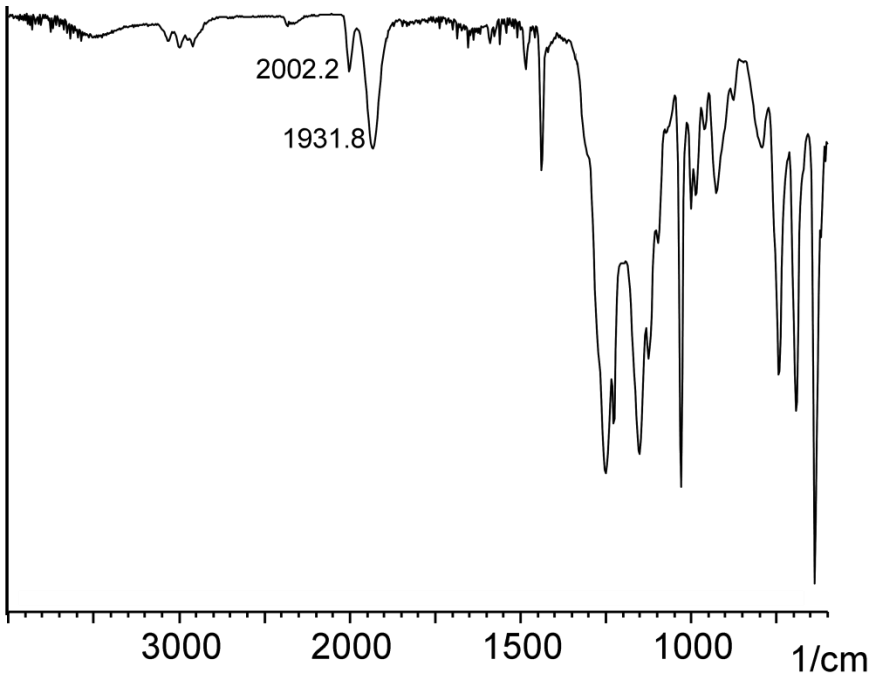

Figure 2.25 IR spectrum of $Ni(CO)[PMe(CH_2PPh_2)_3]^+[OTf]^-$.

On the other hand, the IR spectrum of $Ni(CO)[PMe(CH_2PPh_2)_3]^+[OTf]^-$ (Figure 2.25) shows that the π-backbonding from nickel to CO is substantially reduced as compared to **2**. In fact, the CO stretching frequency is very similar to that of the dicarbonyl nickel complexes **3** and **4**. It is clear that the phosphonium center of the tripod reduces the electron donating strength of the tripod arms. This may hint at the reason for the synthesis of this complex being much less straightforward than that of **2**, and may also foretell slightly better catalytic activity since the phosphine arms should be more labile and allow the substrate to access the metal.

Synthesis and Characterization of (CO)Ni($PPh_2CH_2CH_2$)$_3$SiMe (6)

Due to the unsuitability of **2** as a catalyst, a nickel tripod complex with longer carbon chains in the "arms" was prepared. These longer chains attenuate the chelating strength of the tripod ligand and should make the metal more accessible to the substrate, resulting in higher activity. Several different synthetic routes were attempted, using nickel precursors such as $Ni(CO)_2(PPh_3)_2$ and $NiCl_2(py)_4$, but in all cases a wide distribution of inseparable products resulted. Oligomerization is the most likely reason for the failure of these routes. A straightforward successful synthesis (Scheme 2.02) was finally developed starting from $Ni(CO)(PPh_3)_3$. The benefit of this nickel precursor is probably that the ligand exchange proceeds very rapidly, such that in a sufficiently dilute reaction mixture, the tripod ligand will displace all three PPh_3 ligands from the nickel center before diffusion brings another complex close enough for oligomerization to occur.

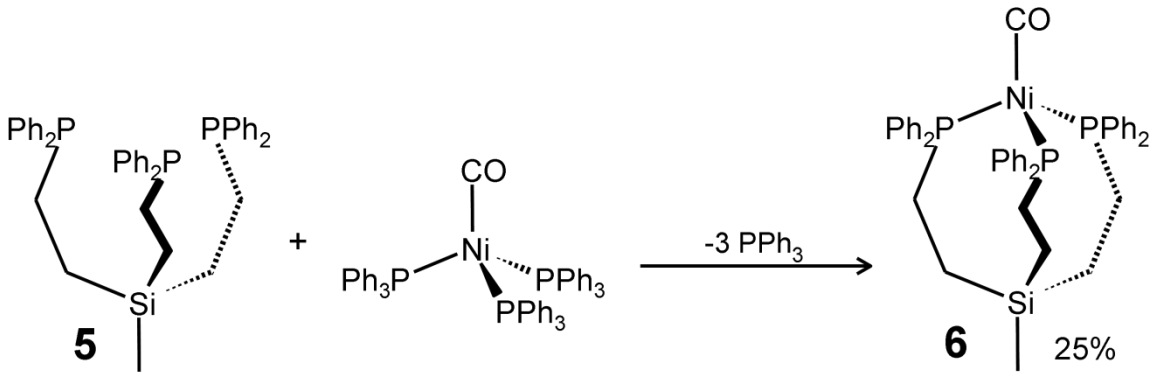

Scheme 2.2 Synthesis of complex **6**.

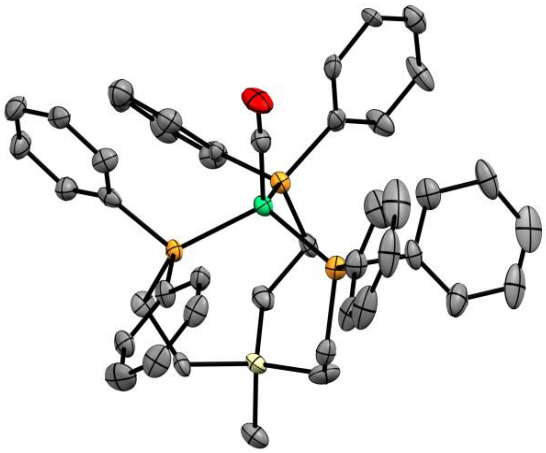

Figure 2.26 Single crystal X-ray structure of **6**. Thermal ellipsoids are shown at the 50% probability level. Hydrogen atoms are omitted for clarity.

Complex **6** has been crystallized from different solvents. The best single crystal X-ray structure of **6**, obtained from toluene and pentane, could be solved and it proves the structure in Scheme 1.02. However, due to twinning and other difficulties, the structure is of lower quality than the other structures shown in this thesis. Even the ^{1}H NMR spectrum of **6** is very clean (Figure 2.27), demonstrating the lack of dimers or oligomers that might be difficult to see in ^{31}P NMR.

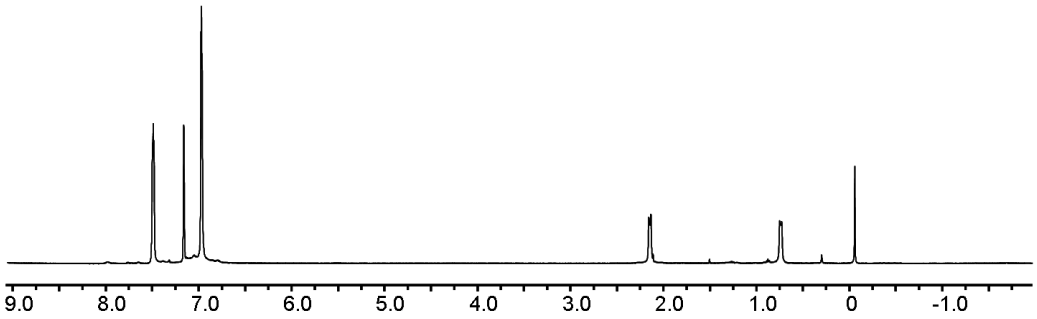

Figure 2.27 ^{1}H NMR spectrum of complex **6** in C_6D_6.

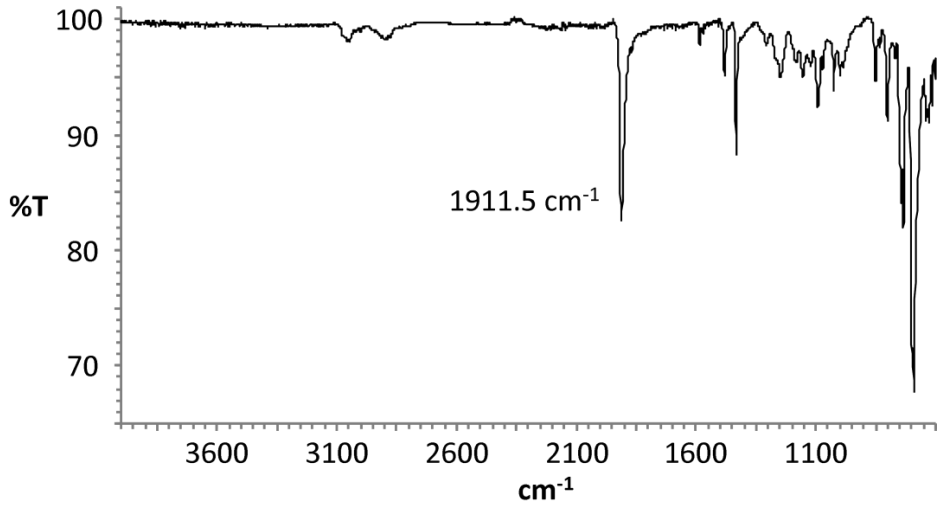

Figure 2.28 IR spectrum of complex **6**.

The CO stretching frequency of complex **6** (1911.5 cm^{-1}, Figure 2.28) is about 25 cm^{-1} higher than that of **2** (1886.5 cm^{-1}, Figure 2.4), indicating that the tripod is slightly less electron donating.

Synthesis and Characterization of $(Ph_3P)Ni(PPh_2CH_2CH_2)_3SiMe$ (7)

The catalytic activity of a nickel tripod complex can also be increased by replacing the very strongly coordinated CO ligand with the more labile PPh_3. Complex **7** was synthesized as shown in Scheme 2.03. **7** must be handled very carefully under inert atmosphere, being extremely oxygen sensitive. In fact, if a flask containing a solution of **7** is opened to air, the red-orange color immediately begins to fade and the solution will be completely colorless in only a few seconds. **7** is also a potent catalyst for the oxidation of PPh_3.

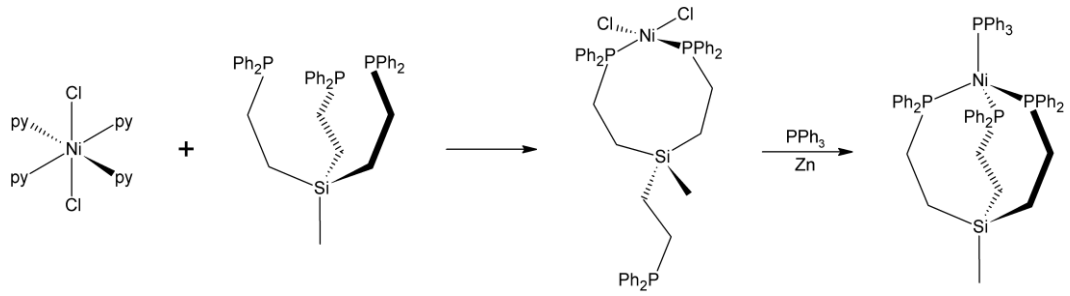

Scheme 2.3 Synthesis of complex **7**.

The ^{31}P NMR spectrum of **7** (Figure 2.29) displays two signals with a coupling constant of 18.1 Hz, a well defined quartet and a doublet.

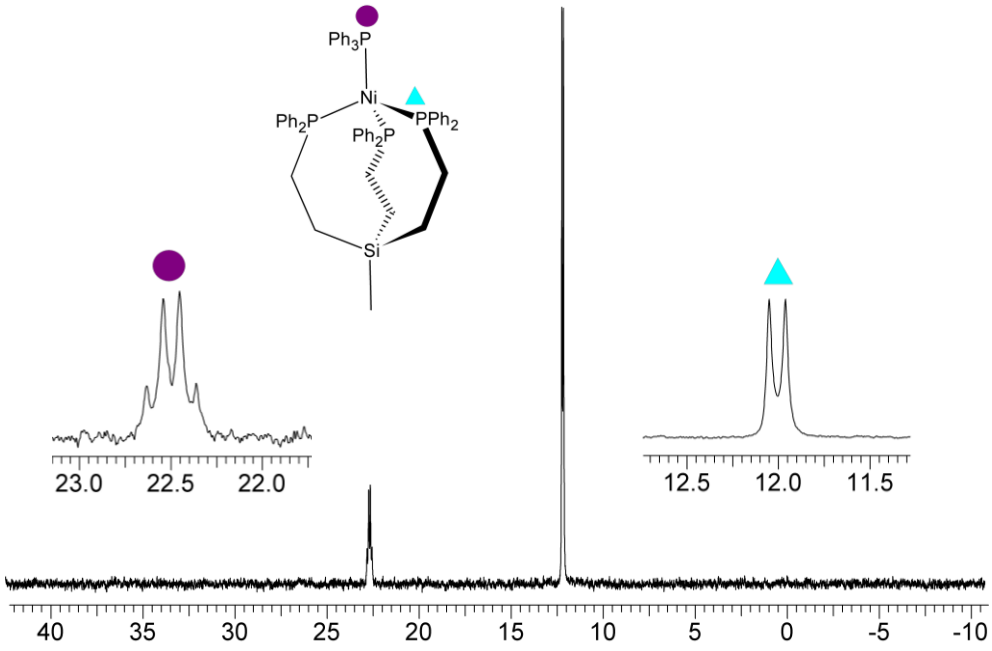

Figure 2.29 ^{31}P NMR spectrum of complex **7**.

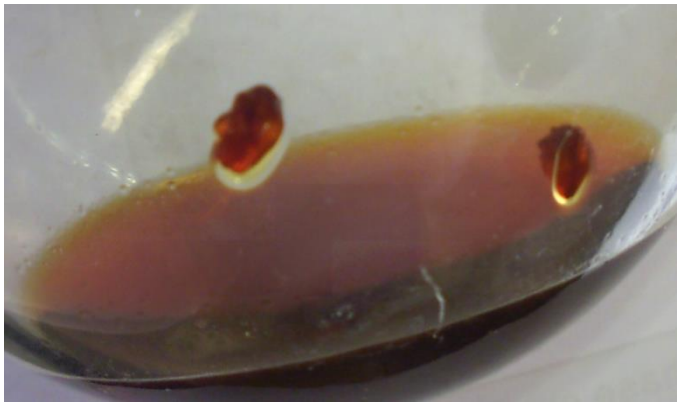

Figure 2.30 Large red crystals of complex **7** from THF and pentane.

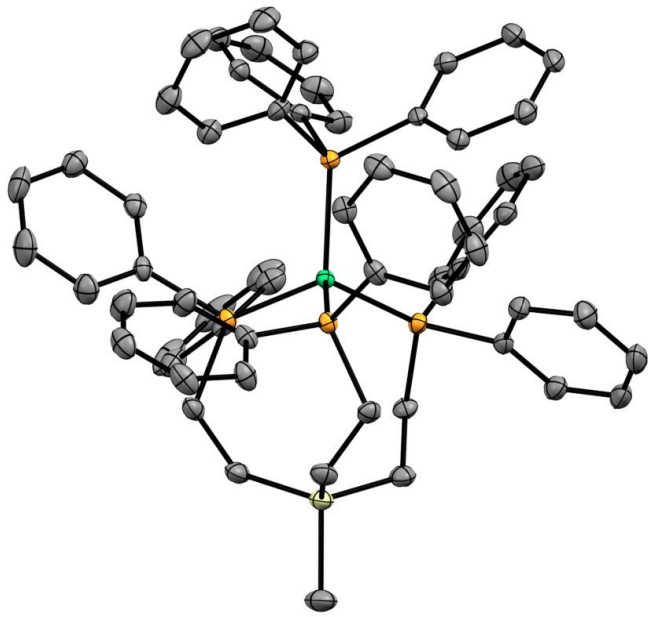

Figure 2.31 Single crystal X-ray structure of **7**. Thermal ellipsoids are shown at the 50% probability level. Hydrogen atoms are omitted for clarity.

Complex **7** crystallizes readily, forming large red crystals (Figure 2.30). Single crystal solid-state NMR was attempted, but was unsuccessful due to miscalibration of the spectrometer. Unfortunately, all crystals obtained later were too small to repeat this analysis.

Single crystal X-ray analysis resulted in a structure of high quality (Figure 2.31). It shows that the nickel center is surrounded tetrahedrally by the phosphine atoms, with the P-Ni-P angles of the tripodal ligand assuming the values 107.13/112.93/109.35°. The Ph_3P-Ni-P angles amount to 111.38/107.42/108.46°. Hereby, the phenyl groups of the tripodal ligand shield the metal center from interacting with other nickel complexes, which might inhibit the formation of nickel nanoparticles and premature deactivation of the catalyst (*vide supra*). The steric demand of the phenyl groups of the tripodal ligand

also interferes with the space occupied by the PPh_3 ligand, which might be the reason for the slightly elongated Ni-PPh_3 bond (2.234 Å) in the molecule, as compared to 2.212/2.207/2.217 Å for the other three Ni-P bond lengths of the coordinated tripodal phosphine ligand. This steric factor might indicate a facilitated release of the PPh_3 ligand and thus explain the high catalytic activity of **7**.

Solid-State NMR Measurements

Complexes **2**, **3**, **4** and **7** were characterized by solid-state NMR.[11] This method grows in importance for the characterization not only of materials like MOFs and POFs[12] and polymers,[13] but it is increasingly applied to insoluble molecular metal complexes.[14] In this field, solid-state NMR is particularly important, because complexes and ligands might not crystallize readily, and only in some cases are the polycrystalline materials of high enough quality for powder diffraction. Naturally, solid-state NMR is indispensable for investigating immobilized catalysts on amorphous supports like oxides that do not allow powder diffraction.[2a] Furthermore, dynamic effects that otherwise complicate the analysis of coordination compounds can be conveniently studied when "frozen" in the solid state.[14a]

The spectra were obtained using magnetization transfer from protons to ^{31}P nuclei (CP, cross polarization)[11] to boost the signal intensities. Magic Angle Spinning (MAS) has been applied to reduce anisotropic line broadening effects in the solid state.[11a]

Besides providing chemical shift information, in favorable cases of clean and polycrystalline materials solid-state NMR spectra result in a wealth of CSA (Chemical Shift Anisotropy) data.[11b] CSA values provide valuable insight about the symmetry of the electronic surroundings of a nucleus, which is of basic interest.[14c,14d] Most importantly, dynamic processes in molecules[14a] and mobilities of adsorbed species on surfaces can be identified and quantified by a reduced or fully collapsed CSA. Finally, from a practical perspective, the CSA is characteristic for each species and thus allows the identification of functional groups in a material or compound. For example, the Bluemel group used CSA values earlier to distinguish surface-bound phosphine oxides from phosphonium salts.[15] More recently, H_2O_2 adducts of phosphine oxides could be described and distinguished from the pure phosphine oxides by their characteristic CSA values.[16] Therefore, one of the goals of this project was to enlarge the CSA data base of nickel phosphine complexes and lay the foundation for further investigation of these catalysts.

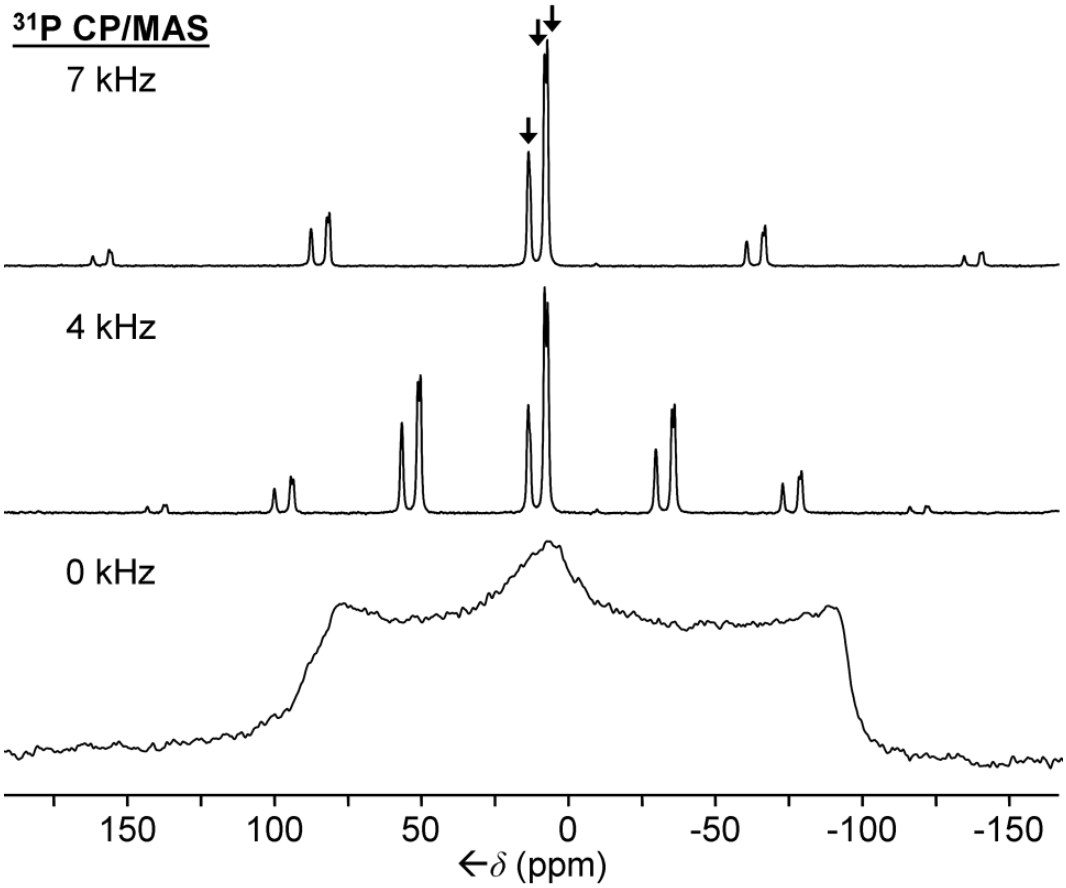

Figure 2.32 ^{31}P CP/MAS NMR spectra of polycrystalline **2**. Vertical arrows indicate the isotropic lines.

The three phosphine functional groups in **2** result in a single resonance in solution ^{31}P NMR (Figure 2.2), but in the solid state, the molecules are stationary and so the phosphorus nuclei are no longer equivalent since each is oriented differently. Because of this, there are three separate isotropic lines in the ^{31}P CP/MAS NMR spectrum (Figure 2.32).

The CSA parameters[11] should reflect the orientation of the functional groups in the unit cell with respect to the external magnetic field. CSA values are important for

making signal assignments in solid-state NMR spectra, because the isotropic chemical shifts can differ substantially from the solution chemical shift values and vary widely, as demonstrated earlier for metal complexes with chelate ligands.[7]

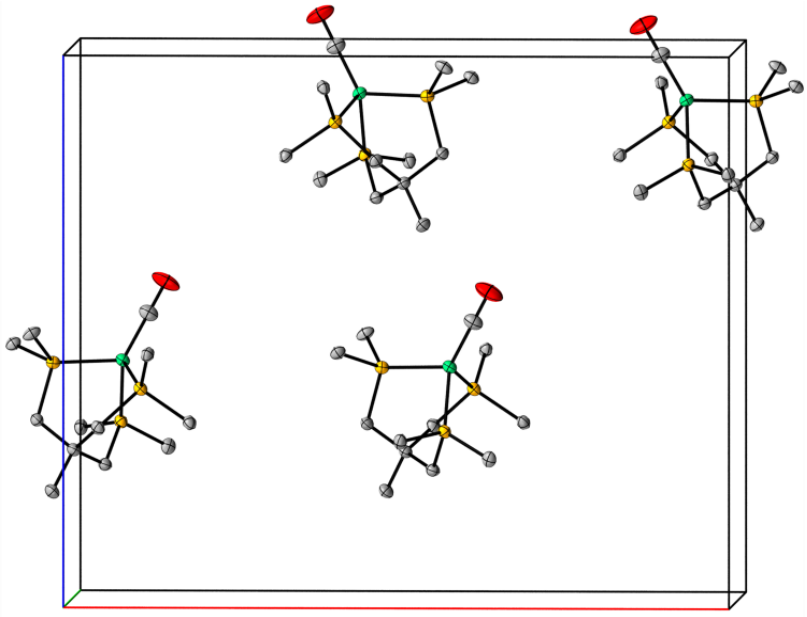

Figure 2.33 Unit cell of **2**. Thermal ellipsoids are shown at the 50% probability level. Hydrogen atoms and phenyl rings, except for the *ipso* carbons, are omitted for clarity.

There are four molecules in the unit cell of **2** (Figure 2.33). Looking along the vertical axis of the unit cell, one can determine that there should be three ^{31}P NMR signals in the solid-state NMR spectrum. Two phosphine groups of each molecule have their phenyl substituents pointing downward while one phosphine points them upward. Therefore, two of the three signals should have similar CSA, the CSA of the third should differ.

The solid-state NMR spectra of polycrystalline **2** (Figure 2.32) can be interpreted in a straightforward manner. The chemical shifts of the isotropic lines do not vary with rotational frequency. Because of this, the isotropic lines were unequivocally identified by recording spectra at different rotational frequencies of 4 and 7 kHz. Three lines can be distinguished and after deconvolution of the two overlapping isotropic lines and simulation,[17] the CSA data for **2** are obtained (Table 2.01). The isotropic lines at 13.5 and 7.1 ppm are the most similar in terms of CSA values (Figure 2.34), differing by only 8 ppm. The isotropic line at 8.1 ppm, on the other hand, has a distinctly smaller CSA value. Since all three lines are very similar, it is difficult to make any further assignment. However, it makes sense that the pair of similar lines will belong to the phosphine groups pointing their phenyl groups downward while the more dissimilar line will belong to the upward-pointing phosphines.

Table 2.1 ^{31}P CP/MAS chemical shift anisotropy NMR data [ppm] for the polycrystalline complex **2**.

δ_{iso}	δ_{11}	δ_{22}	δ_{33}	**CSA**
13.5	107.4	25.6	-92.3	199.7
8.1	93.9	16.0	-85.6	179.5
7.1	96.9	19.3	-94.8	191.7

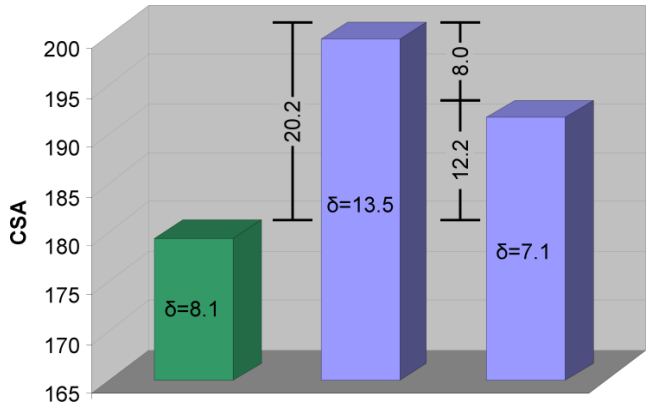

Figure 2.34 Graphical comparison of the CSA (ppm) of the three isotropic lines of **2**.

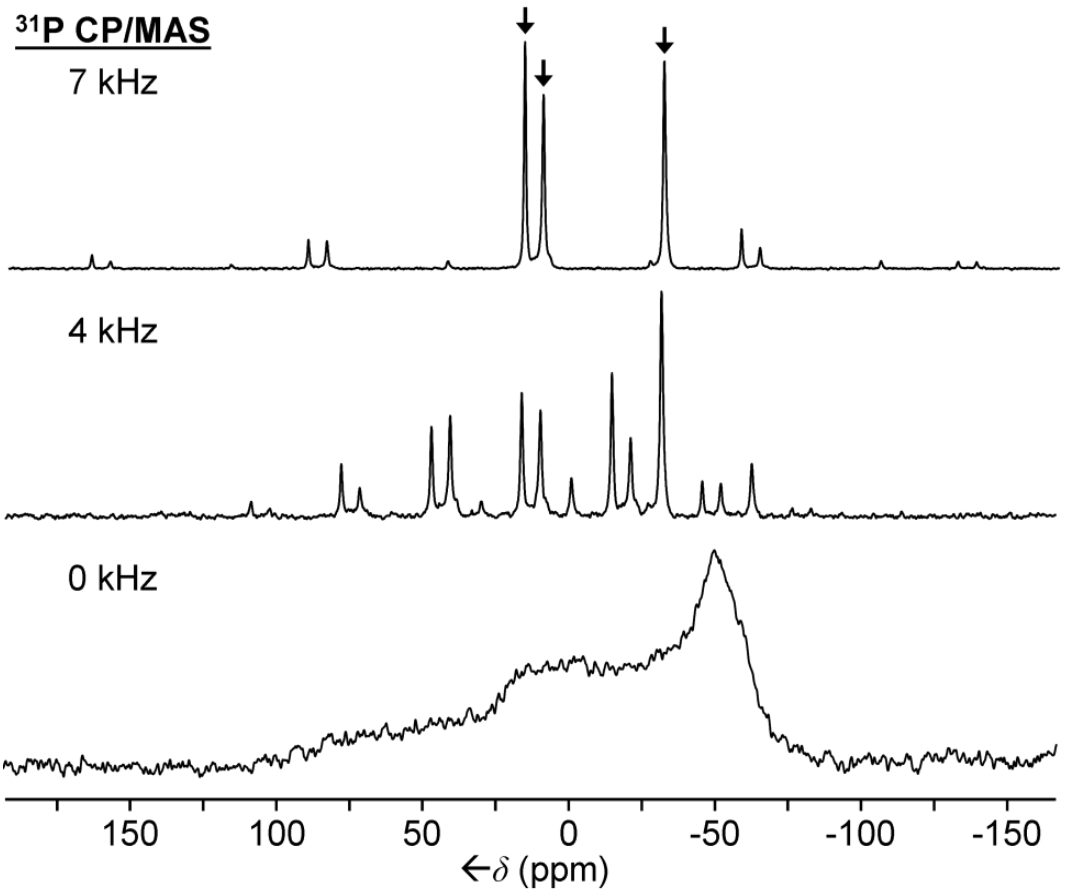

Figure 2.35 ^{31}P CP/MAS NMR spectra of polycrystalline **3**. Vertical arrows indicate the isotropic lines.

The interpretation of the ^{31}P CP/MAS spectra of **3** (Figure 2.35) is rather straightforward. The resonance at -31.9 ppm corresponds to the uncoordinated phosphine group because its chemical shift is closest to the one found for **3** in solution at -27.79 ppm. Even more indicative, however, is its small CSA value of 83.9 ppm (Table 2.02). This is in accordance with the fact that the CSA values of phosphines are much smaller than the values of their metal-coordinated analogs.[1b,3c,11b,14b] Both the chemical shifts of 9.6 and 16.0 ppm and the CSA values of 165.8 and 161.4 ppm for the other two phosphine resonances are very similar, and therefore, the resonances of the coordinated phosphines can not be assigned. This is not surprising given the similar orientation of the coordinated phosphine groups as seen in the unit cell of **3**, for example, when looking along the vertical axis in the display (Figure 2.36).

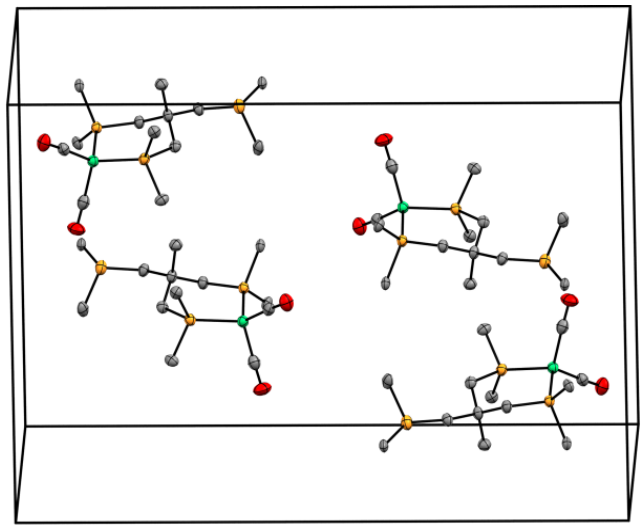

Figure 2.36 Unit cell of **3**. Thermal ellipsoids are shown at the 50% probability level. Hydrogen atoms and phenyl rings, except for the *ipso* carbons, are omitted for clarity.

Table 2.2 ^{31}P CP/MAS chemical shift anisotropy NMR data [ppm] for the polycrystalline complex **3**.

δ_{iso}	δ_{11}	δ_{22}	δ_{33}	CSA
16.0	106.4	0.9	-59.4	165.8
9.6	86.5	17.2	-74.8	161.4
-31.9	17.8	-47.3	-66.1	83.9

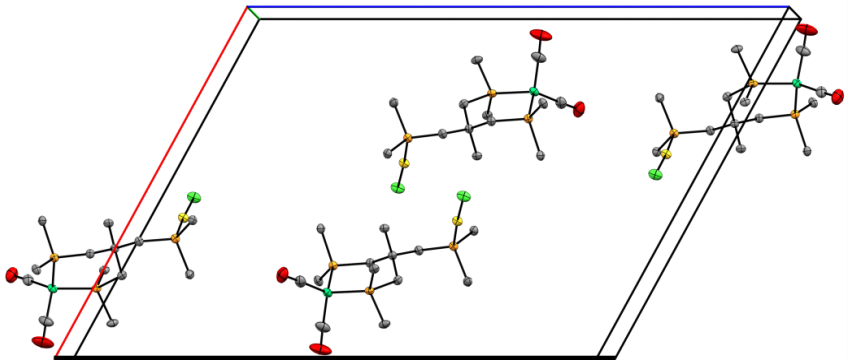

Figure 2.37 Unit cell of **4**. Thermal ellipsoids are shown at the 50% probability level. Hydrogen atoms and phenyl rings, except for the *ipso* carbons, are omitted for clarity.

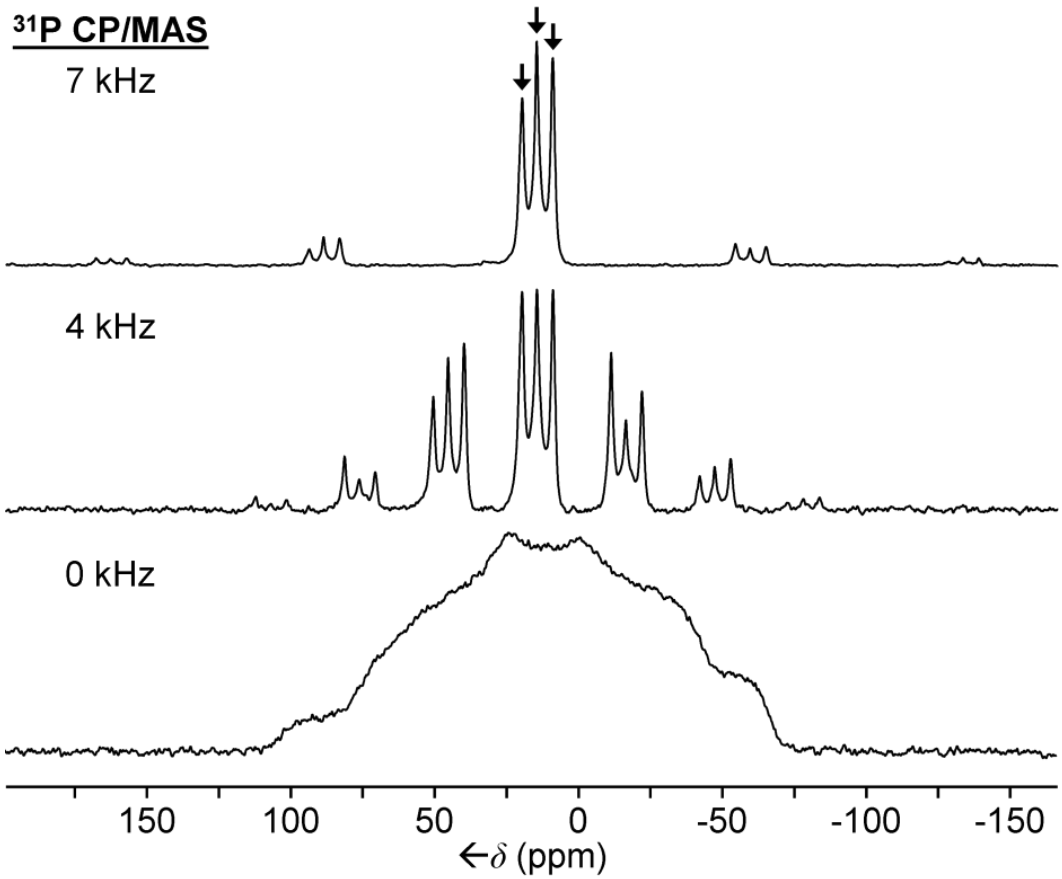

Figure 2.38 ^{31}P CP/MAS NMR spectra of polycrystalline **4**. Vertical arrows indicate the isotropic lines.

The packing of the complexes **4** in the unit cell (Figure 2.37) again resembles that of **3** (Figure 2.36). Comparing the ^{31}P CP/MAS spectra of polycrystalline **3** and **4**, the expectation is that the resonance for the uncoordinated phosphine group vanishes and a new signal appears. The signals of the phosphines coordinated to the nickel center should display similar chemical shifts and CSA values.

At first sight, any attempt to assign the signals in the ^{31}P CP/MAS spectra of polycrystalline **4** (Figure 2.38) seems desperate. However, two of the resonances have

very similar chemical shifts, 19.4 and 8.6 ppm (Table 2.03), compared to those for the nickel-coordinated phosphine groups in **3** (16.0, 9.6 ppm).

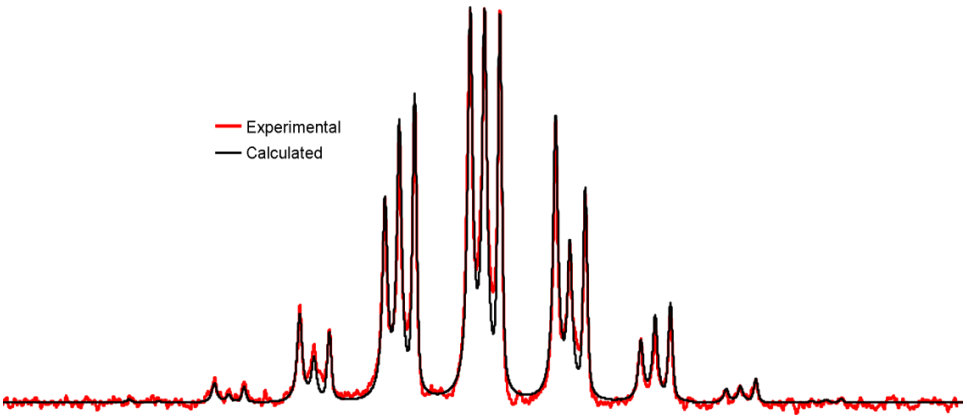

Figure 2.39 Experimental and calculated ^{31}P CP/MAS NMR spectra of the polycrystalline complex **4**.

Furthermore, after fitting the spectrum (Figure 2.39) to extract the CSA information (Table 2.03) one sees that the CSA the two nickel-coordinating phosphines matches perfectly at 143.2 ppm. On the other hand, the middle signal at 14.1 ppm has a distinct CSA of only 130.0 ppm. For this reason, the center signal is attributed to the phosphine group coordinated to the gold atom in **4**.

Table 2.3 ^{31}P CP/MAS chemical shift anisotropy NMR data [ppm] for the polycrystalline complex **4**.

δ_{iso}	δ_{11}	δ_{22}	δ_{33}	CSA
19.4	93.2	8.0	-42.9	143.2
14.1	71.3	29.8	-58.7	130.0
8.6	74.2	20.6	-69.0	143.2

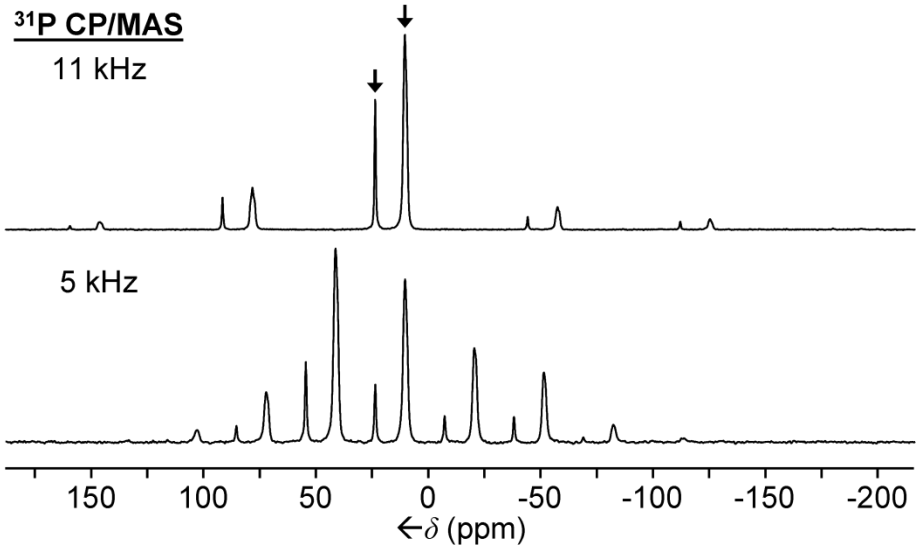

Figure 2.40 ^{31}P CP/MAS NMR spectra of polycrystalline **7**. Vertical arrows indicate the isotropic lines.

Regarding the ^{31}P CP/MAS spectra of polycrystalline **7** (Figure 2.40), the signal assignment is again straightforward. The resonances at 23.6 and 10.3 ppm correspond to the phosphine groups of coordinated PPh_3 and tripodal ligand, respectively. This follows from the comparison with the chemical shifts in solution (22.50 and 12.10 ppm) and the signal intensities of about 1:3.5, including the signal intensities of the rotational

sidebands. Although, in principle, solid-state NMR signals cannot be integrated when CP is used,[11a,14b] in the case of **7** it is obvious that there are more alkyl protons close to the phosphine nuclei in the tripodal ligand than in PPh_3. Since alkyl protons facilitate the transfer of magnetization to the phosphorus nuclei, the found ratio of the signal intensities is not exactly 1:3. As in the cases discussed above, the CSA can be used to corroborate the signal assignment. The electronic surroundings of the ^{31}P nucleus in the PPh_3 ligand is expected to be more symmetric than in the coordinated alkyldiphenylphosphine groups of the tripodal ligand.[15b] Therefore, the CSA of the PPh_3 signal is much smaller with 145.3 ppm than the CSA of the tripodal phosphine signal (162.3 ppm, Table 2.04).

Table 2.4 ^{31}P CP/MAS chemical shift anisotropy NMR data [ppm] for the poly-crystalline complex **7**.

δ_{iso}	δ_{11}	δ_{22}	δ_{33}	**CSA**
23.6	73.8	68.7	-71.5	145.3
10.3	79.2	34.6	-83.0	162.3

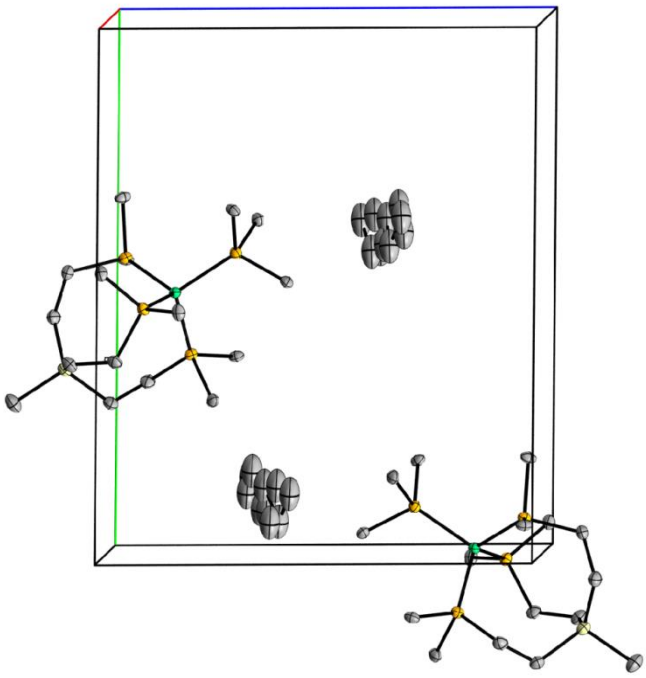

Figure 2.41 Unit cell of **7**. Thermal ellipsoids are shown at the 50% probability level. Hydrogen atoms and phenyl rings, except for the *ipso* carbons, are omitted for clarity.

Upon considering the structure and crystal packing of **7** (Figure 2.41) and comparison to the previous tripod complexes, one might expect to see multiple signals to arise from the different arms of the tripod ligand. In fact, this does occur, and very close examination of the signal in Figure 2.40 reveals that there are several overlapping signals.

Catalysis with Nickel Tripod Complexes

The nickel complexes described in this work are tested for their catalytic activity with respect to the cyclotrimerization of phenylacetylene (Scheme 2.04). This reaction is

important,[18] for example, for natural product syntheses[18a] and it offers many advantages. (a) The reaction does not require a change of the metal oxidation state in contrast, for example, to the Sonogashira reaction.[3] (b) Only one substrate, and no base or co-catalyst are needed. (c) No gases are involved, as in hydrogenation reactions,[2a,2b,2e,2f] and therefore no gas diffusion effects will blur the experimental results. (d) There are two isomers as reaction products, which allow the simultaneous determination of the activity and selectivity. (e) The cyclotrimerization reaction proceeds under ambient pressure and at moderate temperatures, and there is already a solid basis of data for comparisons.[4]

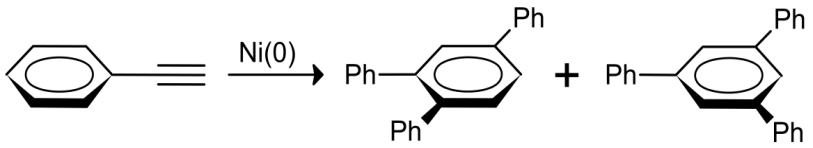

Scheme 2.4 The cyclotrimerization of phenylacetylene to yield the unsymmetric and symmetric product.

Interestingly, all tripodal phosphine ligands with short alkyl chain lengths $(CH_2)_1$, namely **2**, **3**, and **4**, displayed only minimal catalytic activity, even at the elevated temperature of 65 °C (Figure 2.42). This follows a trend observed earlier for immobilized rhodium hydrogenation catalysts of the Wilkinson type.[2b] At that time the low catalytic activity had been attributed to increased decomposition of the catalysts on the reactive silica surface, assuming that the short linker chains do not provide sufficient distance to the support surface. The new results suggest, however, that the coordination

of the tripodal ligands might be too strong to allow access of the substrate to the metal center. This general scenario might also explain the low catalytic activity of **2**-**4**. One should also point out that the presence of Au(I) in **4** besides the Ni(0) center does not lead to a synergistic effect, neither enhancing, nor decreasing the catalytic activity of this heterobimetallic complex.

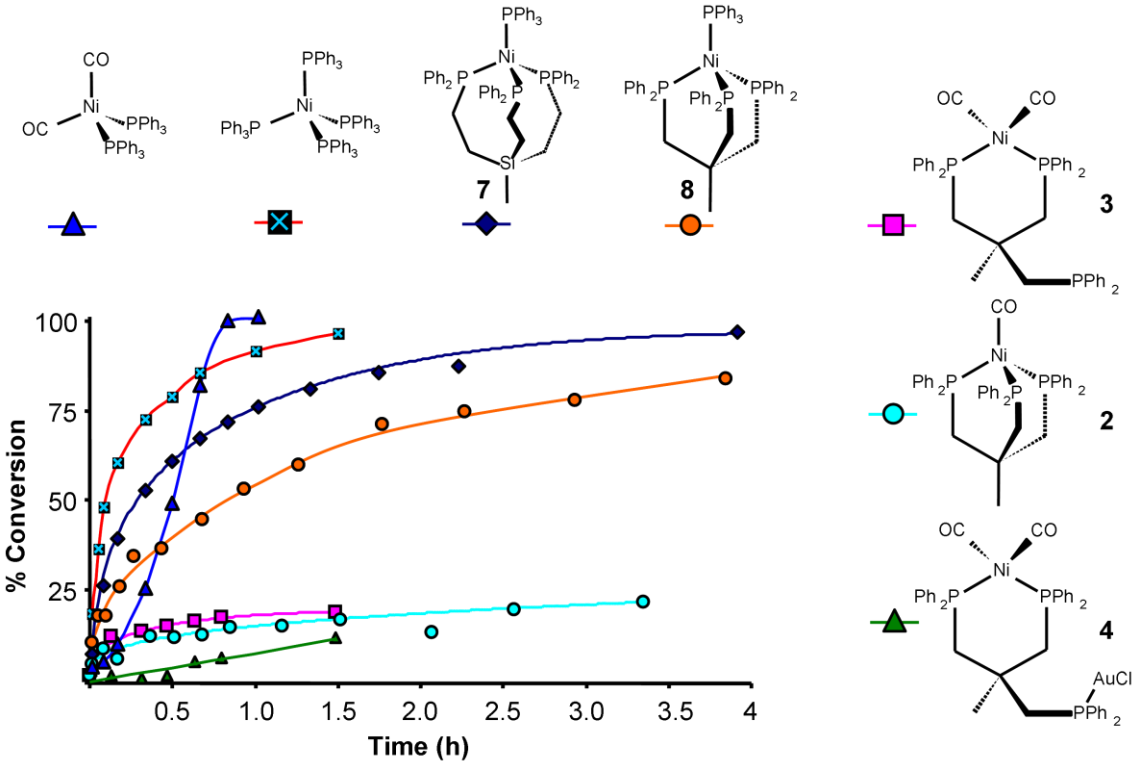

Figure 2.42 Catalytic performance of complexes **2**, **3**, **4**, and **7** compared with $Ni(CO)_2(PPh_3)_2$, $Ni(PPh_3)_4$, and $[CH_3C(CH_2PPh_2)_3]NiPPh_3$ (**8**).

However, nickel complex **7** leads to nearly quantitative conversion of phenylacetylene into the cyclotrimers within only about four hours. This activity

compares very favorably to earlier results, as the highest catalytic activity of a molecular nickel complex known so far corresponds to a quantitative conversion of the substrate at 90 °C within 4.5 hours.[4a] We assume that this high activity, which does not go along with the formation of a typical nickel mirror at the glass wall of the Schlenk tube, is based on the precarious position of the PPh_3 ligand in **7**. As the X-ray structure (Figure 2.31) shows, the phenyl groups of the tripodal phosphine ligand are pushing towards the PPh_3 ligand thus, presumably, facilitating its departure from the metal center and in this way allowing the substrate to coordinate.

In order to test this hypothesis, the nickel complex $[CH_3C(CH_2PPh_2)_3]NiPPh_3$ (**8**)[19] has been synthesized and applied to the catalytic reaction under identical conditions (Figure 2.42). As anticipated, **8** is more active than the carbonyl nickel complexes **2**-**4**. However, it does not quite reach the catalytic activity of **7**. The slightly increased lengths of the alkyl chains of the tripodal ligand in **7** to $(CH_2)_2$ might facilitate further detachment of one or more phosphine groups from the metal center to allow access to coordination sites. However, the ligand detachment seems to be reversible enough to prevent the formation of nickel nanoparticles or a nickel mirror.

For comparison, the reaction was run under identical conditions with $Ni(CO)_2(PPh_3)_2$ and $Ni(PPh_3)_4$ as catalysts. The dicarbonyl nickel catalyst is very active, but has sigmoidal kinetics (Figure 2.42) which indicates that the reaction may be more complicated. It will be discussed further in Chapter II. The tetraphosphine nickel complex is also a very active catalyst, and it has more straightforward kinetics (Figure 2.42). Although $Ni(PPh_3)_4$ catalyzes the reaction faster than any of the tripod complexes,

it is not a good candidate for immobilization since the Bluemel group has already shown that mono- and bidentate nickel catalysts, though active and recyclable, eventually form nanoparticles.

The high selectivity of **7** towards the two possible products (Scheme 2.04) is unprecedented. Nickel catalysts with mono- and bidentate phosphine ligands studied earlier became unselective during the catalytic run,[4a] producing equal amounts of the two isomers. Catalyst **7**, however, reaches a constant ratio of 1,2,4- to 1,3,5-triphenylbenzene of 16 : 1 after about 15 minutes, with an initial product ratio of already 11:1. In comparison, catalyst **8** requires about 30 minutes to reach a constant ratio of 15:1 with an initial product ratio of 9:1. This scenario shows that for **7** the active species is formed most quickly, for example, by releasing the PPh_3 ligand, and that the selectivity is then pushed further towards the product that requires a less sterically demanding transition state. Putting these results into perspective and comparing the advantages of **7** with those of literature known catalyst systems is not quite straightforward because each catalyst is usually optimized towards a specific goal.

Regarding the selectivity for the unsymmetric versus the symmetric cyclotrimerization products, a $CoBr_2$(diimine) complex in combination with Zn and ZnI_2 gives the highest ratio with 97:3.[20] A ruthenium complex was also found to cyclotrimerize phenylacetylene, however, 4 mol% of the catalyst had to be applied, and the reaction took five hours for completion.[21] A very versatile rhodium complex that is efficient for a variety of terminal and internal acetylenes[22] needs, however, 40 hours to produce the cyclotrimers of phenylacetylene with a yield of only 68% in a 1:3 ratio. The

most selective catalyst systems for producing the symmetric versus the unsymmetric cyclotrimerization product are based on niobium and tantalum.[23] Isomer ratios of >99:1 have been obtained, however, the overall yield was, in general, lower than 20%. One recent report on the catalytic cyclotrimerization of phenylacetylene describes the activity of a $NiCl_2$/Zn system in the presence of modified pyridines[24] using 20 mol% of catalyst to obtain a yield of 94%.

In comparison, only 0.5 mol% of **7** is used and quantitative substrate conversion is achieved within four hours. In summary, regarding the complexes presented here, most promising for future studies on homogeneous and immobilized nickel catalyst systems are complexes with tripodal phosphine ligands of medium length, as realized in **7**, which additionally incorporate a ligand that can easily get detached from the metal center.

CONCLUSION

In this chapter new monometallic nickel(0) complexes and one heterobimetallic Ni(0)/Au(I) complex with tripodal phosphine ligands have been described. They have been characterized thoroughly in solution and in the solid state. The single crystal X-ray structures of all complexes have been obtained and discussed in connection with their ^{31}P CP/MAS spectra. The CSA values of the complexes have been analyzed and all solid-state NMR signals could be assigned. Complex **7** displayed unprecedented activity and selectivity with respect to the cyclotrimerization of phenylacetylene, which could be interpreted based on the structural features of the complex. The characteristics of this

nickel catalyst compare favorably with those of other catalyst systems described in the literature.

Tripodal phosphine ligands incorporating the ethoxysilane group for immobilized versions of the nickel complexes on oxide supports[7] will be used to transfer the encouraging results on the homogeneous catalysts presented in this paper to the world of catalysts immobilized on oxide supports.

EXPERIMENTAL

(CO)Ni[(PPh_2CH_2)$_3$CMe] (2)

$Ni(CO)_2(PPh_3)_2$ (213.8 mg, 0.334 mmol) and **1** (208.0 mg, 0.333 mmol) are dissolved in 50 ml of toluene and stirred at 90°C for 3.5 h. The solvent was removed from the yellow solution in vacuo until solid began to precipitate. Then 20 mL of dry pentane was added. The resulting yellow precipitate was filtered, washed with pentane (4x20 mL) and dried in vacuo at 70°C to yield 175.5 mg (0.247 mmol) of **2** which represents a yield of 74% with respect to $Ni(CO)_2(PPh_3)_2$. Single crystals suitable for X-ray diffraction were obtained from a saturated toluene solution of **2** in the course of a few days. The compound has been synthesized previously starting from $Ni(CO)_4$,[25] but not characterized with more recent analytical techniques. The complete data are given below. See Figure 2.43 for the numbering of the nuclei in the complexes.

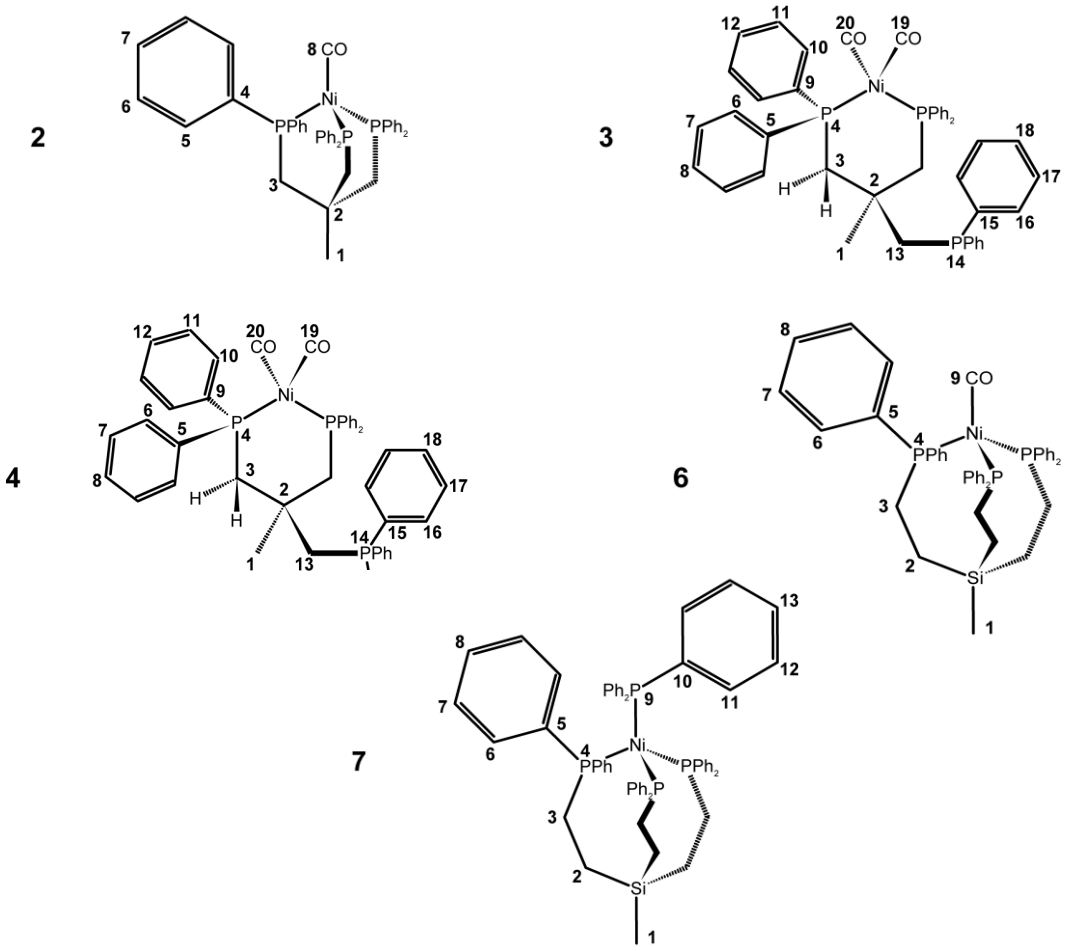

Figure 2.43 Numbering of nuclei in **2**-**4**, **6**, and **7** for NMR signal assignments.

NMR (δ, C_6D_6), $^{31}P\{^1H\}$ NMR (202.28 MHz, C_6D_6) δ = 11.54 (s); ^1H NMR (499.69 MHz, C_6D_6) δ = 7.50 (t, 12H, $^3J(^1H\text{-}^1H)$ = 8.3 Hz, H6), 6.82-6.73 (m, 18H, H5, H7, overlapping), 2.13 (d, 6H, $^2J(^{31}P\text{-}^1H)$ = 7.2 Hz, H3), 1.22 (q, 3H, $^4J(^{31}P\text{-}^1H)$ = 2.7 Hz, H1); ^{13}C NMR (125.66 MHz, C_6D_6, $\delta(^{13}C)$ = 128.00) δ = 207.89 (q, $^2J(^{31}P\text{-}^{13}C)$ = 4.0 Hz, C8), 140.62 (virt. m, $^1J(^{31}P\text{-}^{13}C)$ = 42.9 Hz, C4), 131.93 (d, $^2J(^{31}P\text{-}^{13}C)$ = 16.1 Hz, C5), 128.29 (s, C7), 127.91 (d, $^3J(^{31}P\text{-}^{13}C)$ = 9.8 Hz, C6), 38.17 (q, $^2J(^{31}P\text{-}^{13}C)$ = 10.9 Hz,

C2), 36.73 (q, $^{3}J(^{31}P\text{-}^{13}C)$ = 6.5 Hz, C1), 36.74-36.53 (virt m, C3). IR: ν(CO) = 1886.5 cm^{-1}. mp (decomp.) 158 °C.

$(CO)_2Ni[(PPh_2CH_2)_3CMe]$ (3)

Triphos (198.1 mg, 0.317 mmol) was dissolved in 20 mL of toluene and added to a solution of $Ni(CO)_2(PPh_3)_2$ (197.4 mg, 0.309 mmol) in 22 mL of toluene. The mixture was stirred at RT in the dark for 15 h. The solution was concentrated in vacuum which resulted in a slightly yellow precipitate which was filtered off and washed with hexanes (3 x 10 mL) to give **3** as a white powder (156.3 mg, 0.211 mmol, 69% yield with respect to $Ni(CO)_2(PPh_3)_2$). Single crystals suitable for X-ray diffraction were grown by layering a toluene solution of **3** with pentane.

$^{31}P\{^{1}H\}$ NMR (202.28 MHz, C_6D_6) δ = 13.93 (d, 2P, $^{4}J(^{31}P\text{-}^{31}P)$ = 2.2 Hz, P4), -27.79 (t, 1P, $^{4}J(^{31}P\text{-}^{31}P)$ = 2.2 Hz, P14); ^{1}H NMR (499.69 MHz, C_6D_6) δ = 7.89 (t, 4H, $^{3}J(^{31}P\text{-}^{1}H)$ = 8.8 Hz, $^{3}J(^{1}H\text{-}^{1}H)$ = 7.5 Hz, H10), 7.59 (t, 4H, $^{3}J(^{31}P\text{-}^{1}H)$ = 8.3 Hz, $^{3}J(^{1}H\text{-}^{1}H)$ = 7.5 Hz, H6), 7.35 (t, 4H, $^{3}J(^{31}P\text{-}^{1}H)$ = 7.3 Hz, $^{3}J(^{1}H\text{-}^{1}H)$ = 7.6 Hz, $^{3}J(^{1}H\text{-}^{1}H)$ = 1.7 Hz, H16), 7.10-6.92 (m, 18H, H7, H8, H11, H12, H17, H18), 2.56 (dd, 2H, $^{2}J(^{1}H\text{-}^{1}H)$ = 14.1 Hz, $^{2}J(^{31}P\text{-}^{1}H)$ = 11.7 Hz, $H3_{syn}$), 2.23 (dd, 2H, $^{2}J(^{1}H\text{-}^{1}H)$ = 14.2 Hz, $^{2}J(^{31}P\text{-}^{1}H)$ = 3.2 Hz, $H3_{anti}$), 2.04 (dd, 2H, $^{4}J(^{31}P\text{-}^{1}H)$ = 1.7 Hz, $^{2}J(^{31}P\text{-}^{1}H)$ = 2.7 Hz, H13), 0.69 (s, 3H, H1); ^{13}C NMR (125.66 MHz, C_6D_6) δ = 202.87 (s, C19), 200.03 (t, $^{1}J(^{31}P\text{-}^{13}C)$ = 3.6 Hz, C20), 140.84 (virt. m, $J(^{31}P\text{-}^{13}C)$ = 36.3 Hz, C5*), 140.01 (d, $^{1}J(^{31}P\text{-}^{13}C)$ = 12.7 Hz, C15), 138.93 (virt. m, $J(^{31}P\text{-}^{13}C)$ = 30.9 Hz, C9*), 133.40 (d, $^{2}J(^{31}P\text{-}^{13}C)$ = 20.2 Hz,

C16), 132.90 (virt. m, $^{2/4}J(^{31}P\text{-}^{13}C)$ = 29.1 Hz, C10), 131.78 (virt. m, $^{2/4}J(^{31}P\text{-}^{13}C)$ = 28.2 Hz, C6), 129.50 (s, C8‡), 128.86 (s, C12‡), 128.81-128.70 (m, C17‡, C18†), 128.51 (q, $J(^{31}P\text{-}^{13}C)$ = 4.5 Hz, C7†, C11†), 49.11 (dt, $^{3}J(^{31}P\text{-}^{13}C)$ = 8.5 Hz, $^{1}J(^{31}P\text{-}^{13}C)$ = 17.5 Hz, C13), 40.71 (ddd, $^{3}J(^{31}P\text{-}^{13}C)$ = 8.6 Hz, $^{3}J(^{31}P\text{-}^{13}C)$ = 8.0 Hz, $^{1}J(^{31}P\text{-}^{13}C)$ = 11.3 Hz, C3), 39.09 (dt, $^{2}J(^{31}P\text{-}^{13}C)$ = 13.6 Hz, $^{2}J(^{31}P\text{-}^{13}C)$ = 4.7 Hz, C2), 29.29 (dt, $^{3}J(^{31}P\text{-}^{13}C)$ = 10.0 Hz, $^{3}J(^{31}P\text{-}^{13}C)$ = 6.4 Hz, C1). *,‡,†Assignments interchangeable. IR: ν(CO) = 1998.3, 1931.8 cm^{-1}. mp (quantitative transformation into **2**) 136 °C.

$(CO)_2Ni[(PPh_2CH_2)_3CMe]AuCl$ (4)

Complex **4**: ClAu(tht) (19.0 mg, 0.059 mmol, tht: tetrahydrothiophene) was added to a solution of **3** (45.9 mg, 0.0621 mmol) in 10 mL of toluene. The solution immediately assumed a dark purple color. After stirring the reaction mixture for 20 h, the solvent was removed in vacuo, yielding a purple solid. Then the solid was triturated in 50 mL of ether, stirred briefly and allowed to settle overnight. The clear supernatant solution was then collected and concentrated in vacuo. Then the residue was re-dissolved in THF (2 mL) and the product precipitated as a white powder when pentane (40 mL) was added. The solid was washed with pentane (1 x 10 mL) to yield pure **4** as a white powder (33.1 mg, 58% with respect to AuCl(tht)). Single crystals suitable for X-ray diffraction analysis were grown by slow diffusion of liquid pentane into a THF solution of **4**.

^{31}P**{**^{1}H} NMR (202.28 MHz, C_6D_6) δ = 14.04 (d, 2P, $^{4}J(^{31}P\text{-}^{31}P)$ = 1.3 Hz, P4), 16.20 (m, 1P, P14); ^{1}H NMR (499.69 MHz, C_6D_6) δ = 7.86 (dd, 8H, $^{3}J(^{1}H\text{-}^{1}H)$ = 7.6 Hz, $^{3}J(^{31}P\text{-}^{1}H)$ = 9.22 Hz, H10), 7.84 (dd, 8H, $^{3}J(^{1}H\text{-}^{1}H)$ = 7.6 Hz, $^{3}J(^{31}P\text{-}^{1}H)$ = 9.22 Hz, H6), 7.14 (tm, 4H, $^{3}J(^{1}H\text{-}^{1}H)$ = 7.8 Hz, H7), 7.10 (tm, 4H, $^{3}J(^{1}H\text{-}^{1}H)$ = 7.8 Hz, H11), 7.06 (ddt, 4H, $^{3}J(^{31}P\text{-}^{1}H)$ = 12.8 Hz, $^{3}J(^{1}H\text{-}^{1}H)$ = 7.1 Hz, $^{3}J(^{1}H\text{-}^{1}H)$ = 1.5 Hz, H16), 7.00 (dtt, 2H, $^{5}J(^{31}P\text{-}^{1}H)$ = 1.2 Hz, $^{3}J(^{1}H\text{-}^{1}H)$ = 7.4 Hz, $^{4}J(^{1}H\text{-}^{1}H)$ = 1.2 Hz, H8), 6.92 (dtt, 2H, $^{5}J(^{31}P\text{-}^{1}H)$ = 1.2 Hz, $^{3}J(^{1}H\text{-}^{1}H)$ = 7.4 Hz, $^{4}J(^{1}H\text{-}^{1}H)$ = 1.2 Hz, H12), 6.89 (dtt, 2H, $^{5}J(^{31}P\text{-}^{1}H)$ = 2.1 Hz, $^{3}J(^{1}H\text{-}^{1}H)$ = 7.4 Hz, $^{4}J(^{1}H\text{-}^{1}H)$ = 1.6 Hz, H18), 6.82 (dtt, 4H, $^{4}J(^{31}P\text{-}^{1}H)$ = 2.4 Hz, $^{3}J(^{1}H\text{-}^{1}H)$ = 7.5 Hz, $^{4}J(^{1}H\text{-}^{1}H)$ = 1.5 Hz, H17), 2.68 (dd, 2H, $^{2}J(^{31}P\text{-}^{1}H)$ = 8.2 Hz, $^{2}J(^{1}H\text{-}^{1}H)$ = 14.2 Hz, H3$_{syn}$), 2.27 (dd, 2H, $^{2}J(^{31}P\text{-}^{1}H)$ = 6.7 Hz, $^{2}J(^{1}H\text{-}^{1}H)$ = 14.2 Hz, H3$_{anti}$), 2.01 (d, 2H, $^{2}J(^{31}P\text{-}^{1}H)$ = 11.5 Hz, H13), 0.74 (s, 3H, H1); ^{13}C**{**1H,31P} NMR (125.66 MHz, C_6D_6) δ = 201.25 (s, C19), 201.03 (s, C20), 139.09 (s, C5, C9), 134.16 (s, C15), 133.35 (s, C16), 132.92 (s, C6), 132.35 (s, C10), 131.41 (s, C18), 129.56 (s, C8), 129.43 (s, C12), 129.12 (s, C17), 128.88 (s, C11), 128.72 (s, C7), 43.06 (s, C13), 41.06 (s, C3), 38.67 (s, C2), 31.76 (s, C1). IR: ν(CO) = 1999.3, 1933.7 cm^{-1}. mp (decomp.) 133 °C.

(CO)Ni[(PPh$_2$CH$_2$CH$_2$)$_3$SiMe] (6)

$Ni(CO)(PPh_3)_3$ (0.1117 g, 0.128 mmol) was dissolved in 10 mL of toluene and combined with a solution of **5** (87.2 mg, 0.128 mmol) in 10 mL of toluene. This mixture was stirred for 75 minutes, after which the solvent was evaporated in vacuum. The resulting solid was washed thrice with 10 mL of pentane, then dissolved in 3 mL of toluene and precipitated twice with 10 mL of pentane. The resulting yellow powder was

shown by ^{31}P NMR to contain 34.5 mg (0.045 mmol, 25% yield) of **6** along with a small amount of PPh_3, and presumably oligomeric side products. These impurities were removed by repeated precipitation from a toluene solution by pentane. Crystals suitable for X-ray diffraction were obtained by slow diffusion of liquid pentane into a toluene solution of **6**.

^{31}P**{**^{1}H} NMR (202.28 MHz, toluene) δ = 19.81 (s, P4); ^{1}H**{**^{31}P} NMR (499.69 MHz, C_6D_6) δ = -0.06 (s, 3H, H1), 0.74 m, 6H, H2), 2.15 (m, 6H, H3), 6.95-6.99 (m, 18H, H6, H8), 7.47-7.50 (m, 12H, H7); ^{13}C**{**^{1}H,^{31}P} NMR (125.66 MHz, THF-d_8, δ(^{13}C) = 25.37) δ = 142.41 (C5), 132.35 (C6), 128.55 (C7), 128.31 (C8), 23.73 (C3), 8.40 (C2), 5.79 (C1). IR: ν(CO) = 1911.5 cm^{-1}. mp (decomp.) 113 °C.

$(PPh_3)Ni[(PPh_2CH_2CH_2)_3SiMe]$ (7)

Complex **7**: $NiCl_2py_4$ (103.8 mg, 0.233 mmol) and ligand **5** (157.7 mg, 0.231 mmol) were combined with 40 mL of THF and stirred. The opaque reaction mixture turned red immediately and then the color faded to white within 1 min. Subsequently, PPh_3 (62.6 mg, 0.239 mmol) was added, followed by Zn powder (2 g, 31 mmol). The reaction mixture was degassed in vacuo for 2 min, and then stirred for 16 h. During this time a clear, orange-red solution formed besides solid matter. After settling, the solution was separated from the precipitate via syringe and the solvent was removed in vacuo. The resulting residue was extracted by stirring it with toluene. The solids were allowed to settle and the supernatant was collected, stripped of the solvent, and the residue was

washed once with 10 mL of pentane. The obtained orange-red powder was dried in vacuo, giving 203.4 mg (0.203 mmol), corresponding to a yield of 87%.

$^{31}P\{^{1}H\}$ NMR (202.28 MHz, C_6D_6) δ = 12.01 (d, 3P, $^{2}J(^{31}P\text{-}^{31}P)$ = 18.1 Hz, P4), 22.50 (q, 1P, $^{2}J(^{31}P\text{-}^{31}P)$ = 18.2 Hz, P9); ^{1}H NMR (499.69 MHz, C_6D_6) δ = -0.25 (s, 3H, H1), 0.70 bs, 6H, H2), 2.43 (vbs, 6H, H3), 6.58 (dd, 6H, $^{3}J(^{31}P\text{-}^{1}H)$ = 7.6 Hz, $^{3}J(^{1}H\text{-}^{1}H)$ = 7.0 Hz, H11), 6.81 (t, 6H, $^{3}J(^{1}H\text{-}^{1}H)$ = 7.2 Hz, H12), 6.89 (t, 3H, $^{3}J(^{1}H\text{-}^{1}H)$ = 7.1 Hz, H13), 7.11 (bs, 24H, H6, H7), 7.30 (bs, 6H, H8); $^{13}C\{^{1}H,^{31}P\}$ NMR (125.66 MHz, THF-d_8, $\delta(^{13}C)$ = 25.37) δ = 5.18 (s, C1), 9.02 (s, C2), 27.82 (s, C3), 141.04 (s, C5), 149.86 (s, C10), 134.82 (s, C11), 134.17 (bs, C6), 129.10 (s, C8), 128.21 (s, C13), 128.03 (s, C7), 127.81 (s, C12). mp (decomp.) 38 °C.

$(PPh_3)Ni[(PPh_2CH_2)_3CMe]$ (8)

$Ni(CO)_2(PPh_3)_2$ (10.6 mg .0166 mmol) and **4** (10.1mg .0127 mmol) were dissolved in 2 mL of dry toluene and heated with stirring in a 70 °C water bath. The powder that resulted after removal of the solvent in vacuum was washed with hexanes (5x10ml) and then Et_2O (1x10ml).

CHAPTER III

CATALYSIS

INTRODUCTION

Cyclotrimerization

The cyclotrimerization of phenylacetylene is an ideal test reaction to probe the activity, selectivity, and recyclability of immobilized catalysts. The benefits of this reaction include moderate temperatures, ambient pressure, convenient analysis of all products and reactants by gas chromatography, and only one substrate is required. Furthermore, the oxidation state of the metal does not have to be changed prior to catalysis and no cocatalyst is required.

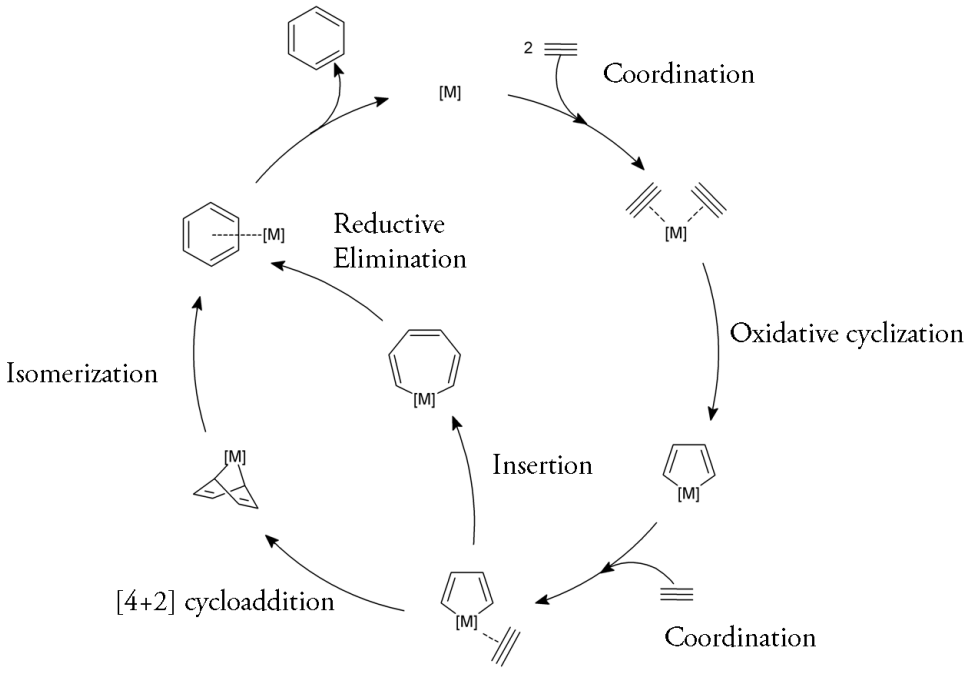

Scheme 3.1 Mechanism of the metal catalyzed cyclotrimerization of alkynes.[18a]

Besides being so conveniently suited to our efforts of developing superior immobilized catalysts and understanding the formation of nanoparticles, the cyclotrimerization reaction (Scheme 3.01) is interesting in its own right in light of the atom economical route that it affords to form three carbon-carbon bonds in a single step to produce valuable trisubstituted benzene rings.[18,26] This powerful reaction, pioneered by Walter Julius Reppe (1892-1969), can be applied to many functional groups besides the usual alkynes, for example nitriles, alkenes, imines, isocyanates and isothiocyanates.[18a] Cyclotrimerization reactions are catalyzed by many different metal complexes including inexpensive nickel catalysts. These nickel catalysts can be complexes with phosphines,[27] carbenes,[28] imines,[29] cyclooctadiene (COD),[30] and many other simple and more sophisticated ligand systems.[5b] Other metals that are active catalysts for cyclotrimerization reactions include cobalt,[20,31] ruthenium,[21,32] rhodium,[22,33] iridium,[34] gold,[35] niobium,[23,36] molybdenum,[37] tungsten,[38] and iron.[39]

Stereoselective cycloadditions have been achieved with various transition metal complexes that employ chiral ligands.[40] The virtues of cyclotrimerization feature prominently in the synthesis of many natural products including sporolide B, anhydrolycorinone, alcyopterosin, citrinadin A, antiostatin A_1, and colchicine.[18a] With so many metal complexes touted as catalysts for this reaction, the question naturally arises, which one is the best? In practice, no catalyst is clearly preferred over the rest since each is optimized for a specific selectivity, or activity towards a chosen substrate (see catalysis section in Chapter II).

Immobilized Catalysts

Homogeneous catalysts are popular in academia because they are highly active, selective and tunable. Heterogeneous catalysts, on the other hand, are greatly favored by the chemical industry due to their recyclability and general ease of handling. Catalysts immobilized on insoluble oxide supports could potentially possess the favorable attributes of both homogeneous and heterogeneous catalysts, but none of the drawbacks. The ideal immobilized catalyst will be as active, selective and tunable as homogeneous catalysts, and yet be as easy to handle and recycle as heterogeneous catalysts. Perhaps the greatest challenge in immobilizing catalysts is leaching and decomposition of the metal complex.[41] Despite these challenges, immobilized catalysts are very promising in the realm of fine chemical production.[1a]

Previous Results

The Bluemel group has previously produced very active and recyclable catalysts immobilized on silica gel.[1b,6,42] This immobilization is achieved using phosphine linkers which contain ethoxysilane groups that bind covalently and irreversibly to silica gel.[1b] Many mono- and bidentate phosphine linkers have been employed to tether nickel catalysts to a silica support, yielding very promising systems for the cyclotrimerization of alkynes.[6] Curiously, the nature of the linker seems to have practically no effect on the activity of the immobilized catalyst in the nickel catalyzed cyclotrimerization of phenylacetylene (Scheme 3.02).

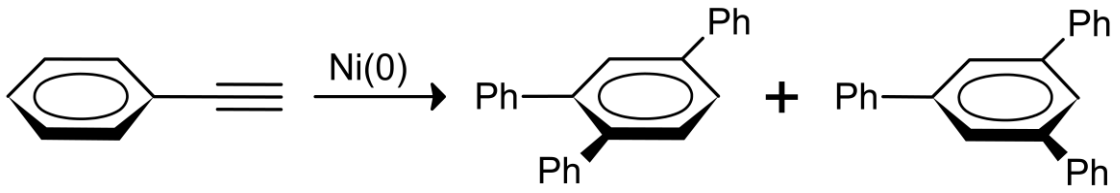

Scheme 3.2 The cyclotrimerization of phenylacetylene to yield the unsymmetric and symmetric cyclotrimers.

Previous studies have shown that while the product ratio of unsymmetric to symmetric cyclotrimer begins at 3:1, after several rounds of batchwise recycling a product ratio of 1:1 is reached.[6a] These results indicate that the catalyst undergoes a change, and it is suspected that nickel nanoparticles are formed which provide the bulk of the reactivity observed. It has also been observed that very small changes in the nature of the solvent can have a dramatic impact on the reaction. For example, the reaction proceeds better in cyclooctane than in n-octane, giving 100% and 90% yields, respectively, and very little product in decane although the physical properties of these solvents are very similar.[6a]

RESULTS AND DISCUSSION

Immobilized Catalysts and Nanoparticles

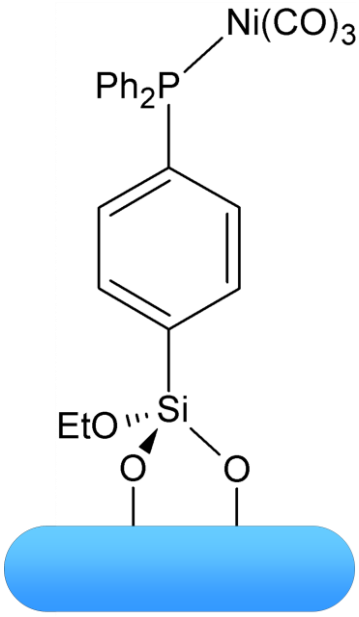

Figure 3.1 An immobilized nickel catalyst previously generated by the Bluemel group.[6a]

First, it was proven that nanoparticles do indeed form via TEM characterization of an immobilized nickel catalyst after three catalytic cycles. After three cycles using the catalyst shown in Figure 3.1, a sample of the silica was taken for TEM analysis which confirmed the presence of nanoparticles (Figure 3.2). These nanoparticles were identified to be nickel nanoparticles via EDX (Figure 3.3).

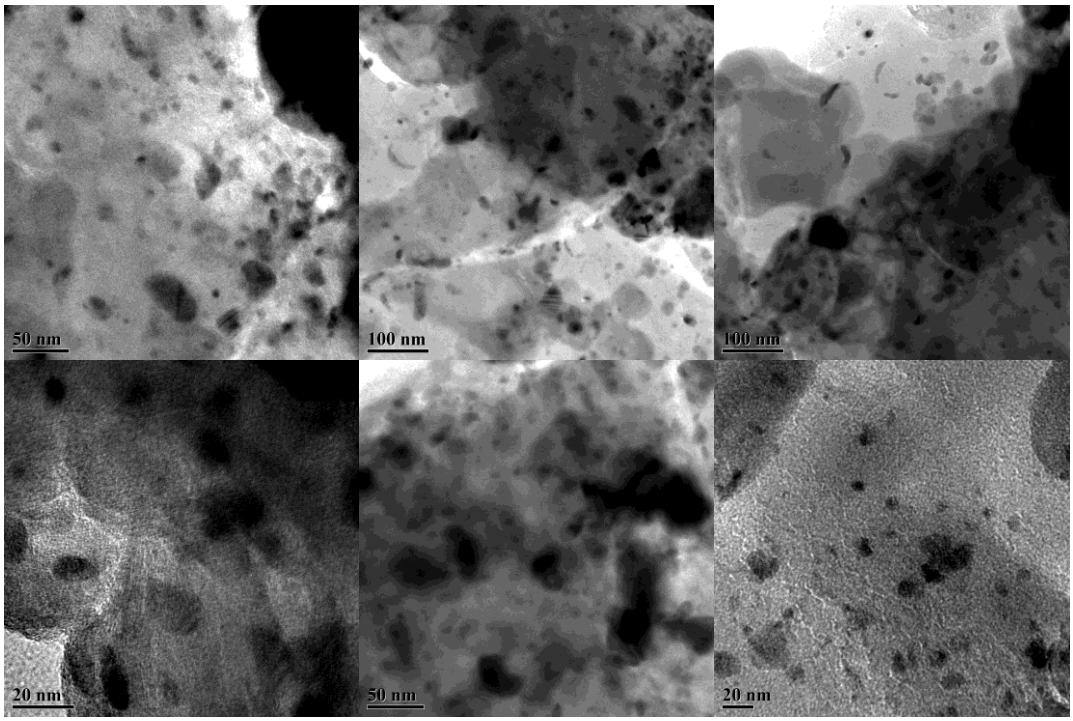

Figure 3.2 TEM images of nickel nanoparticles on silica obtained by recycling the immobilized catalyst shown in Figure 3.1 three times.

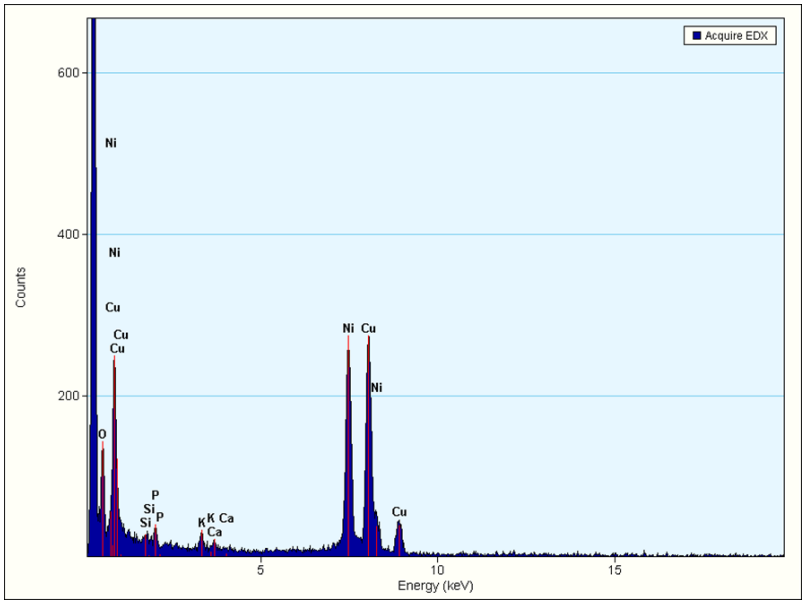

Figure 3.3 EDX spectrum proving the presence of Ni. The Cu peaks observed arise from the Cu TEM grid.

Surprisingly, the vast majority of the nickel nanoparticles are larger than the silica pores (Figure 3.4). This contrasts to a previous case observed in the Bluemel group where the growth of Rh nanoparticles was limited to diameters of about 40 Å, the average diameter of the silica pores.[42a] The only conclusion is that nickel is being leached from the support and transported out of the pores to the exterior surface where it forms the nickel nanoparticles. The mechanism of nanoparticle formation is unknown, but some conclusions may be drawn. We must suppose that the process begins by leaching, whereby a nickel complex fragment is detached from its phosphine linker and therewith the surface. Subsequently, by means of either mobility on the surface, or by moving through solution, it meets a second, third, etc. nickel complex fragment. Whether the second nickel complex is part of an intact, immobilized catalyst unit which then becomes detached, too, or whether it was already in solution is unknown. But clearly the nickel complex fragments combine to give a di- and multinuclear complex or cluster that continues to grow as additional nickel atoms arrive.

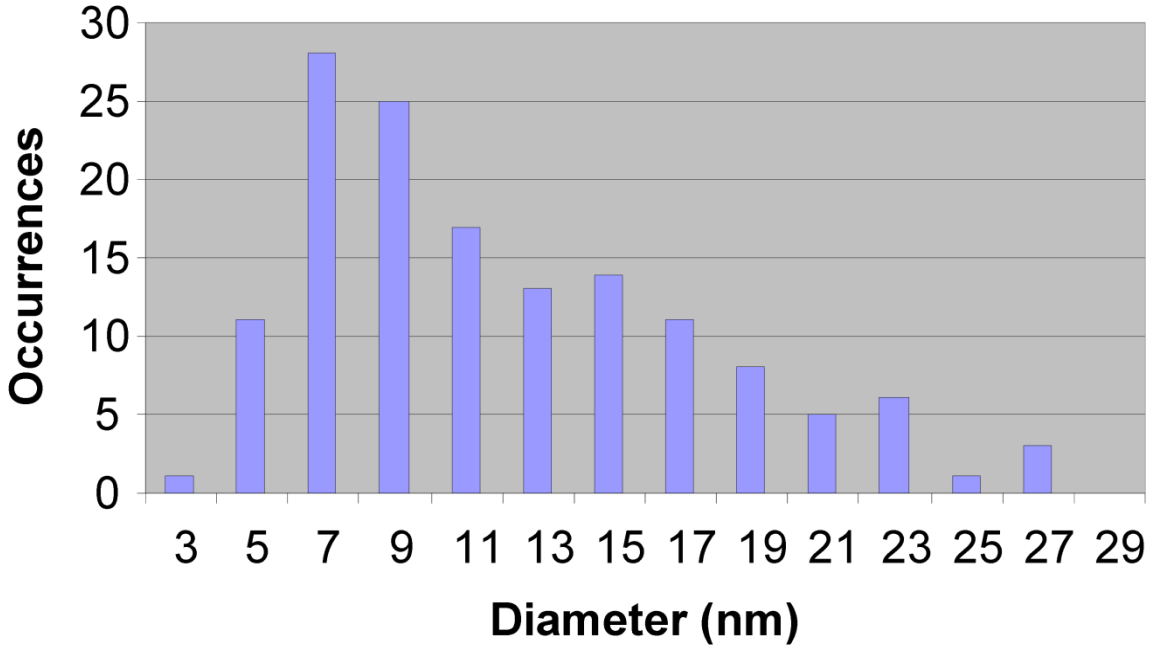

Figure 3.4 Size distribution of nickel nanoparticles formed on the silica support.

One can expect that this process is happening in many locations across the silica surface. Since more than 98% of the surface area of the silica gel in question is located in the interior of the particles with a size distribution of 0.063 to 0.2 mm diameter, we must assume that either the exterior portion of each particle, (which may have fresh, reactive sites exposed because of abrasion during stirring) presents uniquely favorable nucleation sites, or that small nickel nanoparticles form all across the entire surface. In the first case, we can easily account for the fact that the majority of the nickel nanoparticles grow much larger than they would be permitted to do if they remained inside the 20 Å pores. In the second case, we must allow for the mobility of nickel nanoparticles either through solution, or on the SiO_2 surface to allow them to meet and agglomerate on the exterior of the silica particles.

Of course it is also possible that the larger nanoparticles grow via Ostwald ripening, however, given the shape of the particle size distribution in Figure 3.4 which has a long tail towards the larger particles, it is likely that the nanoparticles grow by the migration and coalescence of smaller particles.[43] It should be noted however, that this is a controversial point, and different models predict different shapes so it is not impossible to exclude Ostwald ripening entirely.[43]

Homogeneous Catalysts and Nanoparticles

It was also observed in this work, that even the homogeneous catalyst $Ni(CO)_2(PPh_3)_2$ forms nanoparticles during the reaction. The first indication of nanoparticle formation was the acceleration of the reaction over time (Figure 3.5). Clearly, $Ni(CO)_2(PPh_3)_2$ is not the most active catalyst, and some other species (probably nanoparticles) are formed over time that perform the catalysis more efficiently. This leads to the gradual increase in reaction rate until the substrate begins to be scarce and the reaction subsides.

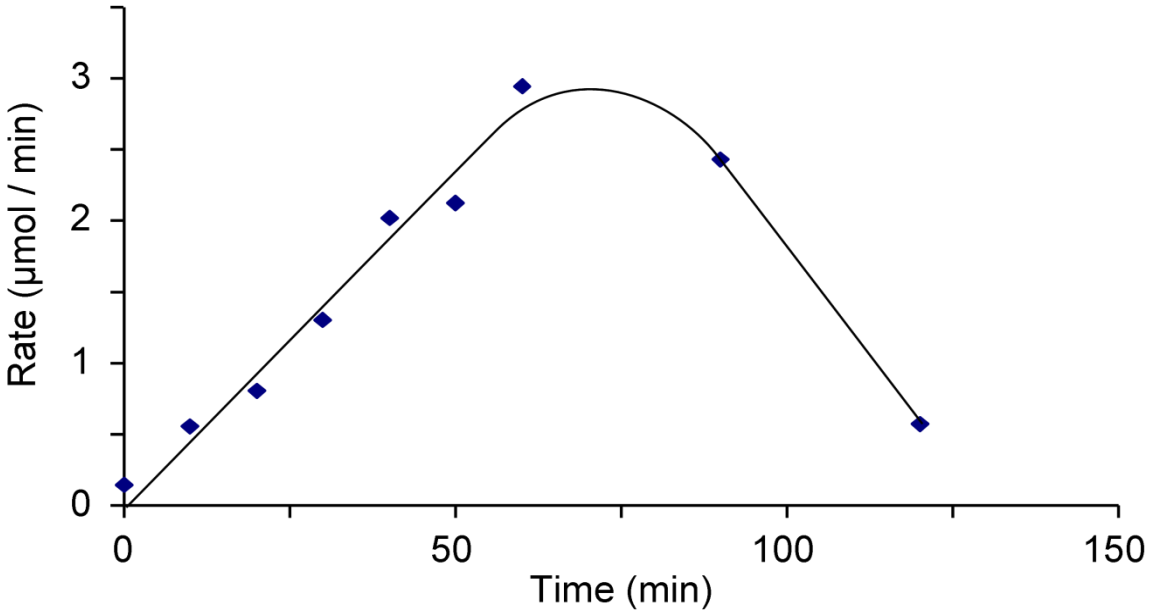

Figure 3.5 The rate of the cyclotrimerization of phenylacetylene with $Ni(CO)_2(PPh_3)_2$ changing over the course of the reaction.

One might argue that $Ni(CO)_2(PPh_3)_2$ is simply a pre-catalyst and that the loss of a ligand and or another modification of the complex yields the active species. This species would then slowly be formed in greater amounts throughout the reaction and this change would ultimately be responsible for the change in the reaction rate. This view, however, must be at least partially discarded since there is also a change in selectivity over the course of the reaction (Figure 3.6). If the selectivity were constant, it would indicate that a single, uniform, catalyst was responsible for 100% of the reactivity. This is not the case, and therefore there must be multiple species present that are able to catalyze the cyclotrimerization while each species leads to its own unique selectivity. As

the ratio of these catalysts evolves during the course of the reaction, the overall rate and selectivity of the reaction change accordingly.

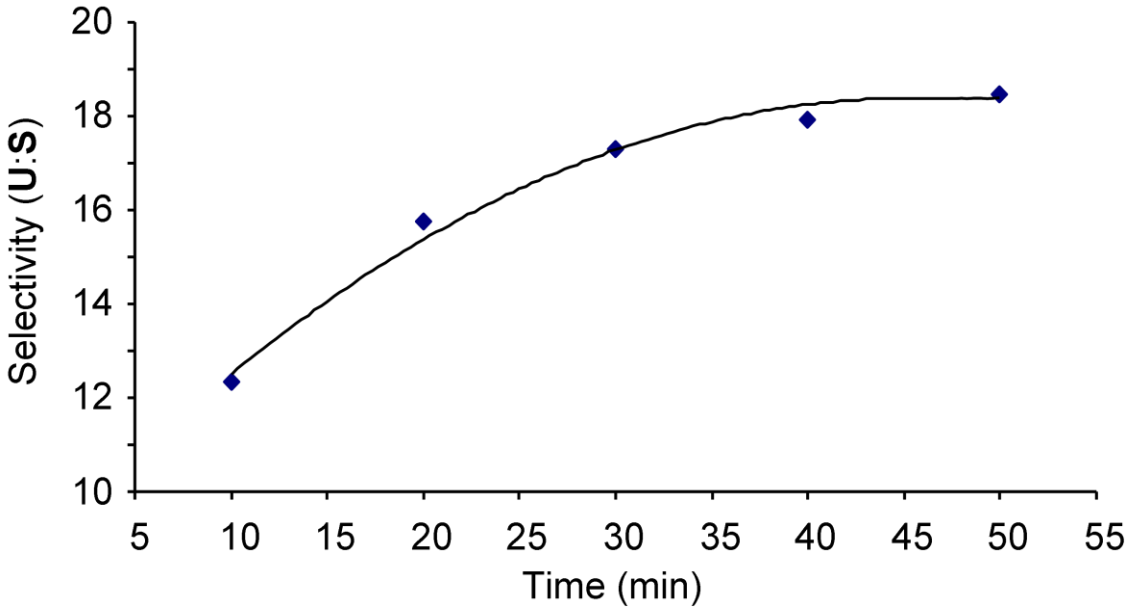

Figure 3.6 Change of selectivity over the course of the cyclotrimerization of phenylacetylene with $Ni(CO)_2(PPh_3)_2$.

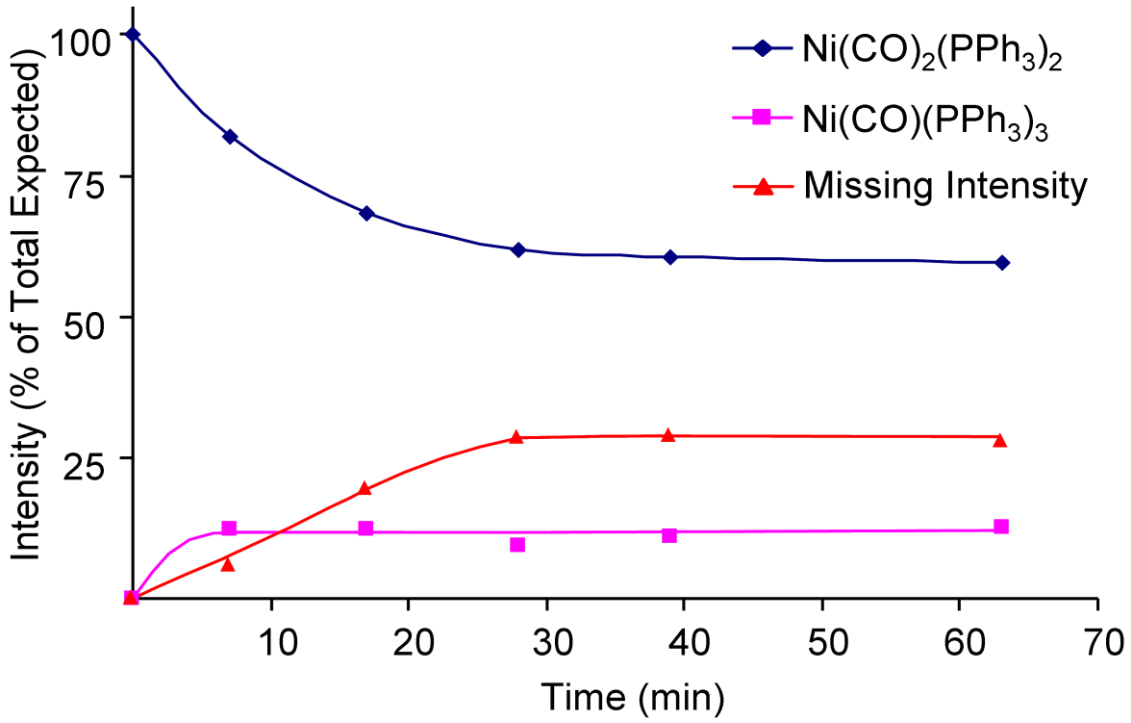

Figure 3.7 Absolute intensities of the ^{31}P NMR signals in the reaction mixture. The red line indicates the percentage of missing ^{31}P signal intensity.

It is clear from ^{31}P NMR measurements of the reaction mixture that the concentration of $Ni(CO)_2(PPh_3)_2$ decreases during the course of the reaction and then remains constant once the substrate is consumed (Figure 3.7). A small amount of $Ni(CO)(PPh_3)_3$ is formed, however, the concentration of this species stays constant throughout the reaction, indicating that the increase in rate shown in Figure 3.5 could not have originated from an increasing concentration of $Ni(CO)(PPh_3)_3$. The most interesting feature of these results is that a significant fraction of the original homogeneous catalyst $Ni(CO)_2(PPh_3)_2$ vanishes in the course of the reaction while no additional ^{31}P NMR signal emerges. It could be assumed that phosphine-free nickel alkyne complexes are

formed, but in this case there should be a signal for uncoordinated PPh_3 in the spectra. The lack of uncoordinated PPh_3 could potentially be attributed to fast exchange processes that lead to a broadening of the PPh_3 signal. However, this is unlikely since no peak is observable for PPh_3 even after the reaction is finished. The likely explanation is that nickel nanoparticles are formed and that PPh_3 ligands associated with the nanoparticles are NMR silent.

A recent study[29] suggests that dinuclear nickel complexes can be highly selective for the formation of the unsymmetric cyclotrimer. Since the selectivity towards the unsymmetric cyclotrimer increases as the reaction progresses, it is tempting to predict that multinuclear nickel complexes or nanoparticles are responsible for the catalysis.

Furthermore, nickel nanoparticles have been observed with TEM after homogeneous catalysis with $Ni(CO)_2(PPh_3)_2$ (Figure 3.8). These nanoparticles are fairly small with average diameters of 1.7 nm and they fall within a narrow size distribution with a standard deviation of only 0.5 nm. The composition of the nanoparticles was verified by EDX (Figure 3.9).

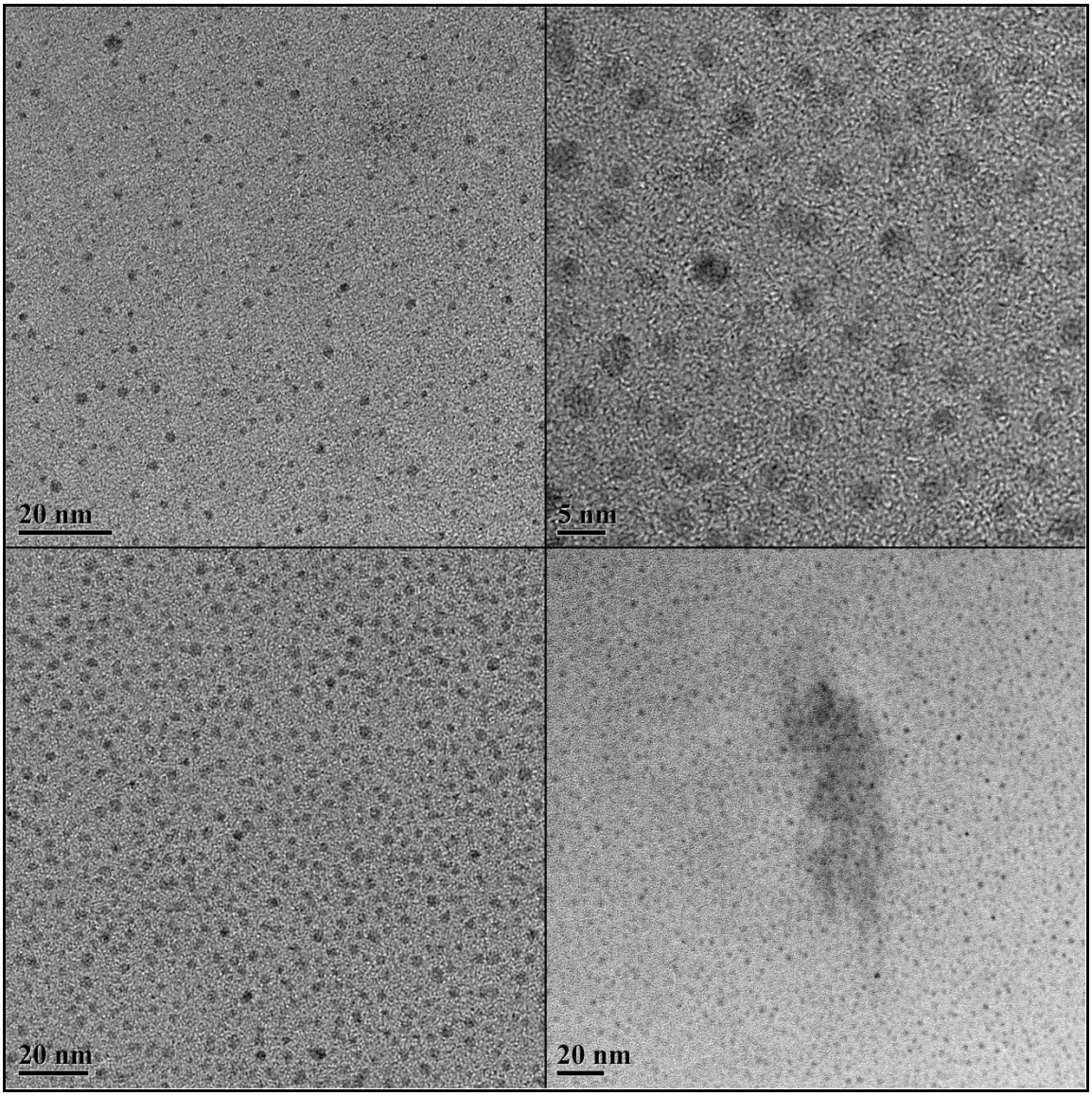

Figure 3.8 TEM image of nickel nanoparticles formed during the cyclotrimerization of phenylacetylene with the homogeneous catalyst $Ni(CO)_2(PPh_3)_2$.

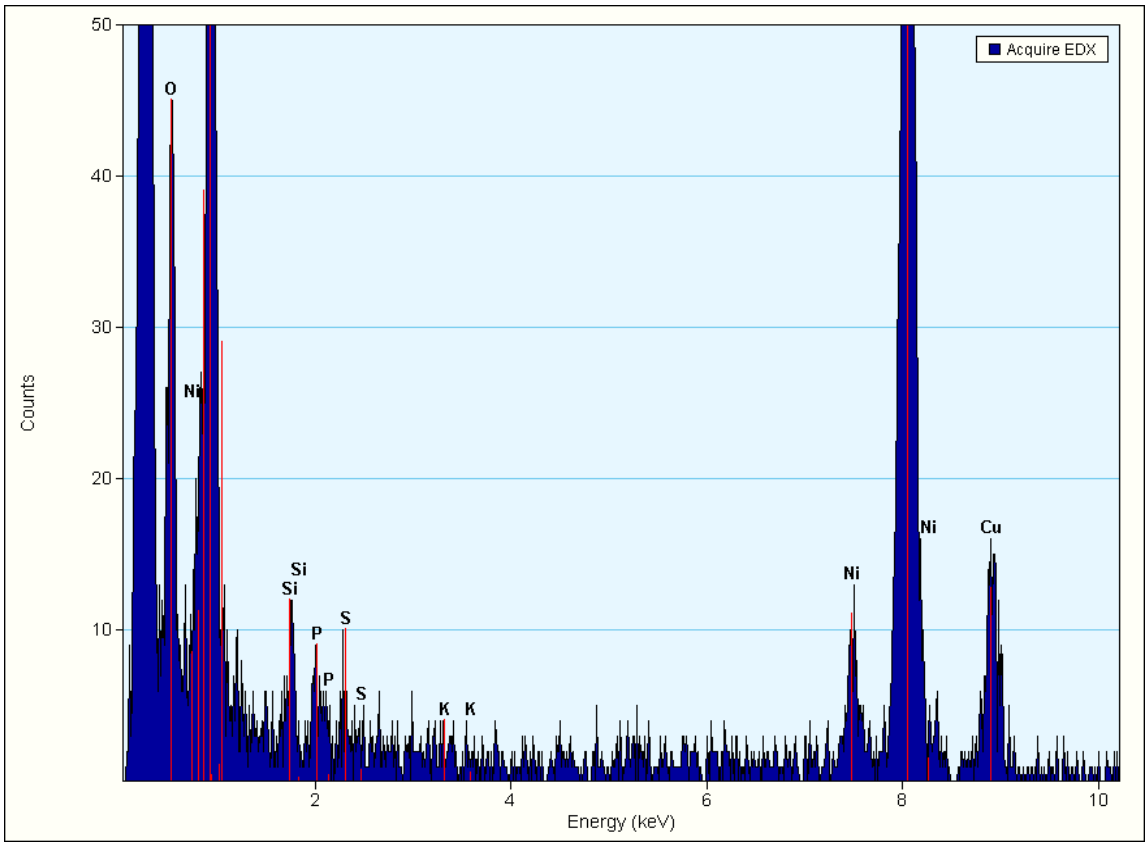

Figure 3.9 EDX spectrum of the nanoparticles shown in Figure 3.8.

Poisoning experiments are commonly used to differentiate homogeneous and heterogeneous catalysts.[44] These experiments consist of monitoring the rate of the reaction in the presence of varying concentrations of a ligand which will saturate all open coordination sites. In the case of a homogeneous catalyst, each individual metal atom will usually require several equivalents of the ligand to render it inert towards the substrate. However, in the case of nanoparticles or bulk metal, a much smaller molar equivalent of the poisoning ligand is required to passivate the surface (Figure 3.10).

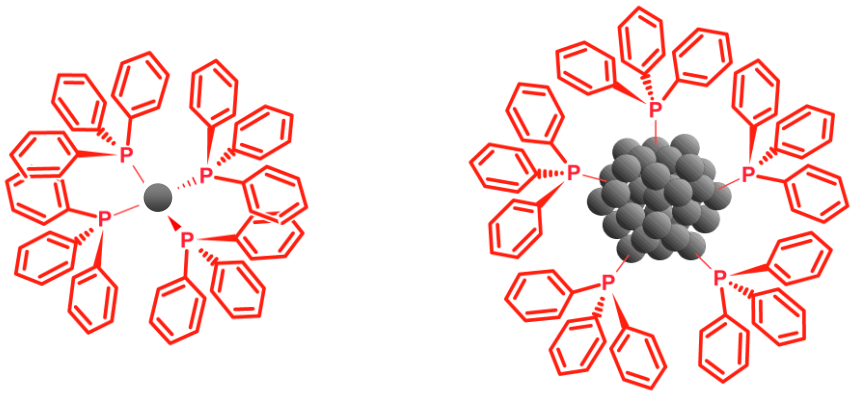

Figure 3.10 Illustration of the two possible results of catalyst poisoning experiments.

Triphos (Figure 3.11), a tridentate phosphine ligand, is an effective poison. When the ligand was added 35 minutes prior to the catalysis (Figure 3.0, "-35" curve), no cyclotrimerization was observed. Adding one equivalent (with respect to nickel) of Triphos part way through the reaction leads to an instantaneous stop of the catalysis. On the other hand, if only 0.5 equivalents are added, the reaction stops, but immediately begins ramping up again and eventually all of the substrate is converted.

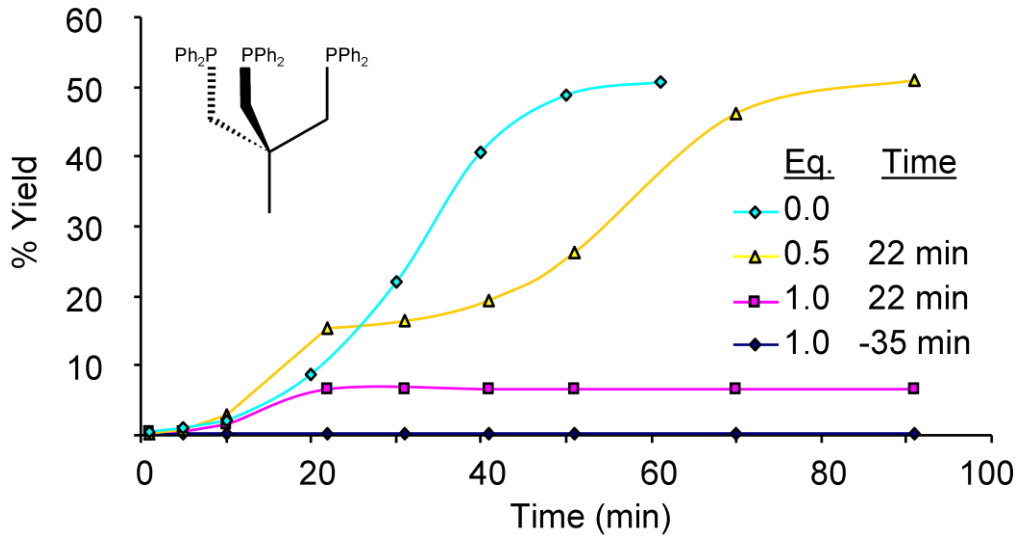

Figure 3.11 Cyclotrimerization of phenylacetylene using the homogeneous catalyst $Ni(CO)_2(PPh_3)_2$ poisoned with varying amounts of Triphos, added either 35 minutes before the reaction (-35) or 22 minutes after the reaction starts (22).

The circumstance that the reaction can be stopped with only 0.5 equivalents of Triphos suggests that nanoparticles could be performing the bulk of the catalysis. The reaction resumes, then, as additional pre-catalyst decomposes and forms new, fresh and unpoisoned nanoparticles. The difficulty lies in the fact that the actual concentration of the active species is unknown. For example, it is still possible that a very reactive molecular species is responsible for the catalysis. This species, present in extremely low concentrations, could be overwhelmed by what is thought to be a sub-stoichiometric amount of poison, but which, relative to the active species, may be an excess of poison..

In summary, the poisoning test can only prove conclusively that $Ni(CO)_2(PPh_3)_2$ is not a particularly active catalyst, and that it is either nanoparticles, or a very small concentration of another molecular species that is the most active catalyst.

Next, it was sought to contrast the effect of Triphos on the reaction with that of PPh_3, a weaker binding phosphine. It was found that, instead of reducing the reaction rate, the addition of up to three equivalents of PPh_3 noticeably increased the rate of the reaction (Figure 3.11). Addition of five equivalents did not cause any perceptible change in the reaction rate. This shows that loss of PPh_3 is not a rate limiting step.

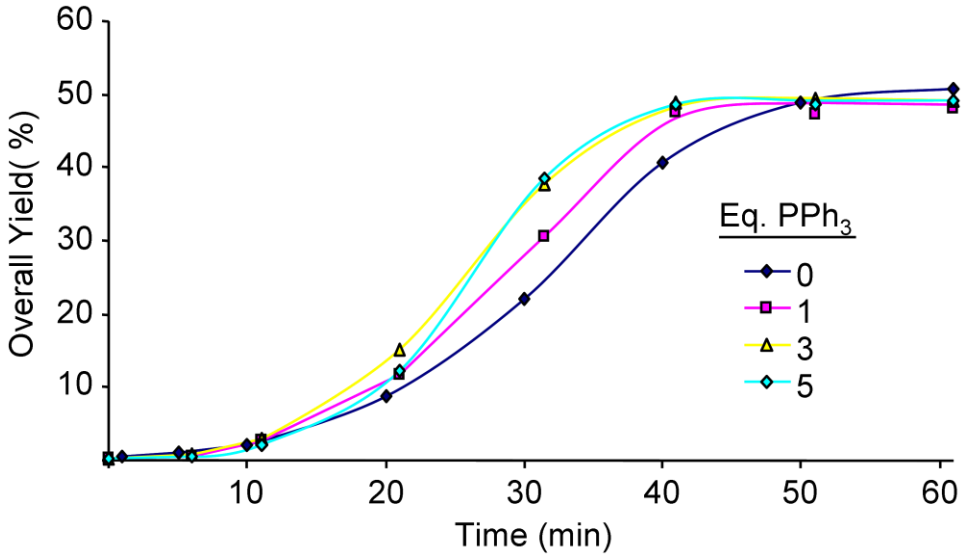

Figure 3.12 Cyclotrimerization of phenylacetylene using the homogeneous catalyst $Ni(CO)_2(PPh_3)_2$ "poisoned" with varying amounts of PPh_3.

Catalysis with Nanoparticles

Ni nanoparticles with an average diameter of 20 nm (Figure 3.13) were purchased from US Nanomaterials and tested with respect to the cyclotrimerization of phenylacetylene. Both with, and without the addition of PPh_3, no cyclotrimerization was

observed. There is a slow conversion of the substrate (Figure 3.14) to linear oligomers and polymers, but no cyclic products are observed.

Figure 3.13 Nickel nanoparticles.

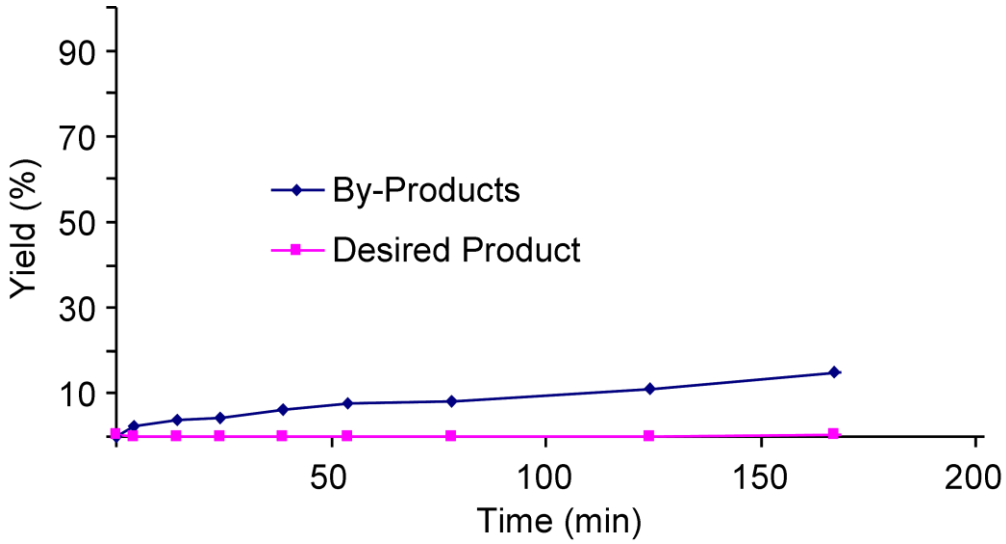

Figure 3.14 Catalysis with purchased nickel nanoparticles (Figure 3.13).

It may be that these nanoparticles are inactive because of surface passivation or their comparatively large size. However, no smaller nickel nanoparticles are currently

commercially available, and no attempt was undertaken to synthesize nanoparticles of smaller size.

Solvent Experiments

Several attempts were made to understand why cyclooctane has been described earlier as a superior solvent for the cyclotrimerization of phenylacetylene.[6a] One possible explanation is that residual amounts of cyclooctene are present in cyclooctane which might coordinate to Ni, either facilitating the activation of molecular catalysts or influencing the size or shape of the nickel nanoparticles. ^{1}H NMR spectrum of commercially available cyclooctane (Alfa Aesar, 99+%) shows that a small amount (concentration 0.007 M) of cyclooctene is indeed present. This may seem like an insignificant amount, but it is, in fact, nearly three times the concentration of the catalyst used for the cyclotrimerization reactions. Several methods were employed to purify the cyclooctane. The most efficient way to remove all olefins from cyclooctane was to stir it over concentrated sulfuric acid for several days. The treated cyclooctane was then washed thoroughly with water and distilled. The resulting solvent had a noticeably weaker smell and the ^{1}H NMR showed no trace of olefinic material.

Surprisingly, this purified solvent performed in exactly the same way as its unpurified counterpart and the pure cyclooctane artificially spiked with 0.1% cyclooctene. At higher levels of 10% and 100%, however, the cyclotrimerization reaction was noticeably affected by the change in solvent (Figure 3.15). The obvious

conclusion from these results is that the small amount of double bond containing contaminants in the cyclooctane has no significant effect on the outcome of the catalysis.

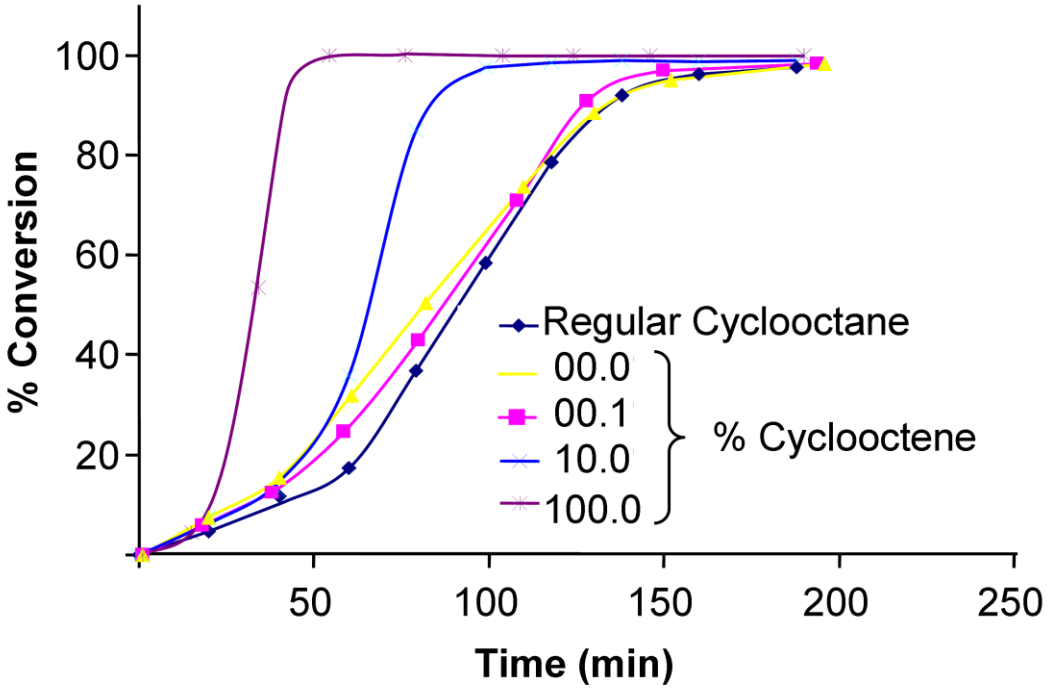

Figure 3.15 Catalysis in the presence of varying amounts of cyclooctene.

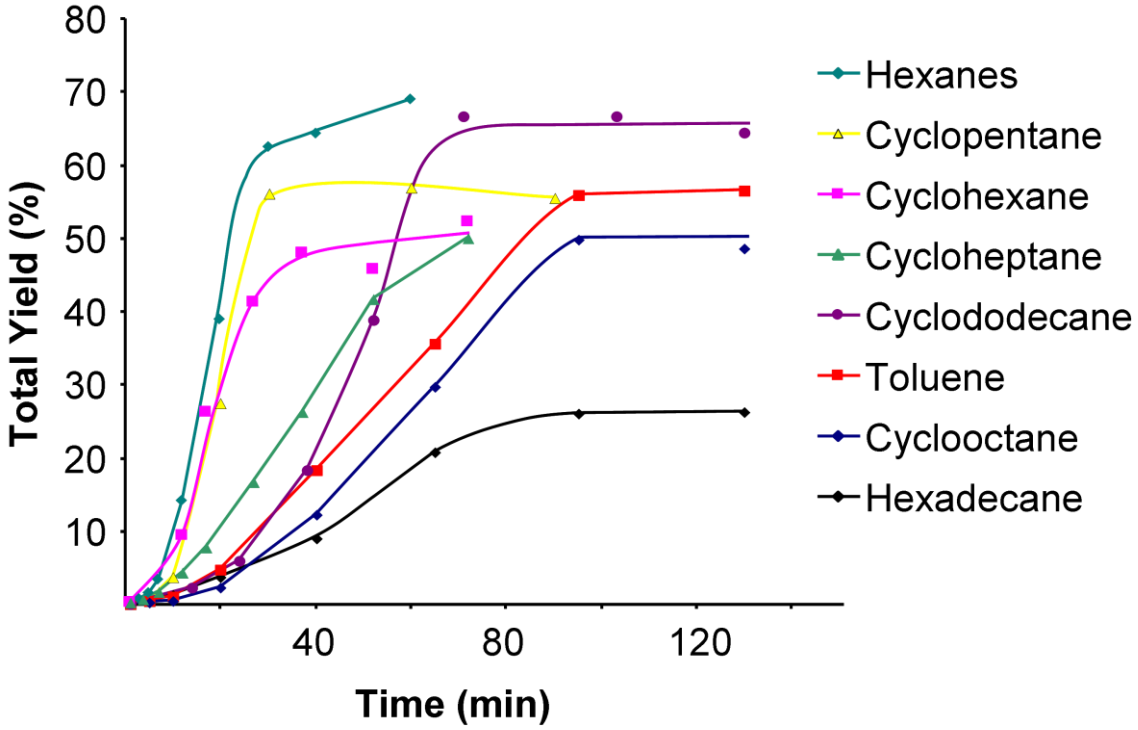

Figure 3.16 Results from the catalysis with $Ni(CO)_2(PPh_3)_2$ in different solvents at 60 °C, except for the reaction with cyclododecane which was conducted at 65 °C.

Various aliphatic solvents were compared (Figure 3.16), and the characteristics for the catalytic runs were very different. However, no clear correlation was found between catalytic activity and the properties of the solvents including density, viscosity, boiling point, surface tension and polarity. In fact, at the lower temperature of 60 °C (versus 100 °C in former studies), which was selected to permit the exploration of several more volatile solvents, cyclooctane offered no observable advantage. In fact, it was outperformed by every solvent except for hexadecane. With no reliable correlation between solvent properties and catalytic performance, it is necessary, therefore, to determine the optimum solvent for each set of reaction conditions, and probably

catalysts, separately. One interesting circumstance is that those solvents that produce the highest yield, generally seem to also have the higher selectivity for the unsymmetric product (U) vs. the symmetric product (S) as shown in Figure 3.17.

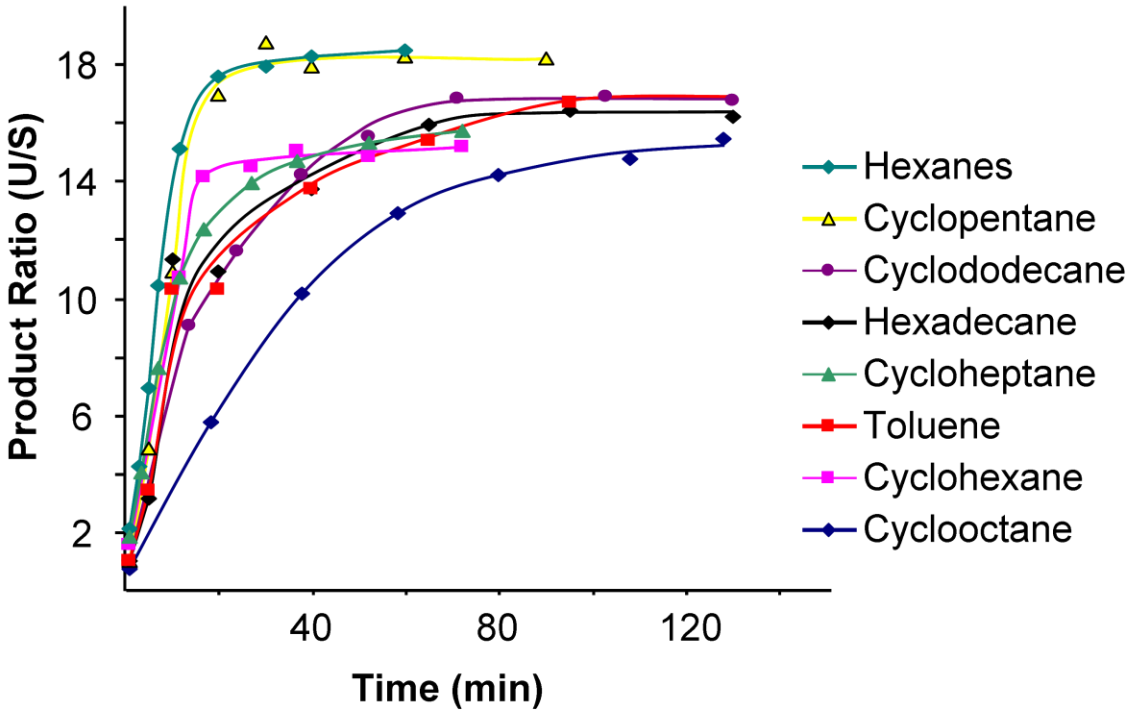

Figure 3.17 Selectivity of the catalysis with $Ni(CO)_2(PPh_3)_2$ in various solvents at 60 °C, except for the reaction with cyclododecane which was conducted at 65 °C.

The reaction temperature of 60 °C is also convenient because the slower reaction allows for the acquisition of more data points before the reaction is finished. When higher temperatures like 100 °C are used, the yield is better and the reaction is completed much more quickly. Unfortunately, it is difficult to take samples sufficiently

quickly to reliably get the reaction kinetics under these conditions, especially when several reactions are running in parallel.

A molecular catalyst would not usually be expected to perform so differently in such similar solvents. The shape, size and therefore activity of nanoparticles, on the other hand, is known to depend strongly on the reaction conditions.[45]

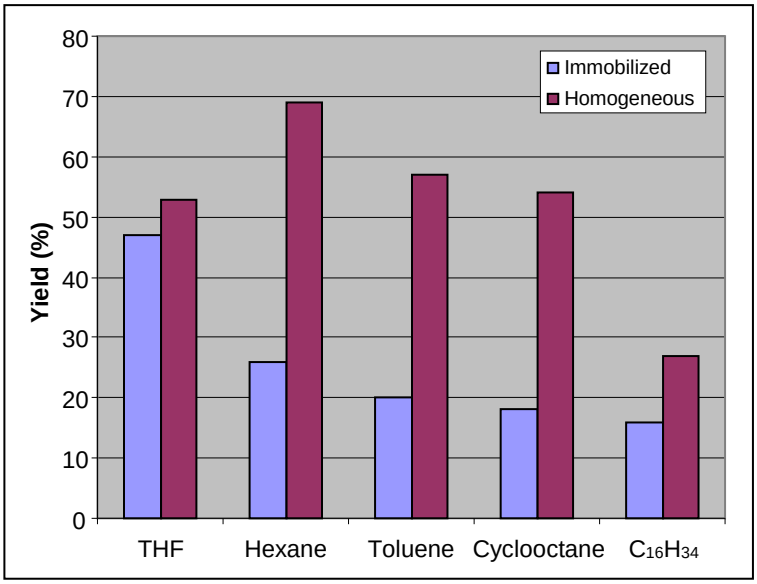

Figure 3.18 Comparison of the overall yields obtained in several solvents at 60 °C with $Ni(CO)_2(PPh_3)_2$, and an immobilized catalyst $(CO)_2Ni[PPh_2CH_2CH_2CH_2Si(OEt)_3]_2$-$SiO_2$. The yields listed are those obtained after the reaction has run its full course over 60-170 minutes for homogeneous and up to 10-24 hours for immobilized catalysts.

For all the solvents tested, the overall yield of cyclotrimer was greater for the homogeneous catalyst than for the immobilized catalyst (Figure 3.18). However, this does not take into consideration the fact that the immobilized catalysts perform much

better at slightly higher temperatures and are, of course, recyclable. The fact that both immobilized and homogeneous catalysts perform about the same in THF may suggest that leaching is occurring in this solvent.

Likewise, for all solvents it is found that the unsymmetric cyclotrimer is more favored in the case of immobilized catalysts except, again, for THF where both homogeneous and immobilized catalysts perform very similarly (Figure 3.19).

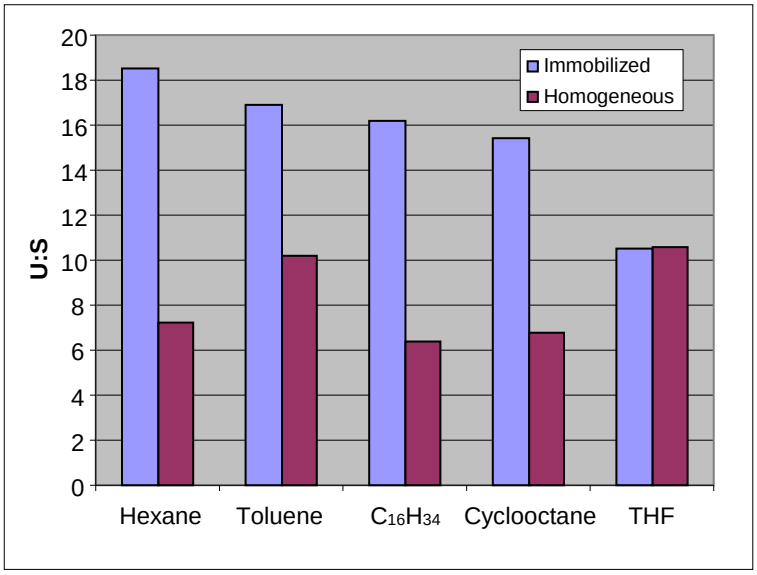

Figure 3.19 Comparison of the product ratio obtained in several solvents at 60 °C with $Ni(CO)_2(PPh_3)_2$, and the immobilized catalyst $(CO)_2Ni[PPh_2CH_2CH_2CH_2Si(OEt)_3]_2$-$SiO_2$. The yields listed are those obtained after the reaction has run its full course over 60-170 minutes for homogeneous and up to 10-24 hours for immobilized catalysts.

Other Reaction Conditions

If, during the course of the reaction, air is admitted into the flask, the catalysis stops and no further conversion takes place. If, however, additional PPh_3 is added, the activity will resume as usual (Figure 3.20). It is possible that the catalyst is simply oxidized and that the subsequently added PPh_3 is acting as a reductant,[46] but it has also been shown unequivocally with NMR experiments that some nickel complexes are potent oxidation catalysts towards PPh_3, and it could be that the additional PPh_3 is only replacing the oxidized ligand.

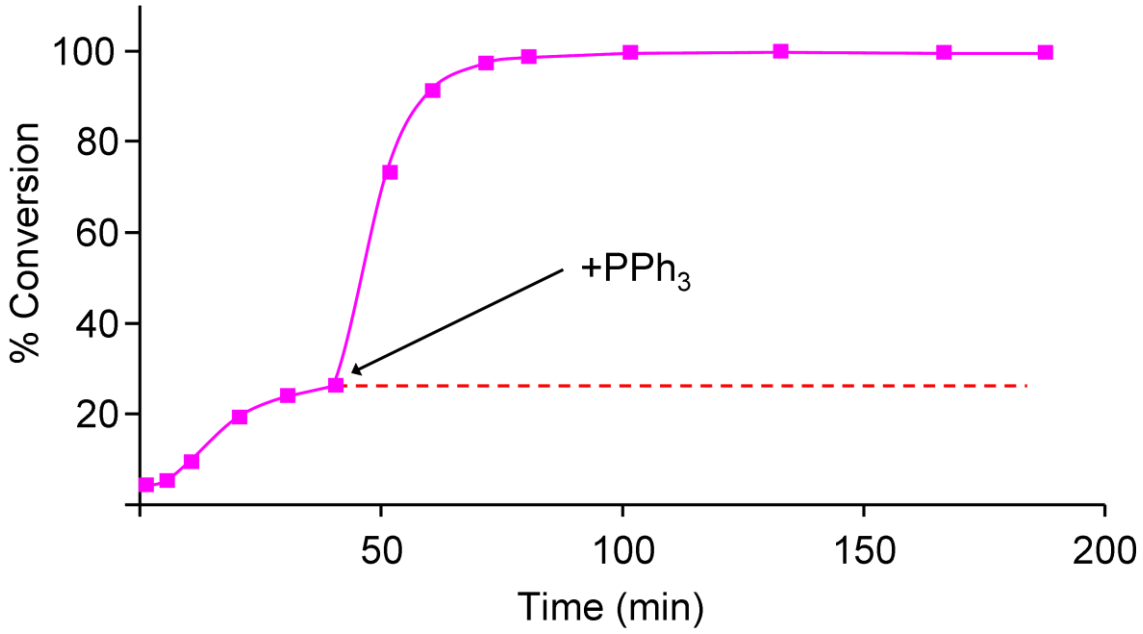

Figure 3.20 Cyclotrimerization reaction in which air was admitted 20 minutes after the start, and PPh_3 was added after 40 minutes.

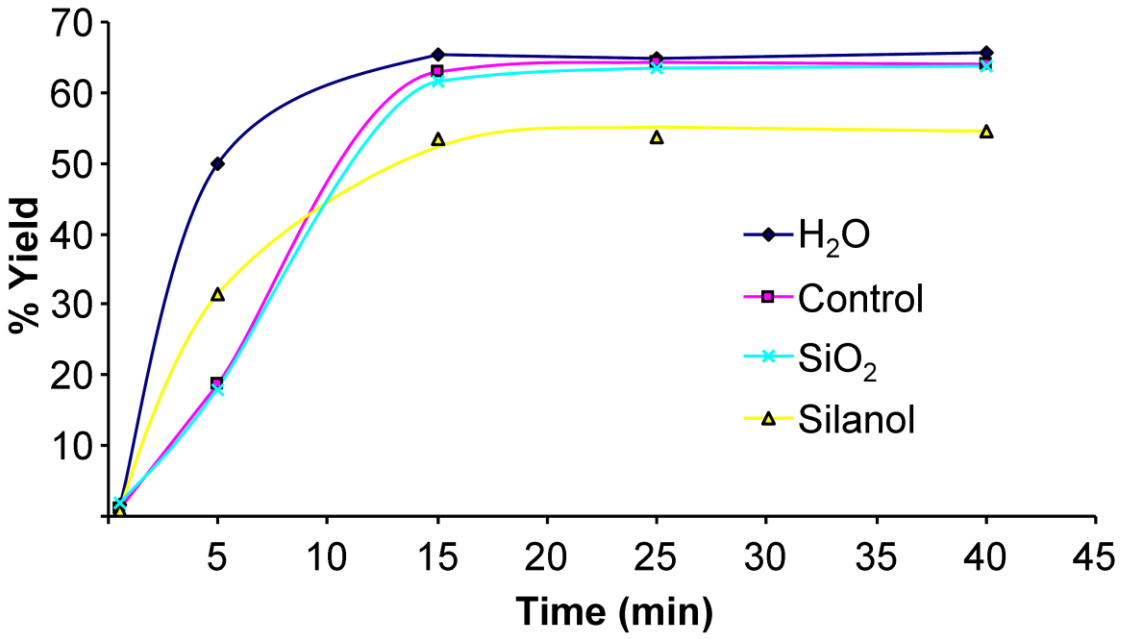

Figure 3.21 Overall yield of the cyclotrimerization with catalyst $Ni(CO)_2(PPh_3)_2$ in the presence of various contaminants (see text).

To test the impact of various contaminants on the catalysis, four standard reactions with $Ni(CO)_2(PPh_3)_2$ as the catalyst (see experimental details) were run in parallel at 100 °C, one of them as the control experiment, and three in the presence of a different contaminant. Triphenylsilanol (57.5 mg, 0.208 mmol) was added to one flask, water (0.1 ml, 5.551 mmol) and dry silica gel (139.0 mg, 2.313 mmol) to the two others. In all cases the solution quickly turned dark orange-brown within minutes of the addition of phenylacetylene. Furthermore, in all four cases the phenylacetylene was practically completely consumed within 15 minutes as determined by GC.

The addition of dry silica gel (139 mg) to an otherwise homogeneous reaction does not cause any significant change in rate, yield or selectivity (Figure 3.21). The

supernatant from such a reaction retains some catalytic activity in a second run without the addition of any silica gel or catalyst. The silica gel, on the other hand, is not imbued with any significant catalytic activity merely by witnessing the homogeneous catalysis going on. This result also shows that leached catalytically active species do not readily react with unmodified silica surfaces to form active heterogeneous catalysts. Furthermore, the formation of catalytically active, silica-supported nanoparticles seems to require prior immobilization.

Water contamination seems to accelerate the reaction somewhat (Figure 3.21), but experiments at lower temperatures, with more data points are needed to confirm this result. It is certain, however, that the presence of a small amount of deionized water does reduce the product ratio (unsymmetric to symmetric) slightly from about 12.4 to 10.9. This result might explain why previous coworkers always observed lower product ratios, as silica gel with different moisture content may impact the selectivity of the reaction.

Triphenylsilanol also seems to accelerate the reaction slightly, but it does not impact the product ratio in the least degree. There is a definite decrease in yield of about 10% when triphenylsilanol is added. Since all of the starting material is consumed, the triphenylsilanol must react to form a side product.

CONCLUSION

Homogeneous and immobilized nickel catalysts for the cyclotrimerization of alkynes have been studied, and the formation of nickel nanoparticles in both cases has been proven via TEM. These nickel nanoparticles are expected to be active catalysts

based on the change in activity and selectivity observed for all catalysts during the course of the reaction. Since commercially available nickel nanoparticles with a diameter of 20 nm are not active catalysts for the cyclotrimerization of phenylacetylene, it may be inferred that only nanoparticles with specific sizes or shapes are catalytically active.

Many solvents have been tested in this reaction in an effort to understand the longstanding question of why cyclooctane performs so well. It was found that cyclooctane actually performed rather similarly to the inexpensive solvent toluene under the reaction conditions employed in these experiments. The solvent that gave the highest activity at 60 °C was hexane. It is suspected that the choice of solvent and reaction conditions together dramatically influence the activity of the nanoparticles produced and so solvent screening should be performed for each case separately.

It was found that the catalytic reaction stops immediately upon admission of oxygen, but that the presence of a small amount of water can actually accelerate the reaction slightly. Importantly, the addition of well dried silica gel to an otherwise homogeneous reaction produced no change, indicating that the catalyst support does not participate directly in the reaction.

EXPERIMENTAL

Homogeneous Catalysis

Typical catalytic reactions were carried out as follows: a dry, degassed Schlenk flask was charged with naphthalene (100 mg 0.780 mmol), $Ni(CO)_2(PPh_3)_2$ (10 mg,

0.016 mmol) and dry, degassed cyclooctane (5 mL). This mixture was stirred and placed in an oil bath which was subsequently heated to 60 °C. Once the proper temperature was reached, freshly distilled phenylacetylene (0.30 mL, 2.732 mmol) was added via syringe. When more volatile solvents were used, the stopper was firmly clamped into place and the stopcock was closed (except when samples were taken) to prevent evaporation of too much solvent. Drop-sized samples were taken at regular intervals and washed through 1 cm of silica gel in a Pasteur pipette with toluene into a GC vial. Subsequent GC analysis provides both yield and selectivity information.

Catalysis with Immobilized Catalysts

Catalysis with immobilized catalysts was performed according to the following typical procedure: 501.6 mg of **1** (Figure 1.01) was stirred in 5 mL of dry cyclooctane in a 100 °C oil bath. 0.31 ml of phenylacetylene was then added. The reaction mixture was stirred for two hours. The supernatant was then removed and the silica was washed three times with 11 mL portions of toluene. Vacuum was applied to remove the remaining toluene. Subsequently, 5 mL of fresh cyclooctane was added, and after lowering the flask back into the oil bath and allowing a few minutes for temperature equilibration, another aliquot of phenylacetylene was added.

Gas Chromatography

A Shimadzu GC-2010, equipped with an autosampler, was used for all GC analyses. The injector delivers 1 μL samples to the injection port which is heated to 300

°C. The sample is further split by a factor of 10 before introduction to the column. The column temperature starts at 50 °C and remains there for 2 minutes, after which the temperature increases at a rate of 40 °C per minute up to the final temperature of 285 °C which is held for 6 minutes for a total program time of 13.88 minutes.

Elution times (minutes) are as follows: phenylacetylene – 3.40, naphthalene – 5.04, 1,2,4-triphenylbenzene – 9.85, and 1,3,5-triphenylbenzene – 11.23.

GC Calculations

A calibration curve was measured for phenyl acetylene, naphthalene and 1,3,5-triphenylbenzene (it is assumed that the FID response to 1,2,4-triphenylbenzene is identical). The curve for naphthalene was used to predict the expected signal intensity if the reaction mixture were measured directly, without any dilution.

The concentration of phenylacetylene, for example, is then calculated by dividing the signal obtained for phenylacetylene by the signal obtained for naphthalene and then multiplying by the expected naphthalene signal previously calculated. The result of this calculation is plugged into the calibration curve for phenylacetylene to give the concentration of phenylacetylene in the reaction mixture at the time of sampling.

Transmission Electron Microscopy

All images were obtained using the FEI Tecnai G2 F20 ST FE-TEM. Solution samples were prepared by dropping the solution directly on the TEM grid (300 mesh Cu grids with a carbon film). Silica-supported samples were prepared by sonicating the

material in ethanol and then dropping several drops onto the TEM grid and then allowing it to dry for a few minutes.

CHAPTER IV

ADSORPTION OF METALLOCENES ON SILICA[†]

INTRODUCTION

Adsorption

Heinrich Gustav Johannes Kayser first used the term "adsorption" in 1881, although "sorption" had already been extensively studied and utilized by ancient peoples. For example, various adsorbents are recommended for use in the drying of wounds in Egyptian writings before 1500 BC.[47] Adsorbents were also used for decoloring, desalination, and other purposes in ancient times.[47] In 1785 Lowitz discovered the decolorizing effects of charcoal which were later applied to decoloring sugar. The first large scale application of activated carbon was in gas masks and on submarines during the first world war.[47]

The first reported example of column chromatography comes from Lester Reed in 1893 who separated colored salts in tubes filled with kaolin.[48] The process was established as a relevant scientific tool by Michael Tswett, a Russian botanist, who worked with chloroplast pigments and separated them by means of adsorption.[48]

[†] Reproduced with permission from "The adsorption of chromocene and ferrocene on silica: A solid-state NMR study" Cluff, K. J.; Schnellbach, M.; Hilliard, C. R.; Blümel, J. *J. Organomet. Chem.* **2013**, *744*, 119-124, Copyright 2013 Elsevier B.V.
and from "Adsorption of Ruthenium and Iron Metallocenes on Silica: A Solid-State NMR Study" Cluff, K. J.; Bhuvanesh, N.; Blümel, J. *Organometallics* **2014**, *33*, 2671-2680, http://pubs.acs.org/doi/abs/10.1021/om500254w, Copyright 2014 American Chemical Society.

Adsorption is crucial in many practical and relevant processes including chromatography, alternative refrigeration techniques,[49] abatement of chemical warfare agents[50] and other toxic compounds and in the production of catalysts. One area that is given increasing attention recently is the removal of pharmaceuticals and other contaminants from water which can be accomplished via adsorption.[51] Adsorption is also very important in the separation of gases.[52] For example, biologically produced H_2 and CH_4 both suffer from the presence of CO_2 which can be removed via adsorption on special activated carbons.[52c] Adsorption on a surface can also change the outcome of a reaction because reaction mechanisms on surfaces are different from those in solutions. For example, the standard kinetic theories do not always hold true when considering surface adsorbed species.[53]

Adsorption of Metallocenes

Metallocenes and their derivatives constitute an important substance class, and they are ubiquitous in catalysis and stereoselective synthesis. Surprisingly, however, their surface chemistry on oxides, such as silica, is basically unexplored, even though chromatography, using original or modified silica, is the standard purification method for metallocenes.

While ferrocene is comparatively robust, chromocene, for example, reacts with silica to result in the Union Carbide polymerization catalyst.[54] In general, the key step leading to reactions with surfaces or chromatographic purification is adsorption, a non-covalent, reversible interaction with the surface. Therefore, it is worthwhile to deepen

our insights into the adsorption process. The strategy employed in this work is twofold. The first priority is to develop a better understanding of the nature of compounds that can be adsorbed versus those that are not adsorbed. For this purpose a rough screening using different compounds with and without aromatic systems is indispensable. Equally important is to investigate the behavior of adsorbed molecules on the surface. Disentangling and quantifying the different modes of mobility of the surface species will significantly enhance our understanding in this respect. ^{2}H solid-state NMR of a deuterated surface-adsorbed compound will be investigated for this purpose.

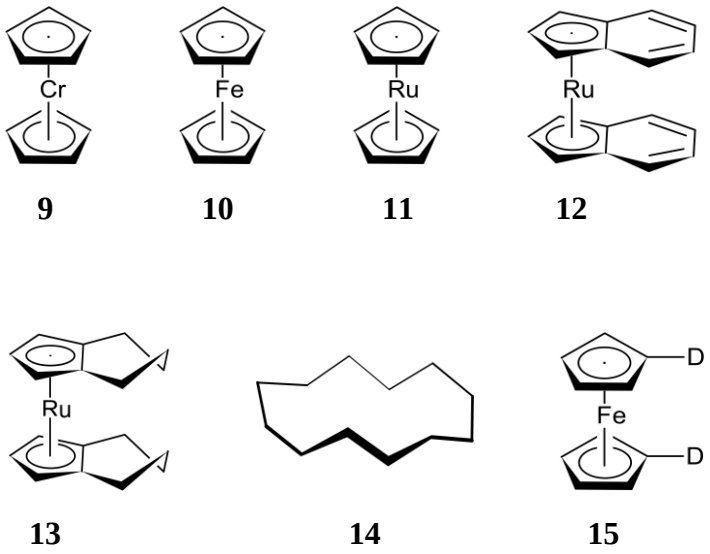

9 **10** **11** **12**

13 **14** **15**

Scheme 4.1 Molecules used for adsorption on silica surfaces.

The research results described here for several representative metallocenes including ruthenocene, ferrocene, and several modified metallocenes provide new

insights into surface adsorption processes and the dynamics of the adsorbed molecules. It will be demonstrated for the first time that metallocenes can be brought onto a silica surface in the form of a monolayer, and that this is even possible in the absence of a solvent.

The substances **9**−**15** (Scheme 4.1) have been adsorbed by grinding the dry components together with silica as described in the Experimental Section to give the adsorbed species **9a**−**15a**. In this chapter it will be demonstrated that the adsorption, and ensuing mobility, of the metallocenes is a universal phenomenon, and new insights into surface adsorption processes and the dynamics of the adsorbed molecules will be presented.

Cp_2Ru (**11**) shows that a larger central metal, and therefore distance between the Cp rings, does not impede the mobility on the surface. $(Ind)_2Ru$ (**12**) allows probing whether an extended aromatic system is still able to adsorb on the non-planar surface of amorphous silica. With $(Ind\text{-}H_4)_2Ru$ (**13**) the effect of the deviation of the aromatic ligand from planarity on the adsorption is investigated. The question whether the polarity of a species plays a role in its adsorption characteristics is answered by adsorbing cyclododecane (**14**) on silica. In order to study the different modes of mobility and to obtain a first estimate about the reorientation time of the surface-adsorbed species, deuterated ferrocene (**15**) is applied (Scheme 4.1).

Academic studies are usually conducted using model systems with planar surfaces, and most of the surface techniques employed for their characterization are invasive or provide only fragmentary data on specific functional groups, such as IR.

Other techniques are not practical for the swift throughput of large numbers of samples. Solid-state NMR spectroscopy,[11,55] on the other hand, provides deep insight into adsorption phenomena. It is not invasive and allows detecting and quantifying dynamic scenarios besides giving structural information about the species interacting with the surface.

^{1}H, ^{13}C, and ^{2}H MAS NMR will be used to describe how the adsorption and the ensuing mobilities of the adsorbed surface species **9a**−**15a**, derived from dry grinding of the polycrystalline substances **9**−**15** with different silica supports, manifest themselves in a chemical shift change of the signals, as well as reduced Chemical Shift Anisotropy (CSA) and residual linewidths compared to the spectra of polycrystalline metallocenes. The results should have far reaching implications, for example, for studying mechanisms in surface catalysis and for an improved insight into solid-solid interactions in general.

The early research by Günther[56] showed that the narrowing of the ^{13}C MAS signals is observed for a variety of adsorbed polycyclic aromatic hydrocarbons (PAHs).[56] When adsorption occurs, the $\delta(^{13}C)$ of the NMR signal changes, and the halfwidths and chemical shift anisotropies (CSA)[11b] of the ^{1}H and ^{13}C MAS resonances are reduced.[56] Besides these pioneering works, nearly all adsorption studies are based on gaseous or liquid phase adsorbates and/or metal surfaces. This literature is extensive and cannot be discussed here. However, some representative adsorption studies with high-melting substances in related fields are mentioned. (a) Phosphine oxides[57] and phosphines[58] have been applied to probe acidic sites on surfaces by ^{31}P solid-state NMR. Most of the adsorbed phosphines[58-59] display high mobility on oxide surfaces. This is

proven, among other means, by the cross polarization (CP) characteristics[14b,58,60] of the ^{31}P CP/MAS resonances. (b) Adsorbed polycyclic aromatic hydrocarbons (PAH) with higher melting points can show high mobilities on different oxide surfaces.[56,61] It has been proven that the NMR investigation of adsorbed PAHs can be especially revealing. For example, there are significant ^{13}C chemical shift changes for the adsorbed as compared to the polycrystalline state, but also the large intrinsic ^{13}C CSA[11a] of the PAHs is reduced due to their higher mobility on the surface. Even substituents and functional groups are tolerated, as in the case of the carbonyl group in benzophenone or the halides in 1,4-dibromonaphthalene.[56a] It has been described additionally that fullerenes adsorb on mesoporous silica (MCM-41) upon dry grinding of the components.[62] The ^{13}C resonances shift upon adsorption,[56] and therefore this process has to be based on the interaction of the π electrons with the surface.

Hence, it is of interest to investigate whether metals sandwiched between the aromatic Cp ligands have a measurable effect on their adsorption. Therefore, in this chapter it will be described whether the adsorption phenomena found for PAH on surfaces[56b,61,63] of mesoporous oxide materials will also be present in the model organometallic compounds chromocene (**9**), ferrocene (**10**), ruthenocene (**11**), bis(indenyl)ruthenocene (**12**), and its hydrogenated version **13** once they are adsorbed on silica to form **9a-13a**. In order to check whether purely aliphatic molecules show the adsorption effects, cyclododecane (**14**) is applied, and for quantifying the modes of mobility, the deuterated ferrocene **15** is adsorbed on silica.

For the paramagnetic metallocene **9** the signals are shifted beyond the diamagnetic region, and therefore they do not overlap with the ^{1}H and ^{13}C background signals of silica and rotor inserts, respectively. In contrast to chromocene, the species **10**−**15** are diamagnetic, and chemical shift changes upon adsorption are straightforward to interpret. The Ru and Fe complexes are comparatively unreactive toward silica surfaces. Only minimal decomposition is expected for **12** and **13**[64] and trace amounts of ferrocenium salts might be formed from **10** and **15**.[65]

Ferrocene is chosen not only because it represents a prominent cornerstone in organometallic chemistry, but because it is robust and only proceeds to generate ferrocenium salts after the adsorption when it is exposed to oxygen.[65] Therefore, the sampling of data can take place over extended periods of time. Finally, being diamagnetic in nature, the chemical shifts of **10** versus **10a** are expected to be more straightforward to interpret than the chemical shift changes of the paramagnetic **9**. Chromocene and ferrocene will constitute an instructive pair of adsorbates because they have high and nearly the same melting points (ferrocene: 172-174 °C, chromocene: 168-170 °C) and similar crystal packing. Hence, only electronic factors should play a role in the adsorption process and mobilities across the surfaces. Therefore, ^{1}H and ^{13}C as well as ^{2}H solid-state NMR methods are applied in this contribution to probe a possible increase in mobility when progressing from the crystal lattice to a surface monolayer.

Additionally, offering different surface polarities with rigorously dried, hydrophobic silica, and also silica with adsorbed water and silane-modified silica,[60]

should enhance the general knowledge about the characteristics of surface-adsorbed species.

RESULTS AND DISCUSSION

The polycrystalline compounds **9**−**15** (Scheme 4.1) have been adsorbed by grinding the dry components together with silica as described in the Experimental Section to give the adsorbed species **9a**−**15a**. The adsorption process is fast, and after grinding the dry components for 1.5 minutes, 88% of the material is adsorbed within the first 5 minutes and 95% within 2 hours. Longer grinding times result in faster adsorption, for example with only 1 minute of grinding the adsorption is a little slower (Figure 4.1). For **10**, the solvent impregnation method results in the same material **10a** as the dry grinding of the components.

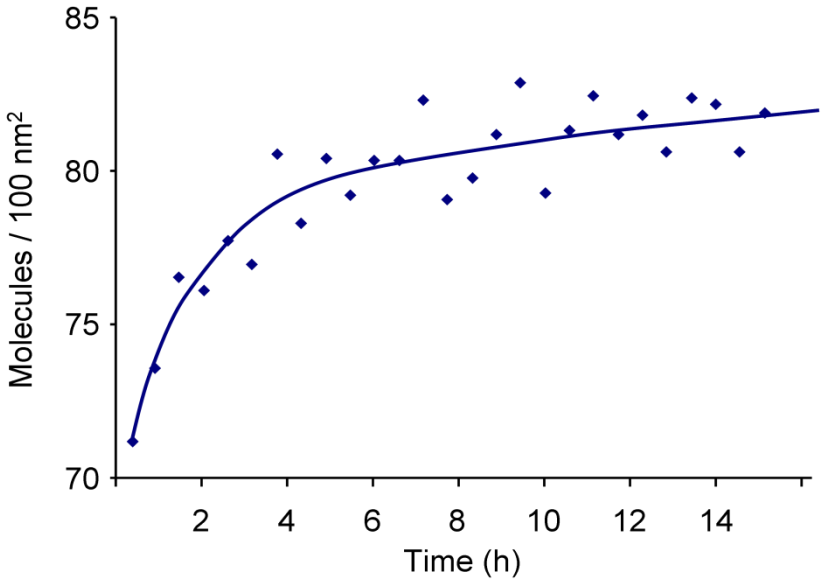

Figure 4.1 The surface coverage of **15a** on silica gel after grinding an excess of **15** with the silica for only one minute.

For the following experiments, the amounts have been calculated to give sub-monolayer coverages, so that the molecules would not be impeded in their movement by overly dense packing on the surface. For **15a**, different amounts have been applied (see below).

Assuming that all metallocenes are adsorbed by interaction of the π systems of their Cp ligands with the surface, in analogy to the PAH, they should "stand upright" on the surface.[56] Several different modes of mobility will be discussed in this chapter, including those depicted for ferrocene in Figure 4.2.

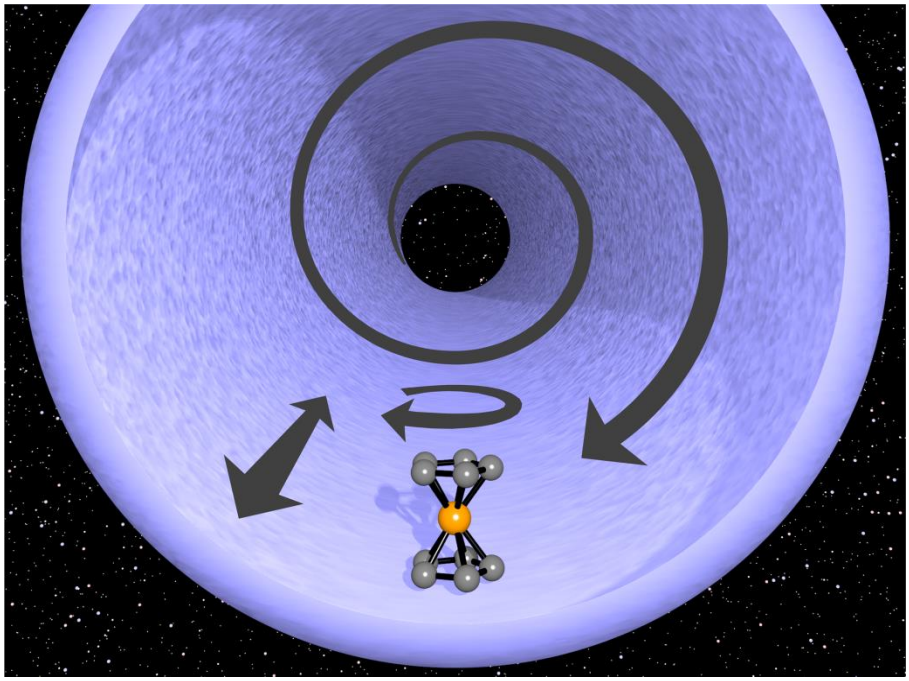

Figure 4.2 Modes of mobility when a metallocene molecule is adsorbed on the surface within an idealized silica pore.

Figure 4.2 shows a to-scale artist's rendering of a metallocene in an idealized straight pore with a diameter of 40 Å. In principle, the metallocene could also lie on the surface sideways, with the Cp−M−Cp axis aligned parallel to the surface and the Cp ligands functioning like the wheels on a car axle. However, this would imply that the Cp rings are oriented perpendicular to the surface and the interaction of the metallocenes with the surface would take place via the hydrogen atoms of the ligands. This scenario is unlikely, because aromatic compounds such as tetraphenylmethane, whose "prickly" geometry excludes a parallel orientation of the phenyl rings to the surface sterically, cannot be adsorbed on a silica surface.[58e] Even at higher temperatures or after dissolving the tetraphenylmethane prior to the adsorption on silica to surmount the lattice energy,

the molecules do not adsorb.[58e] Further evidence against rolling, or sliding sideways on the surface will be given, *vide infra*.

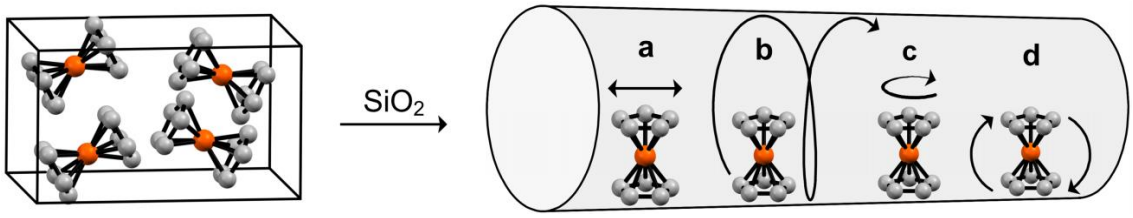

Scheme 4.2 When polycrystalline ferrocene (**10**) is ground with silica, the crystal lattice breaks up and the molecules are adsorbed on the surface within the pores. They can undergo various modes of translational and rotational mobility.

Translational mobility (Scheme 4.2, a) is an indispensable prerequisite for forming a monolayer of molecules by direct interaction of polycrystalline **9**–**15** with silica. There has to be sort of a "melting process", which overcomes the packing forces of the crystal lattice, and enables the ferrocene molecules to glide away from the crystal and make space for successor molecules. It can be assumed that the translational mobility persists also at a later point after consumption of the crystals and formation of the monolayer and is not just present in the initial contact phase. This will be corroborated later by probing the mobilities of **15a** with different surface coverages.

Overcoming the crystal packing forces for **9**–**15** needs substantial efforts, since their melting points are comparatively high (Table 4.1).

Table 4.1 Melting points of compounds **9**-**15**.

Compound	Melting Point (°C)
9	168-170
10	172-174
11[66]	197-200
12[64]	200-201
13[64]	66-67
14[67]	60-61
15	169

Since the surface of the pores within amorphous silica is not planar but concave (Figure 4.2), the adsorbed molecules can travel inside the pores on a spiraling trajectory (Scheme 4.2, scenario b), which results in isotropic reorientation of the molecules in space. This motion might be responsible for the reduction of the CSA and the residual linewidths of the signals of **9a**−**15a**.

It should be pointed out that practically all the surface of the mesoporous silica used is surface inside the pores because the average particle size is very large, between 0.063 and 0.2 mm in diameters. Taking into account that 1 cm^3 of the silica used weighs 0.515 g and that spheres can only fill 74.05% of space, one can calculate that even in the case of the smallest particle diameter of 0.063 mm only about 2% of the whole surface area of 750 m^2/g is contributed by surface outside of the pores. For the applications presented in this chapter this is negligible, and it can be assumed that practically all metallocene molecules are adsorbed on the surface inside the pores.

It is well-known that the Cp rings in metallocenes rotate even in the solid materials,[11a] therefore it is legitimate to assume that this ring rotation also takes place

when the molecules are adsorbed. Additionally, the whole molecules can most probably rotate in their place, as depicted in scenario (c) of Scheme 4.2. Since this mode of mobility is already present in the polycrystalline materials, it is unlikely to contribute to the reduction of the linewidths or the CSA of the adsorbed metallocenes in a major way.

One could also imagine that the metallocene molecules reorient quickly and isotropically around the metal center in sort of a "tumbleweed" scenario (Scheme 4.2, d). This mode of mobility would in principle reduce the residual linewidths and CSA of the adsorbate signals. However, taking into account that the interaction of an aromatic system with the surface is strong enough to break down crystal lattices,[56,68] this mode of mobility seems less likely.

Finally, it should be noted that the drawing in Scheme 4.2 is not according to scale. The average pore diameter of the silica used is 40 Å, while the height of ferrocene, including the Van der Waals radii of the carbon atoms, is about 6.7 Å. Therefore, if one ferrocene molecule is attached to the "bottom" of a pore, and another one to its "ceiling", this still leaves an open gap of 26.6 Å between the ferrocene molecules. Since ferrocene travels on the inner surface of the pores, and its crystals "melt" onto the surface, it cannot get stuck in the pores and block them.

The following results demonstrate that both chromocene and ferrocene are adsorbed on the surface of rigorously dried silica. Both the chemical shift and the CSA[11b] change upon adsorption. The CSA becomes substantially smaller in all cases, due to the increased mobility of the surface species as compared to the molecules confined to their places in the crystal lattice. The mobility reduces anisotropic

interactions in general, and therefore the residual linewidths of the isotropic lines are also substantially smaller.

Table 4.2 Residual linewidths, $\Delta\nu_{1/2}$ [kHz], of the ^{1}H and ^{13}C solid-state NMR signals of polycrystalline chromocene (**9**) and ferrocene (**10**) and their adsorbed forms on silica (**9a**, **10a**). Single pulse experiments at the MAS frequencies [kHz]: [a]13, [b]15, [c]10, and [d]2.

$\Delta\nu_{1/2}$ [kHz]	Chromocene		Ferrocene		
	$^{1}H^{a}$	$^{13}C^{b}$	$^{1}H^{c}$	$^{1}H_{wideline}$	$^{13}C^{d}$
Adsorbed	2.90	0.65	0.24	0.94	0.43
Polycrystalline	4.90	1.20	0.75	14.27	0.93

Table 4.2 summarizes all halfwidth data. It should be mentioned that no indication for stacking of **9a** or **10a** on the surface is found in the spectra. For adsorbed phosphines this is a trivial point because their free electron pair is consumed by the interaction with the surface. However, aromatic compounds and metallocenes have "two sides" and could in principle offer themselves for stacking, as surface-adsorbed phosphine oxides do.[69] In Figure 4.3 the ^{1}H MAS spectra of polycrystalline (**9**) and adsorbed chromocene (**9a**) are compared at 13 kHz spinning speed.

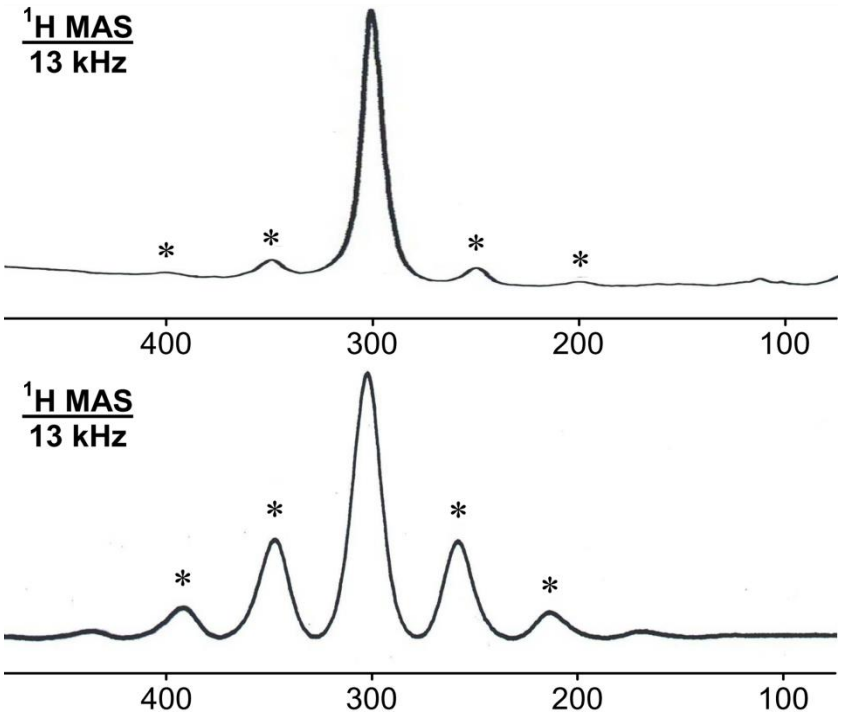

Figure 4.3 ^{1}H MAS NMR spectra of polycrystalline chromocene (**9**, bottom) and chromocene adsorbed on silica (**9a**, top, proton background signal of silica not shown). The asterisks denote rotational sidebands.

The chemical shift of the signal of polycrystalline **9** changes from $\delta(^1H)$ = 315 ppm to $\delta(^1H)$ = 298 ppm for the adsorbed species **9a**. Since the overall chemical shift range of paramagnetic metallocenes is large, the difference between the signal shifts of polycrystalline versus adsorbed chromocene is not too surprising. Especially because, together with mobility effects, the adsorption is also expected to change the electronic state of the organometallic complex. Most obvious in Figure 4.3 is the reduction of the CSA of the ^{1}H signal in **9a** compared to **9**. For the latter, all rotational sidebands are much more intensive, for example, the first order rotational sidebands reach nearly half the height of the isotropic line. In contrast, for **9a** the rotational sidebands barely emerge

from the baseline and might even be due to traces of residual polycrystalline material **9**. Upon adsorption, the residual halfwidth of the isotropic signal is also reduced from about 4.9 kHz in **9** to 2.9 kHz in **9a**. Regarding the spectrum of **9a** in Figure 4.3 it is also noteworthy that once it is adsorbed on the surface, chromocene starts to react with silica within an hour, losing one Cp ligand as cyclopentadiene and forming various half sandwich and dimeric species, as outlined in previous work.[54b] Some of these reaction products contribute to the background signal in the diamagnetic region of the spectrum around 0 ppm. Regarding the spectra displayed in Figure 4.4, the carbon chemical shift of polycrystalline **9** changes from $\delta(^{13}C)$ = 258 ppm (10 kHz) to $\delta(^{13}C)$ = 222 ppm (15 kHz) upon adsorption and formation of **9a**.

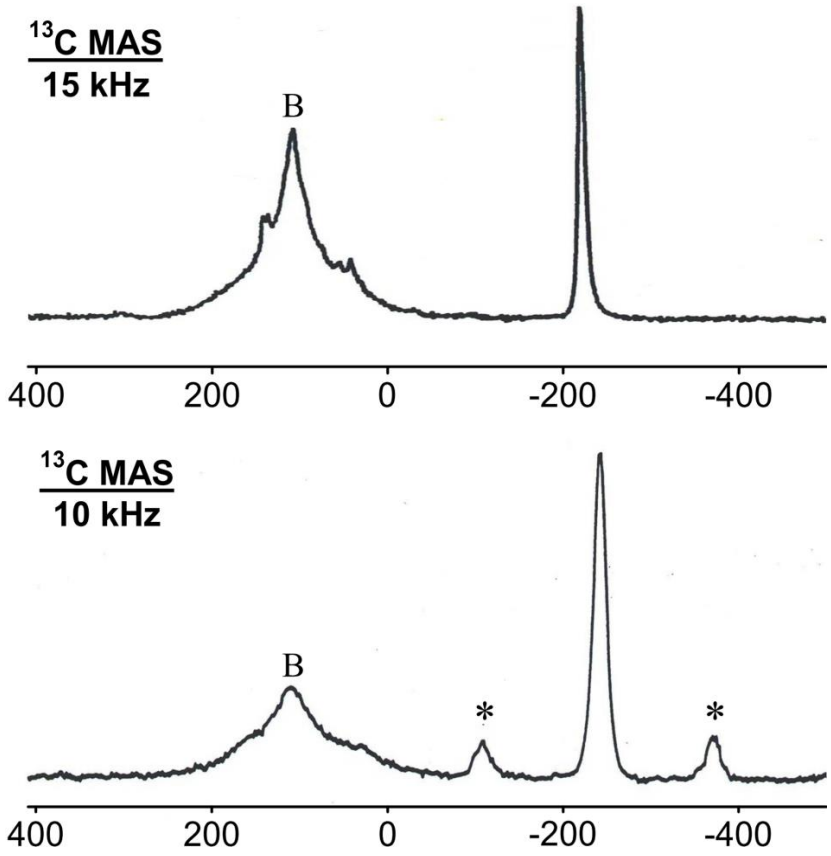

Figure 4.4 ^{13}C MAS NMR spectra of polycrystalline chromocene (**9**, bottom) and chromocene adsorbed on silica (**9a**, top). The asterisks denote rotational sidebands, B the signal of the carbon background of a teflon spacer in the rotor.

About 20 ppm of this signal migration into the diamagnetic region might be attributed to the higher spinning speed for **9a** and the heating due to friction effects.[70] However, about 16 ppm of chemical shift difference remain which can again be explained by changes in the shielding of the Cp rings upon adsorption on the silica surface. The residual halfwidth of the isotropic ^{13}C line is reduced to nearly half its original value on going from **9** (1.20 kHz) to **9a** (0.65 kHz) (Table 4.2). Again, this "slimming" effect can be attributed to the increased mobility of the molecules on the

surface. The very narrow line of **9a** even implies that the motion might be fully isotropic with translational in addition to rotational movements. Probably the adsorbed molecules in **9a** can even cruise along the walls and "ceiling" of the irregularly oriented pores of the silica like a skateboarder in a half-pipe, thus mimicking isotropic, solution-like mobility, as discussed above and depicted in Figure 4.2. The CSA of the ^{13}C MAS signals is reduced substantially when adsorbing **9** on silica to generate **9a**. This can again be deduced from the disappearance of the first order rotational sidebands (Figure 4.4).

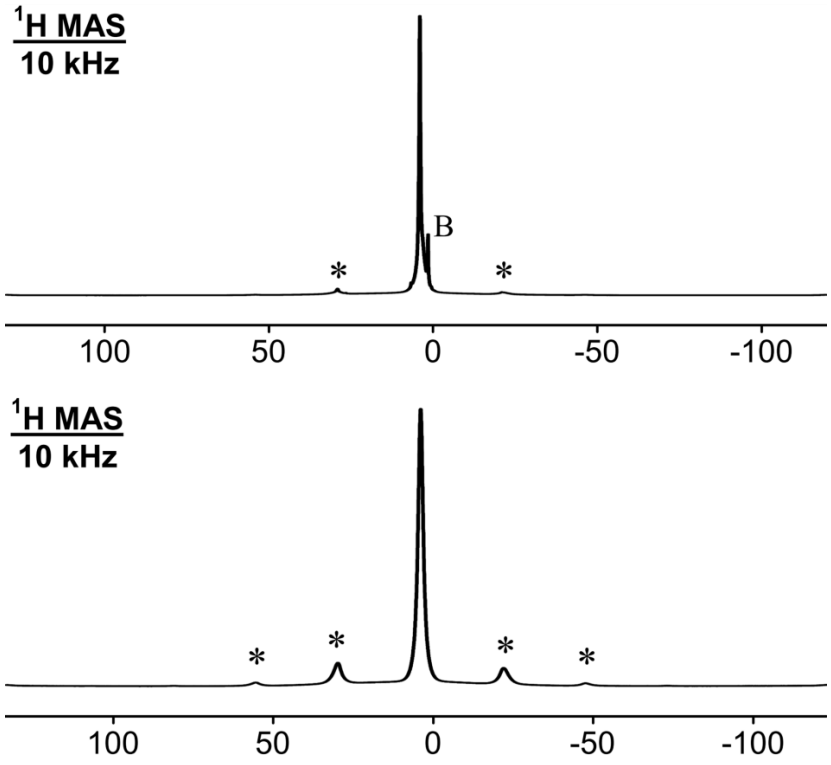

Figure 4.5 ^{1}H MAS NMR spectra of polycrystalline ferrocene (**10**, bottom) and ferrocene adsorbed on silica (**10a**, top) at 10 kHz spinning speed. The asterisks denote rotational sidebands, B the signal of the proton background of the silica.

The ^{1}H MAS spectrum of polycrystalline ferrocene (**10**) shows one isotropic line (Figure 4.5), as expected from the similar crystal packing compared to chromocene. The CSA pattern also looks symmetric and is composed of two sets of rotational sidebands in addition to the isotropic line. When **10** is adsorbed on silica to form **10a**, its chemical shift changes from $\delta(^1H)$ = 4.4 ppm to $\delta(^1H)$ = 4.6 ppm for **10a** at 10 kHz rotational frequency. This, albeit small, downfield shift is a typical trend for adsorbed species, for example, phosphines[58e] or phosphine oxides.[69] At the same time the residual linewidth of the isotropic line is reduced from 750 Hz for the signal of **10** to less than half that value, 240 Hz, for the resonance of **10a** (Table 4.2). The background signal in the ^{1}H MAS spectrum of **10a** (Figure 4.5) stems mainly from the protons in silica. When a rotor is filled with silica and a ^{1}H MAS spectrum is recorded using the same measurement conditions and parameters, including the receiver gain, the small background signal is observed. It can be subtracted from the ^{1}H MAS spectrum of **10a** without distortions of the baseline, yielding a clean spectrum with symmetric center line (not shown).

As in the case of chromocene, the CSA is reduced substantially, and the two miniscule first order rotational sidebands might stem from trace amounts of residual polycrystalline material **10**. The ^{1}H MAS signal of polycrystalline **10** is already rather narrow, and both the CSA and dipolar interactions are small. This is most probably due to the fast rotation of the Cp rings which takes place even in the solid state, because the activation barrier of this process is comparatively low with about 9 kJ/mol.[11a] In order to better see the difference between the signals of **10** and **10a**, the ^{1}H wideline NMR

spectra without rotation have been recorded in order to allow maximal CSA and dipolar interactions for static protons. This trick has been used recently to distinguish between backbone protons and included mobile water molecules in polymers.[13c] Indeed, as Figure 4.6 shows, the difference between the ^{1}H wideline spectra of **10** and **10a** is substantial.

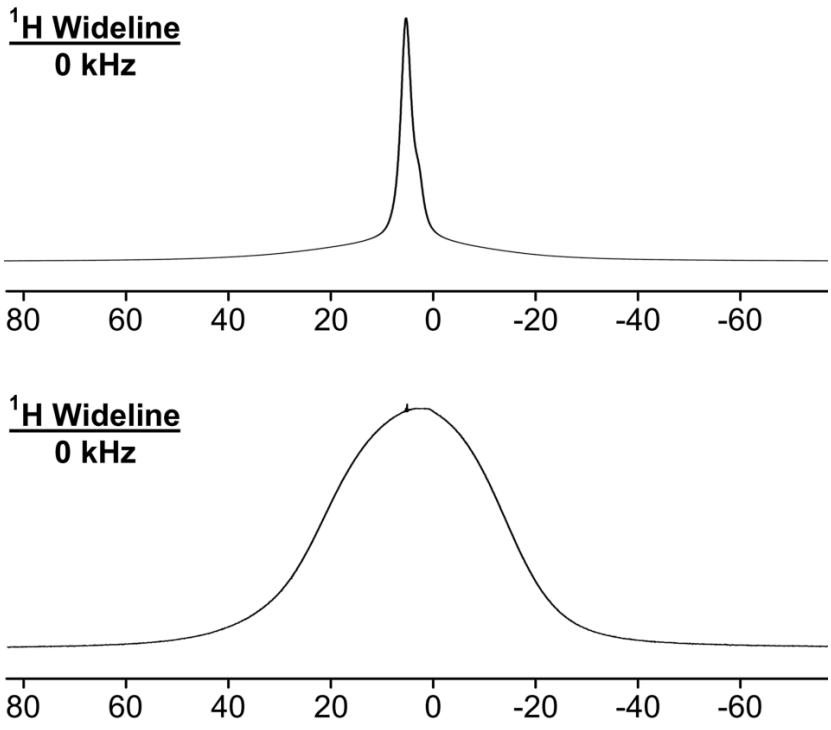

Figure 4.6 ^{1}H wideline NMR spectra of polycrystalline ferrocene (**10**, bottom) and ferrocene adsorbed on silica (**10a**, top).

After deconvolution of the spectrum of **10a** the linewidth of the narrow signal sitting on the background hump can be determined to be 0.94 kHz (Table 4.2). In contrast, the signal of polycrystalline ferrocene has a large halfwidth of 14.27 kHz. Again, this scenario can only be interpreted based on a fast isotropic motion of the

adsorbed ferrocene molecules across the silica surface in the pores (Scheme 4.2, a and b) which reduces the homonuclear dipolar interactions between the protons in ferrocene substantially. The ^{13}C solid-state NMR data (Figure 4.7, Table 4.2) corroborate the assumption that ferrocene is adsorbed on the silica surface and rather mobile. The chemical shift of the signal of polycrystalline **10** changes from $\delta(^{13}C)$ = 69.9 ppm to $\delta(^{13}C)$ = 71.2 ppm for **10a** at 2 kHz rotational frequency.

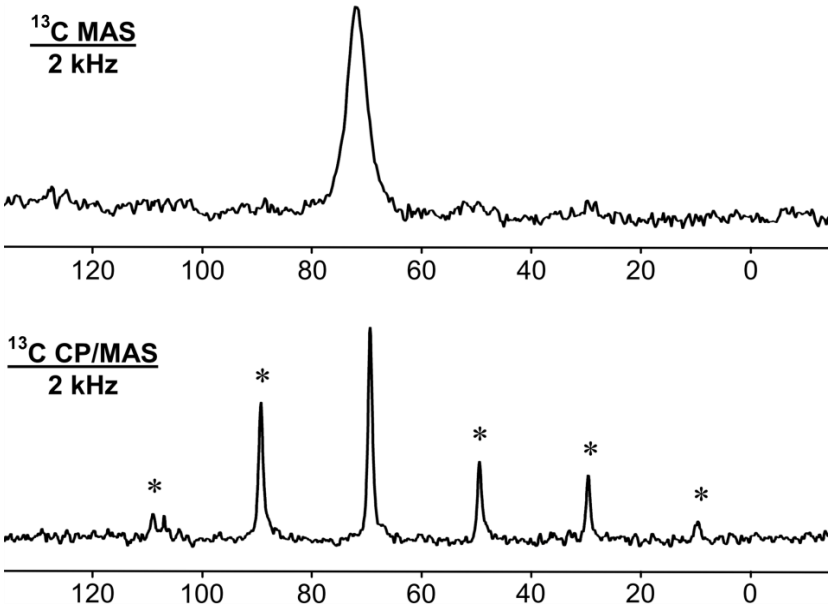

Figure 4.7 ^{13}C CP/MAS NMR spectrum of polycrystalline ferrocene (**10**, bottom) and ^{13}C MAS NMR of ferrocene adsorbed on silica (**10a**, top) at 2 kHz rotational speed. The asterisks denote rotational sidebands.

This is in accordance with the downfield shifts observed for adsorbed phosphines and phosphine oxides.[58e] The comparatively small CSA[11b] for polycrystalline **10** leads to the absence of rotational sidebands at high MAS spinning speeds. Therefore, slow

spinning with 2 kHz has been chosen for most experiments on **10** and **10a** (Figure 4.7). Upon adsorption the CSA is further reduced and at 2 kHz there are no longer sidebands present in the ^{13}C MAS spectrum of **10a**, only the isotropic line. Again, this can be attributed to the fast isotropic mobility of the adsorbed ferrocene across the support surface.

The ^{13}C linewidths of **10** and **10a** deserve some more detailed analysis. They are not directly comparable as shown in Figure 4.7 because different pulse programs have been used to record the spectra with optimal signal to noise (S/N) ratio. As demonstrated for adsorbed molecules in previous work, CP/MAS is no longer efficient because the dipolar interactions are reduced due to the mobility of the molecules.[71] Only the polycrystalline **10** gives good S/N with CP/MAS (Figure 4.7), and the residual linewidth has been determined as 88 Hz. An approximate halfwidth of 290 Hz has been estimated from the ^{13}C CP/MAS spectrum of **10a** with poor S/N. Simple high-power decoupling leads in both cases to the narrowest signals at 2 kHz spinning speed, with 53 Hz for **10** and 264 Hz for **10a**.

It is known from previous work on chromocenes that high-power decoupling can lead to a broadening of the signals of nonquaternary carbon nuclei when the decoupling frequency matches approximately the frequency of the Cp ring rotation.[70] In order to avoid this complication, as well as interferences of the Cp ring rotation with the MAS frequency[72] and splitting of the Hartmann-Hahn matching profile at higher MAS rates,[14b] the ^{13}C MAS spectra of **10** and **10a** (Figure 4.7) have been recorded with single pulse excitation at 2 kHz rotational frequency. This results in the halfwidths of ca. 930 Hz for

10 and 430 Hz for **10a** (Table 4.2), fulfilling the expectation of a line-narrowing effect due to the extra mobility of ferrocene molecules in **10a**.

The finding that adsorbed ferrocene is mobile on silica surfaces is also in accordance with earlier results obtained by photochemical techniques.[73]

Lowering the spinning speed for **10a** to 0 kHz and recording the ^{13}C wideline spectrum still gives a signal with respectable S/N ratio, and the linewidth increases only to 517 Hz. In contrast to this, the wideline spectrum of polycrystalline **10**, recorded with single pulse excitation results in a broad hump that merges into the baseline. Faster spinning with a rotational frequency of 12 kHz reduces the linewidth of the single pulse spectrum of **10** to 398 Hz, but unfortunately all rotational sidebands are spun out of existence in this case and herewith the CSA information is lost.

The residual linewidths for ^{13}C MAS signals of **9a** and **10a** (Table 4.2) are still larger by a factor of about 10 as compared with the spectacular results seen for adsorbed PAH.[56,61,63a,63c,63d] The residual linewidth should be very sensitive with respect to the electron density in the aromatic system because this is one factor determining the strength of surface adsorption and thus the mobility. The electron density is different for aromatic systems bound to metal centers as compared to the uncoordinated aromatic rings in the PAH, like naphthalene and biphenyl,[56,61,63a,63c,63d] and therefore the residual linewidths of the Cp signals in the metallocenes cannot be compared with the linewidths of those PAH. Additionally, in the case of chromocene, the paramagnetism leads to an increased residual linewidth.

Besides the electron density in the Cp rings, the pre-treatment of the support plays a role because the degree of wetness also influences the mobilities of the species on the surface and in turn the residual linewidth. This has been investigated by the Bluemel group in a parallel project about adsorbed phosphines.[69]

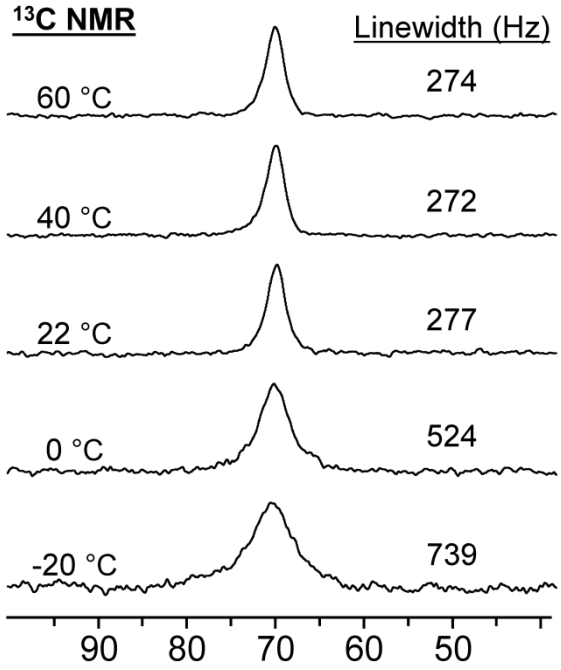

Figure 4.8 $^{13}C\{^{1}H\}$ NMR spectra of **10a** recorded at different temperatures on a liquids NMR instrument (see below). The temperatures and linewidth values (Hz) are listed for each spectrum.

As expected, the mobility of **10a** decreases at lower temperatures which leads to a broader signal (Figure 4.8). Interestingly, there is no further reduction of the linewidths when the measurements are performed above room temperature, indicating that the mobility at room temperature is already fast enough to cancel out the anisotropic

interactions (Figure 4.9). All variable temperature measurements are reversible and no additional signals or sidebands occur. Therefore, phase changes like crystallization at low temperature or sublimation at higher temperatures, as described in the next chapter, can be excluded.

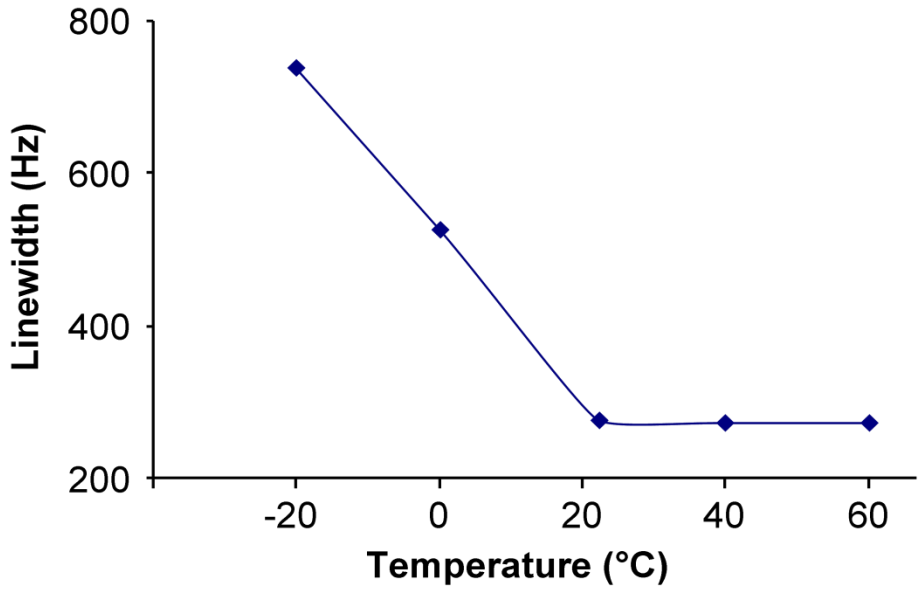

Figure 4.9 Change of the ^{13}C NMR signal linewidth of **10a** with temperature.

At this point one might also contemplate whether the presence of two different Cp signals, one for the ring interacting with the surface and one for the ring without surface contact, can be seen in the spectra of **10a**. In fact, two signals are observable, when the spectrum is recorded without decoupling, and when the surface loading of **10a** is low which leads to narrower lines. A spectrum recorded under these conditions is shown in Figure 4.10. Assignment of these signals is difficult and a series of spectra

were recorded with varying decoupling power (Figure 4.11) in an attempt to differentiate the signals of the two rings based on their rotational frequency.[70,72b] The top Cp ring would be expected to rotate more freely, and therefore faster, because it does not interact directly with the surface.

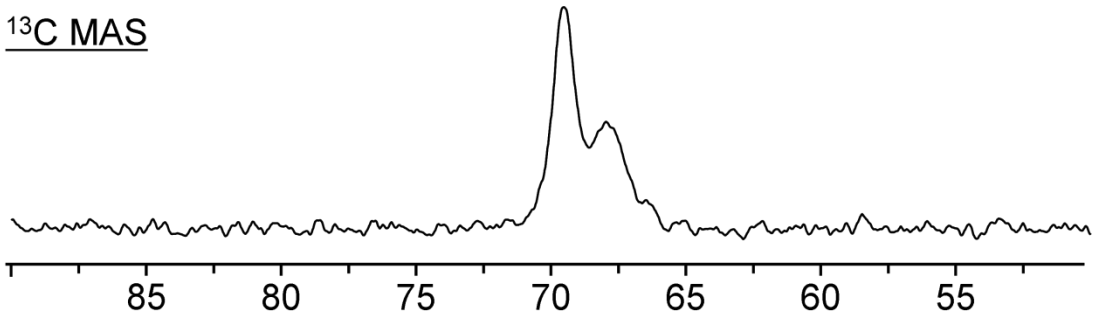

Figure 4.10 ^{13}C MAS spectrum of **10a** recorded using a single pulse sequence without ^{1}H decoupling.

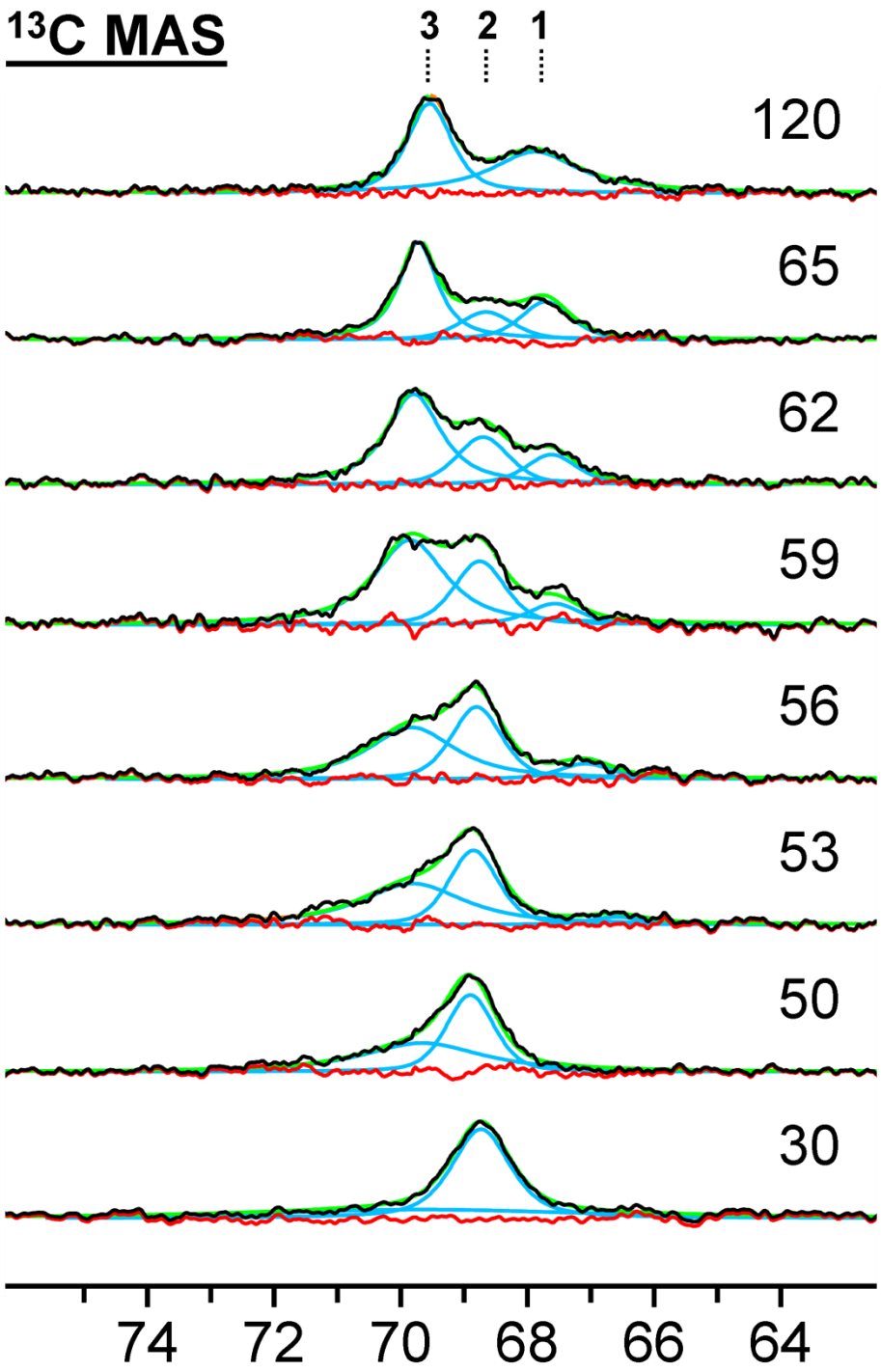

Figure 4.11 ^{13}C MAS spectra of **10a**, recorded with 2 kHz MAS rotational frequency using various values for the decoupling power level pl12 (listed on the right). A pl12 of 120 corresponds to zero decoupling power and 1.5 is the maximum power level tolerated by the 7 mm probe. The results of deconvolution and peak fitting are shown in blue, with the sum in green and the residual in red.

In most spectra, the two lines are too broad to be resolved. However, it is clear that the CSA of both signals is diminished. If one signal would retain the original CSA, all sidebands in the spectrum of adsorbed ferrocene would be visible, with half the intensity of those in the spectrum of polycrystalline **10**, because the ratio of adsorbed to non-adsorbed Cp rings is 1:1. However, since there are no rotational sidebands left in the spectra of adsorbed ferrocene, it must be concluded that the CSA is diminished due to the translational mobility of the ferrocene molecules on the surface, which has to be the same for both Cp rings, irrespective of whether they interact with the surface or not. So, in contrast to adsorbed phosphines, where partial phosphonium formation might reduce the CSA, the CSA reduction of adsorbed metallocenes is entirely due to the translational mobility and not any interactions with the surface.

A similar case, although with less well-defined peaks, has been noted[74] in the ^{13}C NMR spectrum of $Mo(CO)_6$ supported on alumina. In this case, the authors assign the additional signals to less mobile populations in general, or to populations with less isotropic mobility.

Interestingly, the decoupling experiments (Figure 4.11) actually reveal the existence of 3 different signals at 67.19, 68.78 and 69.76 ppm which will be referred to as signals 1, 2, and 3, respectively. The halfwidths (Figure 4.12) of signals 1 and 2 remain practically constant throughout most of the decoupling experiments, varying randomly around averages of 98 and 94 Hz, respectively. Signal 1 broadens significantly at the lowest decoupling power. The linewidth of 83 Hz for signal 3 without decoupling,

on the other hand, increases linearly with increasing decoupling power. When pl12 reaches 50, the halfwidth of signal 3 amounts to 221 Hz.

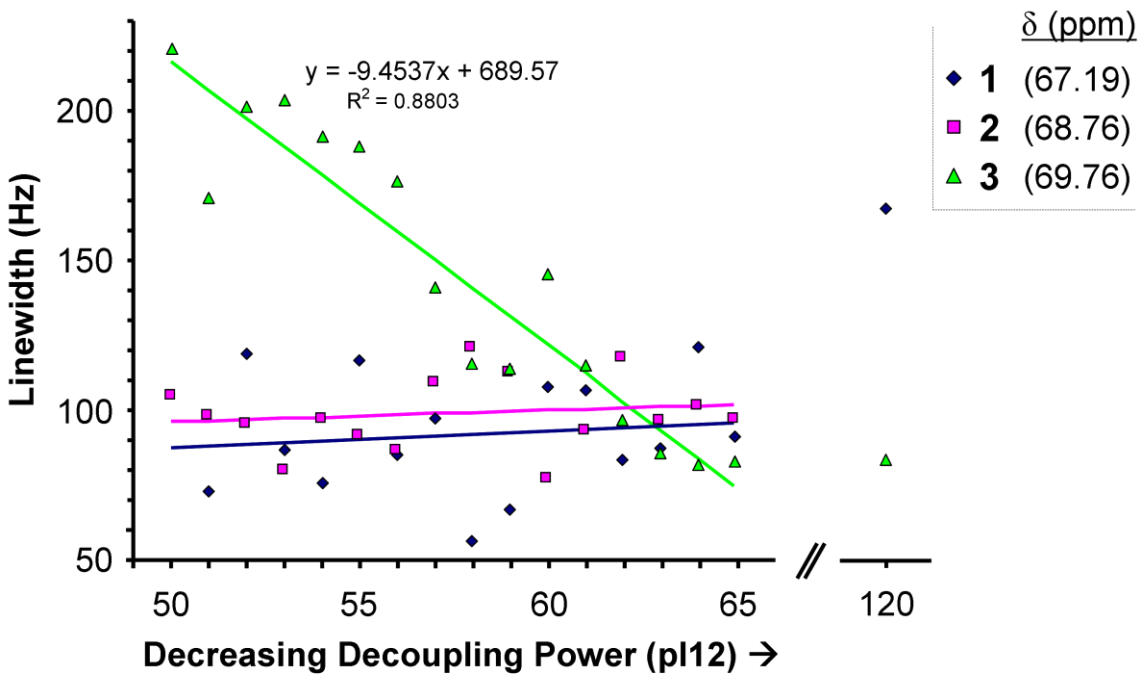

Figure 4.12 Linewidths of signals 1-3 over a range of decoupling powers.

The total intensity of signal 3 is very constant, however, over the course of the decoupling experiments (Figure 4.13) while signal 1 grows with decreasing decoupling power and the intensity of signal 2 decreases with decreasing decoupling power. Signal 3 represents approximately 50% of the combined signal intensities for 1, 2, and 3. The intensities of the signals 1 and 2 together constitute the other 50%. This leads to the assumption that one of the Cp rings gives rise to signal 3 and that the other one can be assigned to both signals 1 and 2 together.

Several questions arise at this point. (a) Does signal 3 belong to the Cp ring interacting with the surface or the ring on top of the ferrocene? (b) Why does the other Cp ring result in two separate signals, and why does the signal intensity seem to move from signal 2 to signal 1 as the decoupling power is decreased? These questions are difficult to answer because three different modes of mobility may be present in the molecule. They might potentially have similar frequencies as the decoupling power at some point which leads to signal broadening of the corresponding resonances.[70] First, the translational mobility of both Cp rings in the adsorbed ferrocene molecule should be the same. Since all three signals react differently on the decoupling power, translational mobility can not be responsible for the residual linewidths. The translational mobility of the whole molecule only leads to a reduction of the CSA, as seen in the absence of rotational sidebands for adsorbed ferrocene. The residual linewidths, however, are governed by the rotations of the Cp rings and the heteronuclear dipolar $^{13}C/^{1}H$ interactions. Based on the fact that signal 3 has the highest intensity and the narrowest line with least disturbance at low decoupling powers, corresponding to low frequencies, one might answer question (a) with yes and assign signal 3 to the Cp ring in ferrocene that has no contact with the surface and thus the fastest ring rotation. In other words, the higher decoupling frequencies at higher powers lead to interferences with the higher frequency of the ring rotation. This corresponds to earlier results obtained by studying the effects of decoupling on the linewidths of quaternary and non-quaternary ^{13}C NMR signals of polycrystalline decamethylchromocene.[70]

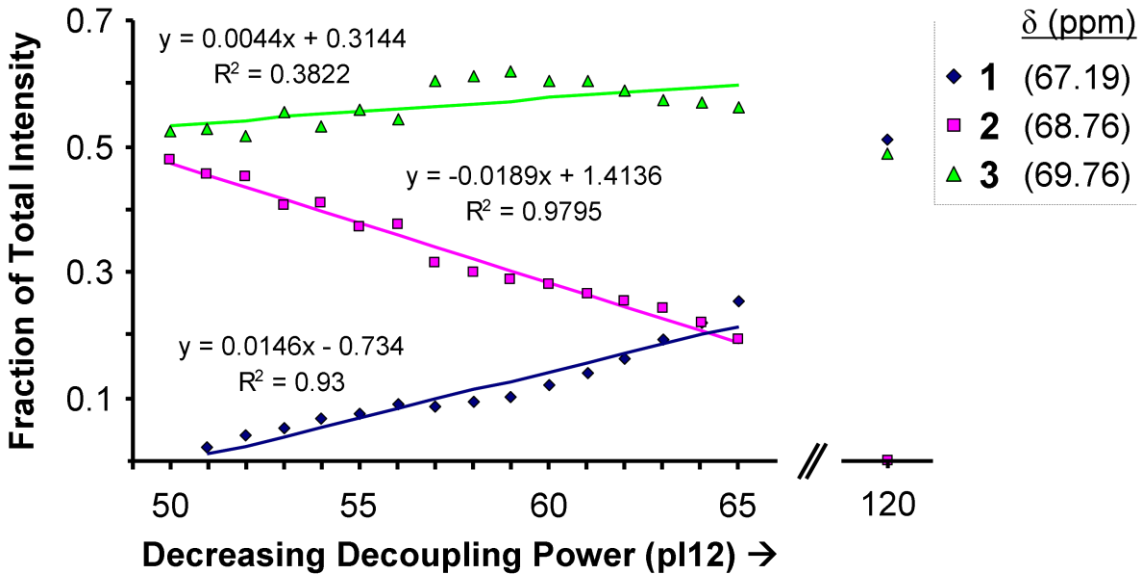

Figure 4.13 Distribution of the total signal intensity between the three observed lines.

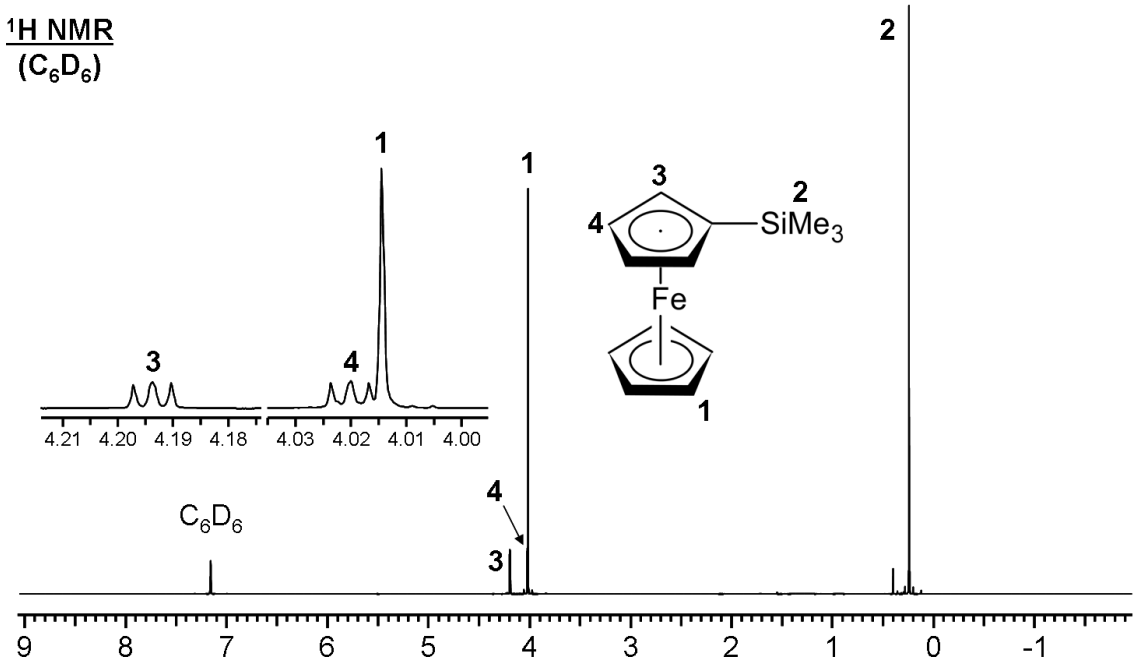

Figure 4.14 ^{1}H NMR spectrum of Me_3Si-substituted ferrocene in C_6D_6.

In an effort to better understand the nature of the peaks 1 and 2, trimethylsilyl-substituted ferrocene (Figure 4.14) was synthesized and adsorbed on silica gel. To generate the monosubstituted product, ferrocene was deprotonated with ^{t}BuLi and then quenched with $ClSiMe_3$. This reaction resulted in a mixture of products, including unsubstituted, monosubstituted and doubly substituted ferrocene (see Appendix, Figure C.21 and Figure C.22). These were separated by column chromatography using hexanes as the eluent to finally give the pure, monosubstituted product (Figure 4.14) as an orange oil. The first compound to elute from the column is the doubly substituted product, possibly because the TMS group hinders adsorption of the Cp rings. Next, the singly substituted ferrocene and lastly the unmodified ferrocene are eluted. Based on this result, it is tempting to say that the monosubstituted ferrocene will preferentially adsorb with the TMS-modified ring on the upside, and the unmodified Cp ring contacting the surface. This analysis, however, does not account for potential differences in solubility or other factors that could influence the elution order during chromatography.

The purified monosilylated ferrocene was adsorbed onto silica gel by means of impregnation via pentane solution because the adsorbate is a liquid. After removal of the solvent the ^{13}C MAS spectrum was recorded (Figure 4.15). The methyl resonance appears at -1.39 ppm with a linewidth of 179 Hz. Deconvolution reveals three signals (denoted a, b, and c) at 73.08, 71.29, and 68.75 ppm with linewidths of 187, 129, and 130 ppm, respectively.

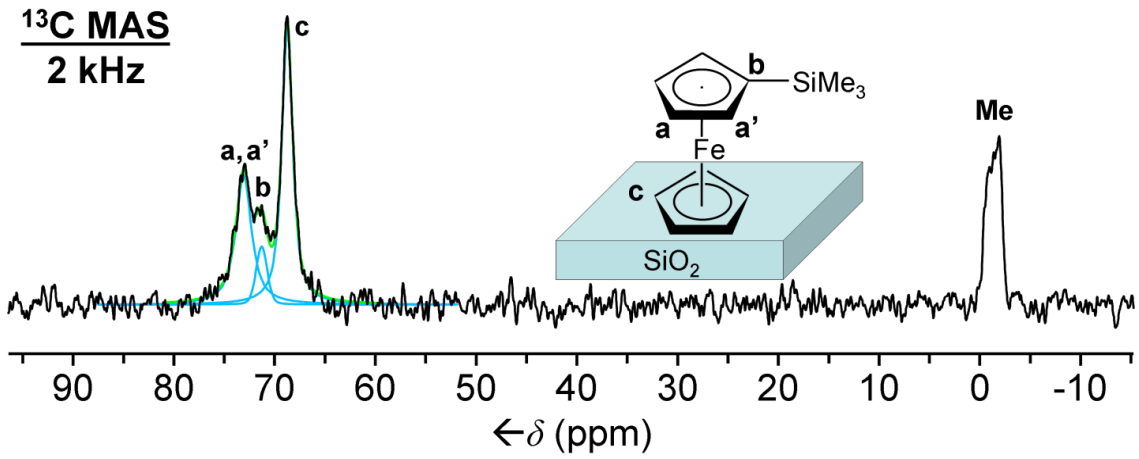

Figure 4.15 ^{13}C MAS spectrum of TMS-ferrocene on silica gel. The three blue lines are the result of deconvolution and the green line represents the sum of the deconvoluted lines. It is important to note that this spectrum was recorded using a single pulse program, without any proton decoupling.

Signals a, b, c, and the methyl peak integrate to 4 : 1 : 5.9 : 3.7 which, together with the ^{13}C NMR chemical shifts from the solution measurement (Appendix Figure C.21) makes the signal assignment straightforward although broad signals of solids will not provide the precision for the integral values that would be possible in spectra of liquids due to deadtime issues. The two signals of the protons in the positions a and a' are overlapping.

The adsorption of unmodified **10** leads to some kind of reduction in symmetry which results in multiple peaks in the solid-state NMR spectrum. The adsorption of TMS-ferrocene, however, does not seem to reduce the symmetry any further. This is clearly seen because no additional signals are observed besides those expected based on the geometry of the molecule. The adsorption of TMS-ferrocene does not result in extra signals because the two rings are already differentiated. This makes sense if the two

signals observed in Figure 4.10 do indeed arise from the "top" and "bottom" Cp rings of **10a**. This hypothesis relies on the assumption that all TMS-ferrocene molecules will adsorb on the surface with the same orientation.

Another interesting feature of the ^{13}C MAS spectrum of adsorbed TMS-ferrocene (Figure 4.15) is the comparatively broad and unsymmetric signal of the methyl protons, along with a lower than expected intensity. The relaxation of methyl protons, even in the solid state, is usually fast due to the rapid rotation of the methyl groups, in this case around the C-Si bond. An additional rotation can take place around the C_{ring}-Si bond. The shape of the methyl resonance is not symmetric and narrow, as expected. Therefore, one might assume that at least one of the rotations is hindered by interactions with the surface. This can occur in case the molecule does not stand perfectly upright, but leans towards the surface with the TMS-modified Cp ring. In a future project temperature dependent measurements and variations of the decoupling power for adsorbed TMS-modified ferrocene will be undertaken to clarify this point.

To summarize this section, although ^{13}C solid-state NMR spectra need extra consideration with respect to line broadening effects due to the Cp ring rotation which can interfere with any high-power decoupling, the assembly of applied techniques still unequivocally supports the results from the ^{1}H wideline NMR spectra. Ferrocene is adsorbed on the silica surface and shows substantial mobility, mostly due to translational movement across the surface. It is suggested that the additional peaks that are visible under conditions of high resolution in combination with variable decoupling powers

correspond to the two CP rings of the ferrocene molecule, with one ring interacting with the surface but not the other one.

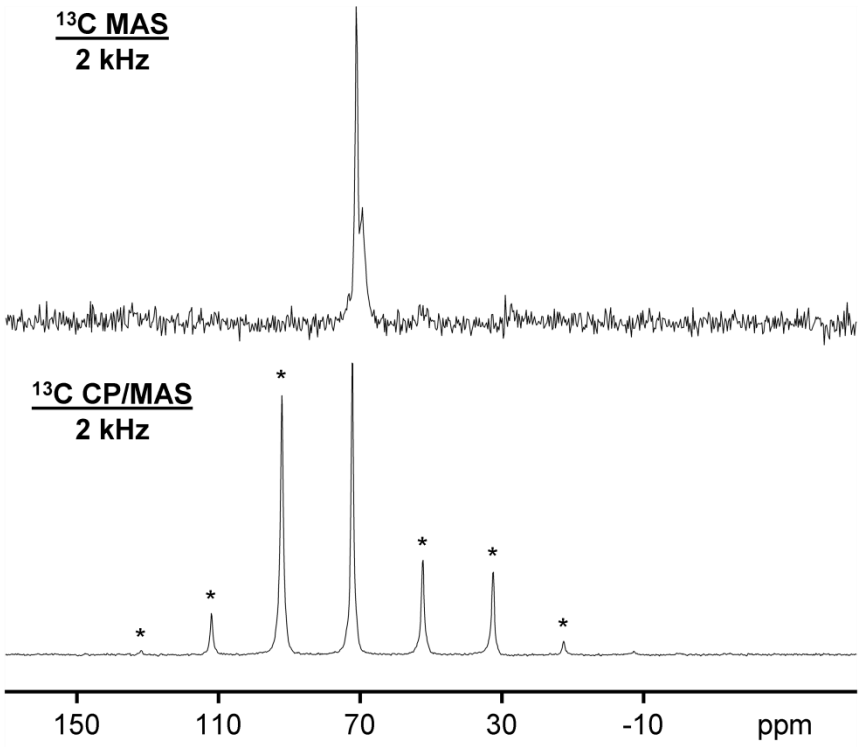

Figure 4.16 100.6 MHz ^{13}C CP/MAS NMR spectrum of polycrystalline **11** (bottom) and single pulse excitation ^{13}C MAS NMR spectrum of adsorbed **11a** (top). The asterisks denote rotational sidebands.

When polycrystalline Cp_2Ru (**11**) is mixed with silica, it is adsorbed on the surface as **11a**. Figure 4.16 shows the drastic change in the ^{13}C solid-state NMR spectra of **11** versus **11a**. The signal of polycrystalline **11** displays a large CSA, with a span[11b] of 81.3 ppm, which manifests itself in a multitude of rotational sidebands when the sample is spun and a large wideline pattern without spinning. The elements of the CSA (δ_{iso} =

72.2, δ_{11} = 99.7, δ_{22} = 98.3, δ_{33} = 18.4 ppm) have been obtained from the wideline pattern and by simulation using the spectrum recorded with rotation.[17] While the isotropic chemical shift changes only minimally upon adsorption, from 72.2 to 71.1 ppm, the CSA basically vanishes. A shoulder at the signal might be attributed to the surface adsorbed ring of the metallocene in analogy with the ferrocene case. Since the residual linewidth of the CP/MAS signal of polycrystalline **11** is already very small, with a value of 63 Hz (Figure 4.16), the change upon adsorption to the resulting linewidth of 91 Hz for **11a** does not seem substantial. It should be mentioned, however, that upon recording the spectrum of **11** with a single pulse program without decoupling, the residual linewidth amounts to 895 Hz, which means that contemplating this comparison the linewidth decreases by 804 Hz upon adsorption.

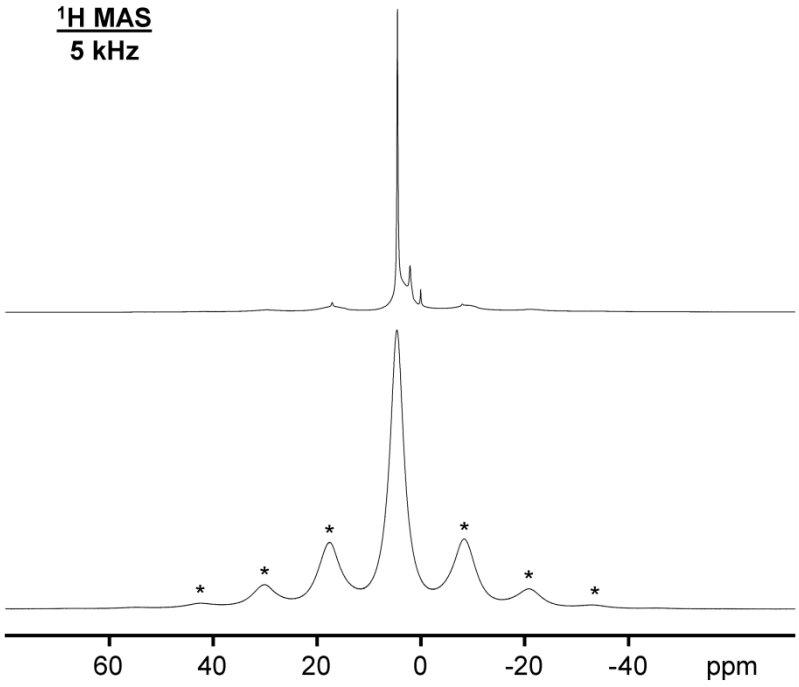

Figure 4.17 Single pulse excitation 400.1 MHz ^{1}H MAS NMR spectra of polycrystalline **11** (bottom) and adsorbed **11**a (top). Asterisks denote rotational sidebands.

Analyzing the ^{1}H MAS spectra of **11** and **11a** (Figure 4.17), however, besides the obvious reduction of the CSA, the residual linewidth is reduced substantially from 1.25 kHz for **11** to merely 88 Hz for **11a**. The low-intensity background signals at high field in the ^{1}H MAS spectrum of **11a** (Figure 4.17, top) stem mainly from the protons in silica and are also observed in the spectra of other adsorbed species. When a rotor is filled with silica and a ^{1}H MAS spectrum is recorded using the same measurement conditions and parameters, including the receiver gain, the small background signal is observed. It can be subtracted from the ^{1}H MAS spectrum of **11a** without distortions of the baseline, yielding a clean spectrum with a symmetric center line. Again, the isotropic chemical shift changes only minimally on going from **11** with δ_{iso} = 4.6 ppm to **11a** with 4.5 ppm.

So, overall, Cp_2Ru behaves very similar to Cp_2Cr and **10** with respect to adsorption and the ensuing changes in the solid-state NMR spectra.[68]

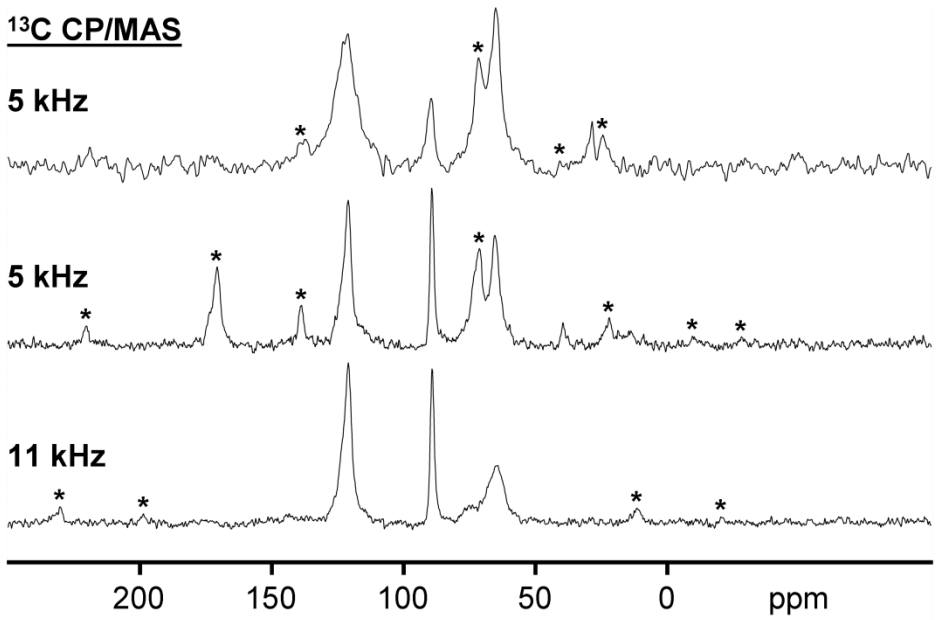

Figure 4.18 100.6 MHz ^{13}C CP/MAS NMR spectra of polycrystalline **12** (bottom: 11 kHz, middle: 5 kHz rotational frequency) and adsorbed **12a** (top, 5 kHz). Asterisks denote rotational sidebands.

Next, in order to test whether an extended aromatic system in the ligand would change the adsorption potential of a metallocene, $(Ind)_2Ru$ (**12**) has been adsorbed in a submonolayer on silica. The ^{13}C CP/MAS spectra are shown in Figure 4.18. At a spinning speed of 11 kHz the signals of polycrystalline **12** have only small first order rotational sidebands left. Therefore, the comparison between **12** and **12a** is based on 5 kHz measurements, where second order rotational sidebands are visible for **12**. Most

relevant diagnostically is the signal of the olefin carbon nuclei at 121.1 ppm[75] with its intrinsically large CSA.[11b] Again, upon adsorption, the number and intensity of the rotational sidebands are greatly diminished, which is best seen by the disappearance of the large sideband of the olefin carbon resonance at 170.8 ppm.

While there is no doubt that adsorption of **11** to form **11a** takes place, due to the reduced CSA, the extended π system of the indenyl ligands makes a difference. The residual linewidth is increased from 297 Hz for **12** to 358 Hz for **12a**. This effect might indicate that the molecules are more strongly adsorbed and therefore less mobile on the surface. Alternatively, one could speculate that, with the extended ligands, potential "tumbleweed" or rolling sideways modes of mobility might be inhibited, in this way leading to adsorbed, but less mobile surface species. It would also be plausible that the larger ligands inhibit the mobility on the nonplanar surface in the pores of the amorphous silica. However, the increased residual linewidths for **12a** could also stem from a slight decomposition of **12** on the surface,[64] creating Ru nanoparticles. This would also account for the relatively poor signal to noise (S/N) ratio (Figure 4.18).[2b]

In order to test this hypothesis, a metallocene with the same center metal Ru and an extended ring system of about equal dimensions, but without a conjugated aromatic system was employed. Bis(tetrahydroindenyl)ruthenium (**13**), offered itself as a logical choice. The proton NMR data of complex **13** have been given in the literature,[64] and I have added the ^{13}C chemical shifts and assigned the signals by an HSQC measurement. Surprisingly, in contrast to the single crystal X-ray data available for **12**,[76] none are in the literature for **13**.

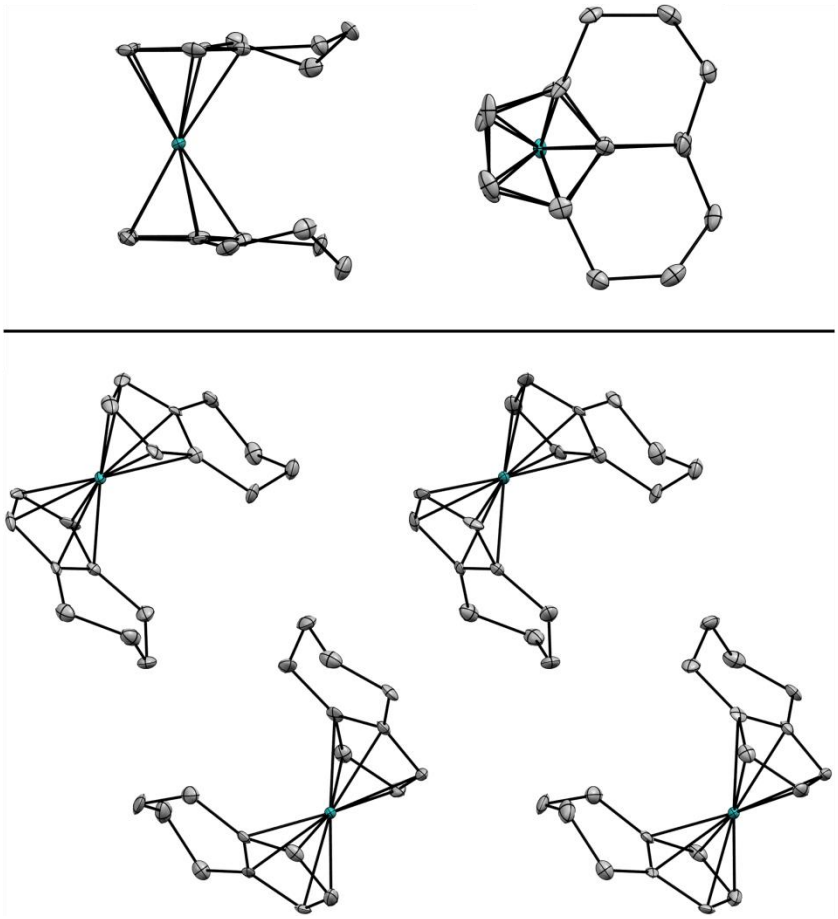

Figure 4.19 Single crystal X-ray structure of **13**. Packing of the molecules in the unit cell (bottom) and side (top left) and top view (top right) of one molecule. Thermal ellipsoids are shown at the 50% probability level. Hydrogen atoms are omitted for clarity.

Figure 4.19 shows the obtained single crystal X-ray structure of **13**. Although not quite intercalated due to steric constraints, the aliphatic substituents are seeking close proximity to each other. The top view (Figure 4.19, top right) shows that the aliphatic rings are eclipsed with a torsion angle of about 67.1°. The side view (Figure 4.19, top left) reveals a substantial deviation of the ligands from planarity. The aliphatic carbons and protons deviate from the plane of the Cp ring by as much as 0.50 and 1.47 Å.

Therefore, by studying the adsorption characteristics of **13**, the effect of slight nonplanarity of the ligands can be observed as well. There are four molecules in the unit cell of **13**, with two sets of magnetically inequivalent ^{13}C nuclei (Figure 4.19, bottom). Therefore, a double signal set is expected in the ^{13}C CP/MAS spectrum of polycrystalline **13**.

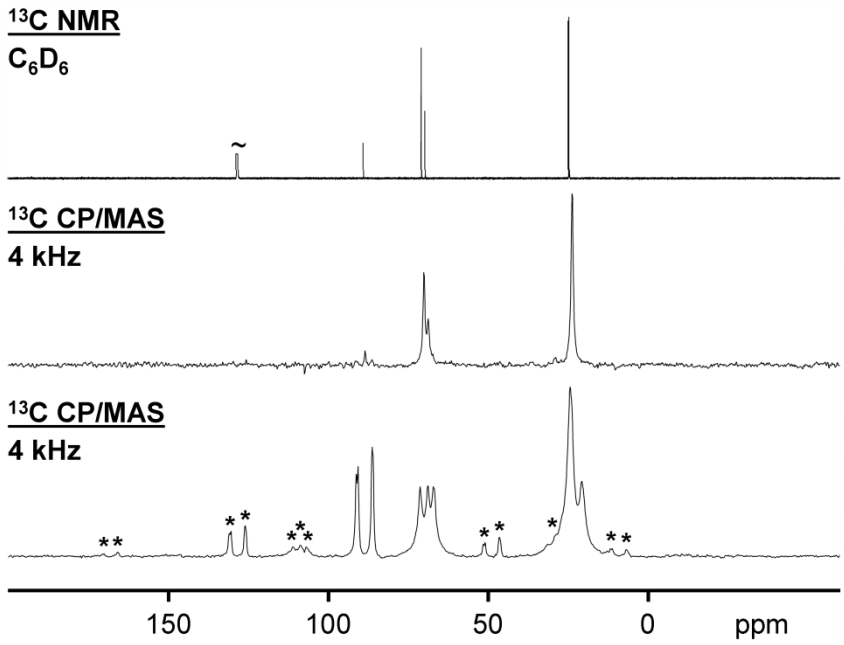

Figure 4.20 100.6 MHz ^{13}C CP/MAS NMR spectra of polycrystalline **13** and adsorbed **13a** (bottom two spectra) and **13** dissolved in benzene-d_6 (top). Asterisks denote rotational sidebands.

The bottom spectrum of Figure 4.20 shows that this is indeed the case. As expected the signals of the aliphatic ^{13}C nuclei at 20.5 and 24.4 ppm have only minimal CSA,[11b] which can be deduced from the absence of rotational sidebands at a spinning

speed of only 4 kHz. The resonances of the Cp ring carbon nuclei in the regions of the CH signals at 67.1, 69.0, and 71.4 ppm and the quaternary C signals at 86.3, 90.8, and 91.4 ppm, however, display the elaborate sets of rotational sidebands similar to those of **11** and **12**.

Upon adsorption, the appearance of the ^{13}C CP/MAS spectrum is thoroughly changed (Figure 4.20, middle). The average linewidth in the spectra decreases from 85 Hz for **13** to 49 Hz for **13a**, and all rotational sidebands are gone. For comparison, the spectrum of **13**, dissolved in benzene-d_6, is added as the top trace in Figure 4.20. This result shows not only that **13** is adsorbed on a silica surface but that, in contrast to anticipation, the cyclic alkyl substituent even seems to facilitate the mobility of the molecules of **13a** across the surface. In fact, the properties of **13a** are more similar to those of dissolved **13** than to polycrystalline **13**. Furthermore, this result rules out that the increased space requirement of the indenyl ligand in **12** is responsible for the comparatively broad residual lines of **12a**.

Finally, one can assume that a tumbleweed type mobility or rolling of **13a** via the ligands on the surface is extremely unlikely, as it is hard to imagine that these processes would not be impeded by the bulky alkyl substituents. Clearly, the extended aryl systems of the ligands in **12a** lead to strong adsorption and the alkyl substituents instead of a conjugated ring system enhance the mobility of **13a** across the silica surface.

Next, the effect of the alkyl substituents in **13** were elucidated by probing the adsorption of an alkane on silica. Cyclododecane (**14**) emerged as a viable candidate due to its comparatively high melting point (see above) and known solid-state NMR

characteristics.[77] Surprisingly, **14** adsorbs readily on silica to give **14a**, which can be seen in the narrower residual linewidth of the ^{13}C CP/MAS signals (Figure 4.21) of **14a** (18 Hz) as compared to **14** (60 Hz). However, even at the low spinning speed of 2 kHz there are no rotational sidebands for the signal of **14**, indicating the intrinsically low CSA of alkanes.[11b] Furthermore, the $\delta(^{13}C)$ changes only minimally from 23.64 ppm for **14** to 23.63 for **14a**.

Therefore, the ^{1}H MAS spectra of **14** and **14a** are diagnostically more valuable, because the large dipolar interactions guarantee multiple sets of rotational sidebands (Figure 4.22, bottom) for the pure material, which vanish upon adsorption due to the increased mobility on the surface (Figure 4.22, top).

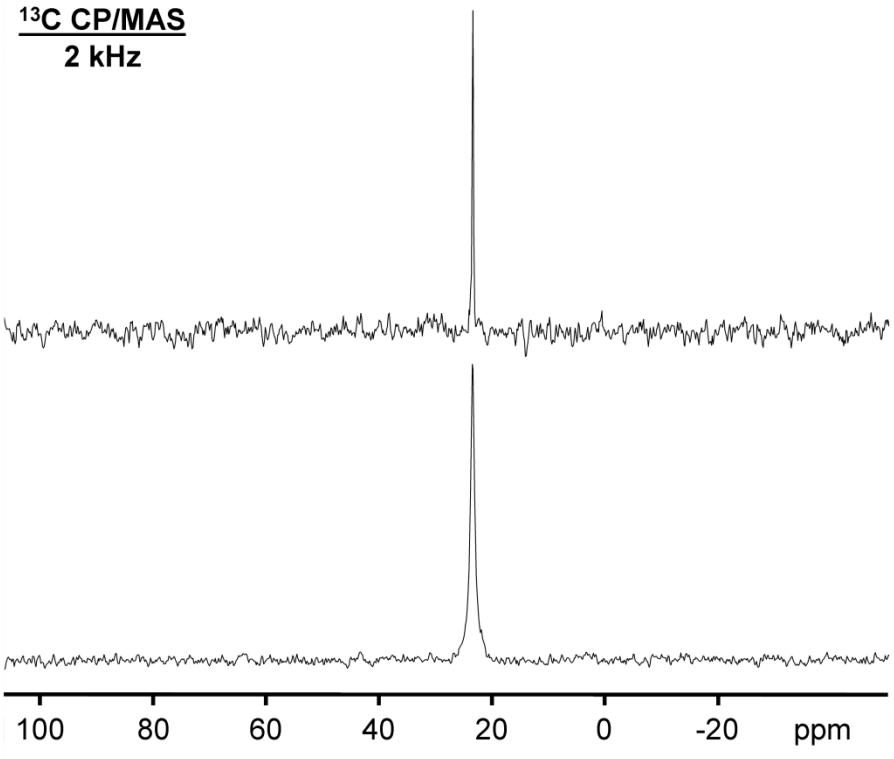

Figure 4.21 100.6 MHz ^{13}C CP/MAS NMR spectra of polycrystalline **14** (bottom) and adsorbed **14a** (top).

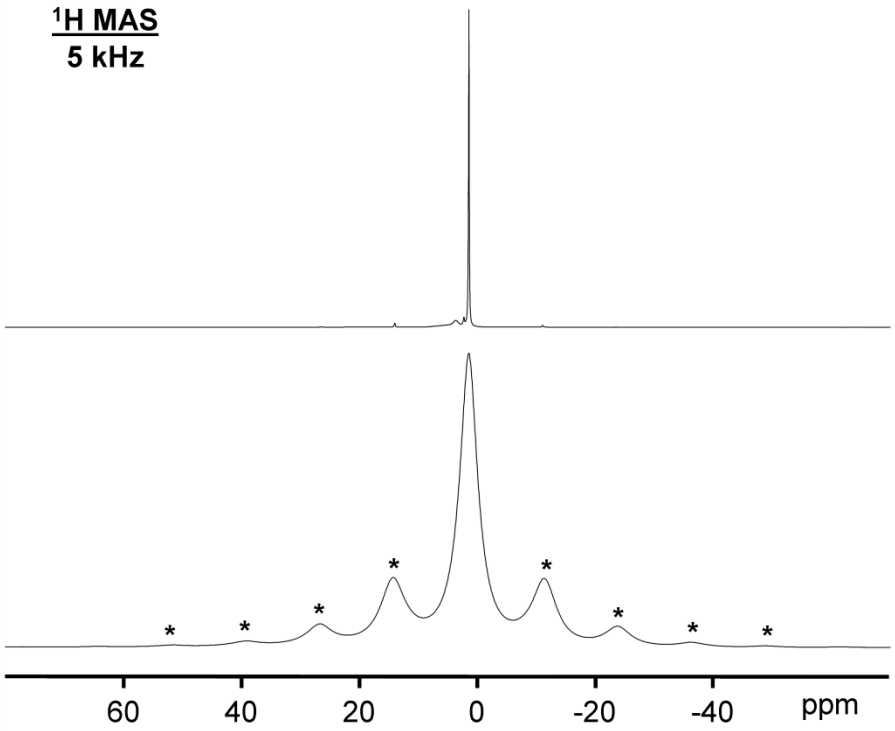

Figure 4.22 400.1 MHz ^{1}H MAS NMR spectra of polycrystalline **14** (bottom) and adsorbed **14a** (top). Asterisks denote rotational sidebands.

The $\delta(^{1}H)$ on the other hand changes minimally from 1.42 ppm for **14** to 1.39 ppm for **14a**. Since the melting point of dodecane is below 100 °C (see above), one could argue that the adsorption on silica might be facilitated by the pressure exerted on the sample during spinning and the slightly raised temperature within the rotor at a rotational speed of 5 kHz.[70] Therefore, the ^{1}H solid-state NMR spectra have also been recorded without sample spinning, a technique that earlier yielded crucial results in adsorption studies[68] and in polymer chemistry.[13c] Indeed, even in the absence of elevated temperatures and pressures the largest effect of adsorbing **14** can be seen in the ^{1}H wideline NMR spectra of **14** as compared to **14a** (Figure 4.23).

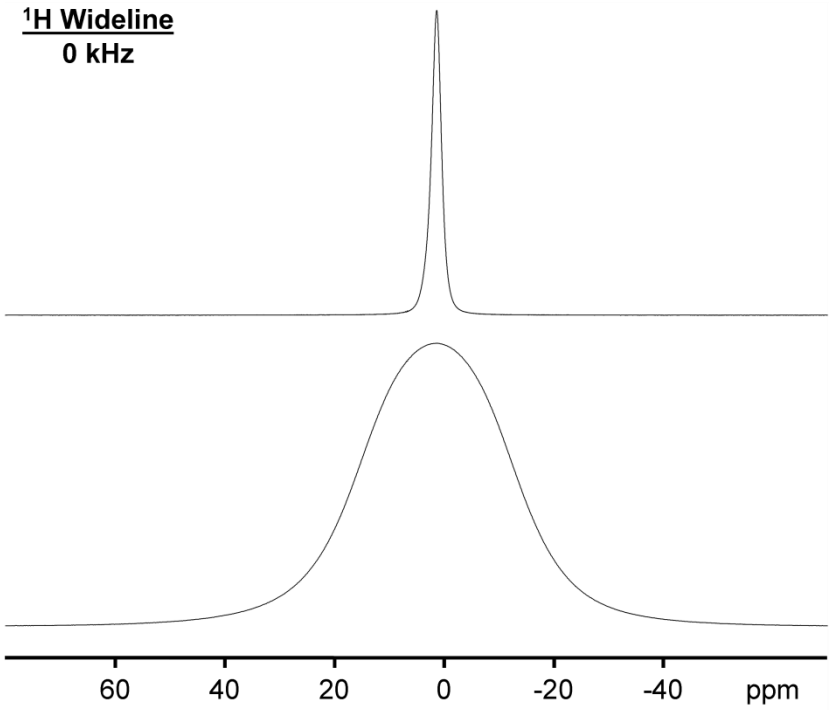

Figure 4.23 400.1 MHz ^{1}H wideline NMR spectra of polycrystalline **14** (bottom) and adsorbed **14a** (top).

The linewidth changes from 12.2 kHz for **14** to only 810 Hz for **14a**. The ^{1}H chemical shifts again undergo only minimal change from 1.4 ppm for **14** to 1.3 ppm for **14a**. The fact that cyclododecane is adsorbed so readily demonstrates impressively that Van der Waals interactions can be responsible for breaking up crystal lattices, leading to the adsorption of alkanes. To explore whether this adsorption is due to the volatility of cyclododecane, paraffin wax was also adsorbed on silica via dry grinding. Paraffin wax (mp 49 °C) is not volatile, yet it does indeed adsorb from the dry state and the ^{13}C NMR signals are dramatically narrowed as seen in Figure 4.24. The resolution is greatly enhanced by adsorption and compares favorably to that of a solution spectrum. This

phenomenon of solvent-free adsorption and mobility of solid alkanes might be interesting for applications in the oil and gas industry.[78]

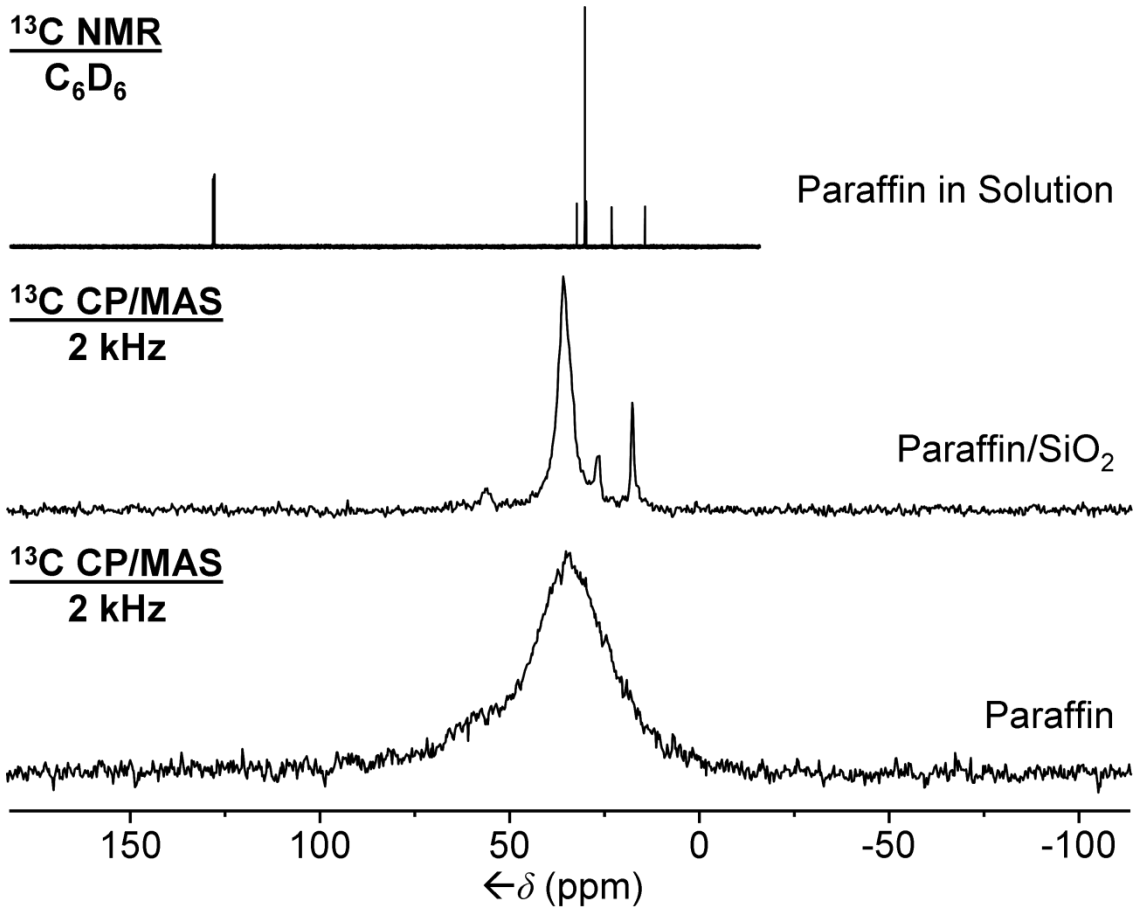

Figure 4.24 ^{13}C MAS spectra of paraffin wax, and of paraffin wax adsorbed by dry grinding with silica gel. The spectrum of paraffin dissolved in C_6D_6 is displayed on top for comparison.

Next, the quest for a more quantitative insight into the mobility of surface-adsorbed species inspired us to study the phenomenon by ^{2}H solid-state NMR spectroscopy. ^{2}H NMR spectroscopy in the solid state yields information on mobilities

via the quadrupolar coupling constant Q_{CC}, which can be derived from the splitting of the most intense lines in the Pake patterns.[11a] The correlation between reorientation times and appearances of the corresponding Pake patterns has been described in detail.[79] Recently, ^{2}H solid-state NMR has also been applied to obtain more quantitative insight into various other dynamic scenarios.[80] For example, the segmental dynamics of polymer chains[80e,80f] and a plasticization of poly(vinyl acetate) adsorbed on silica have been investigated.[80d] It has been shown that a ^{2}H MAS Pake pattern of fully deuterated polycrystalline chromocene can be measured,[70] although the compound is paramagnetic. Therefore, deuterated ferrocene (**15**) was synthesized according to a literature method[81] from the robust and inexpensive **10**. When polycrystalline **15** is measured without sample spinning, a typical Pake pattern results. The splitting of the most intensive lines of the Pake pattern is 72.5 kHz, which is in agreement with the literature.[82] The ^{2}H MAS spectrum of polycrystalline **15** is shown at the bottom of Figure 4.25.

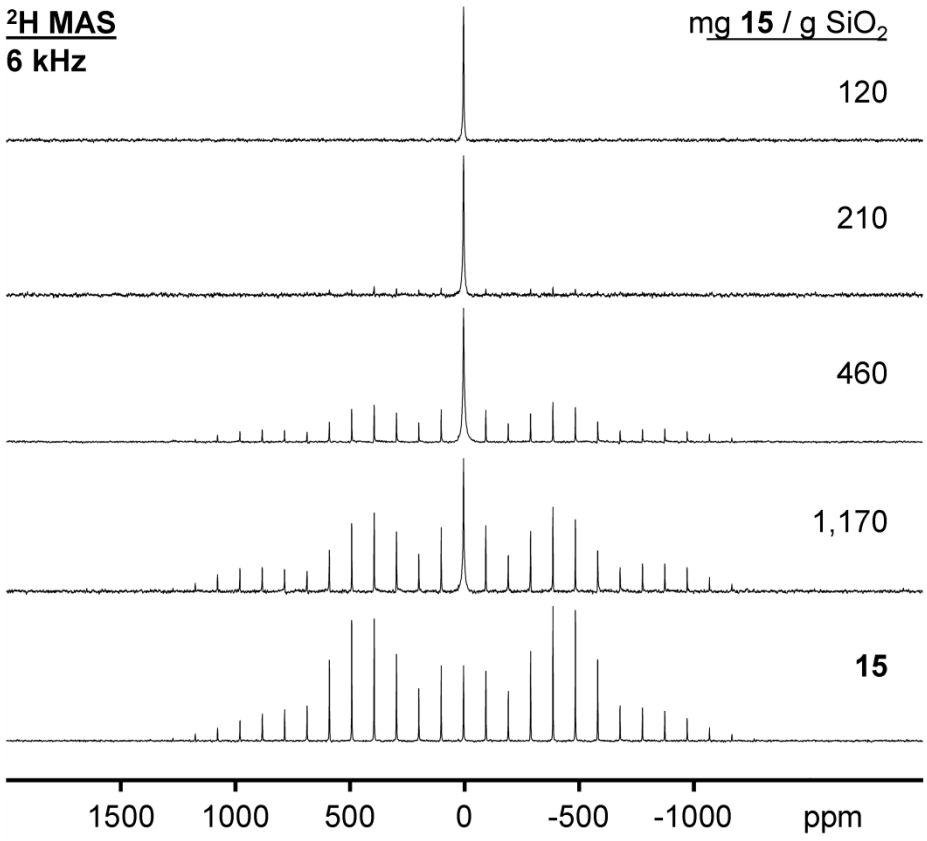

Figure 4.25 61.4 MHz ^{2}H MAS NMR spectra of polycrystalline **15** (bottom) and **15a** adsorbed on silica with the indicated wt% amounts.

The splitting of the most intense lines, as well as the quadrupolar coupling constant[11a] of 96.9 kHz can also be obtained from this spectrum using a line-fitting routine.[17] When **15** is applied to silica in the submonolayer quantity of 120 mg per g of SiO_2 (Figure 4.25, top), the Pake pattern collapses and a narrow line with a halfwidth of merely 170 Hz arises. Together with the absence of any rotational sidebands this indicates that **15** is completely adsorbed to form **15a** and that the molecules must experience isotropic mobility across the surface. A comparison with typical ^{2}H solid-state NMR lineshapes given in the literature[79] indicates that the reorientation time should

be shorter than 1 ns. When increasing amounts of **15** are applied to silica, as indicated in the ^{2}H MAS spectra of Figure 4.25, besides the narrow peak of adsorbed **15a** the Pake pattern of the residual polycrystalline material **15** is growing in intensity. Importantly, the transition from the adsorbed to the polycrystalline state is abrupt. There is no gradual increase of the signal linewidth of **15a**, which would indicate the formation of multilayers on the surface. This clearly shows that there is no stacking of the molecules of **15a** on the surface, as it could be assumed from the packing of **10** in the single crystal.[83]

The ^{2}H MAS spectra obtained after applying different amounts of **15** to silica allow the quantitative determination of adsorbed versus remaining polycrystalline material. With this ratio of **15a**:**15** the maximal surface coverage with molecules of **15a** in a monolayer can be obtained. The only complication in evaluating the spectra such as the ones shown in Figure 4.25 is that the ^{2}H chemical shift does not change substantially when going from **15** with 4.37 ppm to **15a** with 4.43 ppm. Therefore, the isotropic lines are overlapping, as displayed in Figure 4.26, and need to be subjected to deconvolution.[84]

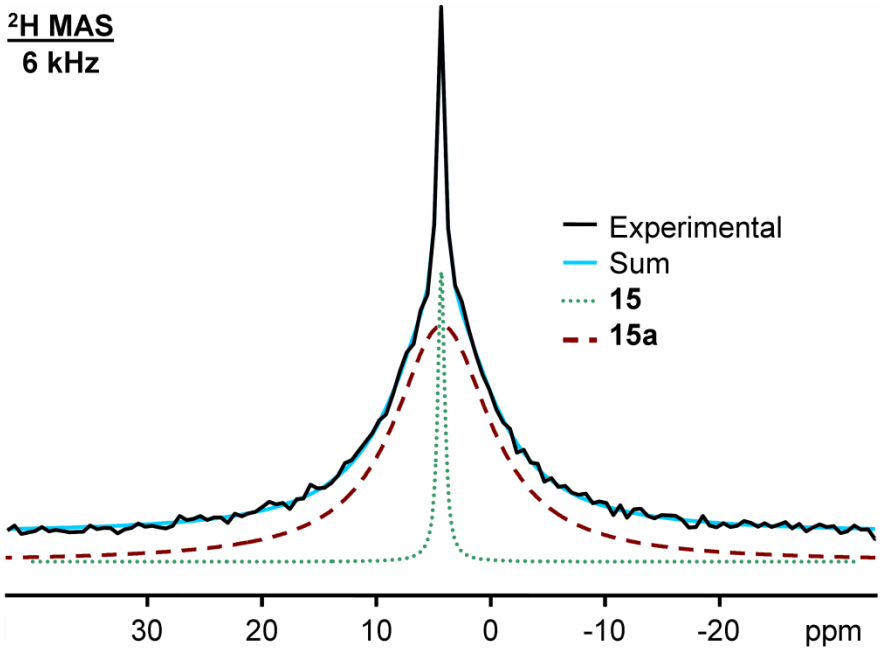

Figure 4.26 Deconvolution[84] of the overlapping isotropic lines of the ^{2}H MAS signals of residual polycrystalline **15** (narrow line) and adsorbed **15a** (broad signal) after grinding 460 mg of polycrystalline **15** with 1 g of silica (Figure 4.25, third trace).

The rotational sidebands and the narrow central line with halfwidths of only 41 Hz belong to the Pake pattern of the polycrystalline material **15**, while the single broader component of the central line stems from adsorbed **15a**. Figure 4.26 demonstrates that the deconvolution process[84] leads to an excellent fit of the sum of the deconvoluted signals with the experimental spectrum. When determining the ratio of **15a**:**15**, one needs to take care to add the intensities of all rotational sidebands of the Pake pattern to the intensity of the central line of **15**. When a large excess of **15** is applied to the silica, the maximal surface coverage of 118 molecules of **15a** per 100 nm^2 of silica surface can be determined from the ratio of adsorbed to polycrystalline material after deconvolution. Figure 4.27 depicts the view on a silica surface with maximal surface coverage.

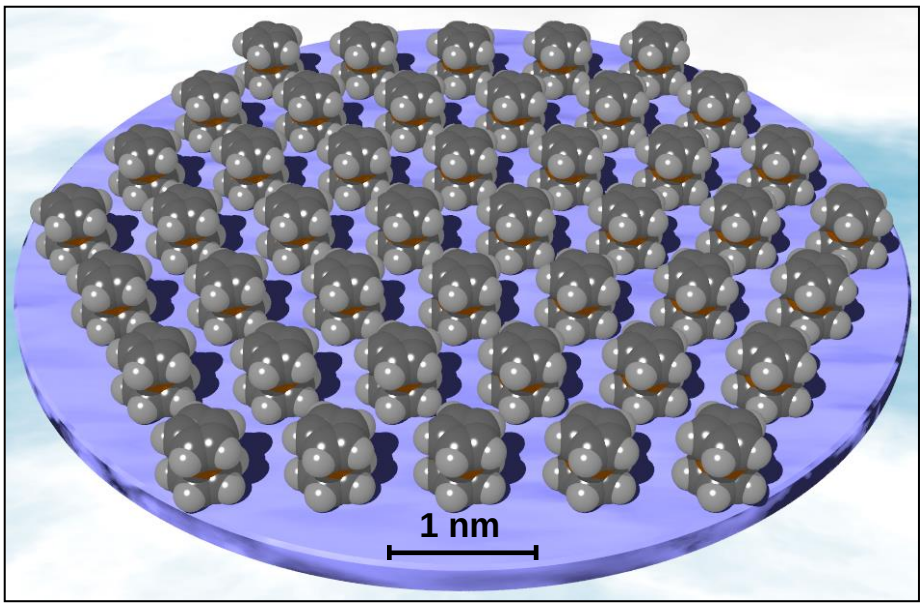

Figure 4.27 To-scale drawing depicting the maximal surface coverage of ferrocene on silica (118 molecules per 100 nm^2).

The footprint of **15a**, standing upright on the surface, was calculated based on the distance between the center of the Cp ring and an H atom (2.302 Å) and taking the Van der Waals radius of H into account to give an overall radius of 3.502 Å. Assuming hexagonal packing of these circles on the surface, about 201 **15** molecules can maximally occupy 100 nm^2 of surface area in a monolayer, corresponding to 2.50 mmol of **15** adsorbed per g of silica. Interestingly, comparing the calculated maximal density of **15a** (201 molecules per 100 nm^2) with the experimental value (118 molecules, Figure 4.27), there seems to be ample free "wiggle space" left between the ferrocene molecules. This is another indication that not only ring rotation but also translational mobility has to occur on the surface. With a theoretically densest packing on the surface there would not be enough room left for this translational movement, and therefore the "melting" of the

crystal onto the silica surface could not happen. The number of adsorbed molecules of **15a** depends on the amount of applied polycrystalline **15**.

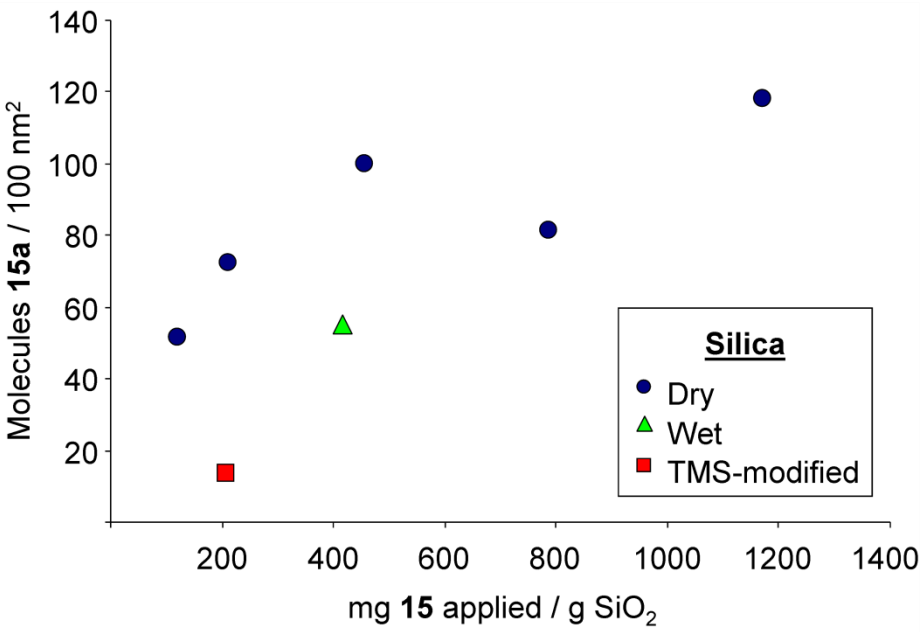

Figure 4.28 Amount of **15a** adsorbed on silica after its treatment with different amounts of **15**.

The graphical display in Figure 4.28 shows that the more **15** is applied, the denser the packing of the surface with **15a** becomes in the case of the well-dried silica. Since it is known that the nature of the surface also acts as a major factor determining surface coverages,[71] wet silica (see Experimental Section), with a hydrophilic surface and maximal number of silanol groups, and the hydrophobic trimethylsilyl (TMS)-modified silica,[60] where the silanol protons are removed by end-capping, have also been

tested with respect to the surface coverage. As Figure 4.28 shows, the surface coverage of **15a** on 100 nm^2 of wet silica is much lower than in the case of well-dried support, when applying a similar amount of **15**. Since **15** is not hydrophilic in nature and should in principle be attracted to TMS-modified silica by Van der Waals interactions, this result shows that surface silanol groups are mainly responsible for the adsorption of **15a**. In the case of an excess of water on the surface, however, **15** might be repelled by the water layer on the surface due to its hydrophobic nature, and therefore the surface water layer prohibits interactions with the surface silanol groups underneath. Although the TMS-modified silica is hydrophobic like the silica dried rigorously at high temperature in vacuo, the adsorption of **15** is minimal, with only 13 molecules of **15a** on 100 nm^2 of the modified silica. In comparison, using the same amount of **15** on well-dried silica, 72 molecules of **15a** are found on the surface. Again, the missing interactions with surface silanol groups might prevent the formation of large amounts of **15a**. Additionally, the TMS groups might act as mechanical obstacles for the translational mobility of **15a**, inhibiting the "flow" of ferrocene molecules from the crystal onto the surface. The assumptions that the $(CH_3)_3Si$ groups on the surface form an obstacle for the adsorbed molecules of **15a** and that surface silanol protons are advantageous for adsorption are also reflected in the comparatively large linewidth at the low surface coverage of 13 molecules on 100 nm^2 of surface area (Figure 4.29).

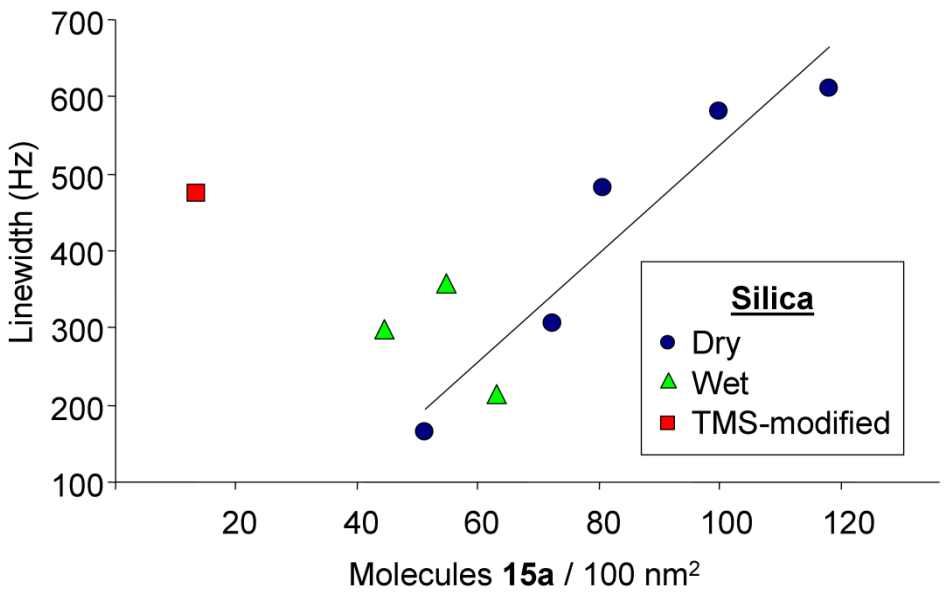

Figure 4.29 Residual linewidths of the ^{2}H MAS signal of **15a** at various surface loadings on dry, wet, and TMS-modified silica gel.

In contrast to the situation with wet silica, in the case of dry silica as the support a correlation between the linewidth and the surface coverage can be found, as indicated by the fitting line in the graph of Figure 4.29. The higher the surface coverages, the larger the residual linewidths of the ^{2}H MAS signals of **15a**. This again speaks for the assumption that less free space on the surface impedes the mobility of the molecules.

Broader lines should also be obtained by using silica gel with larger pores. To test this, a moderate surface loading of 46 molecules of **15** per 100 nm^{2} was applied to silica gel with an average pore diameter of 150 Å. This is less than 50% of the experimentally determined maximum possible loading on silica gel, and according to the data shown in Figure 4.29, a linewidth of 158 Hz is expected for **15a** under these

conditions. The resulting line, however, is more than 11 times broader (Figure 4.30) than would be expected using silica with an average pore diameter of 40 Å. This result corroborates the assumption that a larger average pore size should result in slower reorientation because the curvature of the surface has been reduced and **15a** must now travel further to achieve the one full circle for reorientation.

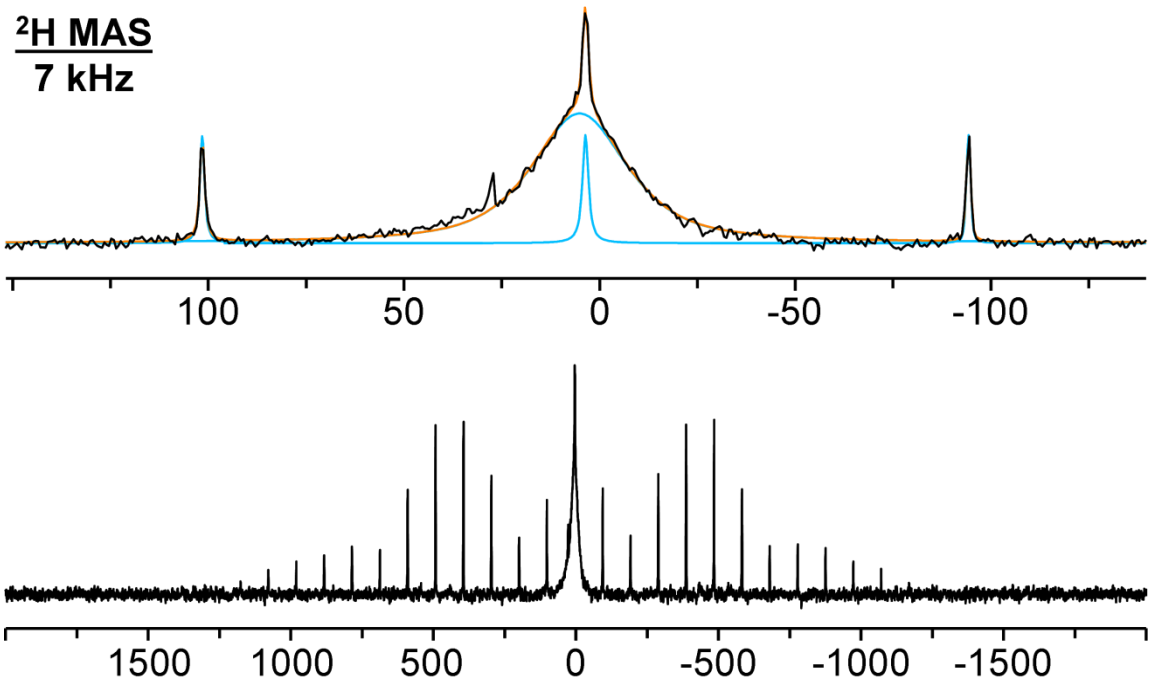

Figure 4.30 ^{2}H MAS NMR of **15a** on silica gel with an average pore diameter of 150 Å. The top trace shows deconvolution results in blue, with the sum of the calculated peaks in orange.

Based on the narrow solid-state NMR lines obtained for the adsorbed species **9a**−**15a**, it seems possible that the fast isotropic reorientation of the molecules would approach the mobility of the molecules in solution. Therefore, it was tested whether ^{1}H

and ^{13}C NMR signals would also be visible when filling a powder of silica with surface-adsorbed **10** into a conventional 5 mm glass NMR tube to a height of 3 cm each and measuring this sample on a liquids NMR instrument. For comparison, polycrystalline **10** has been ground finely and also filled into a 5 mm sample tube. Interestingly, both ^{1}H and ^{13}C NMR signals of adsorbed **10** emerge with high S/N ratios after only 32 and 128 scans, respectively. The ^{13}C NMR spectrum of adsorbed **10** is shown at the top of Figure 4.20.

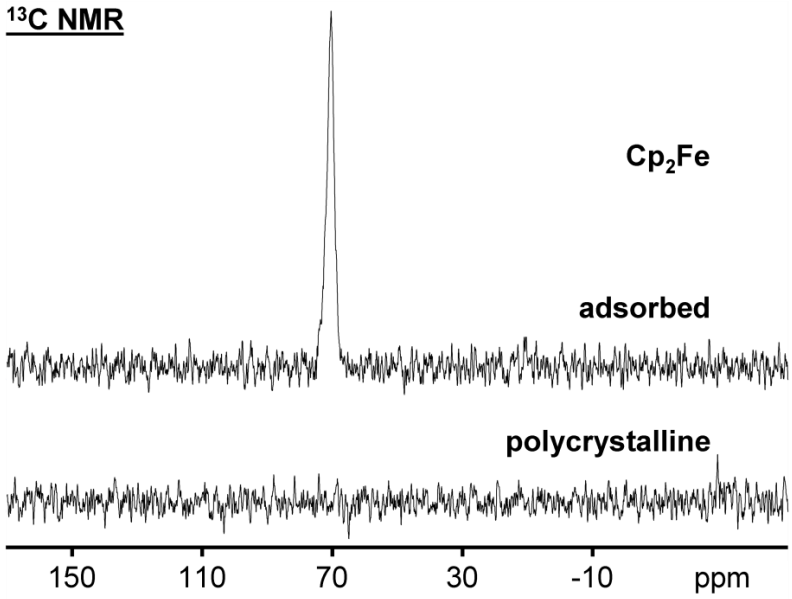

Figure 4.31 125.7 MHz $^{13}C\{^{1}H\}$ (bottom) NMR spectra of polycrystalline **10** (bottom) and silica-adsorbed **10a** (top) recorded on a standard liquids NMR spectrometer.

Being able to observe a narrow signal with a liquids NMR instrument without high-power capabilities means that the mobilities of the **10** molecules across the surface

are indeed fast and isotropic and that they come close to the mobilities of the molecules dissolved in liquids. The ^{1}H NMR signal of a sample of polycrystalline **10** (Appendix Figure C.20) has a linewidth of 23.6 kHz, and there is an obvious background signal of the glass of the sample tube and the probehead visible. The sample of adsorbed **10**, however, exhibits a narrow signal of only 1.1 kHz in the ^{1}H NMR spectrum, and the background signal is broad and of negligible intensity.

The difference between adsorbed and polycrystalline **10** is even more pronounced when comparing their ^{13}C NMR spectra (Figure 4.31). While the polycrystalline **10** gives, as expected, no signal due to the chemical shift anisotropy and large heteronuclear dipolar interactions, the adsorbed ferrocene results in a narrow signal with a halfwidth of only 251 Hz because all anisotropic interactions are diminished substantially by the mobility of the adsorbed species. Therefore, it is possible to record spectra of metallocenes adsorbed on silica surfaces even with conventional liquids NMR spectrometers due to the nearly isotropic fast motion of the adsorbed molecules across the surface as described for Figure 4.2. This fact greatly facilitated the variable temperature ^{13}C**{**^{1}H} NMR measurements of **10a** shown in Figure 4.8 which were recorded on a 500 MHz liquids NMR spectrometer.

In order to probe qualitatively the strength of adsorption and make the “melting” of the crystals onto the silica surface more plausible, the following experiment has been performed: polycrystalline **10** and **10** adsorbed on silica have been subjected to sublimation under the same vacuum. As expected, polycrystalline **10** sublimed already at 55 °C, growing into large crystals. In principle, the adsorbed **10a** could profit from the

advantage of being prearranged in a monolayer, allowing for a quick and simultaneous detachment of all molecules from the surface. However, no trace of sublimed ferrocene forms from the silica-adsorbed material, even after prolonged time to make up for any pore diffusion requirement. Only upon heating to about 73 °C does the adsorbed metallocene sublime. This result again confirms that the attraction of **10** to the surface is stronger than the forces keeping the single crystals packed. A more quantitative study is described in Chapter V.

Knowing that **10a** can be reconverted to **10** by the application of heat and vacuum, the question naturally arises as to whether there is an observable equilibrium between the adsorbed and polycrystalline phases. This was tested in a competition experiment by applying a very small surface loading of **15** (27% of a monolayer) to silica gel to give fully adsorbed **15a** with no residual polycrystalline **15** remaining. Even if the surface loading had been 1.6 times higher, there would have been no polycrystalline material observable in the spectrum (top trace Figure 4.25). A large excess of polycrystalline **10** was then added, and the mixture was allowed to equilibrate overnight.

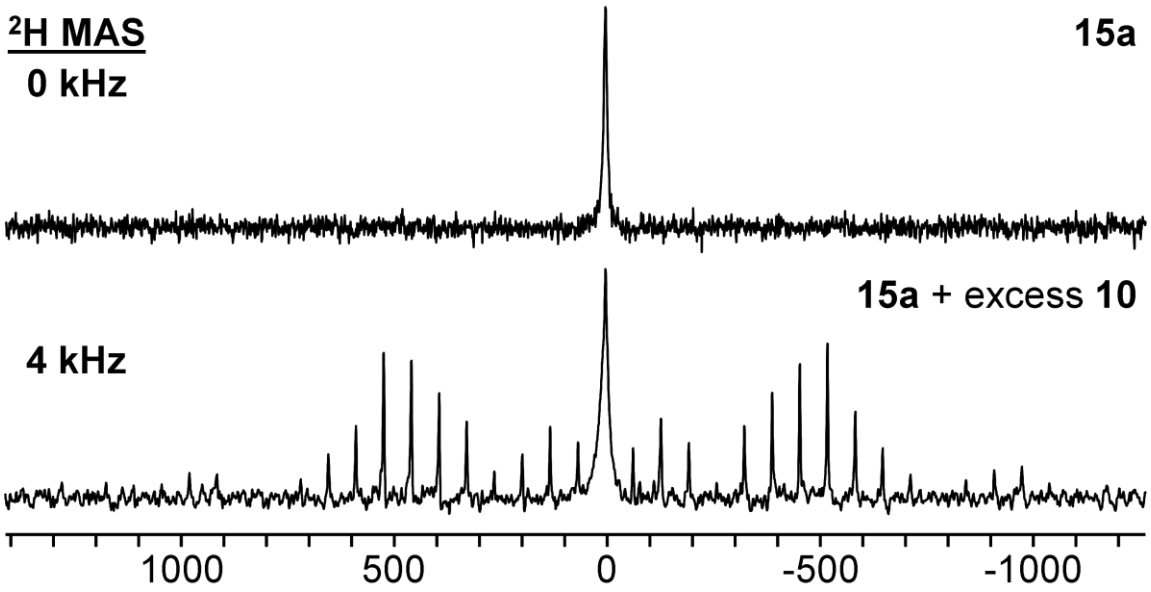

Figure 4.32 ^{2}H MAS spectrum of **15a** after addition of an excess of **10**. During equilibration **15a** has been replaced by **10a** and reverted back to polycrystalline **15**.

The ^{2}H MAS spectrum that was subsequently recorded (Figure 4.32) shows that **15** and **15a** are both now present in the material. Deconvolution and integration indicate that approximately 32% of the original **15a** has remained in the adsorbed state, and the remaining 68% has been displaced from the surface to form crystalline **15** again. The quadrupolar coupling constant of the polycrystalline material **15** was measured using peak-fitting software to be 95.2 kHz which matches well with previous values. The residual linewidth of the peak for residual **15** (89 Hz, measured as the average of the isotropic line and first 8 sidebands on each side) also matches very well with measurements of pure **15** which has a linewidth of 92 Hz. The ratio of **15a** to **15** (32 : 68) has nearly reached the value that would be expected statistically. Taking into account the amounts of **15** and **10** that were applied originally, it can be calculated that

24% of the **15a** should have remained adsorbed. This experiment shows that there is an equilibrium between the adsorbed and the polycrystalline species (Scheme 4.3), and that full equilibration probably requires at least 24 hours and probably several days.

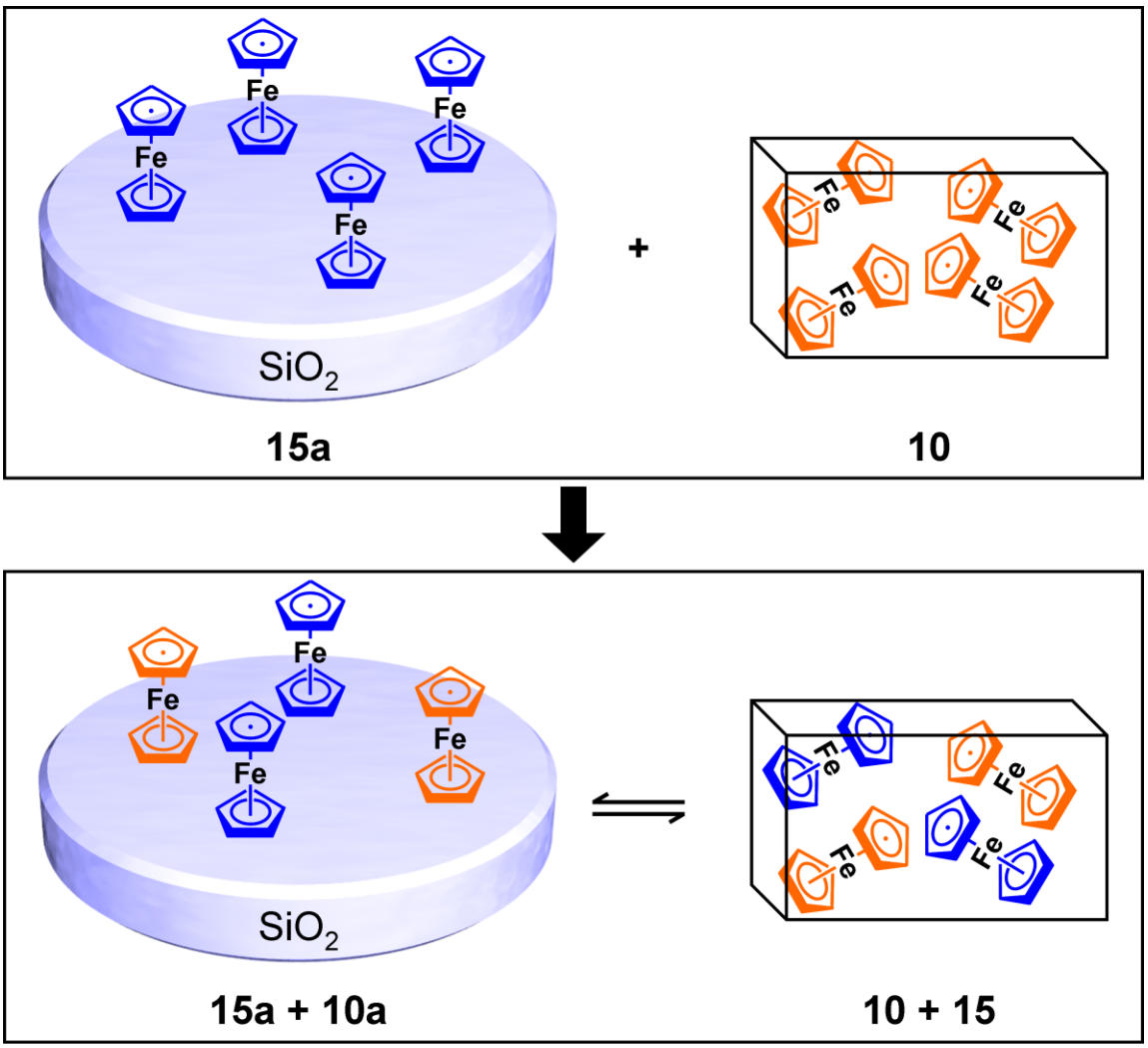

Scheme 4.3 Sketch of the competition experiment between **10** (orange, **10**) and **15** (blue, **15**).

The question then arises, where the polycrystalline material is located. Since the pores are rather large compared to a single ferrocene molecule, it is likely that small clumps of polycrystalline material are formed within the pores. This would agree with Günther's conclusion, based on BET analysis,[56b] that phenanthrene adsorption is hindered by polycrystalline blockages in the pores. However, in the case of ferrocene it seems that the equilibrium is fast enough (Figure 4.32) that the polycrystalline material does not substantially hinder adsorption.

CONCLUSION

It has been demonstrated unequivocally by ^{1}H and ^{13}C solid-state NMR techniques that polycrystalline metallocenes **9**−**13** and **15** are readily adsorbed on silica surfaces even in the absence of a solvent after dry grinding at ambient temperature and that they undergo translational mobility. The forces that drive the surface adsorption are strong enough to break down the crystal lattices of the metallocenes. The scenario can be described as sort of a melting process although the melting points of all solids are higher than room temperature. The fact that the crystalline material "melts" onto the surface and the molecules spread out to produce a sub-monolayer corroborates the findings by solid-state NMR that the molecules must be translationally mobile. The influence of an extended π system, as in **12**, on the adsorption, as well as the impact of hydrophobic substituents with large steric demand, as realized in **13**, have been probed. Additionally, it has been demonstrated that an alkane with a high melting point (**14**) can be adsorbed on a silica surface. Different modes of mobility are discussed, and a timeline for

isotropic reorientation has been established by ^{2}H MAS NMR of adsorbed **15a**. No indication for stacking of the metallocene molecules on the surface has been found, as the transition from the polycrystalline state to an adsorbed monolayer is abrupt. A correlation between the surface coverage and the mobility of the adsorbed molecules has been described. Wet and TMS-endcapped silica as supports lead to smaller amounts of adsorbed material and, in the latter case, lower surface coverages and broader lines. Finally, it has been demonstrated that in the case of **10** the surface-adsorbed species can be measured using a conventional liquids NMR spectrometer because of the short reorientation time that diminishes anisotropic interactions substantially.

EXPERIMENTAL

The solid-state NMR spectra of **9** and **9a** have been previously recorded by Michael Schnellbach on a Bruker MSL 300 instrument.[68] For **10-15** The ^{1}H, ^{13}C, and HSQC measurements of liquids and of silica-adsorbed and polycrystalline ferrocene (Figure 4.31) were performed on a Varian 500 MHz liquids NMR spectrometer. The ^{1}H, ^{2}H, and ^{13}C solid-state NMR spectra were recorded with a Bruker Avance 400 wide bore spectrometer using a 4 mm MAS probehead. Cross polarization was only applied in the case of polycrystalline metallocenes. All samples were measured by packing the whole rotors with finely ground polycrystalline material or filling the silica in loosely. Compressed air was used as both the bearing and drive gas for the MAS measurements. The recycle delays were 3 s for the ^{13}C CP/MAS and 10 s for the single pulse NMR measurements, and 3 s for recording the ^{1}H and ^{2}H NMR spectra. For the ^{13}C MAS

measurements the ^{1}H high-power decoupling was turned off or applied as detailed in the text. Typically 64 transients were accumulated for ^{1}H and 2400 for ^{13}C solid-state NMR measurements, with the exception of **12a** and **13a**, which needed ca. 26,000 scans. The spectra of polycrystalline and adsorbed **10** were obtained on a Varian 500 liquids NMR instrument with Waltz decoupling and a pulse delay of 2 s, and 16 and 128 transients were collected for the ^{1}H and ^{13}C measurements. The ^{13}C NMR signal was referenced relative to benzene in a capillary (128.00 ppm) to give a chemical shift of 70.38 ppm for the resonance of the adsorbed **10**.

The footprint of ferrocene, standing upright on the surface, was calculated based on the distance between the center of the Cp ring and an H atom (2.3 Å) and taking the Van der Waals radius of H into account to give an overall radius of 3.5 Å. Assuming hexagonal packing of these circles on the surface, about 201 ferrocene molecules can maximally occupy 100 nm^2 of surface area in a monolayer, corresponding to 2.50 mmol of ferrocene per g of silica. Accordingly, in order to achieve about 85% of the theoretically possible maximum surface coverage (2.125 mmol ferrocene per g of silica), 139.8 mg of ferrocene (0.7515 mmol) was ground for about 1 min with silica (300.6 mg). The mixture was transferred to a vial and sealed. Then the mixture was allowed to sit undisturbed for two days before the measurements were started. In the course of the two days the color changed from orange to yellow. Alternatively, the corresponding amount of ferrocene was dissolved in pentane and added to a slurry of silica in pentane. Then the solvent was removed in vacuo. Both methods of preparation, dry grinding and impregnation, led to the same material with surface-adsorbed ferrocene.

For obtaining the adsorbed species **11a**−**15a** and adsorbed **10**, the polycrystalline materials have been ground together with the corresponding type and amount of silica by hand for 1.5 min using a mortar and pestle. For **11** and **12** this process was carried out in the glovebox, in all other cases the grinding step was performed on the benchtop. The following values give the amounts with respect to 1 g of support: **11** (268.8 mg, 1.162 mmol), **12** (243.0 mg, 0.733 mmol), **13** (244.1 mg, 0.719 mmol), and **14** (178.7 mg, 1.062 mmol). For **15**, the different amounts are given in Figure 4.25. For this measurement series of **15a** the dry mixtures were allowed to stand for at least 2 h prior to the measurements. For recording the ^{1}H and ^{13}C NMR spectra on the liquids NMR spectrometer (Figure 4.31) an amount corresponding to 488.7 mg (2.627 mmol) per g of silica has been applied. Deconvolution and processing of the spectra was accomplished using ACD/NMR Processor Academic Edition.[84] The quadrupolar coupling constants were derived from the ^{2}H MAS NMR spectra using the NMR simulation program Dmfit.[17] The best fit line in Figure 4.29 was obtained using only the data derived from the dry SiO_2, and the R^2 value was 0.905, which indicates a strong correlation. Conventional silica gel, as used, for example, for column chromatography has been purchased from Merck. Its average pore diameter is 40 Å, the average particle size is 0.063−0.2 mm, and the specific surface area 750 m^2/g. The silica gel was either dried in vacuo at 300 °C for 40 h (referred to as dry SiO_2) or used as received (wet SiO_2). The Me_3Si-modified silica was prepared as described previously.[60] Compounds **11** and **14** were purchased from Strem Chemicals and TCI America, respectively. The crystalline complexes **12** and **13** were used as received from Dr. K. Öfele, TU Munich. While the

^{13}C NMR signal assignments are known for **12**,[75] the NMR signal assignments for **13** have been determined using a 2D HSQC NMR spectrum and the ^{1}H signal assignments given in the literature.[64] δ(^{13}C) (125.66 MHz, C_6D_6 [ppm]): 88.52 (C_q), 70.34 (CHC_q), 69.19 ($CHCHC_q$), 24.33 ($C_qCH_2CH_2$), 24.16 (C_qCH_2). Compound **15** was obtained by preparing 1,1′-dilithioferrocene according to a literature method[81] and subsequent quenching with D_2O. **15** was purified by sublimation followed by washing through a short silica column with hexanes.

Monolithiated ferrocene was prepared according to literature procedures[85] via deprotonation with ^{t}BuLi. The mixture of predominantly monolithiated ferrocene was subsequently quenched with chlorotrimethylsilane and the resulting products were purified by column chromatography.

Since TMS-ferrocene is a liquid at room temperature, the adsorption on silica (25.8 mg, 0.100 mmol on 302.8 mg of silica gel) was accomplished using the solvent impregnation method (hexanes) to give a surface coverage of 26.5 molecules per 100 nm^2.

CHAPTER V

ADSORPTION OF METALLOCENES IN LARGE SILICA GEL PIECES

INTRODUCTION

It has been shown in the preceding chapter that various metallocenes can be adsorbed on high surface area silica gel, and that solid-state NMR measurements prove substantial mobility on the surface. The experiments and results described in this chapter will further support the conclusions drawn heretofore by visualizing the solvent-free adsorption process by using monolithic large pieces of silica gel in combination with metallocenes as powders or single crystals. Besides ferrocene, a half sandwich manganese complex, cymantrene, and an additional metallocene, nickelocene, have been adsorbed. It will also be shown that catalytically active materials, most probably of the single atom catalyst category, can be generated from monolayers of nickelocene by reduction with hydrogen under mild conditions.

RESULTS AND DISCUSSION

Visual Confirmation of Mobility

One of the common questions about the solvent-free adsorption described in the previous chapter is whether the pressure and elevated temperature generated by grinding the ferrocene with the silica gel did contribute to the adsorption and mobility by first melting the metallocene. Then the liquid metallocene would be soaked into the pores of

the support material by capillary forces. To answer this question, as well as to visualize the translational mobility, a new experiment was carried out using large pieces of silica gel with pore diameters of ca. 20 Å and particle diameters around 1 cm, instead of the usual silica powder with particle sizes of only up to 0.2 mm employed for all previous experiments. A large piece of silica gel was brought into contact with a single crystal of ferrocene under an N_2 atmosphere in a Schlenk tube. This tube was then left undisturbed and photographed as the adsorption progressed (Figure 5.1).

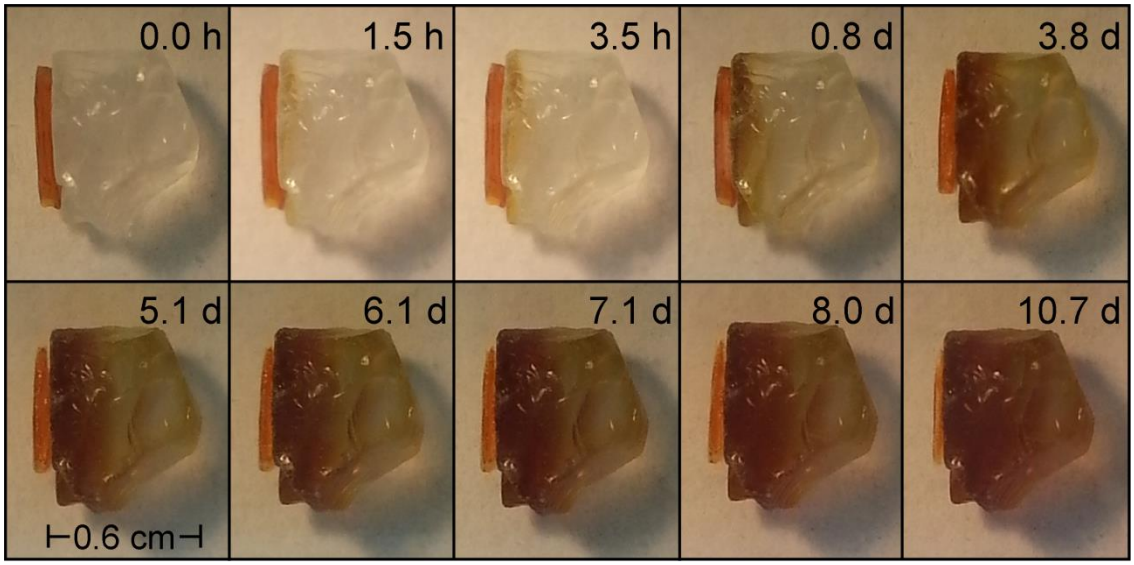

Figure 5.1 A large single crystal of ferrocene adsorbs into a large silica gel piece over time in the absence of a solvent. This experiment was carried out in inert atmosphere.

The results show that even without grinding or heating, and in the absence of any solvent, the adsorption progresses until the silica gel specimen is completely saturated with ferrocene. It is interesting to observe that the "frontier" of ferrocene originates at

the point of contact with the single crystal as it progresses through the silica gel. This visual proof confirms the presence of translational mobility of adsorbed metallocenes.

Figure 5.2 Large silica gel pieces. From left to right: virgin silica gel pieces, with adsorbed ferrocene (**10a**), prepared and stored under N_2, **10a** after partial oxidation in air, and fully oxidized **10a** (ferrocenium salt).

When this experiment is carried out in the presence of oxygen in the open air, the same results with respect to the ferrocene adsorption are observed, except that additional colors (Figure 5.2) are visible. The reason is that the ferrocene is partially oxidized to ferrocenium ions and the combination of blue ferrocenium salt and orange ferrocene in various ratios creates a range of colors (Figure 5.3). In the presence of oxygen ferrocene is oxidized at the sites of acidic surface silanol groups. Once the silanol groups are spent and blocked by the immobile ferrocenium salts, the ferrocene fills the gaps on the surface and is no longer vulnerable to oxidation. The fact that ferrocenium salts do not adsorb into the silica pores, and that they are not mobile on silica surfaces after being deposited from a solution, has been established in a parallel project in the group, and by the following series of experiments.

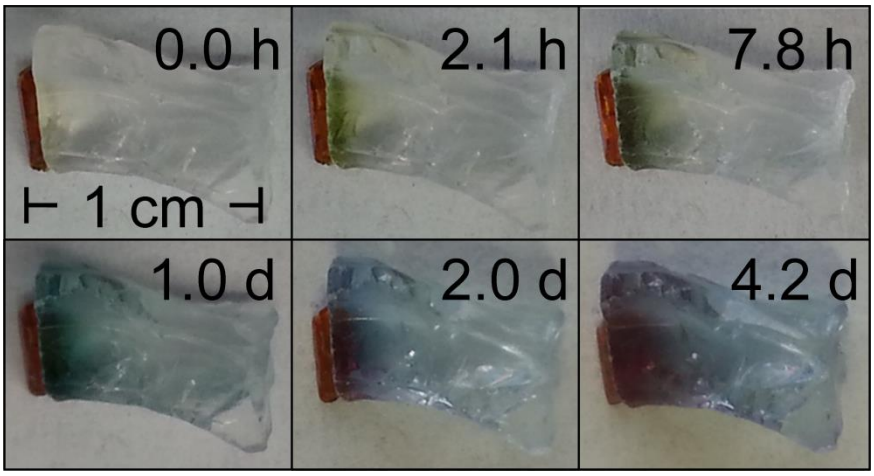

Figure 5.3 A large single crystal of ferrocene adsorbs into large silica gel pieces over time in air, producing a range of colors due to the presence of both ferrocene and ferrocenium ions.

First, a specimen of silica gel was brought in contact with ferrocene for several hours, until a small amount of ferrocene had adsorbed on one end of the specimen. The silica piece was then removed before it could become saturated with ferrocene, and exposed to the air. The small amount of **10**a was quickly oxidized in air to produce a silica piece which had a distinctly blue region, and a pristine colorless section (Figure 5.4) This specimen was observed over time as it remained exposed to the atmosphere on the benchtop. While there may have been a very minor degree of diffusion, possibly attributable to residual ferrocene, even over two months the colorful ferrocenium salt is not evenly distributed over the silica piece, but mainly stays in place. Therefore, it can be concluded that there is very little, if any mobility of ferrocenium salts on silica gel surfaces.

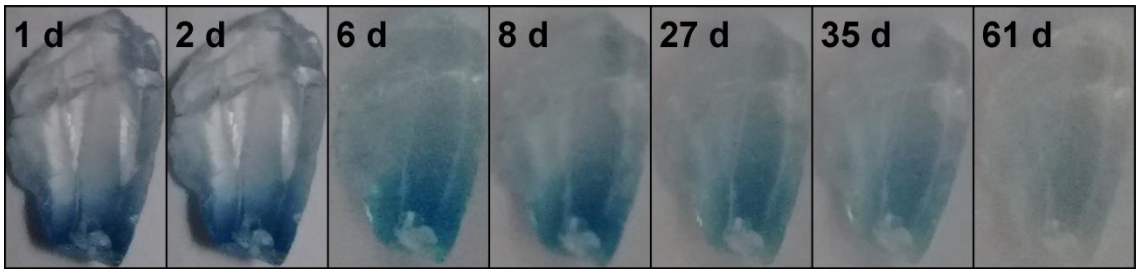

Figure 5.4 Ferrocenium salt generated in the bottom area of a large silica piece does not diffuse throughout the specimen over time, but the color fades.

Another interesting result from this experiment is that the blue color seems to fade over time (Figure 5.4). This could be due to decomposition of the ferrocenium salt to give a colorless, or lightly colored iron salt under release of cyclopentadiene. Unfortunately, treatment of the colorless sample (Figure 5.4) with sodium cyanide, in an effort to create a strongly colored iron complex, did not succeed. Further experiments, for example, ICP-MS, are needed to prove the presence of Fe, in case it "escaped" as ferrocene, which is, however, unlikely due to the fact that ferrocene is readily adsorbed and retained by the silica specimens. The assumption that the iron is lost by sublimation of ferrocene, being generated from ferrocenium in an equilibrium process, can also be discarded, since it would lead to diffusion of the ferrocene throughout the entire volume and subsequent ferrocenium formation, which is not observed. In any case, XPS could be used to determine the oxidation state of the remaining Fe species.

During the course of the above experiments (Figures 5.1 and 5.3), the single crystal of ferrocene visibly shrinks as it is adsorbed into the silica piece. Therefore, the direct contact between the ferrocene and silica gel is maximal at the beginning of the

experiment, and then the contact area shrinks. The question arises whether the ferrocene molecules can be adsorbed from the gas phase. Since ferrocene is known to have a substantial vapor pressure, this is not impossible and the adsorption could proceed even without direct contact. The following experiments clarify this point.

When ferrocene powder is separated from the silica gel by a distance of 1 cm, in a closed vessel the adsorption still occurs, although at a much slower pace. Also, in this case the "frontier" is not as clearly visible, with the coloring proceeding equally from all sides of the silica specimen. It is probable that ferrocene can adsorb from the vapor phase in addition to direct contact.

To further clarify this point, a single crystal of ferrocene (diameter ca. 0.2 cm) was exposed to the laboratory atmosphere and its size was monitored (Figure 5.5). The loss of substance due to sublimation does not become obvious before one month has elapsed. The time scale for this sublimation is much slower than that for the adsorption through the crystal/silica interface for ferrocene. Therefore, it can be concluded that the migration of the ferrocene molecules from the crystal lattice onto the surface of the silica pores occurs predominantly by direct contact and that deposition from the gas phase plays a minor roll. This conclusion is also corroborated by the NMR results described in the previous chapter which confirm that ferrocene stays mobile on the surfaces in the pores although the vapor pressure of adsorbed ferrocene is much lower than that of crystalline ferrocene.

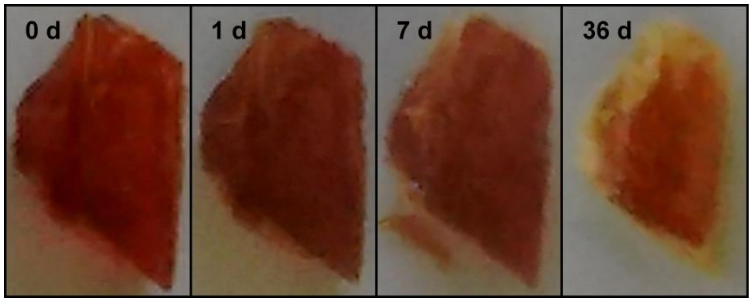

Figure 5.5 A large single crystal of ferrocene (**10**) left open to air for 36 days. Some loss of substance by sublimation is apparent, but only after a significant amount of time has lapsed.

Solid-State NMR of 10a in Large Silica Pieces

It can be readily proven with NMR measurements that even after saturation of the silica gel, adsorbed ferrocene (**10a**) continues to be highly mobile on the surface. This is accomplished by filling large pieces of silica gel into a regular 5 mm glass NMR tube and recording the ^{13}C NMR spectrum (Figure 5.6) with a standard liquids NMR instrument as described in the preceding chapter. The resulting signal, with a linewidth of merely 440 Hz, is recorded with excellent S/N after only 256 scans. The increase in linewidth from 251 Hz, observed for **10a** on powdered silica, to 440 Hz (Figure 4.30) is attributed to a more dense surface loading of ferrocene on the surface which hinders mobility.[86] However, it is noteworthy that no high-power proton decoupling or MAS were needed to obtain a liquid-type spectrum from the solid material.

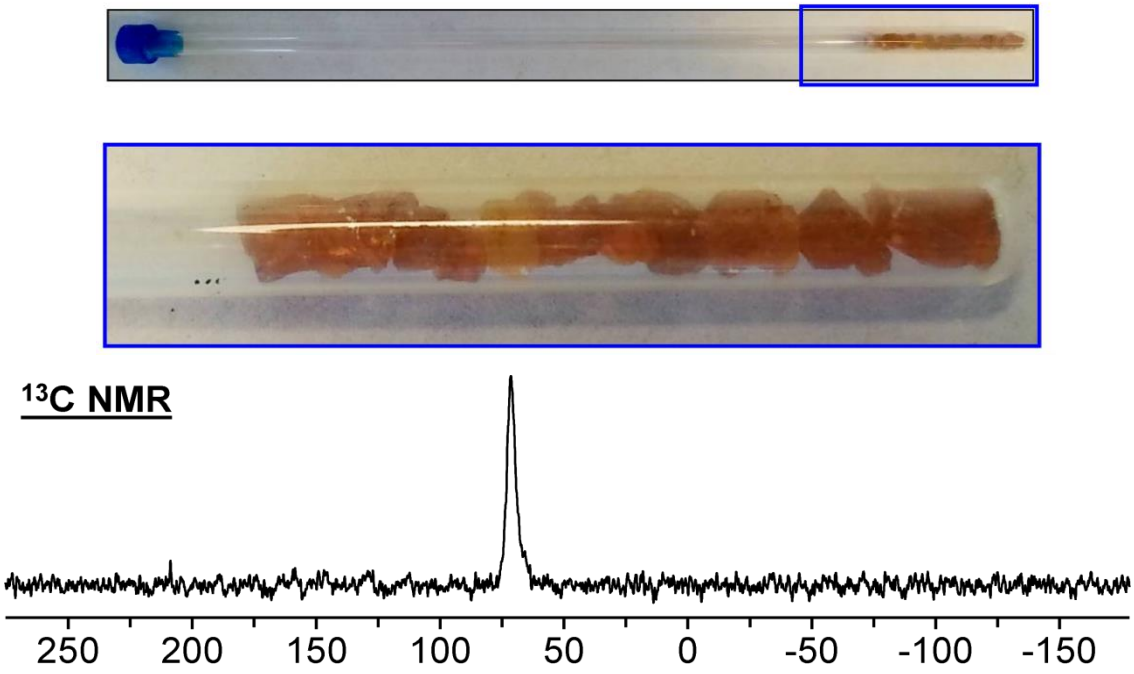

Figure 5.6 ^{13}C NMR spectrum (bottom) of large silica gel pieces filled into a standard 5 mm glass NMR tube (top). This spectrum was recorded on a standard liquids instrument without ^{1}H decoupling or sample rotation.

Comparison to Powdered Silica Gel

It is instructive to compare the results described thus far, using the large silica pieces, with the result that was obtained in a similar experiment using a column of powdered silica gel (Figure 5.7). For this test, a glass Pasteur pipette was packed with silica gel (Merck 60 Å) and a small amount of ferrocene powder was added on top of the silica. Considering that finely powdered **10** releases more ferrocene vapor than a single crystal of **10**, it seems surprising that even after 7 weeks, there is still only minimal adsorption of ferrocene in the lower portion of the column. However, considering that although **10** has a significant vapor pressure and can diffuse from the ferrocene crystals

into the silica gel pores, **10a** does not sublime easily (see desorption experiments below) and so it does not readily bridge the space gap from one particle of silica gel to another by diffusion through air. Additionally, the surface within each silica particle will be partially blocked by ferrocenium salts generated at surface silanol sites, as the green coloring of the material implies (Figure 5.7).

Figure 5.7 Slow migration of ferrocene through a pipette packed with silica gel for 7 weeks. The pipette was oriented vertically during the experiment, but the picture is turned sideways due to space reasons.

Determination of Desorption Temperature

Previous measurements, described in Chapter IV, show that elevated temperatures are necessary to desorb **10a** from silica to give polycrystalline **10**. A more accurate determination was desired, as well as a comparison to the desorption temperature from various other surfaces besides silica.

The first method which was attempted was to use a melting point apparatus and note the temperature at which ferrocene crystals started to appear on the upper part of the sample tube. Special sample tubes were made which allowed the samples to be put under vacuum during the measurement. Although this method worked in principle, it proved

practically impossible to note the exact temperature, and reproducible results were not obtained.

More successful measurements were carried out as follows: First, sample tubes were prepared by sealing off the end of Pasteur pipettes, and correction fluid was then applied to the back half of each tube to provide good contrast (Figure 5.8 left). A small sample of ferrocene adsorbed on silica gel was then added to the sample tube. A vacuum hose was fitted over the top of the tube, and vacuum was applied. The bottom centimeter of the tube was immersed in an oil bath as shown in Figure 5.8. A thermometer and a thermocouple were also inserted into the oil bath to enable convenient and accurate measurement and regulation of the temperature (Figure 5.8, middle). A cell phone was placed in a clamp and used to take pictures of the sample tube as the temperature of the oil bath was slowly increased. These images were then analyzed with the help of computer software (ImageJ) to accurately pinpoint the temperature at which ferrocene crystals began to form on the wall of the sample tube (Figure 5.8, right).

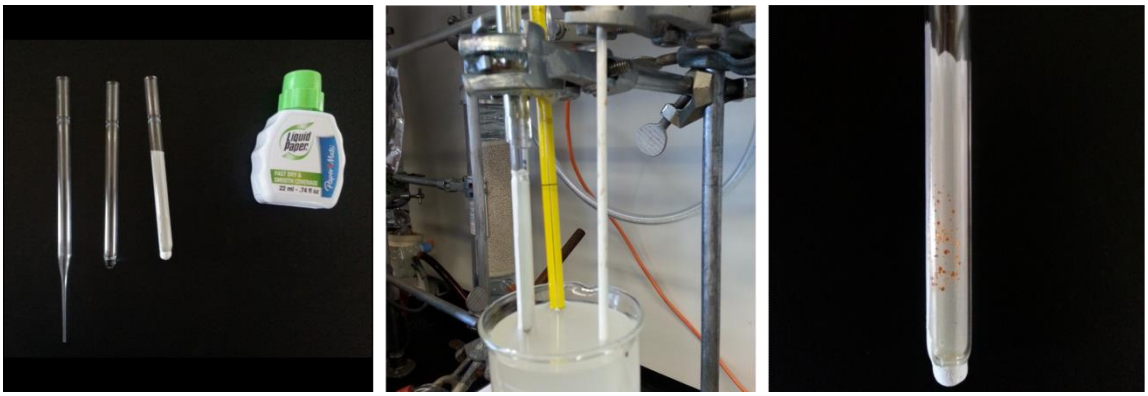

Figure 5.8 Equipment used to measure the desorption temperature of ferrocene on several different surfaces.

This process was repeated with ferrocene adsorbed on several other surfaces as well, which will be described in detail in the next chapter. The results (Figure 5.9) show that ferrocene begins to desorb from silica at 52 °C. For comparison, very finely powdered ferrocene was placed in a sample tube as described above. It was found that the first crystals began to form at 37 °C, or 15 °C lower than **10a**.

The benefit of this method is that it gives very reproducible results, for example three different samples of **10a** on dry silica were measured and they gave very similar results (Figure 5.9). The weakness of this method is that it is only sensitive to the most weakly adsorbed species on the surface, so if there are, for example, multiple modes of adsorption, or different environments on the surface, only the first to desorb will register using this method.

This may be why ferrocene desorbs from both “wet” (as received) silica and “dry” (dried under vacuum at 300 °C for 3 days) silica surfaces at the same temperature (Figure 5.9).

Carbon nanotubes adsorb ferrocene more strongly than silica gel, but this is not surprising since nanotubes are well known to be highly polarizable, and thus to have especially strong Van der Waals interactions. The even stronger adsorption by activated carbon is likely a result of the presence of smaller pores where ferrocene can become trapped. In fact, when predominantly microporous activated carbon is used for the adsorption, broad lines result in ^{13}C NMR, most likely because the adsorbates are getting "stuck" in the micropores.

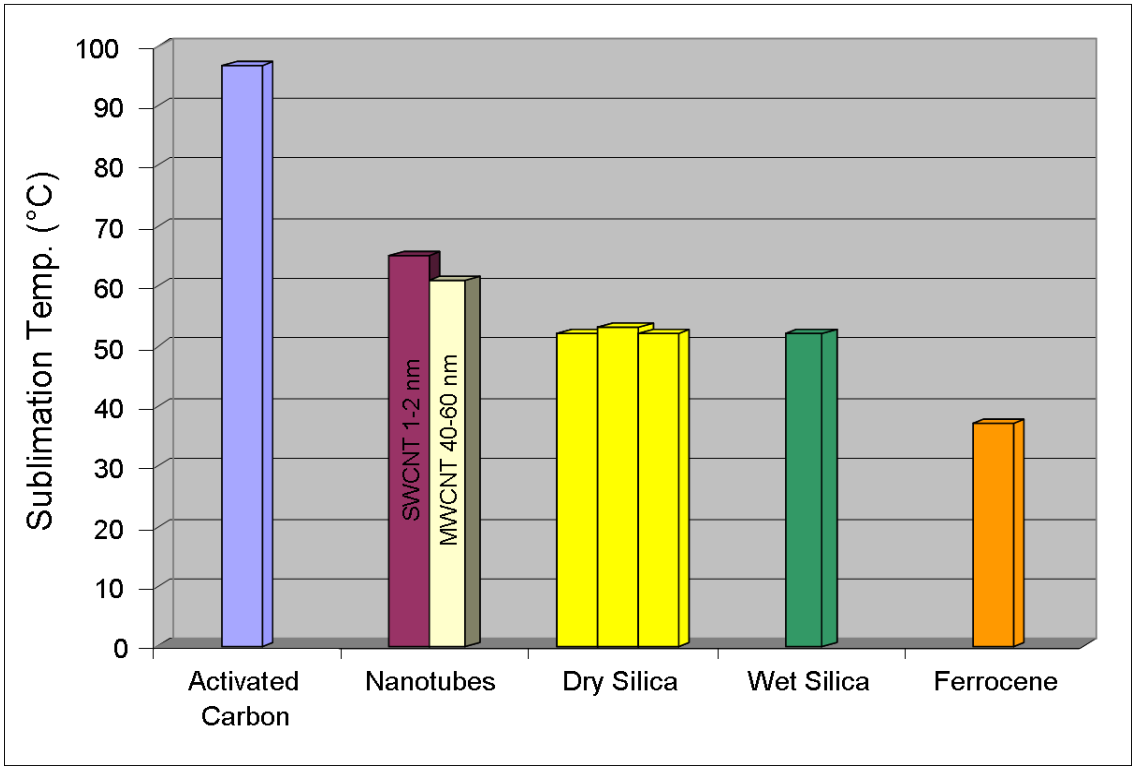

Figure 5.9 Temperatures at which **10a** desorbs as **10** from various surfaces under a vacuum of 0.035 mmHg.

Adsorption of Cymantrene

The half sandwich or piano-stool type complex $CpMn(CO)_3$, cymantrene, has also been adsorbed onto silica gel. This experiment was carried out according to the procedure described above for the adsorption of ferrocene into large silica pieces (Figure 5.1) except that instead of a large single crystal of cymantrene a small pile of polycrystalline material was used (Figure 5.10).

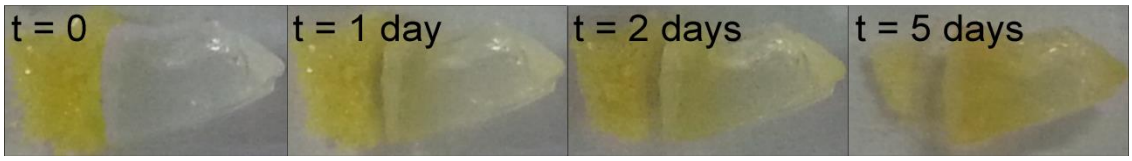

Figure 5.10 Adsorption of cymantrene into a large piece of silica gel.

Adsorption of cymantrene has also been performed using powdered silica samples for NMR measurements. Because of the large CSA of the carbonyl signal, the ^{13}C MAS of polycrystalline cymantrene (Figure 5.11, bottom) has rather low S/N for the carbonyl resonance, which makes it difficult to reliably measure the CSA with the peak-fitting software. Nevertheless, The CSA of metal carbonyl complexes is usually very large, for example, it exceeds 400 ppm in the case of $Mo(CO)_6$ (*vide infra*).

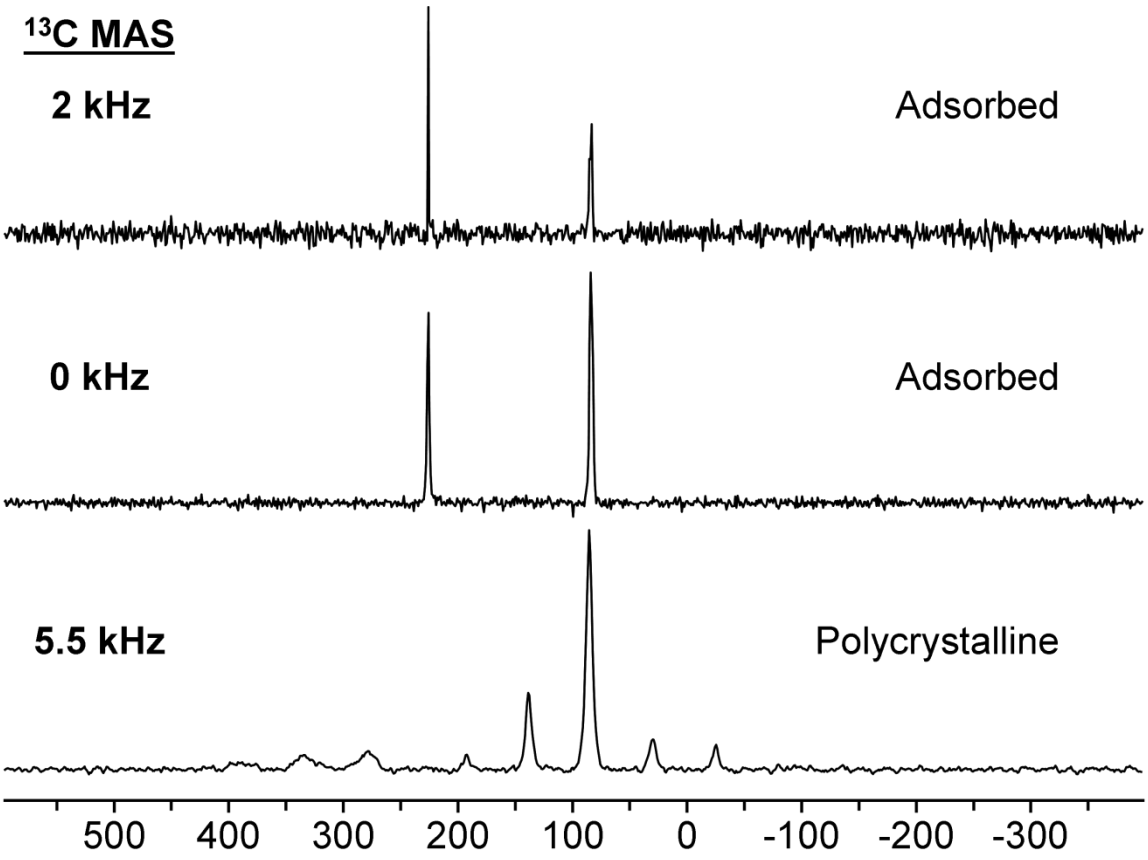

Figure 5.11 Solid-state NMR spectra of polycrystalline cymantrene (bottom), and cymantrene adsorbed on silica gel (Merck, 40 Å pore size, 0.2 mm particle size) at the given rotational frequencies (middle and top).

Even without sample spinning, the adsorbed cymantrene gives two very narrow peaks at 225.73 and 83.76 ppm with linewidths of 225 and 346 Hz, respectively (Figure 5.11, middle). With sample rotation of 2 kHz (Figure 5.11, top) the linewidths are reduced further to 98 and 255 Hz.

An unexpected feature was observed in the ^{13}C NMR spectrum of adsorbed cymantrene in the case of low surface coverage, which provides the highest mobility and narrowest lines. Under these conditions, and when the acquisition time is increased from

0.01 to 0.1 seconds to provide a sufficient number of data points to reliably define the peaks, two signals are observed for the Cp resonance (Figure 5.12). The peaks appear at 84.87 and 83.08 ppm and have linewidths of 39 and 47 Hz, respectively. The intensities of the two peaks are very similar with a ratio of about 1:0.9.

These signals probably correspond to different orientations of cymantrene on the surface. One peak may arise from cymantrene standing on the surface with the Cp ring down, and the other could be assigned to cymantrene with the CO groups pointing towards the surface. Since $Mo(CO)_6$ adsorbs readily on silica and is mobile on the surface (see below), it is plausible that the CO groups of cymantrene can interact with the surface. This assumption is far from certain, and alternative explanations for the presence of two Cp signals for adsorbed cymantrene include different adsorption sites on the silica surface, for example, silanol or siloxane groups. This explanation is tempting, but the ratio of the two peaks, although it varies a little, does not readily correlate with the dryness of the silica and therewith the number of surface silanol groups versus siloxane groups. Another alternative is that multiple layers are generated. The single crystal X-ray structure with the packing of two cymantrene molecules in close proximity would speak for this situation.[87] However, this is a less likely scenario, since the amount of material that adsorbs never exceeds the amount expected for a monolayer, even under conditions of high surface loading. In addition, the ratio of the two peaks is independent of the surface coverage with cymantrene.

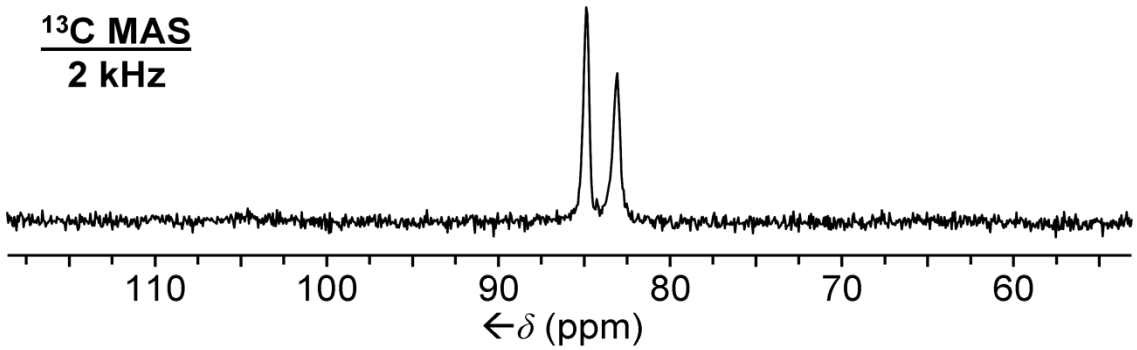

Figure 5.12 ^{13}C MAS spectrum of cymantrene adsorbed on silica with low surface coverage.

In order to elucidate the reason for the presence of two signals (Figure 5.12) and probe the adsorption strength, a competition experiment was performed. Silica was first treated with cymantrene in a fourfold excess to ensure complete saturation of the surface, and left overnight to adsorb completely. Then deuterated ferrocene was applied with an amount corresponding to 38% of that required for a monolayer. The resulting material was analyzed via ^{2}H NMR (Figure 5.13) to reveal a single narrow peak at 4.36 ppm with a linewidth of 717 Hz. This linewidth matches perfectly the expected value for ferrocene adsorbed on silica with maximum surface loading (Figure 5.13). Interestingly, there are no rotational sidebands left in the ^{2}H NMR spectrum which indicates that all of **15** applied to the sample was adsorbed to form **15a**. This contrasts with the example in the previous chapter where **10** and **15** compete for the silica surface and a statistical mixture is formed (Figure 4.31). In this case, it appears that **15** outcompetes the cymantrene and pushes it off of the surface entirely without much resistance.

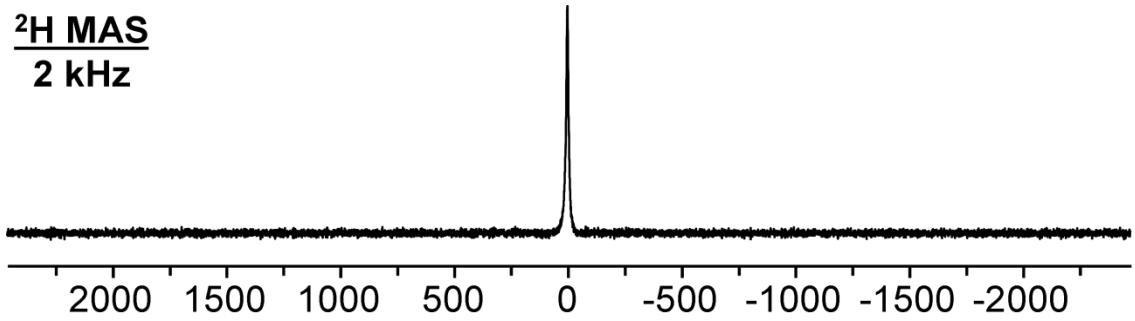

Figure 5.13 ^{2}H Solid-state NMR spectrum recorded after the ferrocene/cymantrene competition experiment.

This unexpected result prompted an additional experiment with the large silica pieces. The silica specimen was first saturated with cymantrene, and then placed next to a single crystal of **10** (Figure 5.14). The most obvious change was that the ferrocene crystal became covered with a yellow powder that looks like cymantrene. It can also be seen, by looking very closely at the silica piece, that very small feathery crystallites of yellow cymantrene have grown on the outer surface of the silica gel specimen. This result agrees with the ^{2}H NMR experiment which indicates that ferrocene adsorbs preferentially, displacing cymantrene easily. At the same time, it should be noted that even after 14 days the ferrocene crystal remained about the same size, which means that only very little has adsorbed. Compared to the results in Figure 5.1 and it is obvious that cymantrene, although it can be displaced by ferrocene, at least slows down the adsorption of ferrocene.

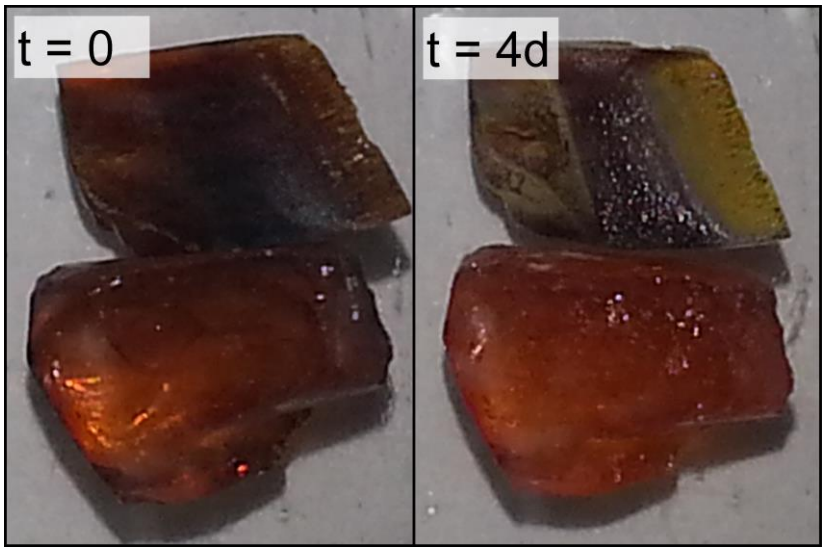

Figure 5.14: Adsorption of ferrocene from a single crystal (top) into silica gel pre-saturated with cymantrene (bottom).

Adsorption of ferrocene into the pores of macroscopic silica gel pieces also facilitated the determination of maximum surface loadings. This experiment consists of weighing several silica specimens, and then adding them to a vial of the adsorbate. The specimens were weighed periodically until the mass no longer increased. The maximum amount of substance adsorbed per g of silica can then be calculated. The results for several compounds are shown in Figure 5.15, the complete data are listed in the Experimental Section.

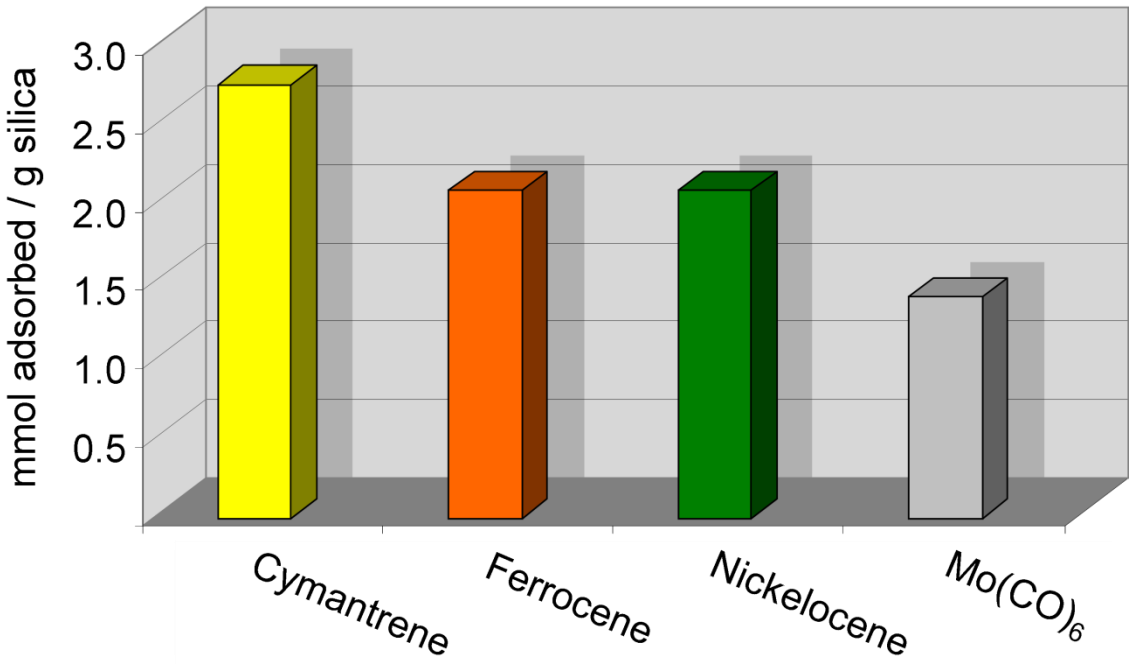

Figure 5.15 Maximum loading of several adsorbents in large silica gel specimens.

It is significant that ferrocene and nickelocene both have the same maximum coverage on silica. This agrees with the expectation since they have virtually identical "footprints" on the surface. Cymantrene, on the other hand, appears to be able to pack a little more tightly onto the surface. Whether this is because of the geometry of the carbonyl "legs" of the piano stool, or whether it is due to a difference in kinetic size, or a difference in the interaction with the surface is not known yet. The difference is not double the loading, however, so one cannot suppose that a double layer forms based on this result. As discussed in Chapter IV, the static footprint of a metallocene molecule would theoretically allow a surface density nearly twice the experimentally determined maximum loading.

$Mo(CO)_6$, which has been shown in the literature to adsorb and be mobile on the surface of alumina,[74,88] was also adsorbed on large silica pieces as well as onto powdered silica samples according to the standard procedure. A lower surface coverage was found for $Mo(CO)_6$ than for the other compounds. This difference can be accounted for by considering that the 2-dimensional footprint of $Mo(CO)_6$ is a circle with a radius of 4.709 Å while it is only 3.502 Å for ferrocene. The larger radius results in a theoretical footprint that is 1.8 times as big, and this matches reasonably well with the 1.5 times higher molar surface coverage for ferrocene.

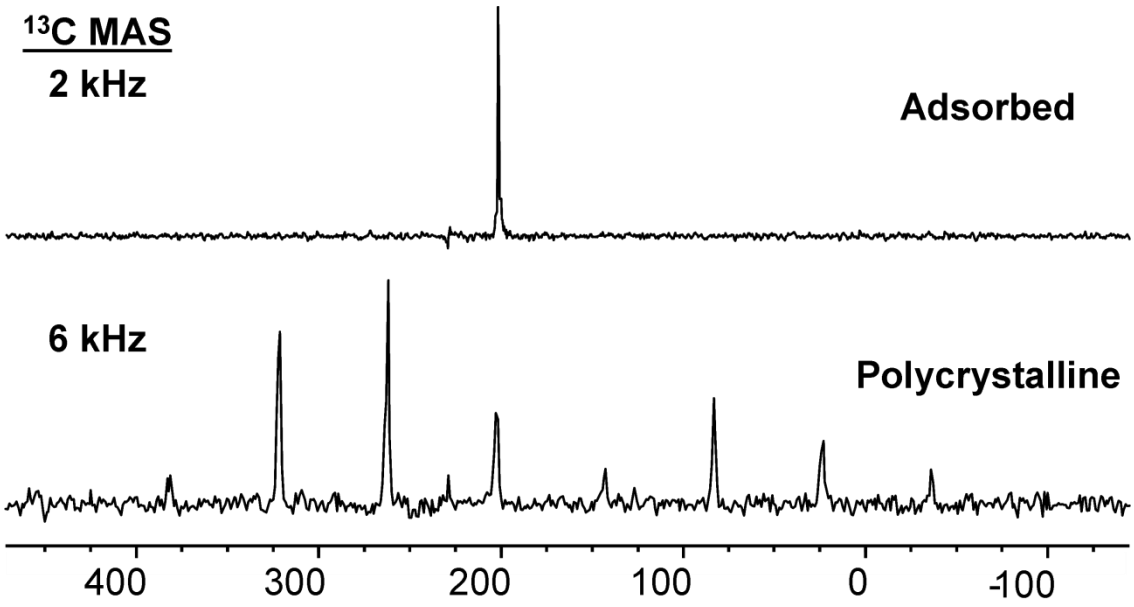

Figure 5.16 ^{13}C MAS spectra of polycrystalline $Mo(CO)_6$ (bottom) and $Mo(CO)_6$ adsorbed on silica gel powder (top).

The mobility of $Mo(CO)_6$ on silica gel was investigated to probe the possibility of cymantrene adsorbing with the CO groups pointing towards the surface. The polycrystalline hexacarbonyl complex gives a characteristically large CSA pattern (Figure 5.16), and for this reason the rotational frequency was increased from the usual 2 kHz to 6 kHz to allow the measurement within a reasonable amount of time (8464 scans). The CSA parameters were extracted via peak fitting and are as follows: δ_{11} = 375.6, δ_{22} = 304.7, and δ_{33} = -72.6 with an overall CSA of 448.1 ppm which is larger by 38.1 ppm than the value reported in the literature.[88] However, this discrepancy is due to the fact that the literature measurements were conducted at a Larmor frequency of 90.5 MHz, and our solid-state NMR spectrometer operates at 100.6 MHz for ^{13}C NMR measurements.

Upon adsorption, the CSA is completely averaged out, and a single narrow line with a halfwidth of only 51 Hz appears at 201.35 ppm, as compared to 137 Hz at 202.55 ppm for the polycrystalline material.

The literature[74,88-89] describes various reactions that occur on the surface of alumina, but none of these reaction products are observed on the surface of silica in the ^{13}C NMR spectrum taken immediately after adsorption. It should be noted, however, that some reaction with the surface appears to take place given sufficient time because within 8 days the large silica gel pieces that contained this adsorbed complex turned yellow (Figure 5.17), just like the alumina samples described in the literature.[74,88-89]

Figure 5.17 Silica specimens after absorbing the maximal amount of $Mo(CO)_6$, nickelocene, ferrocene, and cymantrene (left to right).

Unfortunately, since $Mo(CO)_6$ is obviously highly mobile on silica surfaces, too, as shown by the reduction in its CSA (Figure 5.16), it is impossible to say whether cymantrene adsorbs with the Cp ring down, or with the Cp ring up, or in some alternative manner.

At the same time, having two Cp rings (like in ferrocene) leads to stronger adsorption than having one (like cymantrene). This can be explained in two ways: (1) The carbonyl groups deplete electron density from the metal, and to a lesser extent from the Cp ring, which then is no longer able to hydrogen bond to the surface silanol groups as strongly. (2) having two Cp rings increases the probability of achieving the supposedly more favorable arrangement of having a Cp ring closely contacting the surface. Both of these explanations suggest that the adsorption is most probably driven by the Cp ring interacting with the surface. If any other orientation is relevant to the adsorption, then the carbonyl groups must be interfering in some other way with strong adsorption.

One of the important applications of these adsorption studies is in the synthesis of new catalysts. Accordingly, a new nickel catalyst was prepared by adsorbing

nickelocene onto silica gel with low surface coverage and then heating the resulting material to 195 °C in an atmosphere of H_2. This treatment caused the light green material to turn light brown. The resulting catalyst was washed with toluene to remove any residual metallocene and then dried in vacuum.

TEM analysis of the material (Figure 5.18) does not show any visible nanoparticles, which can be an indication of their small size. Even single atoms on the surface are possible. The EDX spectra do not show the presence of nickel (Appendix Figure B.4), however, this might also be due to the fact that the small Ni particles or atoms are a difficult target. But the presence of nickel is obvious because the material is catalytically active with respect to the cyclotrimerization of phenylacetylene (Figure 5.19). In a future project batches will be produced with a higher loading of nickelocene to create larger nanoparticles, or particles or atoms numerous enough to be observed by TEM.

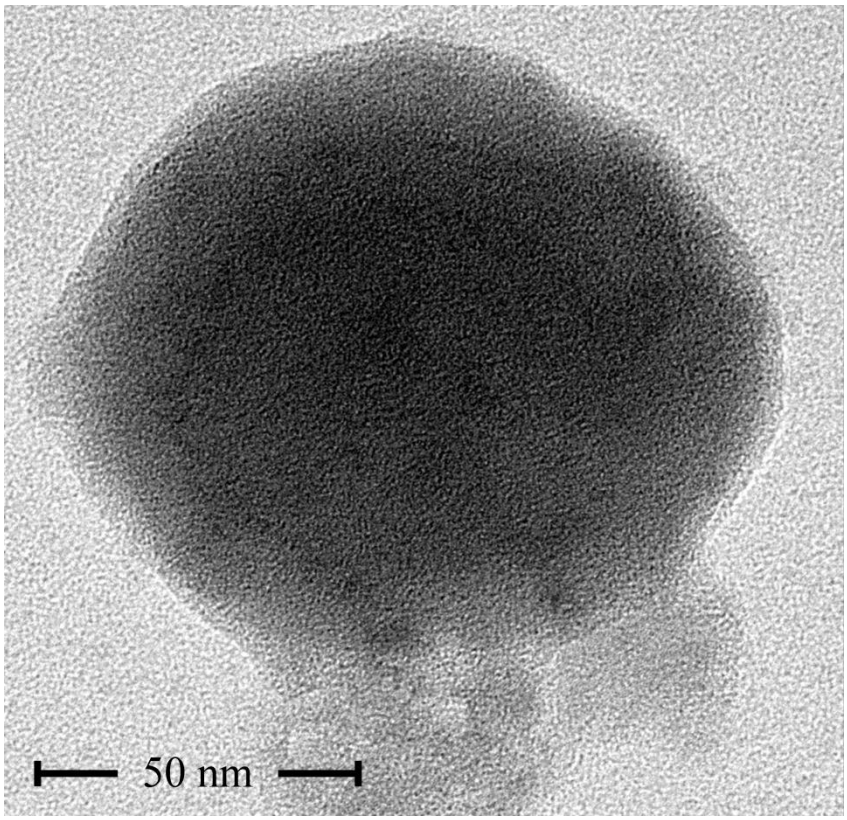

Figure 5.18 TEM image of a nickel catalyst prepared by the adsorption of nickelocene on silica gel and the subsequent reduction with H_2.

Catalysis with this Ni/SiO_2 material was carried out at 100 °C since the activity was too low at 60 °C. While the yield and reaction time are not yet competitive with respect to homogeneous nickel complexes (Chapter II), it should be noted that this is a first, not yet optimized attempt with an extremely low surface coverage. It is interesting to note (Figure 5.20) that the selectivity with this catalyst is dramatically different from any other outcome observed previously. The ratio of unsymmetric (U) to symmetric (S) cyclotrimerization product begins, as usual, very low, but jumps rapidly to nearly 9 within the first half hour. After this point, the ratio decreases, eventually reaching 4 at 20

hours. This contrasts with the results shown in Figure 3.17 with the ratio beginning low and increasing at first for about 20 minutes, and remaining relatively constant after that point.

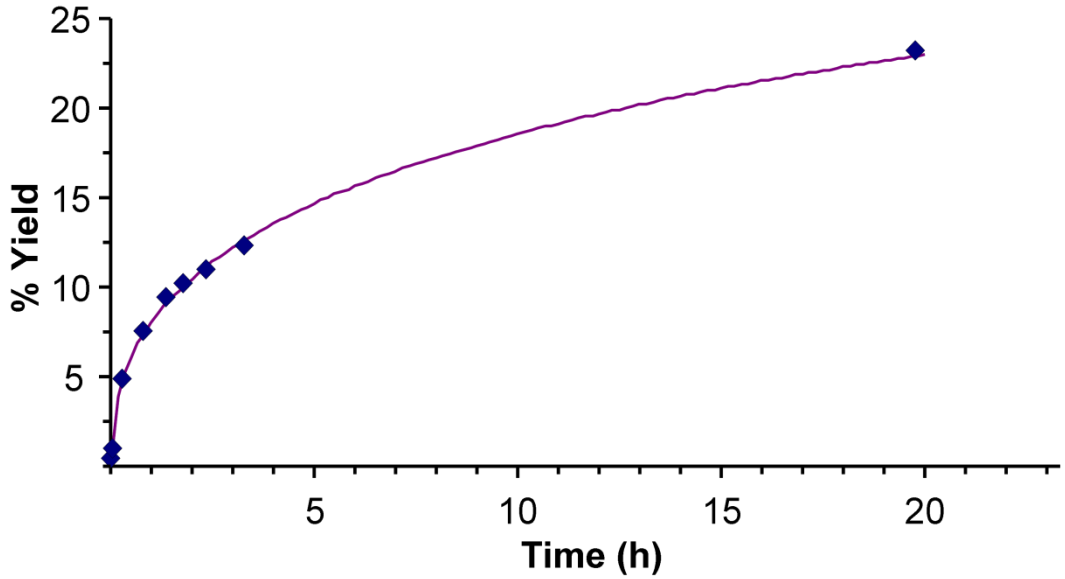

Figure 5.19 Total product yield in the course of the cyclotrimerization of phenylacetylene catalyzed by a supported Ni catalyst prepared via adsorption and reduction of nickelocene on silica gel.

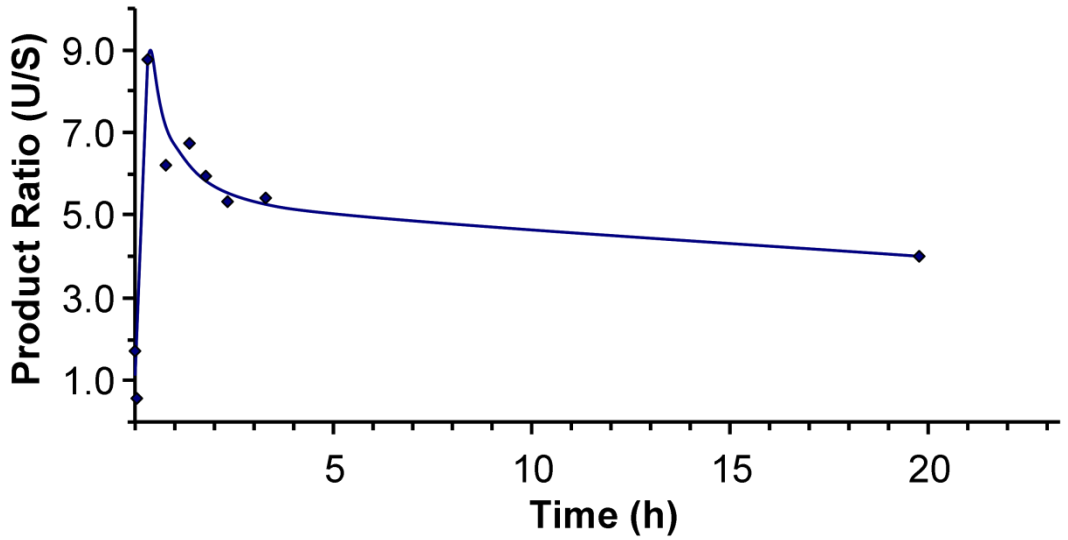

Figure 5.20 Selectivity with respect to the unsymmetric (U) versus symmetric (S) cyclotrimer during the cyclotrimerization of phenylacetylene with the Ni catalyst prepared by adsorption and reduction of nickelocene on silica gel.

CONCLUSION

The translational mobility of metallocenes on silica surfaces has been visually confirmed on a macroscopic scale by using large silica gel pieces. It has been shown that once adsorbed ferrocene is oxidized to ferrocenium at acidic surface silanol sites, it loses all translational mobility. Large silica pieces, saturated with ferrocene, can be filled into a 5 mm glass NMR tube and the ^{1}H and ^{13}C NMR spectra can the be measured using a standard liquids NMR instrument.

A method has been developed to conveniently measure the strength of adsorption on surfaces and it has been found that ferrocene is significantly less volatile after adsorption on silica gel. Carbon nanotubes provide even stronger adsorption, and

activated carbon requires the highest temperatures (100 °C) to release the adsorbed ferrocene under vacuum.

Carbonyl-containing metal complexes such as cymantrene and $Mo(CO)_6$ have also been shown to adsorb onto silica surfaces without the help of a solvent and to be highly mobile on the surface. It has also been shown that the more weakly adsorbing cymantrene can be desorbed from a silica surface by adding the more strongly adsorbing ferrocene.

The maximum loading of an adsorbate on silica surfaces can been determined by weighing large silica pieces before and after saturation with the adsorbate. The maximum surface coverages of ferrocene, nickelocene, cymantrene and $Mo(CO)_6$ have been determined in this manner.

A nickel catalyst has been prepared by first adsorbing nickelocene on silica, and then applying heat and an atmosphere of hydrogen to decompose the metallocene. The resulting catalyst is active in the cyclotrimerization of phenylacetylene. Since no nanoparticles are visible by TEM it is possible that the nanoparticles are either extremely small, or too dilute on the surface to characterize reliably with TEM. It is also possible that single atom catalysts have been formed.

EXPERIMENTAL

General Considerations

All experiments reported in this chapter were carried out under inert atmosphere except for those involving paraffin and HDPE and the experiments that produced blue ferrocenium salts.

The silica gel pieces used for the macro-scale adsorption experiments were purchased from Fisher Scientific Company and have a granulation of 3-8 mesh. The largest pieces were selected and then dried by applying vacuum for 2 hours and gently heating with the heat gun at intervals, with increasing intensity until approximately 200 °C is reached and maintained for one minute. If the silica pieces were heated at once, they tended to fracture and break, but the gradual heating left the samples intact and removed any surface adsorbed water and, most importantly, released adsorbed O_2.

The finely granulated (particle diameters 0.063-0.2 mm) silica gel was purchased from Merck, and it has an average pore size of 40 Å and a specific surface area of 750 m^2/g. Unless otherwise specified, this silica gel was dried at 300 °C under vacuum for 3 days. In contrast to this "dry" silica, "wet" silica refers to the original material, as received, with no additional drying.

NMR

The ^2H NMR spectra were recorded with a Bruker Avance 400 wide bore spectrometer using a 4 mm MAS probehead and the solids echo pulse program with a recycle delay of 3 s.

The ^{13}C solid-state NMR spectra were recorded with a Bruker Avance 400 wide bore spectrometer using a 4 mm MAS probehead. Single pulse programs without cross polarization or proton decoupling were used for all measurements with a recycling delay of 10 s. All samples were packed into the whole rotors as finely ground polycrystalline material. Silica powder was filled in loosely. Compressed air was used as both the bearing and drive gas for the MAS measurements. Typically 2400 transients were recorded.

The ^{13}C NMR spectrum of **10** adsorbed in large silica gel pieces was obtained on a Varian 500 liquids NMR instrument without decoupling and with a pulse delay of 2 s and recording 256 scans. The signal was referenced relative to benzene in a capillary (128.00 ppm).

Deconvolution and processing of the spectra was accomplished using ACD/NMR Processor Academic Edition.[84] The quadrupolar coupling constants were derived from the ^{2}H MAS NMR spectra using the NMR simulation program Dmfit.[17]

Adsorption Experiments

The time-resolved adsorption into the large silica pieces was carried out in a Schlenk flask by carefully positioning the adsorbate and the silica piece with tweezers under a stream of nitrogen. The flask was then closed and stored without disturbance, and photographs were taken at intervals to monitor the progress.

For the competition experiment between **15** and cymantrene, 98.0 mg of silica gel was ground with cymantrene (146 mg, 0.715 mmol) in the glove box for one minute

and then the mixture was left for 36 hours to fully adsorb. **15** (10 mg, 0.053 mmol) was then added and ground in for 1 minute. The ^{2}H NMR spectrum was recorded after allowing the sample to equilibrate for 9 hours.

Maximum Surface Coverage Determinations

Maximum surface coverages were determined by adding several weighed large silica gel specimens to a vial containing an excess of the adsorbate powder. The mass of the silica pieces was then recorded after allowing one month to elapse to ensure complete saturation (Table 5.1).

Table 5.1 Maximum loadings of adsorbates in the large silica gel pieces.

Adsorbate	**Mass of silica pieces (mg)**	**Mass after Adsorption (mg)**	**Adsorbate on silica**	
			(mg/g)	**(mmol/g)**
$CpMn(CO)_3$	259	405	564	2.762
Cp_2Fe	360	500	389	2.090
Cp_2Ni	271	378	395	2.090
$Mo(CO)_6$	414	568	372	1.409

Supported Nickel Catalyst

The nickel catalyst was produced by adsorbing 9 mg of nickelocene into 2.78g of silica gel (1.16% surface loading, 1.4 molecules per 100 nm^2). The resulting material was stored under a H_2 atmosphere for two days, but no change was noted in the light

green color. Heat was then applied (60 °C) for one hour but no change was noted until the temperature was increased to 195 °C for three hours. The resulting light brown material was washed with 10 mL of toluene, which remained clear and colorless, and then the solid was dried in vacuum. The test of the material for catalytic activity for the cyclotrimerization of phenylacetylene was accomplished according to the standard procedure described in Chapter III, but at a temperature of 100 °C.

CHAPTER VI

ADSORPTION AND MOBILITY OF FERROCENE ON CARBON SUPPORTS

INTRODUCTION

The importance and potential of carbon allotropes in modern and future advances in science and engineering can hardly be overstated. Exciting applications range from the popular catalyst Pd/C that is in general use, to the nanometer-scale electronics of the future.[90] In addition, organic and inorganic pollutants can be very efficiently adsorbed onto activated carbon, graphene oxide and CNT from aqueous solution and gas streams.[91]

Activated carbon is a particularly important sorbent in catalysis and in purification. Because of its relatively low price compared to other carbon allotropes, it is widely employed in many forms. For example, biologically produced H_2 and CH_4 both suffer from the presence of CO_2 which may be removed via adsorption on special activated carbons.[52c] Activated carbon is also very important in wastewater treatment to remove heavy metals, including Hg^{2+}, Cr^{6+} and Cd^{2+} species, as well as organic contaminants such as toxic dyes or warfare agents. Activated carbon can be derived from biomass, a feature that increases in importance, and it is amenable to functionalization which can be used to render the material magnetic which further facilitates separations.[92]

Adsorption studies on activated carbon have focused mainly on simple liquids like water, alcohols and benzene.[93] However, solids such as phenanthrene have also been

studied and it has been shown that some biochars are able to adsorb more phenanthrene because of its mobility on the surface, while other adsorbents lead to immobile adsorbates and achieve lower loadings.[94]

Therefore, it will be beneficial to explore the mobility of organometallic complexes on the surface of activated carbon since this may lead to more efficient catalyst production, and perhaps solvent-free methods for forming a monolayer as we have shown is possible on silica surfaces.[68,86] Furthermore, using different support materials will provide a deeper insight into the adsorption process itself and the ensuing mobility. Regarding the studies presented in the previous chapters, it is not yet quite clear, for example, whether an extended aromatic system that adsorbs more strongly on silica, would be equally mobile. Furthermore, extending the findings described in the preceding chapters from the silica surface to a surface with entirely different characteristics would underline the general nature of the phenomenon of surface mobility in the absence of solvents.

Like activated carbon, carbon nanotubes (CNT) are the subject of many adsorption studies aimed at purification and environmental remediation. For example, divalent heavy metal ions[95] and toxic dyes[96] can be removed from solution using CNT. Futhermore, multiwalled carbon nanotubes (MWCNT) in combination with nanoparticles of iron oxide give magnetically separable adsorbents for chromium pollutants and dyes.[97]

In addition to purification, CNT also have great potential in the electronics industry where efforts go forward to produce nanometer scale transistors, diodes and

other electronic components.[90] Of course, to accomplish this, it is desirable to tune the properties of the CNTs by modifying them with organic, inorganic and organometallic compounds. The novel materials formed in such studies may have interesting electronic[90,98] or catalytic properties.[99]

Most research thus far has focused on filling the interior of single-walled carbon nanotubes (SWCNT). For example, it has been shown that endohedral doping of nanotubes with fullerenes can successfully tune the electronic parameters of the material.[90] Even more dramatic changes are noticed upon filling the SWCNT with metal-containing dopants such as a metallofullerene.[98f] Various metals and metal oxides have also been filled into SWCNT in an effort to tune their electronic parameters and to discover novel materials.[98f,98g]

Metallocenes are much more accessible than metallofullerenes, and they have many interesting properties that make them targets for encapsulation in SWCNTs. This was first accomplished in 2002 when ferrocene, chromocene, ruthenocene and vanadocene were successfully filled into SWCNTs.[100] Filled nanotubes are usually characterized with SEM[101] and TEM, which has shown that the metallocenes move one-dimensionally along the nanotubes.[100,102]

These nanotubes modified with metallocenes are also relevant to the energy industry, for example, metallocenes have been used recently to dope SWCNT thin films for making solar cells.[103] Furthermore, encapsulated ferrocene can be decomposed at 700 °C to yield iron nanoparticles inside the nanotubes.[104]

Carbon nanotubes are more reactive on the outside (tending to make covalent bonds when possible because it relieves strain) than the inside because of the curvature which causes a slight pyramidalization and affects the hybridization such that the π orbitals on the outside are larger and softer. It also causes some misalignment of the π orbitals.[105] In spite of this, the adsorption on the exterior of nanotubes is not explored in detail yet.

There are some literature known examples of Zn, Cu, Ni and Co porphyrins which are adsorbed onto the exterior surface of nanotubes.[106] Cp_2ZrCl_2 has also been adsorbed onto the exterior of MWCNT to form an interesting polymerization catalyst which produces polyethylene (PE) with a molecular weight M_w of 1,000,000 and polydispersity index = 1.95 while the metallocene alone produces PE with a M_w of only 300,000. Exohedrally adsorbed ferrocene has been produced as a byproduct of filling the nanotubes with ferrocene but was only characterized by IR spectroscopy.[107] Interestingly, the adsorption is strong enough that the ferrocene cannot be completely washed off by ethanol or acetone and must be removed either by annealing, or washing with toluene.[107] Ferrocene has also been adsorbed onto MWCNT-modified electrodes and studied via electrochemistry.[108]

The adsorption on the outer surface of nanotubes is made even more interesting since nanotubes are strongly held together in bundles. These may be dispersed by adsorbing polymers, or PAH (polyaromatic hydrocarbons) or surfactants on the outside.[105,109] Bundles of nanotubes have several possible adsorption sites including in the channel between two parallel tubes (groove site), in the space between three closely

packed parallel tubes (interstitial site) and on the surface of a single tube (exterior site).[105]

One of the obvious benefits of exterior versus interior adsorption is that both SWCNT and MWCNT are readily accessible for modification by this method whereas endohedral doping is mainly limited to SWCNT and double-walled carbon nanotubes (DWCNT). MWCNT are commercially available in many sizes which will allow the adsorption on nanotubes of various curvatures to be compared. This may be interesting since benzene is predicted by calculations to adsorb more strongly to larger nanotubes with less curvature.[105]

Exterior adsorption also avoids other potential complicating factors. For example, Li and coworkers filled cobaltocene and derivatives thereof into SWCNT, but found that the cobaltocene only adsorbed into nanotubes into which it fit perfectly.[110] They supposed that this is due to maximized interaction with the nanotubes that is strong enough to hold the cobaltocene down while it would otherwise sublime away under the reaction conditions.[110] This situation will most probably be avoided in the case of external adsorption since milder conditions are likely to suffice. It will be worthwhile to investigate the adsorption and mobility of metallocenes on the exterior surface of SWCNT and MWCNT and to experimentally determine the strength of the metallocene-nanotube interaction.

Therefore, in this chapter, the adsorption and mobility of metallocenes on carbon based supports such as activated carbon and carbon nanotubes will be explored. These

studies are of fundamental interest, and have wide ranging potential in fields such as catalysis, electronic devices and the separation sciences.

RESULTS AND DISCUSSION

Molecular species with high melting points have been adsorbed on activated carbon and carbon nanotube surfaces. Variable-temperature multinuclear solid-state NMR spectroscopy has been applied to study dynamic effects of the mobile surface-adsorbed species. It could be demonstrated that on favorable supports the major anisotropic interactions that render solid-state NMR signals broad, can be reduced or eliminated. In some cases the chemical shift anisotropy (CSA), and dipolar, and quadrupolar interactions are reduced to a degree that allows the recording of the spectra of the solid materials on a conventional liquids NMR spectrometer.

Activated Carbon as Support Material

Interestingly, as shown in the previous chapter (Figure 5.9), Cp_2Fe-d_2 (**15**) is adsorbed more strongly on activated carbon than on either silica or SWCNT. This makes activated carbon an ideal potential support for a single-atom catalyst (SAC), or a nanoparticle catalyst which can be generated by decomposing a favorable precursor adsorbed in a well-defined monolayer.

Actually, activated carbon is a surprisingly favorable support for adsorbing **15**. When it is combined with activated carbon, a monolayer forms (Figure 6.1). With a

higher loading the Pake pattern becomes visible, in addition to the narrow signal of the adsorbed species

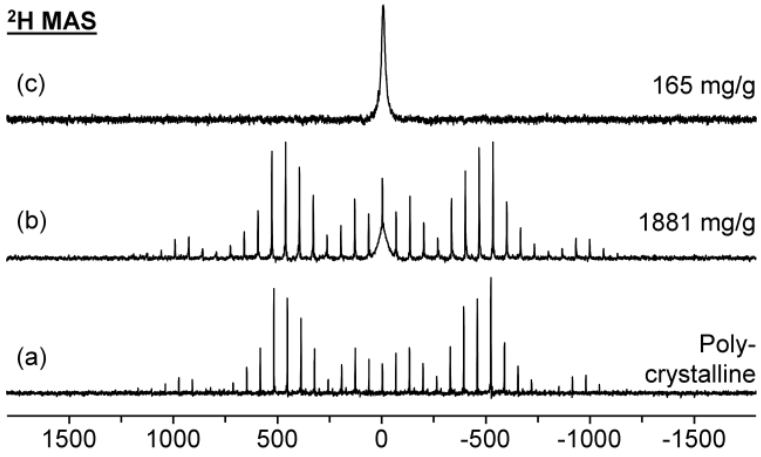

Figure 6.1 ^{2}H MAS spectra of **15** adsorbed onto activated carbon. The bottom two spectra have rotational speeds of 4 kHz while the top is recorded with 6 kHz.

The maximum loading of **15** on activated carbon is 170 mg/g. This is lower than the 274 mg/g for silica and the 356 mg/g adsorbed on SWCNT. In the top spectrum (Figure 6.1) the signal has a residual linewidth of 1256 Hz, while the signal of the adsorbed ferrocene in the middle spectrum is 2911 Hz broad. The polycrystalline material (bottom spectrum) displays a quadrupolar coupling constant Q_{cc} of 96.1 kHz, in accordance with the literature,[82] and the middle spectrum shows practically the same Q_{cc} with 96.9 kHz. The small difference is most likely due to S/N issues and the inherent difficulty of phasing and baseline correcting a spectrum that uses an echo pulse sequence for solid samples. Overall, Figure 6.1 shows that ferrocene is readily adsorbed and

mobile on the surface of activated carbon within the pores. In analogy to ferrocene adsorbed on silica (see previous chapters), ferrocene on activated carbon is mobile enough to allow NMR measurements of the solid samples at a routine liquids NMR spectrometer without MAS or high power decoupling. This effect was exploited for the following temperature dependent measurements.

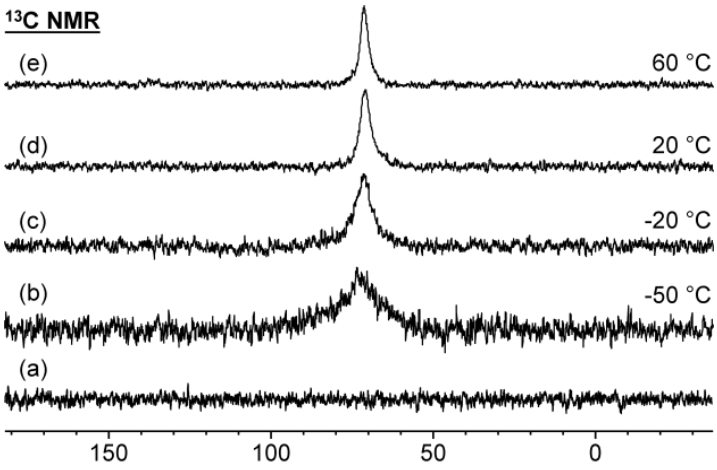

Figure 6.2 ^{13}C NMR spectra of activated carbon (bottom) and Cp_2Fe (**10**) adsorbed in a monolayer on the surface of activated carbon at the indicated temperatures. All spectra were recorded on a conventional liquids NMR spectrometer. Halfwidths are from bottom to top (b) 1920, (c) 810, (d) 480, and (e) 410 Hz.

The ^{13}C and ^{1}H wideline NMR spectra of ferrocene (**10**) adsorbed on activated carbon were recorded on a liquids NMR instrument at variable temperatures (Figures 6.2 and 6.3). For both nuclei the residual lines became broader at lower temperatures. On the high temperature end, once the mobility exceeds that required to average out the

anisotropic line-broadening solid-state NMR interactions, there is no further reduction of the halfwidths. Analogous results are obtained for O=PPh_2(Ph-d_5) adsorbed on silica.[111]

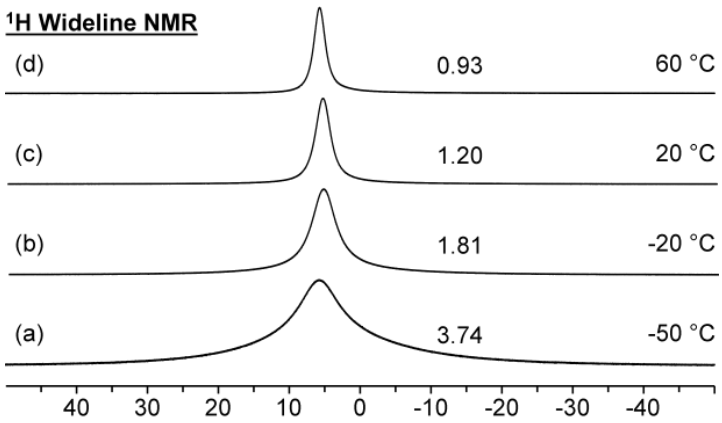

Figure 6.3 ^{1}H NMR spectra of **15a** adsorbed in a monolayer on the surface of activated carbon at the indicated temperatures. All spectra were recorded on a liquids NMR spectrometer. The linewidths (kHz) are listed next to the signals.

In addition, the ^{2}H MAS spectra of **15a**, adsorbed from an excess of polycrystalline material (Figure 6.4), were recorded at low temperatures. Again, the residual signal linewidth for the adsorbed ferrocene broadens at low temperatures, but the high temperature line narrowing limit is already reached at ambient temperature.

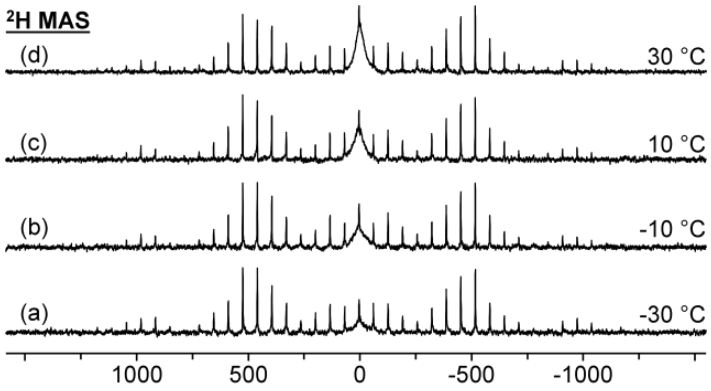

Figure 6.4 ^{2}H MAS spectra of **15a** adsorbed onto activated carbon, recorded at the listed temperatures at a rotational speed 4 kHz. The linewidths of the signals for adsorbed material, from bottom to top are 6.04, 4.06, 3.47 and 2.85 kHz respectively.

All variable temperature ^{13}C, ^{2}H, and ^{1}H NMR spectra of **15** adsorbed on activated carbon show a similar trend (Figure 6.5). With increasing temperature the lines become narrower due to the higher translational mobilities of the adsorbed ferrocene molecules on the surface.

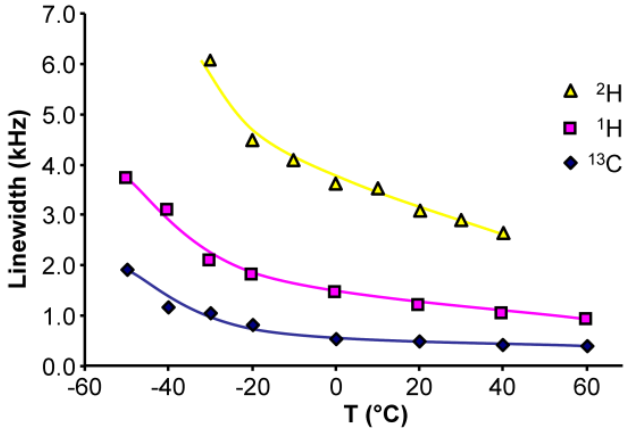

Figure 6.5 Linewidths of **10a** and **15a** adsorbed on activated carbon. The ^{13}C and ^{1}H measurements were performed on a 500 MHz liquids NMR spectrometer using a sample

with submonolayer coverage. The ^{2}H data were obtained from the solid-state NMR spectrometer Avance 400.

Finally, the field dependence of the residual linewidths was investigated in order to be able to distinguish between the line-narrowing effect of translational mobility on the CSA and on dipolar interactions. While the CSA is dependent on the external magnetic field strength and actually increases with higher fields, the dipolar interactions are independent of the magnetic field strength. Interestingly, the residual linewidths of ^{13}C signals practically do not change with the field strengths, while for ^{1}H resonances the linewidth increases with the field (Table 6.1). Therefore, it can be concluded that in the case of ^{13}C the MAS and surface mobility have already efficiently averaged out anisotropic dipolar and CSA interactions. For ^{1}H wideline spectra, there is still a CSA linebroadening component that responds to the change of the field strength in the expected manner with a broader line at higher external magnetic field strength.

Table 6.1 Residual linewidths of ^{1}H wideline and ^{13}C MAS resonances of **10a** adsorbed on activated carbon at different field strengths. 500 and 300 MHz NMR instruments were used for the measurents.

Nucleus	**Halfwidth (Larmor Frequency)**	**Halfwidth (Larmor frequency)**
^{13}C	416 Hz (125.65 MHz)	391 Hz (75.43 MHz)
^{1}H	1253 Hz (499.68 MHz)	841 Hz (299.96 MHz)

Carbon Nanotubes as Support Materials

As a first attempt, for spectroscopic purposes two samples of MWCNT were used to adsorb **15**. The ^{2}H wideline spectra prove that **15a** is indeed adsorbed and mobile on the surface. However, the intensity of the central signal, corresponding to the adsorbed molecules, is small compared to the signal of residual polycrystalline **15**.

Happily, ferrocene is also adsorbed readily and with larger surface coverages on the surface of SWCNT. Even when polycrystalline ferrocene is just combined with SWCNT without grinding, one can observe that the crystals vanish over time (Figure 6.6).

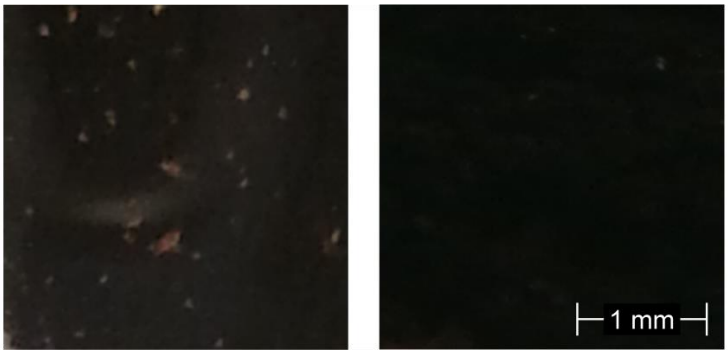

Figure 6.6 Images of a freshly prepared dry mixture of orange crystals of **10** with MWCNT (left) and the same mixture after 12 hours (right).

In contrast to the polycrystalline material (Figure 6.7, bottom), the ^{2}H MAS spectrum of **15a** adsorbed on SWNT shows an intense signal in the center and only sidebands with minor intensities from residual polycrystalline material (Figure 6.7). Therefore, it can be concluded that the surface curvature of the carbon NTs provides a

favorable template for quasi-isotropic rearrangement of the ferrocene molecules and consequently narrowed lines. Even the large quadrupolar interactions are averaged out by the translational mobility of the molecules on the nanotube surfaces.

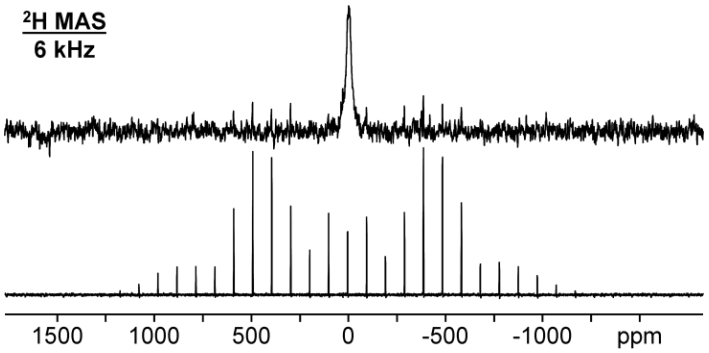

Figure 6.7 ^{2}H MAS spectra of polycrystalline **15** (bottom) and adsorbed **15a** onto 1-2 nm diameter SWCNT (top).

In a next step an attempt was undertaken to correlate the reorientation time of the adsorbed ferrocene with the diameters of the nanotubes. For this purpose, SWCNTs with different diameters were applied as adsorbents. The larger diameter NT were anticipated to lead to longer reorientation times and thus less line narrowing than the NT with smaller diameters which should allow faster circling and reorientation. Figure 6.8 displays the obtained ^{2}H wideline spectra for ferrocene adsorbed on three different SWCNTs. The quadrupolar coupling constants Q_{cc} of the residual Pake patterns are the same for all three, and they are equal to polycrystalline ferrocene. Therefore, the outer lines in the spectra were assigned to residual polycrystalline ferrocene. All spectra display a comparatively narrow center line indicating adsorbed ferrocene with a

collapsed Pake pattern. The residual linewidths are 3.8, 1.7 and 5.1 kHz for the bottom, middle and top spectra respectively.

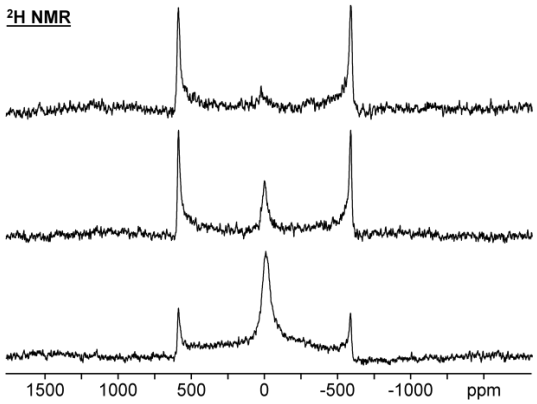

Figure 6.8 ^{2}H wideline NMR spectra of **10a** adsorbed carbon nanotubes. Top: largest diameter 40-60 nm MWCNT, middle: 10-20 nm MWCNT, bottom: 1-2 nm SWCNT. Quadrupolar coupling constants: Q_{cc} = 96.3, 95.6, and 96.4 kHz from top to bottom.

The SWCNT with the smallest diameter obviously has the largest specific surface area and therefore can adsorb more ferrocene than the NTs with larger diameters. The desired correlation of the diameters with correlation times and linewidths could not be established with this series of experiments. One complicating factor might be the different stacking of the carbon nanotubes, allowing for more or less restricted cruising of the ferrocene molecules on the outside of the NT.

The influence of the temperature was studied using ^{1}H NMR spectroscopy (Figure 6.9). While the residual linewidth increases at low temperatures, the high temperature line-narrowing limit was reached around 50 °C. This means that dipolar

interactions are already efficiently averaged out by the quasi-isotropic reorientation of the ferrocene molecules on the SWCNT surface at ambient temperature.

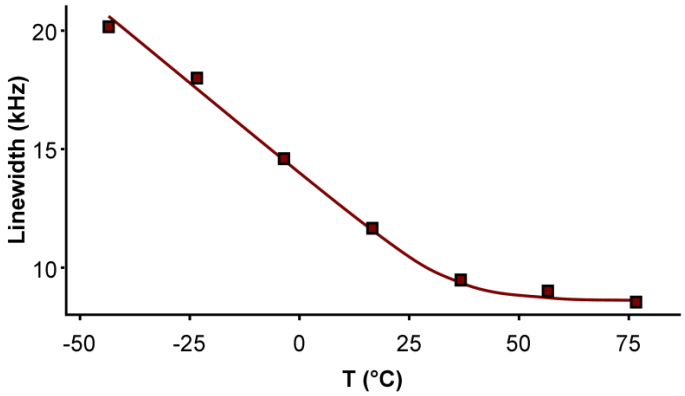

Figure 6.9 Variable temperature ^{1}H wideline NMR linewidths of **10a** adsorbed onto SWCNT (1-2 nm diameter).

Graphite, Graphene and Fullerene as Support Materials

Encouraged by the vigorous adsorption of ferrocene on activated carbon and on carbon nanotubes, other types of carbon surfaces were probed. Unfortunately, when graphite was ground with ferrocene for five minutes, no ^{13}C NMR signal that would indicate adsorption could be detected. Even prolonged exposure and elevated temperatures, or measurement in the wideline mode without MAS to exclude potential problems due to the conductivity of graphite did not result in a narrow NMR signal indicative of fast translational mobility. The ^{2}H wideline NMR spectrum of **15**, combined with graphite, was identical to that of polycrystalline **15**.

While it cannot be excluded that **10** adsorbs on the outer graphite surface due to the expected low S/N ratio with this low surface coverage, it can be safely assumed that intercalation between the layers of the material does not occur. Since in addition there is no short-range curvature of the graphite surface, translational mobility of **15** does not result in isotropic reorientation.

An attempt to increase the surface area by exposing graphene with a much larger surface area than graphite to **15** did not lead to adsorption on a scale measurable by ^{13}C solid-state NMR. In ^{2}H NMR only a trace amount of adsorbed and mobile **15a** is visible. In the case of graphene one might speculate that the "crumpled", nonplanar character of the thin graphene layers, in contrast to the overall more planar graphite layers, might allow a limited amount of quasi-isotropic rearrangement on the two-dimensional surfaces.

When **15** was mixed with the C_{60} fullerene, only a Pake pattern with a quadrupolar coupling constant of 96.2 kHz was obtained by ^{2}H MAS, which matches the literature value of 96.9 kHz.[82] Since in both cases adsorption was expected based on the success with multi walled and single walled carbon nanotube surfaces, we assume that between the graphene sheets and the fullerene molecules there is not enough free space to allow for unimpeded translational mobility of **15a**.

Finally, the influence of the uninterrupted surface area of the support material was probed by mixing ferrocene with anthracene. No adsorption occurred, indicating that the surface area of one single anthracene molecule does not allow for a long enough undisturbed path for translational mobility and that the ferrocene molecules can not

bridge the gaps between the stacked anthracene molecules in the crystal lattice. No co-crystals were obtained from solutions of anthracene and ferrocene in different solvents.

Polymers as Support Materials

The absorption of **10** into HDPE (high density polyethylene) and into paraffin wax provides an interesting extension of the experiments described in the previous chapter with silica gel. Figure 6.10 shows that **10** does absorb into HDPE. Paraffin wax also takes on a slightly orange color. It is noteworthy that this orange color does not progress in a "frontier" from one side of the material to the other, rather it slowly penetrates from all sides (Figure 6.11). Dissection of the paraffin block showed that the ferrocene did not penetrate all the way through, and that the center was still free of ferrocene.

Figure 6.10 Comparison of pristine HDPE (left) and HDPE that has been exposed to **10** for one week.

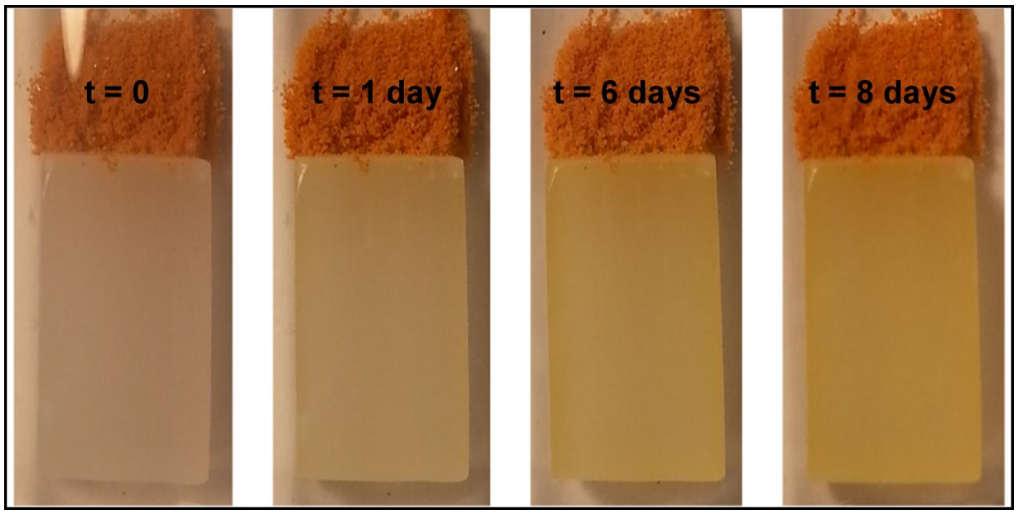

Figure 6.11 The absorption of ferrocene into paraffin wax over time.

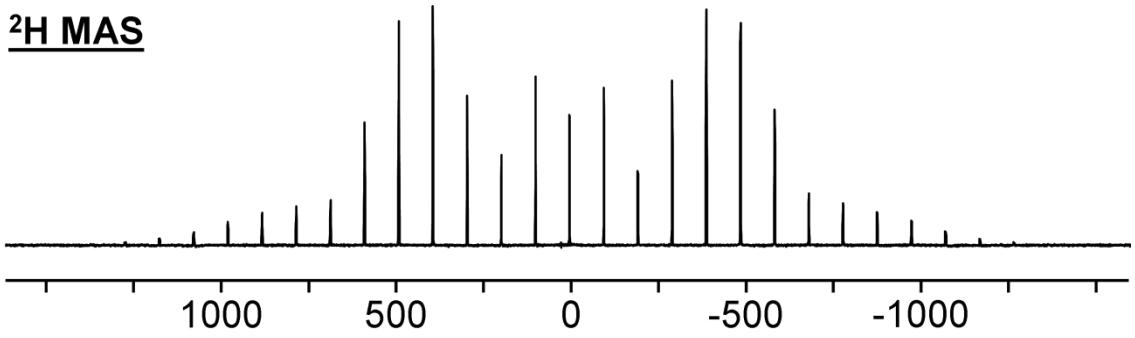

Figure 6.12 ^{2}H MAS NMR spectrum of **15a** absorbed in HDPE and of residual **15**.

To understand these results we must first consider the solid-state ^{2}H MAS NMR spectra of these materials. In both cases the same spectrum results (Figure 6.12). This Pake pattern is identical to that of polycrystalline **15** and arises mainly from the residual polycrystalline material in the sample. Any absorbed ferrocene **15a** either has an identical spectrum to polycrystalline **15**, or the signal is too broad to observe. Either of these conditions would indicate that ferrocene is not mobile in paraffin wax or HDPE. This contrasts with other cases such as PVC and LDPE, both of which give small signals in the center of the spectrum denoting a mobile species (Figure 6.13).

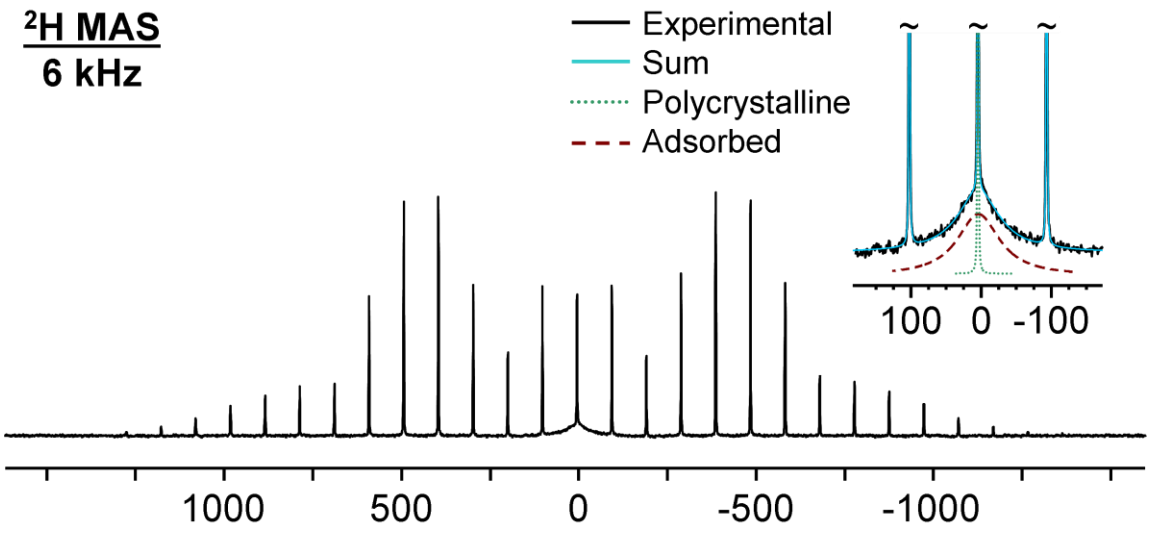

Figure 6.13 ^{2}H MAS NMR of **15a** absorbed into PVC along with residual polycrystalline **15**.

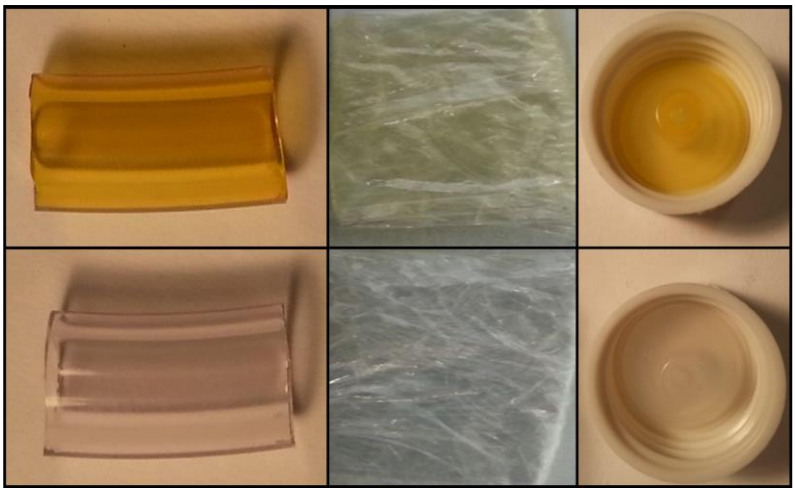

Figure 6.14 Polymer samples before (bottom) and after (top) exposure to ferrocene. The samples are PVC tubing (left), LDPE film (middle) and LDPE vial caps (right).

It is clear from the intense color that PVC tubing and LDPE samples absorb a much greater amount of ferrocene than do HDPE and paraffin wax (Figure 6.14). In fact, PVC tubing absorbs 38 mg of **15** per gram. This result demonstrates that PVC tubing,

although widely used in industrial and academic labs, should not be relied upon when contamination, or loss of material is an issue. Upon absorption, Q_{cc} is averaged out by the mobility of **15a** in the polymer network. Deconvolution of the adsorbed and polycrystalline signals (Figure 6.13) shows that the halfwidth increases from 0.1 to 3.9 kHz. The spectrum of **15a** absorbed in LDPE is very similar to that of **15a** in PVC with the only difference that the linewidth of the signal is only 0.8 kHz rather than 3.9 kHz. This reduction in linewidth could indicate increased mobility relative to PVC.

CONCLUSION

This chapter described a multinuclear solid-state NMR study of the adsorption of ferrocene (**10**) and its deuterated version on activated carbon, carbon nanotubes, graphite, and graphene. In all cases the anisotropic solid-state interactions that prevail in polycrystalline solids were effectively reduced or even eliminated by quasi-isotropic mobility of the adsorbed molecules across favorable surfaces. It was demonstrated that the chemical shift anisotropy (CSA), quadrupolar interactions, and even dipolar interactions were reduced to a degree that measuring the solid materials in a conventional high-resolution NMR spectrometer was possible. The temperature dependence of the dynamic effects was investigated. The new insights gained on this research topic should have major implications for analytics, separation sciences and catalysis.

EXPERIMENTAL

DARCO KB-G activated carbon was purchased from Sigma-Aldrich. Data provided by the supplier indicates that this activated carbon has a surface area of 1700 m^2/g, and a pore volume for micro, meso and macro pores of 0.36, 0.95, and 0.45 mL/g, respectively. This activated carbon was dried/degassed under vacuum at 200 °C for 3 hours before use.

A representative sample of **10a** on activated carbon was prepared as follows: DARCO KB-G activated carbon (405 mg) was ground with ferrocene (202 mg, 1.09 mmol) for one minute in the glove box. The sample was left in the glove box in a tightly sealed vial to avoid ferrocenium formation overnight. For the solid-state NMR measurements the material was packed with moderate firmness into a 4 mm zirconia rotor without inserts.

It needs to be mentioned that another brand of activated carbon, Norit SA 2, purchased from Acros Organics that has a surface area of 900-1050 m^2/g and pore volumes for micro, meso and macropores with pore volumes of 0.28, 0.3 and 0.4 mL/g, respectively was also used in these experiments, however, no narrow lines resulted, probably because of the large fraction of micropores which likely trap the adsorbate. Various treatments of the activated carbon, including moistening, drying, treatment with NaOH and application of a high loading of ferrocene were attempted, but in no case was mobility observed. No signal was obtained on the Varian 500 NMR spectrometer, even after 30 min. measurement time. This contrasts to the case with DARCO KB-G which gave a well-defined signal after only 8 scans.

In order to determine the maximum loading of **10a** on the activated carbon, DARCO KB-G (105 mg) was ground with **10** (144 mg) and **15** (54 mg) in a glove box for 1 min and then left overnight to allow the ferrocene to fully adsorb. The ^{2}H MAS signals of adsorbed and polycrystalline ferrocene in the sample were then deconvoluted and integrated to give the maximum loading of 614 mg **10a** on 1 g of activated carbon. By assuming that **10a** packs onto the surface of activated carbon in the same way that it does onto silica gel (118 molecules per 100 nm^2), it can be calculated that the surface area available for adsorption on this activated carbon is 1685 m^2/g. This value matches surprisingly well with the manufacturers advertised value of 1700 m^2/g.

For a typical sub-monolayer loading, 405 mg of DARCO KB-G activated carbon was ground with ferrocene (202 mg, 1.09 mmol) for one minute in the glove box. The sample was left in the glove box in a tightly sealed vial overnight and then packed into a 5 mm glass NMR tube for measurement. This loading gave 81% of the experimentally determined maximum loading of 614 mg/1 gram.

For the temperature dependent ^{2}H MAS measurements with excess polycrystalline material, (DARCO KB-G (99 mg, dried under vacuum at 200 °C for 3 hours) and **15** (132 mg, 0.703 mmol) was ground for 1 minute in the glove box and then left overnight to ensure complete adsorption. The ferrocene was present in a 2.15-fold excess of that required for a monolayer to ensure that there was both adsorbed and polycrystalline material at every temperature for the purposes of integration.

The smallest SWCNT and DWCNT were obtained from Strem Chemicals. They have a diameter of 1-2 nm and lengths of 5-30 μm. The medium size are MWCNT from

TCI which feature a diameter of 10-20 nm and a length of 5-15 micrometers. The largest nanotubes are MWCNT from TCI, they have a diameter of 40-60 nm and a length of 5-15 μm.

The adsorption into HDPE was accomplished by combining HDPE granules with **15** (which was synthesized as described in Chapter IV) in a tightly sealed vial and allowing it to stand at ambient temperature for 7 days. This sample was then heated to 60 °C for two hours, but no difference was noted.

For the adsorption into paraffin wax **15** (61.8 mg, 0.329 mmol) was smashed together with paraffin wax (430.4 mg) (Gulf Wax brand) with a mortar and pestle several times and then a spatula was used to scrape the material off of the sides. This process was repeated for 6 minutes, until the orange color was evenly distributed.

CHAPTER VII

PALLADIUM "DRONE" COMPLEX

INTRODUCTION

Heterobimetallic complexes have many merits, as described in chapter II of this thesis. Although the Ni/Au combination within a tripodal phosphine complex turned out to be less successful than expected as a catalyst in the phenylacetylene cyclotrimerization reaction, it yet could have potential in other areas such as nanoparticle synthesis. The advantage in this case is the preassembly of different metals in a well-defined stoichiometry within a complex prior to reduction to mixed nanoparticles. The successful synthesis of $Ni(CO)_2$TriphosAuCl prompted an attempt to synthesize an additional metal combination, namely Pd and Cu. This would be a particularly interesting combination of metals in light of their importance in the Sonogashira reaction.[112] The Bluemel group has previously studied some aspects of the Sonogashira reaction mechanism and prepared immobilized palladium and copper catalysts for this reaction.[3a,113] An immobilized catalyst system containing both palladium and copper has been prepared that was catalytically active for C-C coupling reactions, and could be recycled 20 times.[113a] However, the bidentate phosphine ligands used at that point could only coordinate one metal center per ligand. Since a 1 : 1 ratio of Pd to Cu gives the best results in catalysis,[3a] using a tripodal phosphine ligand that can accommodate both metal centers in one molecule with exactly this ratio might be advantageous even if nanoparticle formation takes place during catalysis. Therefore, in a first step efforts were

made to synthesize a palladium complex which retains an uncoordinated phosphine group for the coordination of Cu as the second metal.

RESULTS AND DISCUSSION

$(PdCl_2)_3[(PPh_2CH_2CH_2)_3SiMe]_2$ (16)

The tripodal phosphine ligand $(PPh_2CH_2CH_2)_3SiMe$ did not coordinate palladium in the expected bidentate fashion. Instead, the "drone-like" complex **16**, incorporating three Pd centers was produced in high yield (Figure 7.1). Several similar palladium-phosphine complexes have been reported in the literature.[114] Originally, a 1:1 ratio of ligand and palladium was applied, hoping for the bidentate Pd complex, however, the yield and purity of **16** were improved by using a 2:3 ratio as detailed in the experimental section.

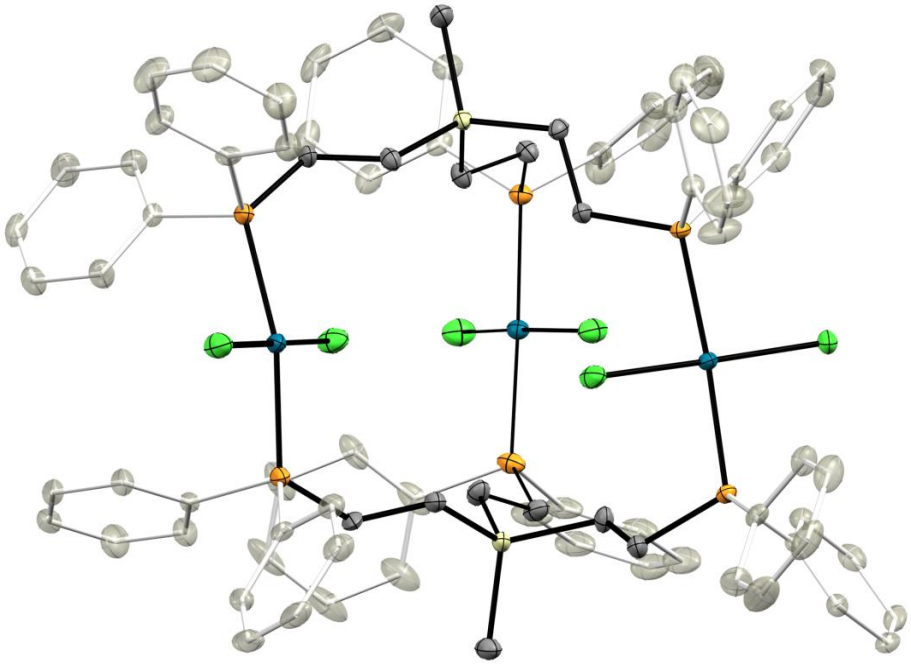

Figure 7.1 Single crystal X-ray structure of $(PdCl_2)_3[(PPh_2CH_2CH_2)_3SiMe]_2$. Thermal ellipsoids are shown at the 50% probability level. Hydrogen atoms are omitted for clarity.

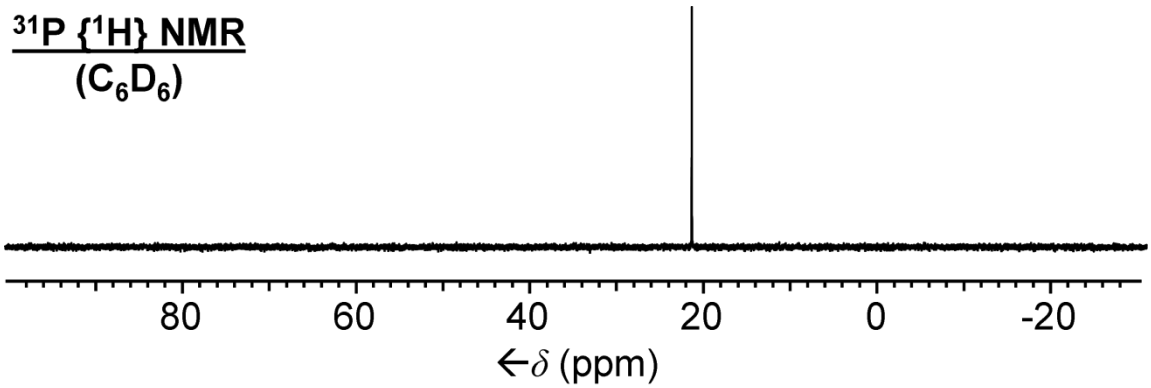

Figure 7.2 ^{31}P NMR of $(PdCl_2)_3[(PPh_2CH_2CH_2)_3SiMe]_2$.

Although the molecule appears slightly lop-sided in the X-ray structure (Figure 7.1), it is clear that in solution there is sufficient flexibility that all six phosphorus nuclei are equivalent because they give rise to a single narrow peak in ^{31}P NMR with a linewidth of only 1.0 Hz (Figure 7.2).

This molecule presents an interesting architecture that might be suitable for the formation and stabilization of very small, well-defined Pd_3 clusters. To test this idea, $NaBH_4$ has been applied both in an excess and as a stoichiometric reagent. The result seems to be about the same in either case, both in methanol and in THF. The resulting material is brown/purple and is initially soluble in THF and CH_2Cl_2, but seems to lose solubility rapidly. Due to poor solubility, most efforts up to this point have focused on crystallization, but have thus far not led to crystals of X-ray quality. In the future, one might consider carrying out the reaction in very dry THF, and under very dilute conditions to help prevent unwanted oligomerization.

Several attempts have been made to go straight to the reduced version of the drone complex, retaining one Cl per Pd atom in analogy to several literature complexes,[114a,115] by using a mixture of Pd_2dba_3 and $PdCl_2(C_6H_5CN)_2$. Unfortunately, although there is strong indication that this route would be viable,[112] a mixture of many unidentified products results. This might be prevented by using a much larger volume of solvent, and adding a dilute solution of the tripod complex very slowly to the solution of the palladium precursor. Another, more opportunistic attempt for future experiments might be to add a favorable Cu precursor and a corresponding amount of phosphine directly to **16** to generate mixed complexes with 1:1 ratios of Pd:Cu.

The "shorter" tripodal phosphine ligand $(Ph_2PCH_2)_3CCH_3$ does not form a complex of this sort with palladium, but it is known to produce bidentate complexes with palladium. Several preliminary efforts have been made to form the Pd/Cu bimetallic complex by adding copper to the uncoordinated phosphine group in $Cl_2Pd(Ph_2PCH_2)_2CMe(CH_2PPh_2)$. Although the time did not allow the completion of this project, it is being carried ahead by the next generation of graduate students.

CONCLUSION

Attempts to produce a palladium complex coordinated in a bidentate manner by the tripodal phosphine ligand $(Ph_2PCH_2CH_2)_3SiMe$, in analogy to the bidentate nickel complex $(CO)_2Ni(Ph_2PCH_2)_2CMe(CH_2PPh_2)$ led to a trinuclear palladium "drone" complex incorporating three $PdCl_2$ units *trans*-coordinated by two phosphine ligands. The interesting geometry of this complex suggests applications in the formation and stabilization of palladium nanoparticles with well-defined and small numbers of palladium atoms and several preliminary efforts have been directed towards the reduction of the palladium (II) in the drone complex to palladium(0).

EXPERIMENTAL

$(Cl_2Pd)_3[(PPh_2CH_2)_3CMe]_2$ (16)

$MeSi(CH_2CH_2PPh_2)_3$ (115.6 mg, 0.169 mmol) was dissolved in 30 mL dry toluene and stirred vigorously. A separate solution of $Pd(C_6H_5CN)_2Cl_2$ (98.1 mg, 0.256 mmol) in 15 mL of toluene was prepared. The Pd solution was divided into three

portions and each was added dropwise with a pause of 30 minutes between the first two aliquots and 90 minutes between the second and third portions. The resulting solution was stirred overnight and then the volatile components were removed in vacuum. The resulting solid was triturated in 50 mL of dry pentane and then stirred for 30 minutes. After allowing the solid to settle, the supernatant was collected and discarded. The solid was suspended in 40 mL of dry dichloromethane and insoluble components were allowed to settle at room temperature under N_2 for 3 days. Then the supernatant was collected and the solvent was removed in vacuum to yield the pure product (139.0 mg, 0.073 mmol) in 86% yield with respect to Pd.

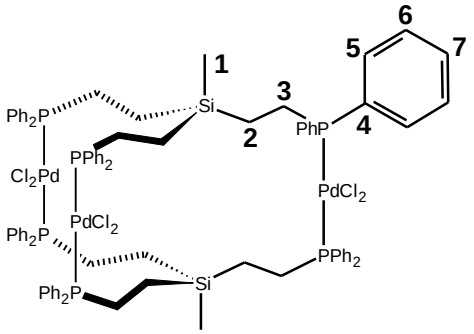

Figure 7.3 Numbering of nuclei for the NMR signal assignment of $(PdCl_2)_3[(PPh_2CH_2CH_2)_3SiMe]_2$ **(16)**.

For the signal assignment see the numbering in Figure 7.3. $^{1}H\{^{1}H\}$ NMR (499.69 MHz, C_6D_6) δ = 8.02-7.99 (m, 24H, H6), 7.04 (d, 12H, $^{3}J(^{1}H\text{-}^{1}H)$ = 1.96 Hz, H7), 7.03 (d, 24H, $^{3}J(^{1}H\text{-}^{1}H)$ = 1.86 Hz, H5), 2.74-2.69 (m, 12H, H3), 1.33-1.28 (m, 12H, H2), -0.62 (s, 6H, H1). $^{31}P\{^{1}H\}$ NMR (202.28 MHz, C_6D_6) δ = 21.34. ^{13}C NMR$\{^{1}H\}$ (125.66 MHz, C_6D_6)

δ = -6.64 (s, C1), 7.55 (s, C2), 20.42 (vt, 12.64 Hz, C3), 131.15 (vt, 21.94 Hz, C4), 130.24 (s, C5), 134.40 (vt, 5.77 Hz, C6), 128.44 (s, C7). mp (decomp.) 175.0 °C.

CHAPTER VIII

SUMMARY

A series of new nickel complexes with tridentate phosphine ligands has been synthesized and characterized in solution and in the solid state. These complexes have also been evaluated with respect to their activity in the cyclotrimerization of acetylene and the most promising candidate for immobilization and further studies (**7**) has been identified and preliminary efforts towards immobilization and evaluation of the catalytic activity have been performed.

A bidentate nickel phosphine complex which possesses an uncoordinated phosphine "arm" has also been synthesized and characterized and it has been shown that heterobimetallic complexes with Ni and Au can be synthesized in high yield and purity. Although this complex is not an active catalyst in cyclotrimerization reactions, it may have an important role in other areas, such as in the synthesis of bimetallic nanoparticles, or in the catalysis of a different chemical reaction.

Efforts to extend the success with the bimetallic Ni/Au complex to Pd/Cu have been started and have resulted in an unexpected $(Cl_2Pd)_3Tripod_2$ complex (**16**). The synthesis of this complex has been optimized and the NMR and X-ray single crystal characterization data have been obtained. Preliminary efforts towards reducing the Pd(II) metals to Pd(I) or Pd(0) have been undertaken, but have not yet yielded analytically favorable results.

The adsorption of metallocenes and other molecules on silica gel has been accomplished from the dry state, by simply grinding the components together with a

mortar and pestle. The high level of mobility of the organometallic and organic adsorbates has been proven using solid-state NMR methods which show that the correlation time of ferrocene on silica is less than 1 ns which is similar to a small protein in solution. This high mobility has been exploited to measure the ^{13}C and ^{1}H NMR spectra of adsorbed ferrocene using only a standard liquids NMR instrument. This mobility allows for adsorption from the solid state, and has exciting implications in many areas including solid-state separations, manufacture of catalysts, solvent-free reactions on surfaces and in the NMR characterization of adsorbed species.

Additional experiments have been conducted using large (~ 0.5 cm) pieces of silica gel, which has permitted the adsorption and translational mobility of several metallocenes as well as a half sandwich, cymantrene, to be observed and monitored visually. These experiments also prove that the heat and pressure generated by grinding is not necessary for the solvent-free adsorption.

Several competition studies have also been conducted in which it has been proven by using both deuterated and non-deuterated ferrocene that polycrystalline and adsorbed ferrocene are in equilibrium on the surface, and that there are likely tiny polycrystalline deposits of ferrocene that form within the pores of the silica gel. Competition studies between deuterated ferrocene and cymantrene have shown that ferrocene adsorbs more strongly than cymantrene to the degree that it is able to displace the half sandwich from the surface, and no observable equilibrium is established. This experiment has also been conducted on a visible scale using large silica gel pieces and it has been observed that tiny crystallites of cymantrene form on the outside of a

cymantrene-saturated piece of silica gel when ferrocene begins to adsorb and displace the cymantrene.

The adsorption and mobility of ferrocene has also been explored on several carbon-based supports including activated carbon, multi walled carbon nanotubes and single walled carbon nanotubes. The solid-state NMR results clearly show that the mobility on these carbon supports is very similar to that on silica gel. Various variable temperature NMR experiments have shown that the mobility is already high enough at room temperature that an increase in temperature does not result in a big reduction in linewidth. Cooling of the sample, however, does result in broader lines due to decreased kinetic energy of the adsorbed molecules.

Desorption experiments have been carried out which show that ferrocene is less volatile when adsorbed on a surface, than it is as a well-ground powder. Furthermore, the adsorption is strongest on activated carbon, and weakest on silica gel. This information is important because it helps with choosing the ideal support for each application. For example, when eventual desorption is desired, as in separations, then silica gel is likely the best candidate because desorption can be accomplished at lower temperatures. Activated carbon, on the other hand, is superior for applications where it is necessary for the adsorbate to remain adsorbed even at elevated temperatures.

These adsorption experiments have culminated in the synthesis of a nickel catalyst via the adsorption and subsequent thermal decomposition and simultaneous reduction of nickelocene with H_2 on silica gel. Investigations will continue in this area, but preliminary results confirm that this material is active in the cyclotrimerization of

phenylacetylene. Excitingly, the lack of observable nickel nanoparticles via TEM may indicate the formation of extremely small nanoparticles or even single atom catalysts on the surface.

REFERENCES

(1) (a) Barbaro, P.; Liguori, F. *Heterogenized Homogeneous Catalysts for Fine Chemical Production*. Springer Netherlands: 2010; Vol. 33; (b) Blümel, J. *Coord. Chem. Rev.* **2008**, *252*, 2410-2423; (c) De Vos, D. E.; Vankelecom, I. F. J.; Jacobs, P. A.; Editors. *Chiral Catalyst Immobilization and Recycling*. Wiley-VCH Verlag GmbH: 2000; p 320 pp; (d) Rothenberg, G. *Catalysis: Concepts and Green Applications*. Wiley-VCH Verlag GmbH Co. KGaA: 2008; p 279 pp.

(2) (a) Silbernagel, R.; Diaz, A.; Steffensmeier, E.; Clearfield, A.; Blümel, J. *J. Mol. Catal. A: Chem.* **2014**, *394*, 217-223; (b) Guenther, J.; Reibenspies, J.; Blümel, J. *Adv. Synth. Catal.* **2011**, *353*, 443-460; (c) Beele, B.; Guenther, J.; Perera, M.; Stach, M.; Oeser, T.; Blümel, J. *New J. Chem.* **2010**, *34*, 2729-2731; (d) Yang, Y.; Beele, B.; Blümel, J. *J. Am. Chem. Soc.* **2008**, *130*, 3771-3773; (e) Merckle, C.; Blümel, J. *Top. Catal.* **2005**, *34*, 5-15; (f) Merckle, C.; Blümel, J. *Adv. Synth. Catal.* **2003**, *345*, 584-588.

(3) (a) Pope, J. C.; Posset, T.; Bhuvanesh, N.; Blümel, J. *Organometallics* **2014**, *33*, 6750-6753; (b) Posset, T.; Guenther, J.; Pope, J.; Oeser, T.; Blümel, J. *Chem. Commun. (Cambridge, U. K.)* **2011**, *47*, 2059-2061; (c) Posset, T.; Blümel, J. *J. Am. Chem. Soc.* **2006**, *128*, 8394-8395.

(4) (a) Reinhard, S.; Soba, P.; Rominger, F.; Blümel, J. *Adv. Synth. Catal.* **2003**, *345*, 589-602; (b) Reinhard, S.; Behringer, K. D.; Blümel, J. *New J. Chem.* **2003**, *27*, 776-778; (c) Behringer, K. D.; Blümel, J. *Chem. Commun.* **1996**, 653-4.

(5) (a) Biel, M. C.; Kessinger, R.; Sommer, J.; Blümel, J. Improved process for production of alkenylphosphonic acid derivatives by addition of hydrophosphonate diesters to alkynes in the presence of nickel catalyst and a base. WO2008113777A1, 2008; (b) Kumar, P.; Louie, J. Nickel-Mediated [2 + 2 + 2] Cycloaddition. In *Transition-Metal-Mediated Aromatic Ring Construction*, John Wiley & Sons, Inc.: 2013; pp 37-70.

(6) (a) Reinhard, S.; Soba, P.; Rominger, F.; Blümel, J. *Adv. Synth. Catal.* **2003**, *345*, 589-602; (b) Reinhard, S.; Behringer, K. D.; Blümel, J. *New J. Chem.* **2003**, *27*, 776-778.

(7) Bogza, M.; Oeser, T.; Blümel, J. *J. Organomet. Chem.* **2005**, *690*, 3383-3389.

(8) (a) Crespo, O.; Gimeno, M. C.; Laguna, A.; Lehtonen, O.; Ospino, I.; Pyykko, P.; Villacampa, M. D. *Chem. - Eur. J.* **2014**, *20*, 3120-3127; (b) Igawa, K.; Yoshinari, N.; Konno, T. *Chem. Commun.* **2014**, *50*, 15573-15576; (c) Lach, J.; Jeremies, A.;

Breite, D.; Abel, B.; Mahns, B.; Knupfer, M.; Matulis, V.; Ivashkevich, O. A.; Kersting, B. *Inorg. Chem.* **2014**, *53*, 10825-10834; (d) Barker, G. K.; Godfrey, N. R.; Green, M.; Parge, H. E.; Stone, F. G. A.; Welch, A. J. *J. Chem. Soc., Chem. Commun.* **1983**, 277-9; (e) Teo, B. K.; Zhang, H.; Shi, X. *Inorg. Chem.* **1994**, *33*, 4086-97; (f) Colacio, E.; Lloret, F.; Kivekaes, R.; Suarez-Varela, J.; Sundberg, M. R.; Uggla, R. *Inorg. Chem.* **2003**, *42*, 560-565; (g) Vitoria, P.; Muga, I.; Gutierrez-Zorrilla, J. M.; Luque, A.; Roman, P.; Lezama, L.; Zuniga, F. J.; Beitia, J. I. *Inorg. Chem.* **2003**, *42*, 960-969; (h) Konno, T.; Usami, M.; Toyota, A.; Hirotsu, M.; Kawamoto, T. *Chem. Lett.* **2005**, *34*, 1146-1147; (i) Zhou, H.-B.; Dong, W.; Liu, Z.-Q.; Liao, D.-Z.; Jiang, Z.-H.; Yan, S.-P.; Cheng, P. *Inorg. Chim. Acta* **2005**, *358*, 3287-3292; (j) Xia, B.-H.; Zhang, H.-X.; Che, C.-M.; Leung, K.-H.; Phillips, D. L.; Zhu, N.; Zhou, Z.-Y. *J. Am. Chem. Soc.* **2003**, *125*, 10362-10374; (k) Byabartta, P. *Transition Met. Chem.* **2007**, *32*, 576-583; (l) Taguchi, M.; Igashira-Kamiyama, A.; Kajiwara, T.; Konno, T. *Angew. Chem., Int. Ed.* **2007**, *46*, 2422-2425; (m) Sameshima, Y.; Yoshinari, N.; Tsuge, K.; Igashira-Kamiyama, A.; Konno, T. *Angew. Chem., Int. Ed.* **2009**, *48*, 8469-8472, S8469/1-S8469/11; (n) Hashimoto, Y.; Taguchi, M.; Yoshinari, N.; Konno, T. *Acta Crystallogr., Sect. C: Cryst. Struct. Commun.* **2010**, *66*, m160-m162; (o) Hashimoto, Y.; Tsuge, K.; Konno, T. *Chem. Lett.* **2010**, *39*, 601-603; (p) Ciabatti, I.; Femoni, C.; Iapalucci, M. C.; Longoni, G.; Zacchini, S.; Fedi, S.; Fabrizi de Biani, F. *Inorg. Chem.* **2012**, *51*, 11753-11761; (q) Igashira-Kamiyama, A.; Matsushita, N.; Lee, R.; Tsuge, K.; Konno, T. *Bull. Chem. Soc. Jpn.* **2012**, *85*, 706-708; (r) Ciabatti, I.; Femoni, C.; Iapalucci, M. C.; Ienco, A.; Longoni, G.; Manca, G.; Zacchini, S. *Inorg. Chem.* **2013**, *52*, 10559-10565; (s) Golecki, M.; Lach, J.; Jeremies, A.; Lungwitz, F.; Fronk, M.; Salvan, G.; Zahn, D. R. T.; Park, J.; Krupskaya, Y.; Kataev, V.; Klingeler, R.; Buechner, B.; Mahns, B.; Knupfer, M.; Siles, P. F.; Grimm, D.; Schmidt, O. G.; Reis, A.; Thiel, W. R.; Breite, D.; Abel, B.; Kersting, B. *Chem. - Eur. J.* **2013**, *19*, 7787-7801; (t) Pinder, T. A.; Montalvo, S. K.; Lunsford, A. M.; Hsieh, C.-H.; Reibenspies, J. H.; Darensbourg, M. Y. *Dalton Trans.* **2014**, *43*, 138-144.

(9) (a) Chaplin, A. B.; Beni, Z.; Hartinger, C. G.; Ben Hamidane, H.; Phillips, A. D.; Scopelliti, R.; Dyson, P. J. *J. Cluster Sci.* **2008**, *19*, 295-309; (b) Fernandez-Anca, D.; Garcia-Seijo, M. I.; Castineiras, A.; Garcia-Fernandez, M. E. *Inorg. Chem.* **2008**, *47*, 5685-5695; (c) Fernandez-Anca, D.; Garcia-Seijo, M. I.; Garcia-Fernandez, M. E. *Dalton Trans.* **2010**, *39*, 2327-2336; (d) Miller, P. W.; White, A. J. P. *J. Organomet. Chem.* **2010**, *695*, 1138-1145.

(10) (a) Claridge, S. A.; Castleman, A. W., Jr.; Khanna, S. N.; Murray, C. B.; Sen, A.; Weiss, P. S. *ACS Nano* **2009**, *3*, 244-255; (b) Wang, D.; Li, Y. *Adv. Mater.* **2011**, *23*, 1044-1060; (c) Ferrando, R.; Jellinek, J.; Johnston, R. L. *Chem. Rev.* **2008**, *108*, 845-910; (d) Jin, R. *Nanoscale* **2015**, *7*, 1549-1565; (e) Barcaro, G.; Sementa, L.; Fortunelli, A.; Stener, M. *Physical chemistry chemical physics : PCCP* **2015**, *17*, 27952-67.

(11) (a) Fyfe, C. A. *Solid State NMR for Chemists*. C.F.C. Press: 1983; (b) Duncan, T. M. *A Compilation of Chemical Shift Anisotropies*. Farragut Press: Chicago, IL, 1990.

(12) Lu, W.; Yuan, D.; Zhao, D.; Schilling, C. I.; Plietzsch, O.; Muller, T.; Brase, S.; Guenther, J.; Blümel, J.; Krishna, R.; Li, Z.; Zhou, H.-C. *Chem. Mater.* **2010**, *22*, 5964-5972.

(13) (a) Pope, J. C.; Sue, H.-J.; Bremner, T.; Blümel, J. *J. Appl. Polym. Sci.* **2015**, *132*, 41421/1-41421/3; (b) Pope, J. C.; Sue, H.-J.; Bremner, T.; Blümel, J. *Polymer* **2014**, *55*, 4577-4585; (c) Guenther, J.; Wong, M.; Sue, H.-J.; Bremner, T.; Blümel, J. *J. Appl. Polym. Sci.* **2013**, *128*, 4395-4404.

(14) (a) Chierotti, M. R.; Gobetto, R. *Eur. J. Inorg. Chem.* **2009**, 2581-2597; (b) Reinhard, S.; Blümel, J. *Magn Reson Chem* **2003**, *41*, 406-416; (c) Eichele, K.; Wasylishen, R. E.; Corrigan, J. F.; Taylor, N. J.; Carty, A. J.; Feindel, K. W.; Bernard, G. M. *J. Am. Chem. Soc.* **2002**, *124*, 1541-1552; (d) Diesveld, J. W.; Menger, E. M.; Edzes, H. T.; Veeman, W. S. *J. Am. Chem. Soc.* **1980**, *102*, 7935-6.

(15) (a) Blümel, J. *Inorg. Chem.* **1994**, *33*, 5050-6; (b) Sommer, J.; Yang, Y.; Rambow, D.; Blümel, J. *Inorg. Chem.* **2004**, *43*, 7561-7563.

(16) Hilliard, C. R.; Bhuvanesh, N.; Gladysz, J. A.; Blümel, J. *Dalton Trans.* **2012**, *41*, 1742-1754.

(17) Massiot, D.; Fayon, F.; Capron, M.; King, I.; Le Calve, S.; Alonso, B.; Durand, J.-O.; Bujoli, B.; Gan, Z.; Hoatson, G. *Magn Reson Chem* **2002**, *40*, 70-76.

(18) (a) Dominguez, G.; Perez-Castells, J. *Chem. Soc. Rev.* **2011**, *40*, 3430-3444; (b) Hua, R.; Abrenica, M. V. A.; Wang, P. *Curr. Org. Chem.* **2011**, *15*, 712-729; (c) Broere, D. L. J.; Ruijter, E. *Synthesis* **2012**, *44*, 2639-2672.

(19) Mautz, J.; Heinze, K.; Wadepohl, H.; Huttner, G. *Eur. J. Inorg. Chem.* **2008**, 1413-1422.

(20) Hilt, G.; Vogler, T.; Hess, W.; Galbiati, F. *Chem. Commun.* **2005**, 1474-1475.

(21) Ozturk, B. O.; Karabulut, S.; Imamoglu, Y. *Appl. Catal., A* **2012**, *433-434*, 214-222.

(22) Anju, V. P.; Roy, D. K.; Anju, R. S.; Ghosh, S. *J. Organomet. Chem.* **2013**, *733*, 79-81.

(23) Matsuura, M.; Fujihara, T.; Kakeya, M.; Sugaya, T.; Nagasawa, A. *J. Organomet. Chem.* **2013**, *745-746*, 288-298.

(24) Xi, C.; Sun, Z.; Liu, Y. *Dalton Trans.* **2013**, *42*, 13327-13330.

(25) Chatt, J.; Hart, F. A. *J. Chem. Soc.* **1965**, 812-13.

(26) (a) Tayebee, R.; Jarrahi, M.; Maleki, B.; Kargar Razi, M.; Mokhtari, Z. B.; Baghbanian, S. M. *RSC Adv.* **2015**, *5*, 10869-10877; (b) Shaaban, M. R.; El-Sayed, R.; Elwahy, A. H. M. *Tetrahedron* **2011**, *67*, 6095-6130.

(27) Ohashi, M.; Shirataki, H.; Kikushima, K.; Ogoshi, S. *J. Am. Chem. Soc.* **2015**, *137*, 6496-6499.

(28) Zhao, J.-P.; Chan, S.-C.; Ho, C.-Y. *Tetrahedron* **2015**, *71*, 4426-4431.

(29) Pal, S.; Uyeda, C. *J. Am. Chem. Soc.* **2015**, *137*, 8042-8045.

(30) Aillard, P.; Retailleau, P.; Voituriez, A.; Marinetti, A. *Chem. Commun. (Cambridge, U. K.)* **2014**, *50*, 2199-2201.

(31) (a) Puenner, F.; Hilt, G. *Chem. Commun.* **2012**, *48*, 3617-3619; (b) Tang, X.; Wang, Z.; Li, Y.; Yan, H. *J. Organomet. Chem.* **2013**, *747*, 90-97; (c) Xu, L.; Yu, R.; Wang, Y.; Chen, J.; Yang, Z. *J. Org. Chem.* **2013**, *78*, 5744-5750; (d) Swami, A.; Ramana, C. V. *Synlett* **2015**, *26*, 604-608; (e) Xie, R.-J.; Han, L.-M.; Zhu, N.; Gao, Y.-Y.; Hong, H.-L.; Suo, Q.-L. *J. Coord. Chem.* **2015**, *68*, 449-460; (f) Gandon, V. Cobalt-Mediated [2 + 2 + 2] Cycloaddition. In *Transition-Metal-Mediated Aromatic Ring Construction*, John Wiley & Sons, Inc.: 2013; pp 1-35.

(32) (a) Mallagaray, A.; Mohammadiannejad-Abbasabadi, K.; Medina, S.; Dominguez, G.; Perez-Castells, J. *Org. Biomol. Chem.* **2012**, *10*, 6665-6672; (b) Medina, S.; Dominguez, G.; Perez-Castells, J. *Org. Lett.* **2012**, *14*, 4982-4985; (c) Melnes, S.; Bayer, A.; Gautun, O. R. *Tetrahedron* **2012**, *68*, 8463-8471; (d) Foster, R. W.; Tame, C. J.; Hailes, H. C.; Sheppard, T. D. *Adv. Synth. Catal.* **2013**, *355*, 2353-2360; (e) Perekalin, D. S.; Karslyan, E. E.; Trifonova, E. A.; Konovalov, A. I.; Loskutova, N. L.; Nelyubina, Y. V.; Kudinov, A. R. *Eur. J. Inorg. Chem.* **2013**, *2013*, 481-493; (f) Zotova, M. A.; Vorobyeva, D. V.; Dixneuf, P. H.; Bruneau, C.; Osipov, S. N. *Synlett* **2013**, *24*, 1517-1522; (g) Alvarez, S.; Medina, S.; Dominguez, G.; Perez-Castells, J. *J. Org. Chem.* **2015**, *80*, 2436-2442; (h) Yamamoto, Y. Ruthenium-Mediated [2 + 2 + 2] Cycloaddition. In *Transition-Metal-Mediated Aromatic Ring Construction*, John Wiley & Sons, Inc.: 2013; pp 71-125.

(33) (a) Mitsudo, K.; Harada, J.; Tanaka, Y.; Mandai, H.; Nishioka, C.; Tanaka, H.; Wakamiya, A.; Murata, Y.; Suga, S. *J. Org. Chem.* **2013**, *78*, 2763-2768; (b) Hara, J.; Ishida, M.; Kobayashi, M.; Noguchi, K.; Tanaka, K. *Angew. Chem., Int. Ed.* **2014**, *53*, 2956-2959; (c) Nairoukh, Z.; Fanun, M.; Schwarze, M.; Schomacker, R.; Blum, J. *J. Mol. Catal. A: Chem.* **2014**, *382*, 93-98; (d) Shibata, Y.; Tanaka, K. *Synthesis* **2012**, *44*, 323-350.

(34) (a) Leibeling, M.; Werz, D. B. *Chem. - Eur. J.* **2012**, *18*, 6138-6141, S6138/1-S6138/43; (b) Takeuchi, R. Iridium-Mediated [2 + 2 + 2] Cycloaddition. In *Transition-Metal-Mediated Aromatic Ring Construction*, John Wiley & Sons, Inc.: 2013; pp 161-181.

(35) Leyva-Perez, A.; Oliver-Meseguer, J.; Cabrero-Antonino, J. R.; Rubio-Marques, P.; Serna, P.; Al-Resayes, S. I.; Corma, A. *ACS Catal.* **2013**, *3*, 1865-1873.

(36) Satoh, Y.; Obora, Y. *J. Org. Chem.* **2013**, *78*, 7771-7776.

(37) Czelusniak, I.; Kociecka, P.; Szymanska-Buzar, T. *J. Organomet. Chem.* **2012**, *716*, 70-78.

(38) Riache, N.; Dery, A.; Callens, E.; Poater, A.; Samantaray, M.; Dey, R.; Hong, J.; Li, K.; Cavallo, L.; Basset, J.-M. *Organometallics* **2015**, *34*, 690-695.

(39) Frazier, B. A.; Williams, V. A.; Wolczanski, P. T.; Bart, S. C.; Meyer, K.; Cundari, T. R.; Lobkovsky, E. B. *Inorg. Chem.* **2013**, *52*, 3295-3312.

(40) Amatore, M.; Aubert, C. *Eur. J. Org. Chem.* **2015**, *2015*, 265-286.

(41) Huebner, S.; de Vries, J. G.; Farina, V. *Adv. Synth. Catal.* **2016**, *358*, 3-25.

(42) (a) Guenther, J.; Reibenspies, J.; Blümel, J. *Adv. Synth. Catal.* **2011**, *353*, 443-460; (b) Beele, B.; Guenther, J.; Perera, M.; Stach, M.; Oeser, T.; Blümel, J. *New J. Chem.* **2010**, *34*, 2729.

(43) Zhdanov, V. P.; Larsson, E. M.; Langhammer, C. *Chemical Physics Letters* **2012**, *533*, 65-69.

(44) (a) Crabtree, R. H. *Chem. Rev.* **2012**, *112*, 1536-1554; (b) Bayram, E.; Finke, R. G. *ACS Catal.* **2012**, *2*, 1967-1975.

(45) (a) Dimitratos, N.; Villa, A.; Prati, L.; Hammond, C.; Chan-Thaw, C. E.; Cookson, J.; Bishop, P. T. *Appl. Catal., A* **2016**, *514*, 267-275; (b) Yanson, A. I.; Antonov, P. V.; Yanson, Y. I.; Koper, M. T. M. *Electrochim. Acta* **2013**, *110*, 796-800; (c)

Tang, L.; Ye, Y.; Zhang, H.; Liao, C.; Zong, S.; Cui, Y.; Zhang, J. *NANO* **2014**, *9*, 1450005/1-1450005/7.

(46) Osborn, J. A.; Jardine, F. H.; Young, J. F.; Wilkinson, G. *J.Chem. Soc. A* **1966**, 1711-1732.

(47) Kiefer, S.; Robens, E. *J. Therm. Anal. Calorim.* **2008**, *94*, 613-618.

(48) Williams, K. R. *J. Chem. Educ.* **2002**, *79*, 922-923.

(49) Sah, R. P.; Choudhury, B.; Das, R. K. *Renewable Sustainable Energy Rev.* **2015**, *45*, 123-134.

(50) (a) Mondloch, J. E.; Katz, M. J.; Isley, W. C., III; Ghosh, P.; Liao, P.; Bury, W.; Wagner, G. W.; Hall, M. G.; De Coste, J. B.; Peterson, G. W.; Snurr, R. Q.; Cramer, C. J.; Hupp, J. T.; Farha, O. K. *Nat. Mater.* **2015**, *14*, 512-516; (b) Davis, E. D.; Gordon, W. O.; Wilmsmeyer, A. R.; Troya, D.; Morris, J. R. *J. Phys. Chem. Lett.* **2014**, *5*, 1393-1399; (c) Wilmsmeyer, A. R.; Gordon, W. O.; Davis, E. D.; Troya, D.; Mantooth, B. A.; Lalain, T. A.; Morris, J. R. *J. Phys. Chem. C* **2013**, *117*, 15685-15697.

(51) (a) Akhtar, J.; Amin, N. A. S.; Shahzad, K. *Desalin. Water Treat.* **2015**, *57*, 12842-12860; (b) Ali, I. *Sep. Purif. Rev.* **2014**, *43*, 175-205.

(52) (a) Choi, S.; Drese, J. H.; Jones, C. W. *ChemSusChem* **2009**, *2*, 796-854; (b) Li, J.-R.; Kuppler, R. J.; Zhou, H.-C. *Chem. Soc. Rev.* **2009**, *38*, 1477-1504; (c) Gil, M. V.; Alvarez-Gutierrez, N.; Martinez, M.; Rubiera, F.; Pevida, C.; Moran, A. *Chem. Eng. J.* **2015**, *269*, 148-158.

(53) Zaera, F. *Acc. Chem. Res.* **2002**, *35*, 129-136.

(54) (a) Rebenstorf, B.; Panda, C. *J. Mol. Catal.* **1991**, *65*, 173-80; (b) Schnellbach, M.; Koehler, F. H.; Blümel, J. *J. Organomet. Chem.* **1996**, *520*, 227-230.

(55) (a) Duer, M. J. *Introduction to Solid-State NMR Spectroscopy*. Blackwell: 2004; p 320 pp; (b) *J. Magn. Reson., Ser. A* **1996**, *121*, 92-93.

(56) (a) Ebener, M.; Von Fircks, G.; Guenther, H. *Helv. Chim. Acta* **1991**, *74*, 1296-304; (b) Gunther, H.; Oepen, S.; Ebener, M.; Francke, V. *Magn Reson Chem* **1999**, *37*, S142-S146.

(57) (a) Baltusis, L.; Frye, J. S.; Maciel, G. E. *J. Am. Chem. Soc.* **1986**, *108*, 7119-20; (b) Chen, W.-H.; Bauer, F.; Bilz, E.; Freyer, A.; Huang, S.-J.; Lai, C.-S.; Liu, S.-B. *Stud. Surf. Sci. Catal.* **2004**, *154C*, 2269-2274; (c) Grigoriev, D. O.; Senkel, O.;

Kretzschmar, G.; Li, J. B.; Noskov, B. A.; Miller, R. *Colloids Surf., A* **1999**, *149*, 81-88.

(58) (a) Sheng, T.; Gay, I. D. *J. Catal.* **1994**, *145*, 10-15; (b) Baltusis, L.; Frye, J. S.; Maciel, G. E. *J. Am. Chem. Soc.* **1987**, *109*, 40-6; (c) Peng, L.; Chupas, P. J.; Grey, C. P. *J. Am. Chem. Soc.* **2004**, *126*, 12254-12255; (d) Gay, I. D.; Hu, B.; Sheng, T.-C. *Langmuir* **1999**, *15*, 6132-6134; (e) Yang, Y. Phosphines and Their Metal complexes, Adsorbed and bound by Ionic Interactions on Oxide Supports: A solid-State NMR Study. Doctoral Dissertation, University of Heidelberg, Germany, 2007.

(59) Hilliard, C. R.; Kharel, S.; Cluff, K. J.; Bhuvanesh, N.; Gladysz, J. A.; Blümel, J. *Chem. - Eur. J.* **2014**, *20*, 17292-17295.

(60) Blümel, J. *J. Am. Chem. Soc.* **1995**, *117*, 2112-13.

(61) Fyfe, C. A.; Brouwer, D. H. *Can. J. Chem.* **2006**, *84*, 345-355.

(62) Minakata, S.; Tsuruoka, R.; Komatsu, M. *J. Am. Chem. Soc.* **2008**, *130*, 1536-1537.

(63) (a) Fyfe, C. A.; Lee, J. S. J. *J. Phys. Chem. C* **2008**, *112*, 500-513; (b) Ebener, M.; Von, F. G.; Guenther, H. *Helv. Chim. Acta* **1991**, *74*, 1296-1304; (c) Bjarneson, D. W.; Petersen, N. O. *Langmuir* **1991**, *7*, 2821-6; (d) Lechert, H.; Basler, W. D. *J. Phys. Chem. Solids* **1989**, *50*, 497-521.

(64) Osiecki, J. H.; Hoffman, C. J.; Hollis, D. P. *J. Organomet. Chem.* **1965**, *3*, 107-12.

(65) Sato, H. *Hyperfine Interact.* **1990**, *57*, 2089-94.

(66) Mercier, A.; Yeo, W. C.; Chou, J.; Chaudhuri, P. D.; Bernardinelli, G.; Kundig, E. P. *Chem. Commun.* **2009**, 5227-5229.

(67) Ruzicka, L.; Stoll, M.; Huyser, H. W.; Boekenoogen, H. A. *Helv. Chim. Acta* **1930**, *13*, 1152-85.

(68) Cluff, K. J.; Schnellbach, M.; Hilliard, C. R.; Blümel, J. *J. Organomet. Chem.* **2013**, *744*, 119-124.

(69) Hilliard, C. R.; Yang, Y.; Blümel, J. Adsorption and Mobilities of Phosphines and Phosphine Oxides on Silica.

(70) Blümel, J.; Herker, M.; Hiller, W.; Koehler, F. H. *Organometallics* **1996**, *15*, 3474-3476.

(71) Merckle, C.; Blümel, J. *Chem. Mater.* **2001**, *13*, 3617-3623.

(72) (a) Shannon, I. J.; Harris, K. D. M.; Arumugam, S. *Chem. Phys. Lett.* **1992**, *196*, 588-94; (b) Kitchin, S. J.; Harris, K. D. M.; Aliev, A. E.; Apperley, D. C. *Chem. Phys. Lett.* **2000**, *323*, 490-497.

(73) Marro, M. A. T.; Thomas, J. K. *J. Photochem. Photobiol., A* **1993**, *72*, 251-9.

(74) Shirley, W. M.; McGarvey, B. R.; Maiti, B.; Brenner, A.; Cichowlas, A. *J. Mol. Catal.* **1985**, *29*, 259-67.

(75) Kudinov, A. R.; Petrovskii, P. V.; Struchkov, Y. T.; Yanovskii, A. I.; Rybinskaya, M. I. *J. Organomet. Chem.* **1991**, *421*, 91-115.

(76) Webb, N. C.; Marsh, R. E. *Acta Crystallogr.* **1967**, *22*, 382-7.

(77) Drotloff, H.; Koegler, G.; Oelfin, D.; Moeller, M. *Conformationally disordered mesomorphic phases of cyclododecane and cyclotetradecane*. Elsevier: 1988; p 154-8.

(78) Zheng, Q.; Cai, Z.; Gong, S. *J. Mater. Chem. A* **2014**, *2*, 3110-3118.

(79) Xiong, J.; Lock, H.; Chuang, I. S.; Keeler, C.; Maciel, G. E. *Environ. Sci. Technol.* **1999**, *33*, 2224-2233.

(80) (a) Hepp, M. A.; Ramamurthy, V.; Corbin, D. R.; Dybowski, C. *J. Phys. Chem.* **1992**, *96*, 2629-32; (b) Fyfe, C. A.; Diaz, A. C.; Grondey, H.; Lewis, A. R.; Foerster, H. *J. Am. Chem. Soc.* **2005**, *127*, 7543-7558; (c) Gould, S. L.; Tranchemontagne, D.; Yaghi, O. M.; Garcia-Garibay, M. A. *J. Am. Chem. Soc.* **2008**, *130*, 3246-3247; (d) Nambiar, R. R.; Blum, F. D. *Macromolecules* **2009**, *42*, 8998-9007; (e) Metin, B.; Blum, F. D. *Langmuir* **2010**, *26*, 5226-5231; (f) Hetayothin, B.; Cabaniss, R. A.; Blum, F. D. *Macromolecules* **2012**, *45*, 9128-9138.

(81) Bishop, J. J.; Davison, A.; Katcher, M. L.; Lichtenberg, D. W.; Merrill, R. E.; Smart, J. C. *J. Organomet. Chem.* **1971**, *27*, 241-9.

(82) Ackerman, J. L.; Eckman, R.; Pines, A. *Chem. Phys.* **1979**, *42*, 423-8.

(83) Seiler, P.; Dunitz, J. D. *Acta Crystallogr., Sect. B* **1982**, *B38*, 1741-5.

(84) *ACD/NMR Processor*, 12.01; Advanced Chemistry Development, Inc.: Toronto, ON, Canada, 2010.

(85) Rebiere, F.; Samuel, O.; Kagan, H. B. *Tetrahedron Lett.* **1990**, *31*, 3121-3124.

(86) Cluff, K. J.; Bhuvanesh, N.; Blümel, J. *Organometallics* **2014**, *33*, 2671-2680.

(87) Berndt, A. F.; Marsh, R. E. *Acta Crystallogr.* **1963**, *16*, 119-24.

(88) Walter, T. H.; Thompson, A.; Keniry, M.; Shinoda, S.; Brown, T. L.; Gutowsky, H. S.; Oldfield, E. *J. Am. Chem. Soc.* **1988**, *110*, 1065-8.

(89) Hanson, B. E.; Wagner, G. W.; Davis, R. J.; Motell, E. *Inorg. Chem.* **1984**, *23*, 1635-6.

(90) Hornbaker, D. J.; Kahng, S. J.; Misra, S.; Smith, B. W.; Johnson, A. T.; Mele, E. J.; Luzzi, D. E.; Yazdani, A. *Science* **2002**, *295*, 828-831.

(91) (a) Li, Y.; Du, Q.; Liu, T.; Peng, X.; Wang, J.; Sun, J.; Wang, Y.; Wu, S.; Wang, Z.; Xia, Y.; Xia, L. *Chem. Eng. Res. Des.* **2013**, *91*, 361-368; (b) Gupta, V. K.; Saleh, T. A. *Environ. Sci. Pollut. Res.* **2013**, *20*, 2828-2843; (c) Zhao, J.; Ren, W.; Cheng, H.-M. *J. Mater. Chem.* **2012**, *22*, 20197-20202; (d) Liu, T.; Li, Y.; Du, Q.; Sun, J.; Jiao, Y.; Yang, G.; Wang, Z.; Xia, Y.; Zhang, W.; Wang, K.; Zhu, H.; Wu, D. *Colloids Surf., B* **2012**, *90*, 197-203; (e) Zhao, G.; Li, J.; Ren, X.; Chen, C.; Wang, X. *Environ. Sci. Technol.* **2011**, *45*, 10454-10462; (f) Yang, S.-T.; Chen, S.; Chang, Y.; Cao, A.; Liu, Y.; Wang, H. *J. Colloid Interface Sci.* **2011**, *359*, 24-29; (g) Ren, X.; Chen, C.; Nagatsu, M.; Wang, X. *Chem. Eng. J. (Amsterdam, Neth.)* **2011**, *170*, 395-410; (h) Yang, K.; Xing, B. *Chem. Rev. (Washington, DC, U. S.)* **2010**, *110*, 5989-6008.

(92) Cazetta, A. L.; Pezoti, O.; Bedin, K. C.; Silva, T. L.; Junior, A. P.; Asefa, T.; Almeida, V. C. *ACS Sustainable Chem. Eng.* **2016**, *4*, 1058-1068.

(93) (a) Dubinin, M. M.; Vartapetyan, R. S.; Voloshchuk, A. M.; Kaerger, J.; Pfeifer, H. *Carbon* **1988**, *26*, 515-20; (b) Heinen, A. W.; Peters, J. A.; van Bekkum, H. *Appl. Catal., A* **2000**, *194-195*, 193-202; (c) Omichi, H.; Ueda, T.; Eguchi, T. *Adsorption* **2015**, *21*, 273-282.

(94) Park, J.; Hung, I.; Gan, Z.; Rojas, O. J.; Lim, K. H.; Park, S. *Bioresour. Technol.* **2013**, *149*, 383-389.

(95) Tofighy, M. A.; Mohammadi, T. *J. Hazard. Mater.* **2011**, *185*, 140-147.

(96) (a) Ghaedi, M.; Hassanzadeh, A.; Kokhdan, S. N. *J. Chem. Eng. Data* **2011**, *56*, 2511-2520; (b) Yao, Y.-J.; Xu, F.-F.; Chen, M.; Xu, Z.-X.; Zhu, Z.-W. *Bioresour. Technol.* **2010**, *101*, 3040-3046.

(97) (a) Gupta, V. K.; Agarwal, S.; Saleh, T. A. *Water Res.* **2011**, *45*, 2207-2212; (b) Ai, L.; Zhang, C.; Liao, F.; Wang, Y.; Li, M.; Meng, L.; Jiang, J. *J. Hazard. Mater.* **2011**, *198*, 282-290.

(98) (a) Lee, J.; Kim, H.; Kahng, S. J.; Kim, G.; Son, Y. W.; Ihm, J.; Kato, H.; Wang, Z. W.; Okazaki, T.; Shinohara, H.; Kuk, Y. *Nature* **2002**, *415*, 1005-8; (b) Garcia-Suarez, V. M.; Ferrer, J.; Lambert, C. J. *Phys. Rev. B: Condens. Matter Mater. Phys.* **2006**, *74*, 205421/1-205421/11; (c) Garcia-Suarez, V. M.; Ferrer, J.; Lambert, C. J. *Phys. Rev. Lett.* **2006**, *96*, 106804/1-106804/4; (d) Shiozawa, H.; Pichler, T.; Kramberger, C.; Grueneis, A.; Knupfer, M.; Buechner, B.; Zolyomi, V.; Koltai, J.; Kuerti, J.; Batchelor, D.; Kataura, H. *Los Alamos Nat. Lab. Prepr. Arch., Condens. Matter* **2007**, 1-5, arXiv:0709.1330v1 [cond-mat.mtrl-sci]; (e) Shiozawa, H.; Pichler, T.; Kramberger, C.; Gruneis, A.; Knupfer, M.; Buchner, B.; Zolyomi, V.; Koltai, J.; Kurti, J.; Batchelor, D.; Kataura, H. *Phys. Rev. B: Condens. Matter Mater. Phys.* **2008**, *77*, 153402/1-153402/4; (f) Tsang, S. C.; Chen, Y. K.; Harris, P. J. F.; Green, M. L. H. *Nature* **1994**, *372*, 159-162; (g) Guerret-Piecourt, C.; Le Bouar, Y.; Loiseau, A.; Pascard, H. *Nature* **1994**, *372*, 761-5.

(99) Park, S.; Yoon, S. W.; Lee, K.-B.; Kim, D. J.; Jung, Y. H.; Do, Y.; Paik, H.-j.; Choi, I. S. *Macromol. Rapid Commun.* **2006**, *27*, 47-50.

(100) Stercel, F.; Nemes, N. M.; Fischer, J. E.; Luzzi, D. E. *Mater. Res. Soc. Symp. Proc.* **2002**, *706*, 245-250.

(101) Smith, B. W.; Monthioux, M.; Luzzi, D. E. *Nature* **1998**, *396*, 323-324.

(102) Suenaga, K.; Tence, M.; Mory, C.; Colliex, C.; Kato, H.; Okazaki, T.; Shinohara, H.; Hirahara, K.; Bandow, S.; Iijima, S. *Science* **2000**, *290*, 2280-2.

(103) Li, X.; Guard, L. M.; Jiang, J.; Sakimoto, K.; Huang, J.-S.; Wu, J.; Li, J.; Yu, L.; Pokhrel, R.; Brudvig, G. W.; Ismail-Beigi, S.; Hazari, N.; Taylor, A. D. *Nano Lett.* **2014**, *14*, 3388-3394.

(104) Li, Y.; Hatakeyama, R.; Kaneko, T.; Okada, T. *Jpn. J. Appl. Phys., Part 2* **2006**, *45*, L428-L431.

(105) Britz, D. A.; Khlobystov, A. N. *Chem Soc Rev* **2006**, *35*, 637-59.

(106) Rybak-Akimova, E. V.; Voronina, O. E.; Wikstrom, J. *Metal-containing compounds on carbon nanotubes*. American Scientific Publishers: 2008; Vol. 2.

(107) Kocsis, D.; Kaptas, D.; Botos, A.; Pekker, A.; Kamaras, K. *Phys. Status Solidi B* **2011**, *248*, 2512-2515.

(108) (a) Zheng, D.; Li, H.; Lu, B.; Xu, Z.; Chen, H. *Thin Solid Films* **2008**, *516*, 2151-2157; (b) Wu, J.; Fu, Q.; Lu, B.; Li, H.; Xu, Z. *Thin Solid Films* **2010**, *518*, 3240-3245.

(109) Tasis, D.; Tagmatarchis, N.; Bianco, A.; Prato, M. *Chem. Rev. (Washington, DC, U. S.)* **2006**, *106*, 1105-1136.

(110) Li, L.-J.; Khlobystov, A. N.; Wiltshire, J. G.; Briggs, G. A. D.; Nicholas, R. J. *Nat Mater* **2005**, *4*, 481-5.

(111) Hilliard, C. R.; Kharel, S.; Cluff, K. J.; Bhuvanesh, N.; Gladysz, J. A.; Blümel, J. *Chem. - Eur. J.* **2014**, *20*, 17292-17295.

(112) Murahashi, T.; Kurosawa, H. *Coord. Chem. Rev.* **2002**, *231*, 207-228.

(113) (a) Posset, T.; Blümel, J. *J. Am. Chem. Soc.* **2006**, *128*, 8394-8395; (b) Posset, T.; Guenther, J.; Pope, J.; Oeser, T.; Blümel, J. *Chem. Commun.* **2011**, *47*, 2059-61.

(114) (a) Olmstead, M. M.; Guimerans, R. R.; Farr, J. P.; Balch, A. L. *Inorg. Chim. Acta* **1983**, *75*, 199-208; (b) Aizawa, S.-i.; Kawamoto, T.; Nishigaki, S.; Sasaki, A. *J. Organomet. Chem.* **2011**, *696*, 2471-2476; (c) Stickel, M.; Maichle-Moessmer, C.; Mayer, H. A. *Eur. J. Inorg. Chem.* **2014**, *2014*, 518-525.

(115) (a) Stockland, R. A., Jr.; Anderson, G. K.; Rath, N. P. *Organometallics* **1997**, *16*, 5096-5101; (b) Kirss, R. U. *Inorg. Chem.* **1992**, *31*, 3451-8; (c) Arsenault, G. J.; Puddephatt, R. J. *Can. J. Chem.* **1989**, *67*, 1800-6.

APPENDIX A

CRYSTALLOGRAPHIC DATA FOR STRUCTURES

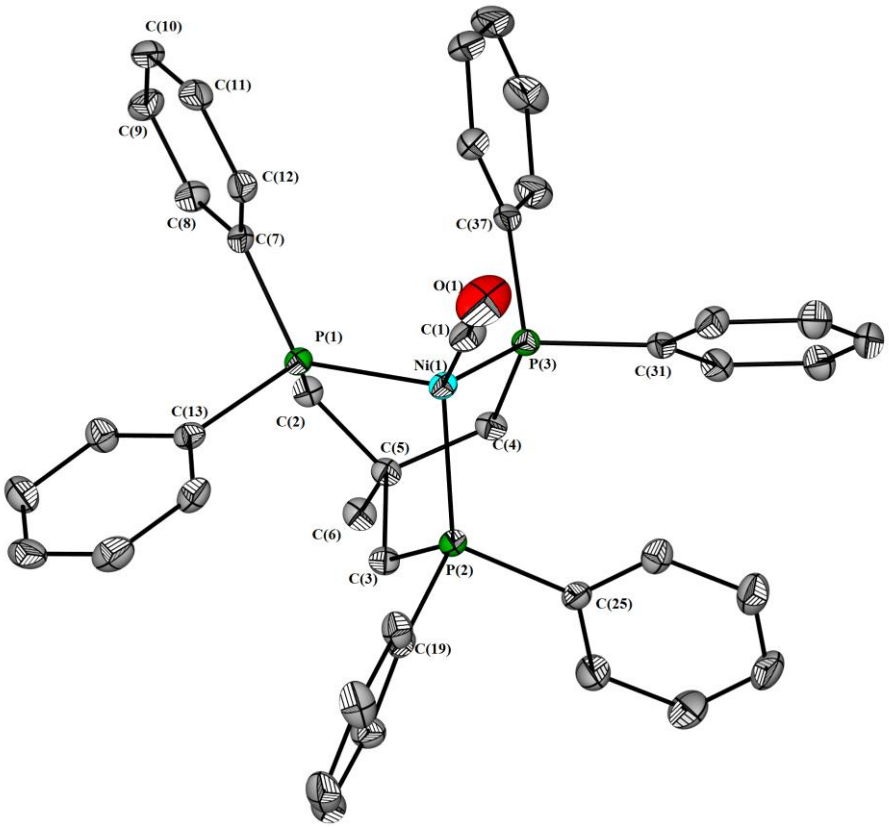

Figure A.1 X-ray structure of (CO)Ni[(PPh_2CH_2)$_3$CMe].

Table A.1 Crystal data and structure refinement for (CO)Ni[(PPh_2CH_2)$_3$CMe].

Identification code	aaa25
Empirical formula	C42 H39 Ni O P3
Formula weight	711.35

Temperature	110(2) K	
Wavelength	0.71073 Å	
Crystal system	Orthorhombic	
Space group	Pna2(1)	
Unit cell dimensions	a = 20.564(5) Å	α= 90°.
	b = 10.117(3) Å	α= 90°.
	c = 16.976(5) Å	γ = 90°.
Volume	3531.7(16) $Å^3$	
Z	4	
Density (calculated)	1.338 Mg/m^3	
Absorption coefficient	0.718 mm^{-1}	
F(000)	1488	
Crystal size	0.60 x 0.50 x 0.20 mm^3	
Theta range for data collection	2.24 to 27.48°.	
Index ranges	-26<=h<=26, -13<=k<=13, -22<=l<=21	
Reflections collected	38188	
Independent reflections	8036 [R(int) = 0.0526]	
Completeness to theta = 27.48°	99.7 %	
Absorption correction	Semi-empirical from equivalents	
Max. and min. transmission	0.8697 and 0.6726	
Refinement method	Full-matrix least-squares on F^2	
Data / restraints / parameters	8036 / 1 / 424	
Goodness-of-fit on F^2	1.027	
Final R indices [I>2sigma(I)]	R1 = 0.0270, wR2 = 0.0657	
R indices (all data)	R1 = 0.0293, wR2 = 0.0669	
Absolute structure parameter	0.007(7)	
Largest diff. peak and hole	0.292 and -0.223 $e.Å^{-3}$	

Table A.2 Atomic coordinates (x 10^4) and equivalent isotropic displacement parameters ($Å^2$ x 10^3) for (CO)Ni[($PPh_2CH_2)_3CMe$]. U(eq) is defined as one third of the trace of the orthogonalized U^{ij} tensor.

x	y	z	U(eq)	
Ni(1)	9345(1)	782(1)	9195(1)	17(1)
P(1)	9028(1)	2690(1)	8737(1)	17(1)
P(2)	9397(1)	-206(1)	8055(1)	17(1)
P(3)	10376(1)	1304(1)	9166(1)	17(1)
C(1)	8971(1)	129(2)	10032(1)	26(1)
C(2)	9652(1)	3316(2)	8048(1)	19(1)
C(3)	9605(1)	1070(2)	7317(1)	19(1)
C(4)	10609(1)	1706(2)	8136(1)	19(1)
C(5)	10043(1)	2218(2)	7616(1)	18(1)
C(6)	10351(1)	2851(2)	6879(1)	22(1)
C(7)	8885(1)	4088(2)	9400(1)	19(1)
C(8)	9078(1)	5380(2)	9247(1)	24(1)
C(9)	8924(1)	6399(2)	9763(1)	27(1)
C(10)	8576(1)	6131(2)	10438(1)	26(1)
C(11)	8379(1)	4847(2)	10601(1)	27(1)
C(12)	8536(1)	3831(2)	10088(1)	23(1)
C(13)	8288(1)	2834(2)	8129(1)	19(1)
C(14)	8143(1)	3980(2)	7708(1)	25(1)
C(15)	7595(1)	4054(2)	7232(1)	30(1)
C(16)	7183(1)	2991(2)	7182(1)	32(1)
C(17)	7313(1)	1856(2)	7606(1)	34(1)
C(18)	7860(1)	1774(2)	8082(1)	26(1)
C(19)	8704(1)	-1038(2)	7581(1)	20(1)
C(20)	8228(1)	-1608(2)	8053(1)	25(1)
C(21)	7695(1)	-2234(2)	7710(2)	34(1)
C(22)	7639(1)	-2292(2)	6901(2)	34(1)
C(23)	8112(1)	-1738(2)	6428(1)	32(1)
C(24)	8643(1)	-1125(2)	6766(1)	26(1)

C(25)	10030(1)	-1478(2)	7908(1)	21(1)
C(26)	10201(1)	-2236(2)	8557(1)	24(1)
C(27)	10662(1)	-3249(2)	8491(2)	33(1)
C(28)	10952(1)	-3486(2)	7776(2)	38(1)
C(29)	10786(1)	-2734(3)	7128(2)	46(1)
C(30)	10328(1)	-1733(2)	7192(1)	36(1)
C(31)	11005(1)	121(2)	9467(1)	19(1)
C(32)	10855(1)	-750(2)	10072(1)	25(1)
C(33)	11315(1)	-1638(2)	10349(1)	30(1)
C(34)	11930(1)	-1673(2)	10020(1)	31(1)
C(35)	12086(1)	-806(2)	9418(1)	28(1)
C(36)	11629(1)	83(2)	9145(1)	25(1)
C(37)	10662(1)	2745(2)	9733(1)	22(1)
C(38)	11251(1)	3379(2)	9592(1)	30(1)
C(39)	11465(1)	4386(2)	10087(1)	40(1)
C(40)	11089(1)	4759(2)	10728(1)	43(1)
C(41)	10506(1)	4144(2)	10870(1)	37(1)
C(42)	10287(1)	3145(2)	10372(1)	28(1)
O(1)	8725(1)	-289(2)	10590(1)	52(1)

Table A.3 Bond Lengths [Å] for (CO)Ni[$(PPh_2CH_2)_3CMe$].

Ni(1)-C(1)	1.744(2)	P(3)-C(31)	1.8360(18)
Ni(1)-P(1)	2.1805(7)	P(3)-C(37)	1.8438(19)
Ni(1)-P(2)	2.1820(7)	P(3)-C(4)	1.8574(19)
Ni(1)-P(3)	2.1855(7)	C(1)-O(1)	1.154(2)
P(1)-C(7)	1.8309(18)	C(2)-C(5)	1.556(2)
P(1)-C(13)	1.8441(19)	C(2)-H(2A)	0.9900
P(1)-C(2)	1.8485(18)	C(2)-H(2B)	0.9900
P(2)-C(19)	1.8389(19)	C(3)-C(5)	1.555(2)
P(2)-C(25)	1.8481(18)	C(3)-H(3A)	0.9900
P(2)-C(3)	1.8490(19)	C(3)-H(3B)	0.9900

C(4)-C(5)	1.550(2)	C(21)-C(22)	1.380(4)
C(4)-H(4A)	0.9900	C(21)-H(21A)	0.9500
C(4)-H(4B)	0.9900	C(22)-C(23)	1.380(3)
C(5)-C(6)	1.541(2)	C(22)-H(22A)	0.9500
C(6)-H(6A)	0.9800	C(23)-C(24)	1.382(3)
C(6)-H(6B)	0.9800	C(23)-H(23A)	0.9500
C(6)-H(6C)	0.9800	C(24)-H(24A)	0.9500
C(7)-C(8)	1.390(2)	C(25)-C(30)	1.385(3)
C(7)-C(12)	1.395(3)	C(25)-C(26)	1.387(3)
C(8)-C(9)	1.390(3)	C(26)-C(27)	1.401(3)
C(8)-H(8A)	0.9500	C(26)-H(26A)	0.9500
C(9)-C(10)	1.377(3)	C(27)-C(28)	1.372(3)
C(9)-H(9A)	0.9500	C(27)-H(27A)	0.9500
C(10)-C(11)	1.389(3)	C(28)-C(29)	1.380(4)
C(10)-H(10A)	0.9500	C(28)-H(28A)	0.9500
C(11)-C(12)	1.385(3)	C(29)-C(30)	1.387(3)
C(11)-H(11A)	0.9500	C(29)-H(29A)	0.9500
C(12)-H(12A)	0.9500	C(30)-H(30A)	0.9500
C(13)-C(18)	1.389(2)	C(31)-C(32)	1.388(3)
C(13)-C(14)	1.394(3)	C(31)-C(36)	1.395(3)
C(14)-C(15)	1.390(3)	C(32)-C(33)	1.386(3)
C(14)-H(14A)	0.9500	C(32)-H(32A)	0.9500
C(15)-C(16)	1.371(3)	C(33)-C(34)	1.383(3)
C(15)-H(15A)	0.9500	C(33)-H(33A)	0.9500
C(16)-C(17)	1.382(3)	C(34)-C(35)	1.385(3)
C(16)-H(16A)	0.9500	C(34)-H(34A)	0.9500
C(17)-C(18)	1.388(3)	C(35)-C(36)	1.380(3)
C(17)-H(17A)	0.9500	C(35)-H(35A)	0.9500
C(18)-H(18A)	0.9500	C(36)-H(36A)	0.9500
C(19)-C(20)	1.390(3)	C(37)-C(42)	1.391(3)
C(19)-C(24)	1.393(3)	C(37)-C(38)	1.392(3)
C(20)-C(21)	1.394(3)	C(38)-C(39)	1.392(3)
C(20)-H(20A)	0.9500	C(38)-H(38A)	0.9500

C(39)-C(40)	1.386(4)	C(41)-H(41A)	0.9500
C(39)-H(39A)	0.9500	C(42)-H(42A)	0.9500
C(40)-C(41)	1.373(4)		
C(40)-H(40A)	0.9500		
C(41)-C(42)	1.392(3)		

Table A.4 Angles [°] for (CO)Ni[(PPh_2CH_2)$_3$CMe].

C(1)-Ni(1)-P(1)	119.63(6)	O(1)-C(1)-Ni(1)	179.19(19)
C(1)-Ni(1)-P(2)	124.77(7)	C(5)-C(2)-P(1)	114.41(12)
P(1)-Ni(1)-P(2)	95.95(2)	C(5)-C(2)-H(2A)	108.7
C(1)-Ni(1)-P(3)	122.49(7)	P(1)-C(2)-H(2A)	108.7
P(1)-Ni(1)-P(3)	93.91(2)	C(5)-C(2)-H(2B)	108.7
P(2)-Ni(1)-P(3)	92.447(19)	P(1)-C(2)-H(2B)	108.7
C(7)-P(1)-C(13)	98.69(8)	H(2A)-C(2)-H(2B)	107.6
C(7)-P(1)-C(2)	103.61(8)	C(5)-C(3)-P(2)	115.82(13)
C(13)-P(1)-C(2)	101.08(8)	C(5)-C(3)-H(3A)	108.3
C(7)-P(1)-Ni(1)	120.80(6)	P(2)-C(3)-H(3A)	108.3
C(13)-P(1)-Ni(1)	121.06(6)	C(5)-C(3)-H(3B)	108.3
C(2)-P(1)-Ni(1)	108.75(6)	P(2)-C(3)-H(3B)	108.3
C(19)-P(2)-C(25)	99.65(8)	H(3A)-C(3)-H(3B)	107.4
C(19)-P(2)-C(3)	101.72(9)	C(5)-C(4)-P(3)	114.60(12)
C(25)-P(2)-C(3)	103.38(9)	C(5)-C(4)-H(4A)	108.6
C(19)-P(2)-Ni(1)	124.06(6)	P(3)-C(4)-H(4A)	108.6
C(25)-P(2)-Ni(1)	118.26(6)	C(5)-C(4)-H(4B)	108.6
C(3)-P(2)-Ni(1)	106.99(6)	P(3)-C(4)-H(4B)	108.6
C(31)-P(3)-C(37)	98.33(8)	H(4A)-C(4)-H(4B)	107.6
C(31)-P(3)-C(4)	102.88(8)	C(6)-C(5)-C(4)	107.07(14)
C(37)-P(3)-C(4)	103.63(9)	C(6)-C(5)-C(3)	106.51(15)
C(31)-P(3)-Ni(1)	121.37(6)	C(4)-C(5)-C(3)	111.78(14)
C(37)-P(3)-Ni(1)	119.24(6)	C(6)-C(5)-C(2)	107.39(14)
C(4)-P(3)-Ni(1)	108.97(6)	C(4)-C(5)-C(2)	110.93(14)

C(3)-C(5)-C(2)	112.80(15)	C(14)-C(15)-H(15A)	120.1
C(5)-C(6)-H(6A)	109.5	C(15)-C(16)-C(17)	120.0(2)
C(5)-C(6)-H(6B)	109.5	C(15)-C(16)-H(16A)	120.0
H(6A)-C(6)-H(6B)	109.5	C(17)-C(16)-H(16A)	120.0
C(5)-C(6)-H(6C)	109.5	C(16)-C(17)-C(18)	120.67(18)
H(6A)-C(6)-H(6C)	109.5	C(16)-C(17)-H(17A)	119.7
H(6B)-C(6)-H(6C)	109.5	C(18)-C(17)-H(17A)	119.7
C(8)-C(7)-C(12)	118.57(17)	C(17)-C(18)-C(13)	120.08(19)
C(8)-C(7)-P(1)	124.43(14)	C(17)-C(18)-H(18A)	120.0
C(12)-C(7)-P(1)	116.94(13)	C(13)-C(18)-H(18A)	120.0
C(9)-C(8)-C(7)	120.98(19)	C(20)-C(19)-C(24)	118.86(18)
C(9)-C(8)-H(8A)	119.5	C(20)-C(19)-P(2)	118.90(15)
C(7)-C(8)-H(8A)	119.5	C(24)-C(19)-P(2)	122.24(15)
C(10)-C(9)-C(8)	119.77(18)	C(19)-C(20)-C(21)	120.2(2)
C(10)-C(9)-H(9A)	120.1	C(19)-C(20)-H(20A)	119.9
C(8)-C(9)-H(9A)	120.1	C(21)-C(20)-H(20A)	119.9
C(9)-C(10)-C(11)	120.10(17)	C(22)-C(21)-C(20)	120.1(2)
C(9)-C(10)-H(10A)	119.9	C(22)-C(21)-H(21A)	120.0
C(11)-C(10)-H(10A)	119.9	C(20)-C(21)-H(21A)	120.0
C(12)-C(11)-C(10)	120.04(18)	C(21)-C(22)-C(23)	120.19(19)
C(12)-C(11)-H(11A)	120.0	C(21)-C(22)-H(22A)	119.9
C(10)-C(11)-H(11A)	120.0	C(23)-C(22)-H(22A)	119.9
C(11)-C(12)-C(7)	120.54(18)	C(22)-C(23)-C(24)	119.9(2)
C(11)-C(12)-H(12A)	119.7	C(22)-C(23)-H(23A)	120.0
C(7)-C(12)-H(12A)	119.7	C(24)-C(23)-H(23A)	120.0
C(18)-C(13)-C(14)	118.48(17)	C(23)-C(24)-C(19)	120.81(19)
C(18)-C(13)-P(1)	119.60(14)	C(23)-C(24)-H(24A)	119.6
C(14)-C(13)-P(1)	121.92(14)	C(19)-C(24)-H(24A)	119.6
C(15)-C(14)-C(13)	121.08(18)	C(30)-C(25)-C(26)	118.79(17)
C(15)-C(14)-H(14A)	119.5	C(30)-C(25)-P(2)	124.06(15)
C(13)-C(14)-H(14A)	119.5	C(26)-C(25)-P(2)	117.13(14)
C(16)-C(15)-C(14)	119.7(2)	C(25)-C(26)-C(27)	120.80(19)
C(16)-C(15)-H(15A)	120.1	C(25)-C(26)-H(26A)	119.6

C(27)-C(26)-H(26A)	119.6	C(36)-C(35)-C(34)	120.13(19)
C(28)-C(27)-C(26)	119.5(2)	C(36)-C(35)-H(35A)	119.9
C(28)-C(27)-H(27A)	120.2	C(34)-C(35)-H(35A)	119.9
C(26)-C(27)-H(27A)	120.2	C(35)-C(36)-C(31)	120.86(19)
C(27)-C(28)-C(29)	120.0(2)	C(35)-C(36)-H(36A)	119.6
C(27)-C(28)-H(28A)	120.0	C(31)-C(36)-H(36A)	119.6
C(29)-C(28)-H(28A)	120.0	C(42)-C(37)-C(38)	118.87(18)
C(28)-C(29)-C(30)	120.5(2)	C(42)-C(37)-P(3)	117.43(15)
C(28)-C(29)-H(29A)	119.7	C(38)-C(37)-P(3)	123.51(15)
C(30)-C(29)-H(29A)	119.7	C(37)-C(38)-C(39)	120.5(2)
C(25)-C(30)-C(29)	120.3(2)	C(37)-C(38)-H(38A)	119.7
C(25)-C(30)-H(30A)	119.8	C(39)-C(38)-H(38A)	119.7
C(29)-C(30)-H(30A)	119.8	C(40)-C(39)-C(38)	119.8(2)
C(32)-C(31)-C(36)	118.50(17)	C(40)-C(39)-H(39A)	120.1
C(32)-C(31)-P(3)	117.58(14)	C(38)-C(39)-H(39A)	120.1
C(36)-C(31)-P(3)	123.88(14)	C(41)-C(40)-C(39)	120.1(2)
C(33)-C(32)-C(31)	120.66(19)	C(41)-C(40)-H(40A)	119.9
C(33)-C(32)-H(32A)	119.7	C(39)-C(40)-H(40A)	119.9
C(31)-C(32)-H(32A)	119.7	C(40)-C(41)-C(42)	120.3(2)
C(34)-C(33)-C(32)	120.25(19)	C(40)-C(41)-H(41A)	119.9
C(34)-C(33)-H(33A)	119.9	C(42)-C(41)-H(41A)	119.9
C(32)-C(33)-H(33A)	119.9	C(37)-C(42)-C(41)	120.4(2)
C(33)-C(34)-C(35)	119.60(18)	C(37)-C(42)-H(42A)	119.8
C(33)-C(34)-H(34A)	120.2	C(41)-C(42)-H(42A)	119.8
C(35)-C(34)-H(34A)	120.2		

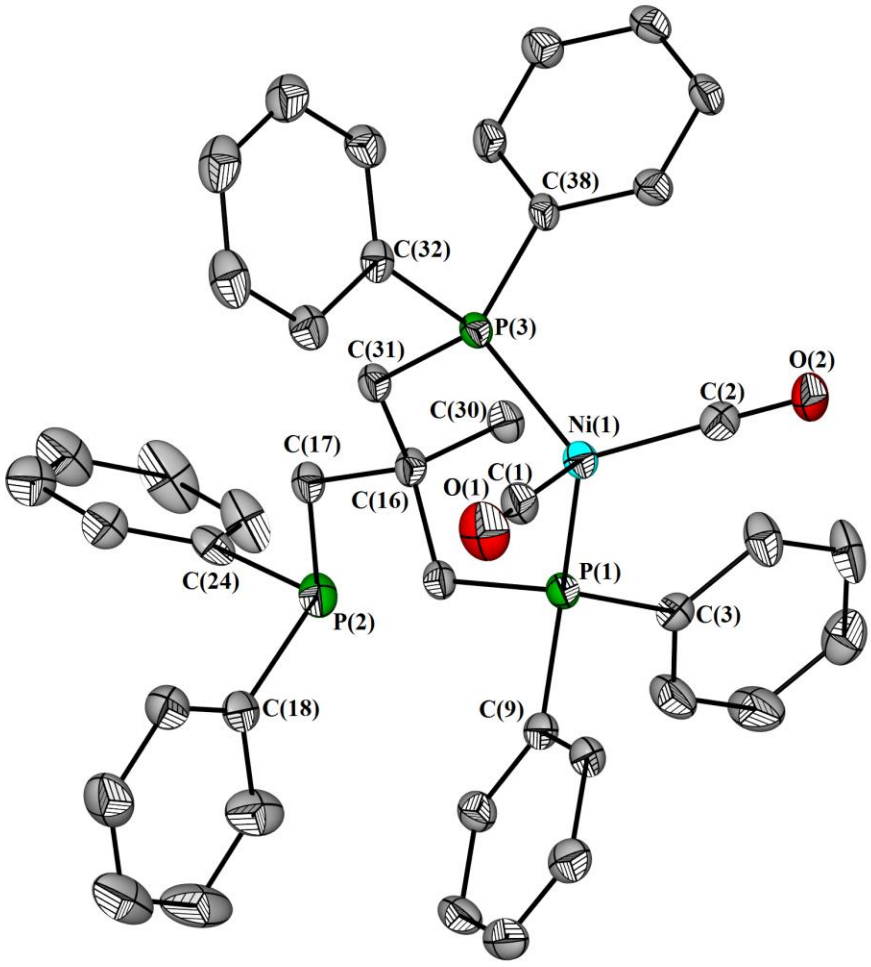

Figure A.2 X-ray structure of $(CO)_2Ni[(PPh_2CH_2)_3CMe]$.

Table A.5 Crystal data and structure refinement for $(CO)_2Ni[(PPh_2CH_2)_3CMe]$.

Identification code	mono
Empirical formula	C43 H39 Ni O2 P3
Formula weight	739.36

Temperature	110(2) K	
Wavelength	1.54178 Å	
Crystal system	Monoclinic	
Space group	P2(1)/n	
Unit cell dimensions	a = 8.5795(12) Å	□= 90°.
	b = 24.844(3) Å	□= 99.801(8)°.
	c = 17.483(3) Å	□ = 90°.
Volume	3672.2(9) $Å^3$	
Z	4	
Density (calculated)	1.337 Mg/m^3	
Absorption coefficient	2.276 mm^{-1}	
F(000)	1544	
Crystal size	0.20 x 0.20 x 0.04 mm^3	
Theta range for data collection	3.12 to 59.99°.	
Index ranges	-9<=h<=9, -27<=k<=27, -19<=l<=18	
Reflections collected	40181	
Independent reflections	5336 [R(int) = 0.0946]	
Completeness to theta = 59.99°	97.6 %	
Absorption correction	Semi-empirical from equivalents	
Max. and min. transmission	0.9145 and 0.6588	
Refinement method	Full-matrix least-squares on F^2	
Data / restraints / parameters	5336 / 0 / 443	
Goodness-of-fit on F^2	1.031	
Final R indices [I>2sigma(I)]	R1 = 0.0477, wR2 = 0.1163	
R indices (all data)	R1 = 0.0612, wR2 = 0.1206	
Extinction coefficient	0.0047(2)	
Largest diff. peak and hole	0.365 and -0.615 $e.Å^{-3}$	

Table A.6 Atomic coordinates (x 10^4) and equivalent isotropic displacement parameters ($Å^2$ x 10^3) for $(CO)_2Ni[(PPh_2CH_2)_3CMe]$. U(eq) is defined as one third of the trace of the orthogonalized U^{ij} tensor.

	x	y	z	U(eq)
Ni(1)	1399(1)	1350(1)	1678(1)	23(1)
P(1)	745(1)	2199(1)	1483(1)	23(1)
P(3)	3841(1)	1373(1)	1443(1)	21(1)
P(2)	4153(1)	3699(1)	1015(1)	30(1)
O(2)	-730(3)	596(1)	740(1)	39(1)
O(1)	1409(3)	1056(1)	3298(1)	46(1)
C(43)	3165(4)	735(1)	118(2)	28(1)
C(40)	5909(4)	950(1)	-437(2)	31(1)
C(16)	3815(3)	2541(1)	1153(2)	23(1)
C(33)	5386(4)	1142(1)	2943(2)	32(1)
C(42)	3452(4)	481(1)	-549(2)	30(1)
C(10)	-1289(4)	2157(1)	2563(2)	29(1)
C(32)	5333(4)	1027(1)	2154(2)	24(1)
C(41)	4835(4)	587(1)	-823(2)	28(1)
C(30)	3289(4)	2456(1)	282(2)	28(1)
C(14)	-194(4)	3031(1)	2436(2)	30(1)
C(11)	-2084(4)	2354(1)	3139(2)	35(1)
C(38)	4236(3)	1096(1)	523(2)	21(1)
C(18)	3890(4)	4004(1)	1944(2)	30(1)
C(12)	-1925(4)	2888(2)	3357(2)	39(1)
C(24)	5980(4)	4048(1)	881(2)	28(1)
C(29)	7305(4)	4081(1)	1451(2)	34(1)
C(4)	-846(4)	2019(1)	-32(2)	37(1)
C(17)	5004(4)	3020(1)	1275(2)	24(1)
C(3)	-485(4)	2394(1)	552(2)	26(1)
C(13)	-995(4)	3224(1)	3012(2)	36(1)
C(9)	-332(4)	2493(1)	2207(2)	26(1)
C(39)	5617(4)	1205(1)	228(2)	29(1)

C(36)	7554(4)	421(1)	2518(2)	38(1)
C(31)	4751(4)	2053(1)	1524(2)	24(1)
C(37)	6432(4)	663(1)	1958(2)	32(1)
C(1)	1435(4)	1181(1)	2669(2)	32(1)
C(34)	6526(4)	902(1)	3502(2)	42(1)
C(15)	2413(3)	2677(1)	1562(2)	24(1)
C(35)	7603(4)	540(1)	3284(2)	42(1)
C(28)	8688(5)	4311(1)	1312(2)	42(1)
C(8)	-1029(5)	2914(1)	408(2)	40(1)
C(2)	116(4)	898(1)	1094(2)	27(1)
C(23)	4558(4)	3832(2)	2683(2)	40(1)
C(19)	2978(5)	4470(1)	1890(3)	47(1)
C(6)	-2276(4)	2675(2)	-875(2)	44(1)
C(5)	-1739(5)	2155(2)	-743(2)	43(1)
C(22)	4350(5)	4122(2)	3330(2)	52(1)
C(7)	-1909(5)	3055(2)	-300(2)	51(1)
C(27)	8757(6)	4523(2)	592(2)	52(1)
C(25)	6065(5)	4267(1)	155(2)	48(1)
C(21)	3461(5)	4583(2)	3264(3)	60(1)
C(20)	2762(6)	4757(2)	2547(3)	64(1)
C(26)	7477(6)	4506(2)	25(2)	62(1)

Table A.7 Bond Lengths [Å] for $(CO)_2Ni[(PPh_2CH_2)_3CMe]$.

Ni(1)-C(2)	1.770(3)	P(3)-C(32)	1.839(3)
Ni(1)-C(1)	1.777(4)	P(3)-C(31)	1.856(3)
Ni(1)-P(1)	2.1937(10)	P(2)-C(24)	1.841(3)
Ni(1)-P(3)	2.2041(10)	P(2)-C(18)	1.841(3)
P(1)-C(9)	1.840(3)	P(2)-C(17)	1.863(3)
P(1)-C(3)	1.847(3)	O(2)-C(2)	1.150(4)
P(1)-C(15)	1.847(3)	O(1)-C(1)	1.147(4)
P(3)-C(38)	1.833(3)	C(43)-C(42)	1.384(4)

C(43)-C(38)	1.389(4)	C(24)-C(25)	1.392(5)
C(43)-H(43A)	0.9500	C(29)-C(28)	1.376(5)
C(40)-C(41)	1.381(4)	C(29)-H(29A)	0.9500
C(40)-C(39)	1.384(4)	C(4)-C(3)	1.378(4)
C(40)-H(40A)	0.9500	C(4)-C(5)	1.387(5)
C(16)-C(30)	1.528(4)	C(4)-H(4A)	0.9500
C(16)-C(31)	1.535(4)	C(17)-H(17A)	0.9900
C(16)-C(15)	1.538(4)	C(17)-H(17B)	0.9900
C(16)-C(17)	1.559(4)	C(3)-C(8)	1.382(4)
C(33)-C(34)	1.394(5)	C(13)-H(13A)	0.9500
C(33)-C(32)	1.403(4)	C(39)-H(39A)	0.9500
C(33)-H(33A)	0.9500	C(36)-C(35)	1.366(5)
C(42)-C(41)	1.378(5)	C(36)-C(37)	1.388(5)
C(42)-H(42A)	0.9500	C(36)-H(36A)	0.9500
C(10)-C(9)	1.390(4)	C(31)-H(31A)	0.9900
C(10)-C(11)	1.397(4)	C(31)-H(31B)	0.9900
C(10)-H(10A)	0.9500	C(37)-H(37A)	0.9500
C(32)-C(37)	1.392(4)	C(34)-C(35)	1.388(5)
C(41)-H(41A)	0.9500	C(34)-H(34A)	0.9500
C(30)-H(30A)	0.9800	C(15)-H(15A)	0.9900
C(30)-H(30B)	0.9800	C(15)-H(15B)	0.9900
C(30)-H(30C)	0.9800	C(35)-H(35A)	0.9500
C(14)-C(9)	1.395(4)	C(28)-C(27)	1.375(5)
C(14)-C(13)	1.397(5)	C(28)-H(28A)	0.9500
C(14)-H(14A)	0.9500	C(8)-C(7)	1.381(5)
C(11)-C(12)	1.384(5)	C(8)-H(8A)	0.9500
C(11)-H(11A)	0.9500	C(23)-C(22)	1.379(5)
C(38)-C(39)	1.396(4)	C(23)-H(23A)	0.9500
C(18)-C(23)	1.387(5)	C(19)-C(20)	1.390(6)
C(18)-C(19)	1.394(5)	C(19)-H(19A)	0.9500
C(12)-C(13)	1.365(5)	C(6)-C(5)	1.377(5)
C(12)-H(12A)	0.9500	C(6)-C(7)	1.377(5)
C(24)-C(29)	1.381(5)	C(6)-H(6A)	0.9500

C(5)-H(5A)	0.9500	C(21)-C(20)	1.365(6)
C(22)-C(21)	1.369(6)	C(21)-H(21A)	0.9500
C(22)-H(22A)	0.9500	C(20)-H(20A)	0.9500
C(7)-H(7A)	0.9500	C(26)-H(26A)	0.9500
C(27)-C(26)	1.349(6)		
C(27)-H(27A)	0.9500		
C(25)-C(26)	1.402(6)		
C(25)-H(25A)	0.9500		

Table A.8 Angles [°] for $(CO)_2Ni[(PPh_2CH_2)_3CMe]$.

C(2)-Ni(1)-C(1)	108.58(15)	C(42)-C(43)-C(38)	121.8(3)
C(2)-Ni(1)-P(1)	113.73(10)	C(42)-C(43)-H(43A)	119.1
C(1)-Ni(1)-P(1)	109.91(11)	C(38)-C(43)-H(43A)	119.1
C(2)-Ni(1)-P(3)	115.25(11)	C(41)-C(40)-C(39)	120.6(3)
C(1)-Ni(1)-P(3)	109.18(11)	C(41)-C(40)-H(40A)	119.7
P(1)-Ni(1)-P(3)	99.90(3)	C(39)-C(40)-H(40A)	119.7
C(9)-P(1)-C(3)	102.88(14)	C(30)-C(16)-C(31)	110.9(2)
C(9)-P(1)-C(15)	99.57(14)	C(30)-C(16)-C(15)	111.9(2)
C(3)-P(1)-C(15)	102.49(14)	C(31)-C(16)-C(15)	111.8(2)
C(9)-P(1)-Ni(1)	114.83(11)	C(30)-C(16)-C(17)	108.5(2)
C(3)-P(1)-Ni(1)	118.83(10)	C(31)-C(16)-C(17)	105.2(2)
C(15)-P(1)-Ni(1)	115.60(10)	C(15)-C(16)-C(17)	108.3(2)
C(38)-P(3)-C(32)	101.93(14)	C(34)-C(33)-C(32)	120.3(3)
C(38)-P(3)-C(31)	105.68(14)	C(34)-C(33)-H(33A)	119.9
C(32)-P(3)-C(31)	97.96(13)	C(32)-C(33)-H(33A)	119.9
C(38)-P(3)-Ni(1)	118.54(10)	C(41)-C(42)-C(43)	119.5(3)
C(32)-P(3)-Ni(1)	115.83(10)	C(41)-C(42)-H(42A)	120.2
C(31)-P(3)-Ni(1)	114.24(10)	C(43)-C(42)-H(42A)	120.2
C(24)-P(2)-C(18)	98.84(14)	C(9)-C(10)-C(11)	120.7(3)
C(24)-P(2)-C(17)	98.71(14)	C(9)-C(10)-H(10A)	119.6
C(18)-P(2)-C(17)	104.97(15)	C(11)-C(10)-H(10A)	119.6

C(37)-C(32)-C(33)	117.7(3)	C(3)-C(4)-C(5)	121.4(3)
C(37)-C(32)-P(3)	124.1(2)	C(3)-C(4)-H(4A)	119.3
C(33)-C(32)-P(3)	118.2(2)	C(5)-C(4)-H(4A)	119.3
C(42)-C(41)-C(40)	119.8(3)	C(16)-C(17)-P(2)	116.0(2)
C(42)-C(41)-H(41A)	120.1	C(16)-C(17)-H(17A)	108.3
C(40)-C(41)-H(41A)	120.1	P(2)-C(17)-H(17A)	108.3
C(16)-C(30)-H(30A)	109.5	C(16)-C(17)-H(17B)	108.3
C(16)-C(30)-H(30B)	109.5	P(2)-C(17)-H(17B)	108.3
H(30A)-C(30)-H(30B)	109.5	H(17A)-C(17)-H(17B)	107.4
C(16)-C(30)-H(30C)	109.5	C(4)-C(3)-C(8)	118.0(3)
H(30A)-C(30)-H(30C)	109.5	C(4)-C(3)-P(1)	119.9(2)
H(30B)-C(30)-H(30C)	109.5	C(8)-C(3)-P(1)	122.1(2)
C(9)-C(14)-C(13)	120.5(3)	C(12)-C(13)-C(14)	120.4(3)
C(9)-C(14)-H(14A)	119.7	C(12)-C(13)-H(13A)	119.8
C(13)-C(14)-H(14A)	119.7	C(14)-C(13)-H(13A)	119.8
C(12)-C(11)-C(10)	119.9(3)	C(10)-C(9)-C(14)	118.3(3)
C(12)-C(11)-H(11A)	120.1	C(10)-C(9)-P(1)	118.2(2)
C(10)-C(11)-H(11A)	120.1	C(14)-C(9)-P(1)	123.4(2)
C(43)-C(38)-C(39)	117.8(3)	C(40)-C(39)-C(38)	120.5(3)
C(43)-C(38)-P(3)	119.0(2)	C(40)-C(39)-H(39A)	119.8
C(39)-C(38)-P(3)	123.1(2)	C(38)-C(39)-H(39A)	119.8
C(23)-C(18)-C(19)	117.2(3)	C(35)-C(36)-C(37)	120.0(3)
C(23)-C(18)-P(2)	127.0(3)	C(35)-C(36)-H(36A)	120.0
C(19)-C(18)-P(2)	115.7(3)	C(37)-C(36)-H(36A)	120.0
C(13)-C(12)-C(11)	120.1(3)	C(16)-C(31)-P(3)	120.2(2)
C(13)-C(12)-H(12A)	119.9	C(16)-C(31)-H(31A)	107.3
C(11)-C(12)-H(12A)	119.9	P(3)-C(31)-H(31A)	107.3
C(29)-C(24)-C(25)	118.0(3)	C(16)-C(31)-H(31B)	107.3
C(29)-C(24)-P(2)	123.4(2)	P(3)-C(31)-H(31B)	107.3
C(25)-C(24)-P(2)	118.5(3)	H(31A)-C(31)-H(31B)	106.9
C(28)-C(29)-C(24)	121.7(3)	C(36)-C(37)-C(32)	121.7(3)
C(28)-C(29)-H(29A)	119.1	C(36)-C(37)-H(37A)	119.1
C(24)-C(29)-H(29A)	119.1	C(32)-C(37)-H(37A)	119.1

O(1)-C(1)-Ni(1)	177.1(3)	C(5)-C(6)-H(6A)	120.2
C(35)-C(34)-C(33)	120.3(3)	C(7)-C(6)-H(6A)	120.2
C(35)-C(34)-H(34A)	119.8	C(6)-C(5)-C(4)	119.8(3)
C(33)-C(34)-H(34A)	119.8	C(6)-C(5)-H(5A)	120.1
C(16)-C(15)-P(1)	118.7(2)	C(4)-C(5)-H(5A)	120.1
C(16)-C(15)-H(15A)	107.6	C(21)-C(22)-C(23)	121.0(4)
P(1)-C(15)-H(15A)	107.6	C(21)-C(22)-H(22A)	119.5
C(16)-C(15)-H(15B)	107.6	C(23)-C(22)-H(22A)	119.5
P(1)-C(15)-H(15B)	107.6	C(6)-C(7)-C(8)	120.2(3)
H(15A)-C(15)-H(15B)	107.1	C(6)-C(7)-H(7A)	119.9
C(36)-C(35)-C(34)	120.0(3)	C(8)-C(7)-H(7A)	119.9
C(36)-C(35)-H(35A)	120.0	C(26)-C(27)-C(28)	120.3(4)
C(34)-C(35)-H(35A)	120.0	C(26)-C(27)-H(27A)	119.8
C(27)-C(28)-C(29)	119.6(4)	C(28)-C(27)-H(27A)	119.8
C(27)-C(28)-H(28A)	120.2	C(24)-C(25)-C(26)	119.6(4)
C(29)-C(28)-H(28A)	120.2	C(24)-C(25)-H(25A)	120.2
C(7)-C(8)-C(3)	121.2(3)	C(26)-C(25)-H(25A)	120.2
C(7)-C(8)-H(8A)	119.4	C(20)-C(21)-C(22)	119.6(4)
C(3)-C(8)-H(8A)	119.4	C(20)-C(21)-H(21A)	120.2
O(2)-C(2)-Ni(1)	177.4(3)	C(22)-C(21)-H(21A)	120.2
C(22)-C(23)-C(18)	120.9(4)	C(21)-C(20)-C(19)	119.8(4)
C(22)-C(23)-H(23A)	119.6	C(21)-C(20)-H(20A)	120.1
C(18)-C(23)-H(23A)	119.6	C(19)-C(20)-H(20A)	120.1
C(20)-C(19)-C(18)	121.5(4)	C(27)-C(26)-C(25)	120.7(4)
C(20)-C(19)-H(19A)	119.2	C(27)-C(26)-H(26A)	119.6
C(18)-C(19)-H(19A)	119.2	C(25)-C(26)-H(26A)	119.6
C(5)-C(6)-C(7)	119.5(3)		

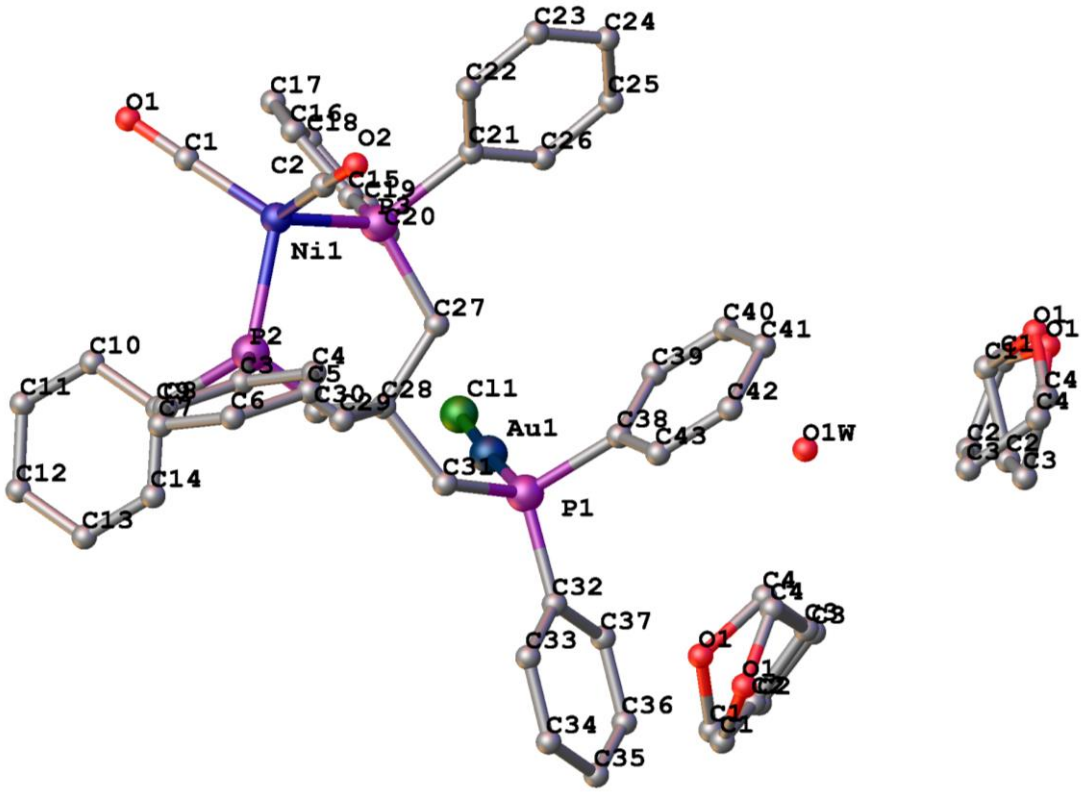

Figure A.3 X-ray structure of $(CO)_2Ni[(PPh_2CH_2)_3CMe]AuCl$.

Table A.9 Crystal data for $(CO)_2Ni[(PPh_2CH_2)_3CMe]AuCl$.

Identification code	jb09	
Empirical formula	C50.20 H53.60 Au Cl Ni O3.90 P3	
Formula weight	1103.37	
Temperature	110(2) K	
Wavelength	0.71073 Å	
Crystal system	Monoclinic	
Space group	C2/c	
Unit cell dimensions	a = 38.030(3) Å	□= 90°.
	b = 11.0474(8) Å	□= 118.848(4)°.
	c = 25.887(2) Å	□ = 90°.

Volume	9526.1(13) $Å^3$
Z	8
Density (calculated)	1.539 Mg/m^3
Absorption coefficient	3.671 mm^{-1}
F(000)	4440
Crystal size	0.34 x 0.16 x 0.09 mm^3
Theta range for data collection	2.23 to 28.90°.
Index ranges	-51<=h<=51, -14<=k<=14, -35<=l<=34
Reflections collected	134594
Independent reflections	11777 [R(int) = 0.0629]
Completeness to theta = 28.90°	93.9 %
Absorption correction	Semi-empirical from equivalents
Max. and min. transmission	0.7335 and 0.3640
Refinement method	Full-matrix least-squares on F^2
Data / restraints / parameters	11777 / 220 / 646
Goodness-of-fit on F^2	1.028
Final R indices [I>2sigma(I)]	R1 = 0.0266, wR2 = 0.0585
R indices (all data)	R1 = 0.0378, wR2 = 0.0635
Largest diff. peak and hole	0.876 and -0.748 $e.Å^{-3}$

Table A.10 Atomic coordinates (x 10^4) and equivalent isotropic displacement parameters ($Å^2$ x 10^3) for $(CO)_2Ni[(PPh_2CH_2)_3CMe]AuCl$. U(eq) is defined as one third of the trace of the orthogonalized U^{ij} tensor.

	x	y	z	U(eq)
Au(1)	2069(1)	1330(1)	9175(1)	19(1)
Ni(1)	1060(1)	1698(1)	10864(1)	19(1)
Cl(1)	2389(1)	-462(1)	9246(1)	28(1)
P(1)	1743(1)	3079(1)	9053(1)	16(1)
P(2)	1470(1)	3255(1)	11085(1)	17(1)
P(3)	1073(1)	957(1)	10080(1)	16(1)
O(1)	1281(1)	-64(2)	11812(1)	44(1)

O(2)	277(1)	2836(2)	10459(2)	63(1)
C(1)	1199(1)	624(3)	11438(1)	28(1)
C(2)	584(1)	2381(3)	10626(2)	35(1)
C(3)	1278(1)	4647(2)	11252(1)	20(1)
C(4)	928(1)	5179(3)	10806(1)	24(1)
C(5)	764(1)	6205(3)	10918(2)	30(1)
C(6)	943(1)	6703(3)	11479(2)	32(1)
C(7)	1283(1)	6178(3)	11927(1)	31(1)
C(8)	1450(1)	5156(3)	11812(1)	25(1)
C(9)	1994(1)	3218(2)	11684(1)	19(1)
C(10)	2124(1)	2279(3)	12092(1)	24(1)
C(11)	2522(1)	2239(3)	12543(1)	29(1)
C(12)	2792(1)	3116(3)	12586(1)	27(1)
C(13)	2667(1)	4052(3)	12177(1)	27(1)
C(14)	2272(1)	4098(3)	11735(1)	24(1)
C(15)	1359(1)	-442(2)	10167(1)	18(1)
C(16)	1341(1)	-1331(2)	10536(1)	25(1)
C(17)	1523(1)	-2450(3)	10596(1)	29(1)
C(18)	1731(1)	-2695(3)	10291(2)	31(1)
C(19)	1753(1)	-1816(3)	9925(2)	32(1)
C(20)	1568(1)	-705(3)	9863(1)	26(1)
C(21)	591(1)	491(2)	9449(1)	22(1)
C(22)	250(1)	425(3)	9509(2)	40(1)
C(23)	-115(1)	47(4)	9041(2)	52(1)
C(24)	-140(1)	-283(4)	8517(2)	53(1)
C(25)	193(1)	-210(5)	8449(2)	68(1)
C(26)	559(1)	175(4)	8914(2)	50(1)
C(27)	1241(1)	2039(2)	9700(1)	17(1)
C(28)	1608(1)	2844(2)	10080(1)	16(1)
C(29)	1516(1)	3780(2)	10447(1)	16(1)
C(30)	1979(1)	2093(2)	10475(1)	19(1)
C(31)	1693(1)	3681(2)	9671(1)	17(1)
C(32)	1984(1)	4312(2)	8876(1)	19(1)

C(33)	2035(1)	5462(3)	9125(1)	28(1)
C(34)	2239(1)	6350(3)	8999(2)	36(1)
C(35)	2391(1)	6117(3)	8622(1)	29(1)
C(36)	2336(1)	4987(3)	8363(1)	26(1)
C(37)	2137(1)	4086(3)	8492(1)	21(1)
C(38)	1240(1)	2975(3)	8430(1)	22(1)
C(39)	1102(1)	1886(3)	8133(2)	43(1)
C(40)	716(1)	1796(4)	7661(2)	58(1)
C(41)	470(1)	2773(4)	7478(2)	46(1)
C(42)	603(1)	3871(4)	7762(2)	47(1)
C(43)	986(1)	3972(3)	8239(2)	38(1)
O(1W)	3(19)	6359(19)	7430(20)	60(9)
O11	992(2)	7924(8)	8150(3)	63(2)
C11	1319(3)	8212(11)	8047(6)	55(2)
C21	1326(4)	7235(17)	7644(8)	43(2)
C31	892(5)	6904(16)	7291(6)	39(2)
C41	727(3)	7143(10)	7679(4)	40(2)
O12	880(2)	8630(7)	7889(3)	63(2)
C12	1282(2)	8495(10)	7989(6)	53(2)
C22	1306(4)	7346(15)	7695(8)	45(2)
C32	880(4)	6943(15)	7345(6)	48(2)
C42	686(2)	7487(8)	7649(5)	42(2)
O13	-722(2)	4935(5)	5695(3)	49(2)
C13	-359(2)	4269(5)	5938(4)	52(2)
C23	-20(2)	5172(5)	6189(3)	54(2)
C33	-211(2)	6280(5)	6278(3)	52(2)
C43	-627(2)	6192(6)	5823(4)	56(2)
O14	-721(4)	4725(13)	5773(11)	30(3)
C14	-310(5)	4358(11)	6053(10)	33(4)
C24	-93(4)	5356(13)	5925(8)	31(3)
C34	-329(4)	6462(10)	5896(9)	31(3)
C44	-720(4)	6024(13)	5769(11)	31(3)

Table A.11 Bond Lengths [Å] for $(CO)_2Ni[(PPh_2CH_2)_3CMe]AuCl$.

Au(1)-P(1)	2.2341(7)	C(10)-H(10A)	0.9500
Au(1)-Cl(1)	2.2845(7)	C(11)-C(12)	1.377(4)
Ni(1)-C(1)	1.770(3)	C(11)-H(11A)	0.9500
Ni(1)-C(2)	1.773(3)	C(12)-C(13)	1.389(4)
Ni(1)-P(2)	2.2040(8)	C(12)-H(12A)	0.9500
Ni(1)-P(3)	2.2113(8)	C(13)-C(14)	1.383(4)
P(1)-C(38)	1.815(3)	C(13)-H(13A)	0.9500
P(1)-C(32)	1.819(3)	C(14)-H(14A)	0.9500
P(1)-C(31)	1.826(3)	C(15)-C(20)	1.389(4)
P(2)-C(29)	1.838(3)	C(15)-C(16)	1.395(4)
P(2)-C(3)	1.841(3)	C(16)-C(17)	1.389(4)
P(2)-C(9)	1.842(3)	C(16)-H(16A)	0.9500
P(3)-C(15)	1.842(3)	C(17)-C(18)	1.385(4)
P(3)-C(21)	1.845(3)	C(17)-H(17A)	0.9500
P(3)-C(27)	1.846(3)	C(18)-C(19)	1.388(4)
O(1)-C(1)	1.150(4)	C(18)-H(18A)	0.9500
O(2)-C(2)	1.149(4)	C(19)-C(20)	1.386(4)
C(3)-C(8)	1.389(4)	C(19)-H(19A)	0.9500
C(3)-C(4)	1.403(4)	C(20)-H(20A)	0.9500
C(4)-C(5)	1.391(4)	C(21)-C(26)	1.374(5)
C(4)-H(4A)	0.9500	C(21)-C(22)	1.381(4)
C(5)-C(6)	1.386(5)	C(22)-C(23)	1.394(5)
C(5)-H(5A)	0.9500	C(22)-H(22A)	0.9500
C(6)-C(7)	1.382(5)	C(23)-C(24)	1.363(6)
C(6)-H(6A)	0.9500	C(23)-H(23A)	0.9500
C(7)-C(8)	1.397(4)	C(24)-C(25)	1.361(6)
C(7)-H(7A)	0.9500	C(24)-H(24A)	0.9500
C(8)-H(8A)	0.9500	C(25)-C(26)	1.396(5)
C(9)-C(10)	1.391(4)	C(25)-H(25A)	0.9500
C(9)-C(14)	1.394(4)	C(26)-H(26A)	0.9500
C(10)-C(11)	1.398(4)	C(27)-C(28)	1.542(3)

C(27)-H(27A)	0.9900	C(43)-H(43A)	0.9500
C(27)-H(27B)	0.9900	O(1W)-H(1W)	0.8499
C(28)-C(30)	1.529(3)	O(1W)-H(2W)	0.8498
C(28)-C(29)	1.552(3)	O11-C11	1.430(6)
C(28)-C(31)	1.554(3)	O11-C41	1.436(6)
C(29)-H(29A)	0.9900	C11-C21	1.509(6)
C(29)-H(29B)	0.9900	C11-H1A1	0.9900
C(30)-H(30A)	0.9800	C11-H1B1	0.9900
C(30)-H(30B)	0.9800	C21-C31	1.494(5)
C(30)-H(30C)	0.9800	C21-H2A1	0.9900
C(31)-H(31A)	0.9900	C21-H2B1	0.9900
C(31)-H(31B)	0.9900	C31-C41	1.442(6)
C(32)-C(37)	1.395(4)	C31-H3A1	0.9900
C(32)-C(33)	1.396(4)	C31-H3B1	0.9900
C(33)-C(34)	1.382(4)	C41-H4B1	0.9900
C(33)-H(33A)	0.9500	C41-H4C1	0.9900
C(34)-C(35)	1.380(4)	O12-C12	1.430(5)
C(34)-H(34A)	0.9500	O12-C42	1.443(6)
C(35)-C(36)	1.383(4)	C12-C22	1.505(6)
C(35)-H(35A)	0.9500	C12-H1C2	0.9900
C(36)-C(37)	1.384(4)	C12-H1D2	0.9900
C(36)-H(36A)	0.9500	C22-C32	1.494(5)
C(37)-H(37A)	0.9500	C22-H2C2	0.9900
C(38)-C(39)	1.388(4)	C22-H2D2	0.9900
C(38)-C(43)	1.389(4)	C32-C42	1.442(6)
C(39)-C(40)	1.386(5)	C32-H3C2	0.9900
C(39)-H(39A)	0.9500	C32-H3D2	0.9900
C(40)-C(41)	1.357(6)	C42-H4D2	0.9900
C(40)-H(40A)	0.9500	C42-H4E2	0.9900
C(41)-C(42)	1.382(6)	O13-C13	1.415(5)
C(41)-H(41A)	0.9500	O13-C43	1.433(5)
C(42)-C(43)	1.388(5)	C13-C23	1.507(5)
C(42)-H(42A)	0.9500	C13-H1E3	0.9900

C13-H1F3	0.9900	C14-H1J4	0.9900
C23-C33	1.495(5)	C24-C34	1.496(6)
C23-H2E3	0.9900	C24-H2G4	0.9900
C23-H2F3	0.9900	C24-H2H4	0.9900
C33-C43	1.450(6)	C34-C44	1.443(6)
C33-H3E3	0.9900	C34-H3G4	0.9900
C33-H3F3	0.9900	C34-H3H4	0.9900
C43-H4F3	0.9900	C44-H4H4	0.9900
C43-H4G3	0.9900	C44-H4I4	0.9900
O14-C14	1.426(6)		
O14-C44	1.435(6)		
C14-C24	1.508(6)		
C14-H1I4	0.9900		

Table A.12 Angles [°] for $(CO)_2Ni[(PPh_2CH_2)_3CMe]AuCl$.

P(1)-Au(1)-Cl(1)	176.87(3)	C(29)-P(2)-Ni(1)	112.04(9)
C(1)-Ni(1)-C(2)	114.77(15)	C(3)-P(2)-Ni(1)	113.68(9)
C(1)-Ni(1)-P(2)	114.63(10)	C(9)-P(2)-Ni(1)	122.97(9)
C(2)-Ni(1)-P(2)	103.47(10)	C(15)-P(3)-C(21)	98.66(12)
C(1)-Ni(1)-P(3)	113.09(10)	C(15)-P(3)-C(27)	105.83(12)
C(2)-Ni(1)-P(3)	108.03(12)	C(21)-P(3)-C(27)	99.27(12)
P(2)-Ni(1)-P(3)	101.59(3)	C(15)-P(3)-Ni(1)	118.16(9)
C(38)-P(1)-C(32)	105.52(12)	C(21)-P(3)-Ni(1)	117.59(10)
C(38)-P(1)-C(31)	106.91(13)	C(27)-P(3)-Ni(1)	114.56(9)
C(32)-P(1)-C(31)	103.06(12)	O(1)-C(1)-Ni(1)	178.1(3)
C(38)-P(1)-Au(1)	110.27(10)	O(2)-C(2)-Ni(1)	178.2(4)
C(32)-P(1)-Au(1)	111.75(9)	C(8)-C(3)-C(4)	118.2(3)
C(31)-P(1)-Au(1)	118.38(9)	C(8)-C(3)-P(2)	122.8(2)
C(29)-P(2)-C(3)	99.68(12)	C(4)-C(3)-P(2)	118.9(2)
C(29)-P(2)-C(9)	103.24(12)	C(5)-C(4)-C(3)	120.9(3)
C(3)-P(2)-C(9)	102.23(12)	C(5)-C(4)-H(4A)	119.6

C(3)-C(4)-H(4A)	119.6	C(16)-C(15)-P(3)	116.9(2)
C(6)-C(5)-C(4)	119.9(3)	C(17)-C(16)-C(15)	121.1(3)
C(6)-C(5)-H(5A)	120.0	C(17)-C(16)-H(16A)	119.5
C(4)-C(5)-H(5A)	120.0	C(15)-C(16)-H(16A)	119.5
C(7)-C(6)-C(5)	120.0(3)	C(18)-C(17)-C(16)	120.1(3)
C(7)-C(6)-H(6A)	120.0	C(18)-C(17)-H(17A)	120.0
C(5)-C(6)-H(6A)	120.0	C(16)-C(17)-H(17A)	120.0
C(6)-C(7)-C(8)	119.9(3)	C(17)-C(18)-C(19)	119.4(3)
C(6)-C(7)-H(7A)	120.0	C(17)-C(18)-H(18A)	120.3
C(8)-C(7)-H(7A)	120.0	C(19)-C(18)-H(18A)	120.3
C(3)-C(8)-C(7)	121.1(3)	C(20)-C(19)-C(18)	120.2(3)
C(3)-C(8)-H(8A)	119.5	C(20)-C(19)-H(19A)	119.9
C(7)-C(8)-H(8A)	119.5	C(18)-C(19)-H(19A)	119.9
C(10)-C(9)-C(14)	118.2(3)	C(19)-C(20)-C(15)	121.1(3)
C(10)-C(9)-P(2)	120.0(2)	C(19)-C(20)-H(20A)	119.4
C(14)-C(9)-P(2)	121.8(2)	C(15)-C(20)-H(20A)	119.4
C(9)-C(10)-C(11)	120.2(3)	C(26)-C(21)-C(22)	117.9(3)
C(9)-C(10)-H(10A)	119.9	C(26)-C(21)-P(3)	122.0(2)
C(11)-C(10)-H(10A)	119.9	C(22)-C(21)-P(3)	120.1(2)
C(12)-C(11)-C(10)	120.7(3)	C(21)-C(22)-C(23)	120.9(3)
C(12)-C(11)-H(11A)	119.7	C(21)-C(22)-H(22A)	119.6
C(10)-C(11)-H(11A)	119.7	C(23)-C(22)-H(22A)	119.6
C(11)-C(12)-C(13)	119.6(3)	C(24)-C(23)-C(22)	120.4(4)
C(11)-C(12)-H(12A)	120.2	C(24)-C(23)-H(23A)	119.8
C(13)-C(12)-H(12A)	120.2	C(22)-C(23)-H(23A)	119.8
C(14)-C(13)-C(12)	119.6(3)	C(25)-C(24)-C(23)	119.3(3)
C(14)-C(13)-H(13A)	120.2	C(25)-C(24)-H(24A)	120.3
C(12)-C(13)-H(13A)	120.2	C(23)-C(24)-H(24A)	120.3
C(13)-C(14)-C(9)	121.6(3)	C(24)-C(25)-C(26)	120.6(4)
C(13)-C(14)-H(14A)	119.2	C(24)-C(25)-H(25A)	119.7
C(9)-C(14)-H(14A)	119.2	C(26)-C(25)-H(25A)	119.7
C(20)-C(15)-C(16)	118.1(3)	C(21)-C(26)-C(25)	120.9(4)
C(20)-C(15)-P(3)	124.8(2)	C(21)-C(26)-H(26A)	119.6

C(25)-C(26)-H(26A)	119.6	C(33)-C(32)-P(1)	122.6(2)
C(28)-C(27)-P(3)	118.24(18)	C(34)-C(33)-C(32)	120.3(3)
C(28)-C(27)-H(27A)	107.8	C(34)-C(33)-H(33A)	119.8
P(3)-C(27)-H(27A)	107.8	C(32)-C(33)-H(33A)	119.8
C(28)-C(27)-H(27B)	107.8	C(35)-C(34)-C(33)	120.6(3)
P(3)-C(27)-H(27B)	107.8	C(35)-C(34)-H(34A)	119.7
H(27A)-C(27)-H(27B)	107.1	C(33)-C(34)-H(34A)	119.7
C(30)-C(28)-C(27)	111.9(2)	C(34)-C(35)-C(36)	119.5(3)
C(30)-C(28)-C(29)	111.1(2)	C(34)-C(35)-H(35A)	120.2
C(27)-C(28)-C(29)	111.9(2)	C(36)-C(35)-H(35A)	120.2
C(30)-C(28)-C(31)	110.4(2)	C(35)-C(36)-C(37)	120.4(3)
C(27)-C(28)-C(31)	109.4(2)	C(35)-C(36)-H(36A)	119.8
C(29)-C(28)-C(31)	101.7(2)	C(37)-C(36)-H(36A)	119.8
C(28)-C(29)-P(2)	119.10(17)	C(36)-C(37)-C(32)	120.4(3)
C(28)-C(29)-H(29A)	107.5	C(36)-C(37)-H(37A)	119.8
P(2)-C(29)-H(29A)	107.5	C(32)-C(37)-H(37A)	119.8
C(28)-C(29)-H(29B)	107.5	C(39)-C(38)-C(43)	118.5(3)
P(2)-C(29)-H(29B)	107.5	C(39)-C(38)-P(1)	120.1(2)
H(29A)-C(29)-H(29B)	107.0	C(43)-C(38)-P(1)	121.3(2)
C(28)-C(30)-H(30A)	109.5	C(40)-C(39)-C(38)	120.5(3)
C(28)-C(30)-H(30B)	109.5	C(40)-C(39)-H(39A)	119.8
H(30A)-C(30)-H(30B)	109.5	C(38)-C(39)-H(39A)	119.8
C(28)-C(30)-H(30C)	109.5	C(41)-C(40)-C(39)	120.6(4)
H(30A)-C(30)-H(30C)	109.5	C(41)-C(40)-H(40A)	119.7
H(30B)-C(30)-H(30C)	109.5	C(39)-C(40)-H(40A)	119.7
C(28)-C(31)-P(1)	121.67(18)	C(40)-C(41)-C(42)	120.0(3)
C(28)-C(31)-H(31A)	106.9	C(40)-C(41)-H(41A)	120.0
P(1)-C(31)-H(31A)	106.9	C(42)-C(41)-H(41A)	120.0
C(28)-C(31)-H(31B)	106.9	C(41)-C(42)-C(43)	120.1(4)
P(1)-C(31)-H(31B)	106.9	C(41)-C(42)-H(42A)	120.0
H(31A)-C(31)-H(31B)	106.7	C(43)-C(42)-H(42A)	120.0
C(37)-C(32)-C(33)	118.7(2)	C(42)-C(43)-C(38)	120.3(3)
C(37)-C(32)-P(1)	118.6(2)	C(42)-C(43)-H(43A)	119.8

C(38)-C(43)-H(43A)	119.8	H1C2-C12-H1D2	108.4
H(1W)-O(1W)-H(2W)	85.9	C32-C22-C12	104.1(4)
C11-O11-C41	107.0(4)	C32-C22-H2C2	110.9
O11-C11-C21	106.0(5)	C12-C22-H2C2	110.9
O11-C11-H1A1	110.5	C32-C22-H2D2	110.9
C21-C11-H1A1	110.5	C12-C22-H2D2	110.9
O11-C11-H1B1	110.5	H2C2-C22-H2D2	108.9
C21-C11-H1B1	110.5	C42-C32-C22	103.6(4)
H1A1-C11-H1B1	108.7	C42-C32-H3C2	111.0
C31-C21-C11	102.5(4)	C22-C32-H3C2	111.0
C31-C21-H2A1	111.3	C42-C32-H3D2	111.0
C11-C21-H2A1	111.3	C22-C32-H3D2	111.0
C31-C21-H2B1	111.3	H3C2-C32-H3D2	109.0
C11-C21-H2B1	111.3	O12-C42-C32	108.1(5)
H2A1-C21-H2B1	109.2	O12-C42-H4D2	110.1
C41-C31-C21	104.6(5)	C32-C42-H4D2	110.1
C41-C31-H3A1	110.8	O12-C42-H4E2	110.1
C21-C31-H3A1	110.8	C32-C42-H4E2	110.1
C41-C31-H3B1	110.8	H4D2-C42-H4E2	108.4
C21-C31-H3B1	110.8	C13-O13-C43	108.6(3)
H3A1-C31-H3B1	108.9	O13-C13-C23	107.1(4)
O11-C41-C31	109.8(4)	O13-C13-H1E3	110.3
O11-C41-H4B1	109.7	C23-C13-H1E3	110.3
C31-C41-H4B1	109.7	O13-C13-H1F3	110.3
O11-C41-H4C1	109.7	C23-C13-H1F3	110.3
C31-C41-H4C1	109.7	H1E3-C13-H1F3	108.5
H4B1-C41-H4C1	108.2	C33-C23-C13	103.4(4)
C12-O12-C42	105.5(4)	C33-C23-H2E3	111.1
O12-C12-C22	108.5(4)	C13-C23-H2E3	111.1
O12-C12-H1C2	110.0	C33-C23-H2F3	111.1
C22-C12-H1C2	110.0	C13-C23-H2F3	111.1
O12-C12-H1D2	110.0	H2E3-C23-H2F3	109.0
C22-C12-H1D2	110.0	C43-C33-C23	103.9(4)

C43-C33-H3E3	111.0	C34-C24-C14	103.2(5)
C23-C33-H3E3	111.0	C34-C24-H2G4	111.1
C43-C33-H3F3	111.0	C14-C24-H2G4	111.1
C23-C33-H3F3	111.0	C34-C24-H2H4	111.1
H3E3-C33-H3F3	109.0	C14-C24-H2H4	111.1
O13-C43-C33	107.9(4)	H2G4-C24-H2H4	109.1
O13-C43-H4F3	110.1	C44-C34-C24	105.4(5)
C33-C43-H4F3	110.1	C44-C34-H3G4	110.7
O13-C43-H4G3	110.1	C24-C34-H3G4	110.7
C33-C43-H4G3	110.1	C44-C34-H3H4	110.7
H4F3-C43-H4G3	108.4	C24-C34-H3H4	110.7
C14-O14-C44	106.4(5)	H3G4-C34-H3H4	108.8
O14-C14-C24	105.1(6)	O14-C44-C34	109.8(5)
O14-C14-H1I4	110.7	O14-C44-H4H4	109.7
C24-C14-H1I4	110.7	C34-C44-H4H4	109.7
O14-C14-H1J4	110.7	O14-C44-H4I4	109.7
C24-C14-H1J4	110.7	C34-C44-H4I4	109.7
H1I4-C14-H1J4	108.8	H4H4-C44-H4I4	108.2

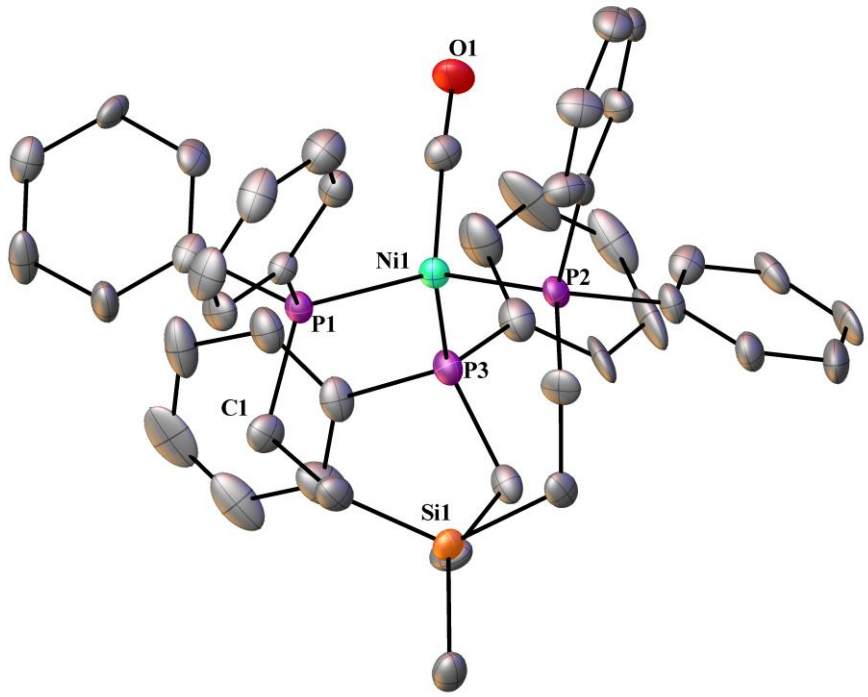

Figure A.4 X-ray structure of (CO)Ni[($PPh_2CH_2CH_2$)$_3$SiMe].

Table A.13 Crystal data for (CO)Ni[($PPh_2CH_2CH_2$)$_3$SiMe].

Identification code	twin4	
Empirical formula	C44 H45 Ni O P3 Si	
Formula weight	769.51	
Temperature	110.15 K	
Wavelength	1.54178 Å	
Crystal system	Triclinic	
Space group	P-1	
Unit cell dimensions	a = 10.465(2) Å	□= 84.37(3)°.
	b = 10.485(2) Å	□= 89.55(3)°.
	c = 18.592(4) Å	□ = 76.42(3)°.
Volume	1973.4(7) Å^3	
Z	2	

Density (calculated)	1.295 Mg/m^3
Absorption coefficient	2.398 mm^{-1}
F(000)	808
Crystal size	0.14 x 0.06 x 0.02 mm^3
Theta range for data collection	2.388 to 60.604°.
Index ranges	-11<=h<=11, -11<=k<=11, 0<=l<=21
Reflections collected	5736
Independent reflections	5736 [R(int) = ?]
Completeness to theta = 67.679°	81.9 %
Absorption correction	Semi-empirical from equivalents
Max. and min. transmission	0.752 and 0.613
Refinement method	Full-matrix least-squares on F^2
Data / restraints / parameters	5736 / 93 / 453
Goodness-of-fit on F^2	1.029
Final R indices [I>2sigma(I)]	R1 = 0.0771, wR2 = 0.1986
R indices (all data)	R1 = 0.0898, wR2 = 0.2088
Extinction coefficient	n/a
Largest diff. peak and hole	0.868 and -0.781 e.$Å^{-3}$

Table A.14 Atomic coordinates (x 10^4) and equivalent isotropic displacement parameters ($Å^2$ x 10^3) for (CO)Ni[($PPh_2CH_2CH_2)_3SiMe$]. U(eq) is defined as one third of the trace of the orthogonalized U^{ij} tensor.

	x	y	z	U(eq)
Ni(1)	5476(1)	7062(1)	2278(1)	19(1)
P(1)	3399(2)	7880(2)	1948(1)	19(1)
P(2)	6383(2)	8611(2)	2617(1)	19(1)
P(3)	5521(2)	5523(2)	3177(1)	22(1)
Si(1)	3548(2)	8702(2)	3974(1)	22(1)
O(1)	7204(6)	5943(7)	1144(4)	40(2)
C(1)	2181(9)	8102(8)	2673(5)	27(2)

C(2)	2354(9)	9130(9)	3181(5)	29(2)
C(3)	5480(8)	9964(8)	3107(5)	24(2)
C(4)	5006(9)	9498(8)	3873(5)	24(2)
C(5)	5400(8)	5999(8)	4114(5)	24(2)
C(6)	4050(10)	6888(10)	4289(5)	34(2)
C(7)	2587(9)	9456(9)	4751(5)	32(2)
C(8)	6496(9)	6369(8)	1579(5)	26(2)
C(9)	2676(9)	6926(8)	1333(4)	24(2)
C(10)	1438(9)	6689(10)	1413(5)	34(2)
C(11)	916(9)	6010(9)	924(6)	39(2)
C(12)	1667(9)	5574(8)	323(5)	31(2)
C(13)	2934(9)	5762(8)	258(4)	26(2)
C(14)	3437(9)	6444(9)	756(5)	27(2)
C(15)	2963(8)	9515(7)	1411(4)	18(2)
C(16)	3963(9)	9908(9)	991(5)	28(2)
C(17)	3691(10)	11105(9)	540(5)	39(2)
C(18)	2395(10)	11911(9)	509(5)	38(2)
C(19)	1429(10)	11552(9)	925(5)	37(2)
C(20)	1707(8)	10348(9)	1380(5)	30(2)
C(21)	7891(8)	7994(9)	3169(5)	25(2)
C(22)	8673(9)	6708(8)	3123(5)	28(2)
C(23)	9804(8)	6192(10)	3538(5)	33(2)
C(24)	10203(8)	6931(10)	4037(5)	34(2)
C(25)	9463(10)	8218(12)	4091(5)	45(3)
C(26)	8326(9)	8749(9)	3663(5)	28(2)
C(27)	7032(8)	9565(9)	1876(4)	24(2)
C(28)	8131(8)	8934(9)	1497(4)	27(2)
C(29)	8623(8)	9581(9)	914(4)	26(2)
C(30)	8000(9)	10916(9)	669(5)	32(2)
C(31)	6922(10)	11531(9)	1049(5)	33(2)
C(32)	6428(10)	10881(9)	1640(5)	30(2)
C(33)	4291(9)	4496(8)	3156(5)	27(2)
C(34)	3928(9)	4258(9)	2477(5)	33(2)

C(35)	3026(9)	3452(9)	2410(7)	43(2)
C(36)	2523(10)	2918(9)	3061(8)	51(3)
C(37)	2875(10)	3135(9)	3701(8)	49(2)
C(38)	3771(10)	3921(9)	3759(6)	40(2)
C(39)	7034(9)	4165(9)	3263(5)	32(2)
C(40)	7308(10)	3356(10)	2700(7)	48(3)
C(41)	8440(11)	2285(10)	2741(9)	63(4)
C(42)	9276(10)	2045(10)	3331(8)	53(3)
C(43)	9019(9)	2863(11)	3881(7)	47(3)
C(44)	7905(8)	3879(10)	3859(6)	34(2)

Table A.15 Bond Lengths [Å] for (CO)Ni[($PPh_2CH_2CH_2)_3SiMe$].

Ni(1)-P(1)	2.209(3)	C(1)-H(1B)	0.9900
Ni(1)-P(2)	2.206(3)	C(1)-C(2)	1.543(11)
Ni(1)-P(3)	2.199(3)	C(2)-H(2A)	0.9900
Ni(1)-C(8)	1.776(9)	C(2)-H(2B)	0.9900
P(1)-C(1)	1.842(9)	C(3)-H(3A)	0.9900
P(1)-C(9)	1.864(8)	C(3)-H(3B)	0.9900
P(1)-C(15)	1.857(8)	C(3)-C(4)	1.575(12)
P(2)-C(3)	1.830(8)	C(4)-H(4A)	0.9900
P(2)-C(21)	1.839(8)	C(4)-H(4B)	0.9900
P(2)-C(27)	1.842(9)	C(5)-H(5A)	0.9900
P(3)-C(5)	1.855(9)	C(5)-H(5B)	0.9900
P(3)-C(33)	1.865(9)	C(5)-C(6)	1.551(12)
P(3)-C(39)	1.861(9)	C(6)-H(6A)	0.9900
Si(1)-C(2)	1.890(9)	C(6)-H(6B)	0.9900
Si(1)-C(4)	1.903(9)	C(7)-H(7A)	0.9800
Si(1)-C(6)	1.885(10)	C(7)-H(7B)	0.9800
Si(1)-C(7)	1.884(8)	C(7)-H(7C)	0.9800
O(1)-C(8)	1.145(10)	C(9)-C(10)	1.379(13)
C(1)-H(1A)	0.9900	C(9)-C(14)	1.395(13)

C(10)-H(10)	0.9500	C(28)-H(28)	0.9500
C(10)-C(11)	1.396(13)	C(28)-C(29)	1.382(12)
C(11)-H(11)	0.9500	C(29)-H(29)	0.9500
C(11)-C(12)	1.412(14)	C(29)-C(30)	1.430(13)
C(12)-H(12)	0.9500	C(30)-H(30)	0.9500
C(12)-C(13)	1.388(13)	C(30)-C(31)	1.387(13)
C(13)-H(13)	0.9500	C(31)-H(31)	0.9500
C(13)-C(14)	1.400(12)	C(31)-C(32)	1.396(13)
C(14)-H(14)	0.9500	C(32)-H(32)	0.9500
C(15)-C(16)	1.414(12)	C(33)-C(34)	1.382(13)
C(15)-C(20)	1.395(12)	C(33)-C(38)	1.389(14)
C(16)-H(16)	0.9500	C(34)-H(34)	0.9500
C(16)-C(17)	1.410(13)	C(34)-C(35)	1.420(14)
C(17)-H(17)	0.9500	C(35)-H(35)	0.9500
C(17)-C(18)	1.418(14)	C(35)-C(36)	1.432(17)
C(18)-H(18)	0.9500	C(36)-H(36)	0.9500
C(18)-C(19)	1.368(15)	C(36)-C(37)	1.306(17)
C(19)-H(19)	0.9500	C(37)-H(37)	0.9500
C(19)-C(20)	1.420(13)	C(37)-C(38)	1.397(15)
C(20)-H(20)	0.9500	C(38)-H(38)	0.9500
C(21)-C(22)	1.414(13)	C(39)-C(40)	1.397(15)
C(21)-C(26)	1.412(12)	C(39)-C(44)	1.404(13)
C(22)-H(22)	0.9500	C(40)-H(40)	0.9500
C(22)-C(23)	1.386(13)	C(40)-C(41)	1.425(14)
C(23)-H(23)	0.9500	C(41)-H(41)	0.9500
C(23)-C(24)	1.391(14)	C(41)-C(42)	1.374(19)
C(24)-H(24)	0.9500	C(42)-H(42)	0.9500
C(24)-C(25)	1.402(15)	C(42)-C(43)	1.384(17)
C(25)-H(25)	0.9500	C(43)-H(43)	0.9500
C(25)-C(26)	1.406(13)	C(43)-C(44)	1.380(14)
C(26)-H(26)	0.9500	C(44)-H(44)	0.9500
C(27)-C(28)	1.407(11)		
C(27)-C(32)	1.405(13)		

Table A.16 Angles [°] for (CO)Ni[($PPh_2CH_2CH_2$)$_3$SiMe].

P(2)-Ni(1)-P(1)	111.11(10)	P(1)-C(1)-H(1A)	108.8
P(3)-Ni(1)-P(1)	107.59(10)	P(1)-C(1)-H(1B)	108.8
P(3)-Ni(1)-P(2)	110.35(10)	H(1A)-C(1)-H(1B)	107.7
C(8)-Ni(1)-P(1)	114.2(3)	C(2)-C(1)-P(1)	113.6(6)
C(8)-Ni(1)-P(2)	104.8(3)	C(2)-C(1)-H(1A)	108.8
C(8)-Ni(1)-P(3)	108.8(3)	C(2)-C(1)-H(1B)	108.8
C(1)-P(1)-Ni(1)	117.1(3)	Si(1)-C(2)-H(2A)	106.8
C(1)-P(1)-C(9)	101.8(4)	Si(1)-C(2)-H(2B)	106.8
C(1)-P(1)-C(15)	101.7(4)	C(1)-C(2)-Si(1)	122.3(6)
C(9)-P(1)-Ni(1)	116.5(3)	C(1)-C(2)-H(2A)	106.8
C(15)-P(1)-Ni(1)	118.2(3)	C(1)-C(2)-H(2B)	106.8
C(15)-P(1)-C(9)	98.5(4)	H(2A)-C(2)-H(2B)	106.6
C(3)-P(2)-Ni(1)	122.5(3)	P(2)-C(3)-H(3A)	108.8
C(3)-P(2)-C(21)	102.3(4)	P(2)-C(3)-H(3B)	108.8
C(3)-P(2)-C(27)	99.6(4)	H(3A)-C(3)-H(3B)	107.7
C(21)-P(2)-Ni(1)	114.6(3)	C(4)-C(3)-P(2)	113.7(6)
C(21)-P(2)-C(27)	99.3(4)	C(4)-C(3)-H(3A)	108.8
C(27)-P(2)-Ni(1)	115.0(3)	C(4)-C(3)-H(3B)	108.8
C(5)-P(3)-Ni(1)	118.7(3)	Si(1)-C(4)-H(4A)	107.0
C(5)-P(3)-C(33)	102.8(4)	Si(1)-C(4)-H(4B)	107.0
C(5)-P(3)-C(39)	100.3(4)	C(3)-C(4)-Si(1)	121.4(6)
C(33)-P(3)-Ni(1)	117.6(3)	C(3)-C(4)-H(4A)	107.0
C(39)-P(3)-Ni(1)	115.9(3)	C(3)-C(4)-H(4B)	107.0
C(39)-P(3)-C(33)	98.2(4)	H(4A)-C(4)-H(4B)	106.7
C(2)-Si(1)-C(4)	114.4(4)	P(3)-C(5)-H(5A)	108.8
C(6)-Si(1)-C(2)	114.3(4)	P(3)-C(5)-H(5B)	108.8
C(6)-Si(1)-C(4)	112.7(4)	H(5A)-C(5)-H(5B)	107.6
C(7)-Si(1)-C(2)	104.8(4)	C(6)-C(5)-P(3)	114.0(6)
C(7)-Si(1)-C(4)	105.2(4)	C(6)-C(5)-H(5A)	108.8
C(7)-Si(1)-C(6)	104.1(4)	C(6)-C(5)-H(5B)	108.8

Si(1)-C(6)-H(6A)	106.6	C(20)-C(15)-C(16)	118.6(7)
Si(1)-C(6)-H(6B)	106.6	C(15)-C(16)-H(16)	119.6
C(5)-C(6)-Si(1)	123.0(7)	C(17)-C(16)-C(15)	120.8(8)
C(5)-C(6)-H(6A)	106.6	C(17)-C(16)-H(16)	119.6
C(5)-C(6)-H(6B)	106.6	C(16)-C(17)-H(17)	120.5
H(6A)-C(6)-H(6B)	106.5	C(16)-C(17)-C(18)	119.1(9)
Si(1)-C(7)-H(7A)	109.5	C(18)-C(17)-H(17)	120.5
Si(1)-C(7)-H(7B)	109.5	C(17)-C(18)-H(18)	119.7
Si(1)-C(7)-H(7C)	109.5	C(19)-C(18)-C(17)	120.6(9)
H(7A)-C(7)-H(7B)	109.5	C(19)-C(18)-H(18)	119.7
H(7A)-C(7)-H(7C)	109.5	C(18)-C(19)-H(19)	119.9
H(7B)-C(7)-H(7C)	109.5	C(18)-C(19)-C(20)	120.2(9)
O(1)-C(8)-Ni(1)	176.5(8)	C(20)-C(19)-H(19)	119.9
C(10)-C(9)-P(1)	123.9(7)	C(15)-C(20)-C(19)	120.8(9)
C(10)-C(9)-C(14)	118.8(8)	C(15)-C(20)-H(20)	119.6
C(14)-C(9)-P(1)	117.3(7)	C(19)-C(20)-H(20)	119.6
C(9)-C(10)-H(10)	119.0	C(22)-C(21)-P(2)	120.7(6)
C(9)-C(10)-C(11)	121.9(9)	C(26)-C(21)-P(2)	122.9(7)
C(11)-C(10)-H(10)	119.0	C(26)-C(21)-C(22)	116.4(8)
C(10)-C(11)-H(11)	120.5	C(21)-C(22)-H(22)	118.6
C(10)-C(11)-C(12)	119.0(9)	C(23)-C(22)-C(21)	122.8(9)
C(12)-C(11)-H(11)	120.5	C(23)-C(22)-H(22)	118.6
C(11)-C(12)-H(12)	120.5	C(22)-C(23)-H(23)	119.8
C(13)-C(12)-C(11)	119.1(8)	C(22)-C(23)-C(24)	120.3(9)
C(13)-C(12)-H(12)	120.5	C(24)-C(23)-H(23)	119.8
C(12)-C(13)-H(13)	119.7	C(23)-C(24)-H(24)	120.7
C(12)-C(13)-C(14)	120.7(8)	C(23)-C(24)-C(25)	118.5(8)
C(14)-C(13)-H(13)	119.7	C(25)-C(24)-H(24)	120.7
C(9)-C(14)-C(13)	120.3(8)	C(24)-C(25)-H(25)	119.4
C(9)-C(14)-H(14)	119.9	C(24)-C(25)-C(26)	121.1(9)
C(13)-C(14)-H(14)	119.9	C(26)-C(25)-H(25)	119.4
C(16)-C(15)-P(1)	117.4(6)	C(21)-C(26)-H(26)	119.6
C(20)-C(15)-P(1)	124.0(7)	C(25)-C(26)-C(21)	120.8(9)

C(25)-C(26)-H(26)	119.6	C(34)-C(35)-C(36)	117.7(11)
C(28)-C(27)-P(2)	119.0(7)	C(36)-C(35)-H(35)	121.2
C(32)-C(27)-P(2)	122.8(6)	C(35)-C(36)-H(36)	118.8
C(32)-C(27)-C(28)	118.0(8)	C(37)-C(36)-C(35)	122.5(11)
C(27)-C(28)-H(28)	119.2	C(37)-C(36)-H(36)	118.8
C(29)-C(28)-C(27)	121.7(8)	C(36)-C(37)-H(37)	120.4
C(29)-C(28)-H(28)	119.2	C(36)-C(37)-C(38)	119.2(12)
C(28)-C(29)-H(29)	119.8	C(38)-C(37)-H(37)	120.4
C(28)-C(29)-C(30)	120.3(8)	C(33)-C(38)-C(37)	122.2(11)
C(30)-C(29)-H(29)	119.8	C(33)-C(38)-H(38)	118.9
C(29)-C(30)-H(30)	121.2	C(37)-C(38)-H(38)	118.9
C(31)-C(30)-C(29)	117.5(8)	C(40)-C(39)-P(3)	117.6(7)
C(31)-C(30)-H(30)	121.2	C(40)-C(39)-C(44)	117.7(9)
C(30)-C(31)-H(31)	118.9	C(44)-C(39)-P(3)	124.7(8)
C(30)-C(31)-C(32)	122.2(9)	C(39)-C(40)-H(40)	119.9
C(32)-C(31)-H(31)	118.9	C(39)-C(40)-C(41)	120.2(11)
C(27)-C(32)-H(32)	119.9	C(41)-C(40)-H(40)	119.9
C(31)-C(32)-C(27)	120.2(9)	C(40)-C(41)-H(41)	119.8
C(31)-C(32)-H(32)	119.9	C(42)-C(41)-C(40)	120.4(12)
C(34)-C(33)-P(3)	115.9(7)	C(42)-C(41)-H(41)	119.8
C(34)-C(33)-C(38)	118.7(9)	C(41)-C(42)-H(42)	120.3
C(38)-C(33)-P(3)	125.3(7)	C(41)-C(42)-C(43)	119.4(9)
C(33)-C(34)-H(34)	120.1	C(43)-C(42)-H(42)	120.3
C(33)-C(34)-C(35)	119.8(10)	C(42)-C(43)-H(43)	119.6
C(35)-C(34)-H(34)	120.1	C(44)-C(43)-C(42)	120.8(10)
C(34)-C(35)-H(35)	121.2	C(44)-C(43)-H(43)	119.6
C(39)-C(44)-H(44)	119.3		
C(43)-C(44)-C(39)	121.4(11)		
C(43)-C(44)-H(44)	119.3		

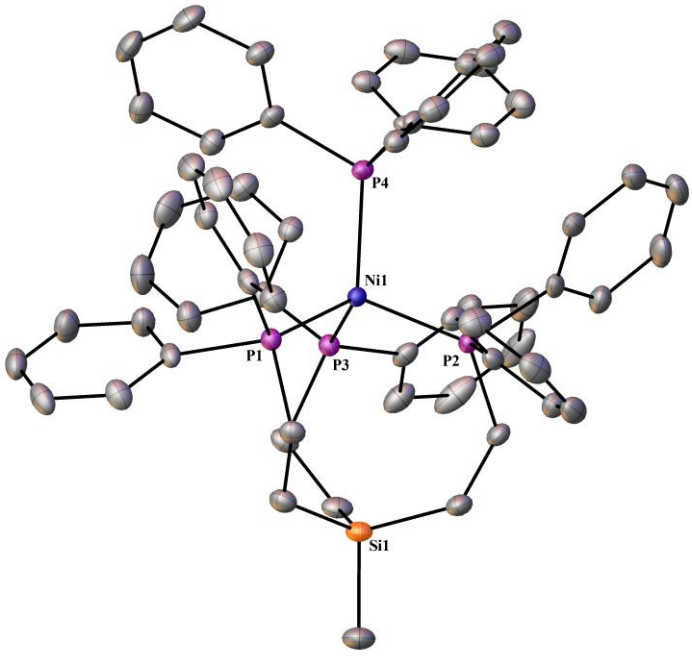

Figure A.5 X-ray structure of $(PPh_3)Ni[(PPh_2CH_2)_3CMe]$.

Table A.17 Crystal data and structure refinement for $(PPh_3)Ni[(PPh_2CH_2)_3CMe]$.

Identification code	jbb	
Empirical formula	C66 H72 Ni P4 Si	
Formula weight	1075.92	
Temperature	110(2) K	
Wavelength	0.71073 Å	
Crystal system	Monoclinic	
Space group	P2(1)	
Unit cell dimensions	a = 13.2287(11) Å	□= 90°.
	b = 16.4601(14) Å	□= 108.1480(10)°.
	c = 13.7514(12) Å	□ = 90°.
Volume	2845.4(4) Å^3	
Z	2	
Density (calculated)	1.256 Mg/m^3	

Absorption coefficient	0.515 mm^{-1}
F(000)	1140
Crystal size	0.55 x 0.32 x 0.30 mm^3
Theta range for data collection	2.24 to 27.50°.
Index ranges	-17<=h<=17, -21<=k<=21, -17<=l<=17
Reflections collected	66464
Independent reflections	13033 [R(int) = 0.0244]
Completeness to theta = 27.50°	99.7 %
Absorption correction	Semi-empirical from equivalents
Max. and min. transmission	0.8609 and 0.7649
Refinement method	Full-matrix least-squares on F^2
Data / restraints / parameters	13033 / 18 / 646
Goodness-of-fit on F^2	1.023
Final R indices [I>2sigma(I)]	R1 = 0.0259, wR2 = 0.0653
R indices (all data)	R1 = 0.0273, wR2 = 0.0660
Absolute structure parameter	0.008(5)
Largest diff. peak and hole	0.563 and -0.568 e.$Å^{-3}$

Table A.18 Atomic coordinates (x 10^4) and equivalent isotropic displacement parameters ($Å^2$ x 10^3) for $(PPh_3)Ni[(PPh_2CH_2)_3CMe]$. U(eq) is defined as one third of the trace of the orthogonalized U^{ij} tensor.

	x	y	z	U(eq)
Ni(1)	7872(1)	5003(1)	1688(1)	13(1)
P(1)	6580(1)	4396(1)	492(1)	15(1)
P(2)	9161(1)	5256(1)	1022(1)	15(1)
P(3)	7241(1)	6178(1)	2037(1)	15(1)
P(4)	8510(1)	4247(1)	3096(1)	15(1)
Si(1)	6858(1)	6468(1)	-871(1)	20(1)
C(1)	6570(1)	3271(1)	410(1)	18(1)
C(2)	6858(1)	2838(1)	-330(1)	23(1)

C(3)	6900(2)	1992(1)	-306(2)	29(1)
C(4)	6649(2)	1570(1)	455(2)	31(1)
C(5)	6343(2)	1993(1)	1187(2)	27(1)
C(6)	6300(1)	2837(1)	1160(1)	21(1)
C(7)	5163(1)	4483(1)	429(1)	18(1)
C(8)	4324(1)	4228(1)	-418(2)	24(1)
C(9)	3286(1)	4240(1)	-384(2)	27(1)
C(10)	3064(1)	4494(1)	484(2)	28(1)
C(11)	3884(2)	4758(1)	1320(2)	32(1)
C(12)	4923(1)	4749(1)	1281(1)	25(1)
C(13)	6467(1)	4668(1)	-844(1)	19(1)
C(14)	6016(1)	5520(1)	-1172(1)	22(1)
C(15)	10552(1)	5274(1)	1891(1)	19(1)
C(16)	11091(1)	4543(1)	2196(1)	23(1)
C(17)	12094(2)	4530(1)	2915(2)	29(1)
C(18)	12578(2)	5250(2)	3341(2)	35(1)
C(19)	12072(2)	5978(2)	3031(2)	32(1)
C(20)	11063(1)	5994(1)	2297(1)	25(1)
C(21)	9457(1)	4585(1)	67(1)	18(1)
C(22)	9138(1)	3778(1)	18(1)	22(1)
C(23)	9432(2)	3222(1)	-605(2)	30(1)
C(24)	10035(2)	3473(1)	-1214(2)	30(1)
C(25)	10334(1)	4281(1)	-1194(1)	27(1)
C(26)	10064(1)	4828(1)	-558(1)	23(1)
C(27)	9132(1)	6246(1)	381(1)	20(1)
C(28)	8312(1)	6320(1)	-692(1)	23(1)
C(29)	6576(1)	6243(1)	3041(1)	17(1)
C(30)	7201(1)	6205(1)	4069(1)	20(1)
C(31)	6746(2)	6217(1)	4854(2)	26(1)
C(32)	5650(2)	6278(1)	4625(2)	35(1)
C(33)	5028(2)	6344(2)	3620(2)	37(1)
C(34)	5480(2)	6322(1)	2833(2)	28(1)
C(35)	8181(1)	7006(1)	2582(1)	20(1)

C(36)	9231(2)	6794(1)	3084(1)	25(1)
C(37)	9962(2)	7370(2)	3629(2)	37(1)
C(38)	9653(2)	8157(2)	3665(2)	42(1)
C(39)	8614(2)	8384(1)	3167(2)	41(1)
C(40)	7877(2)	7808(1)	2630(2)	28(1)
C(41)	6228(1)	6719(1)	1003(1)	22(1)
C(42)	6632(2)	7103(1)	176(1)	23(1)
C(43)	9444(1)	3414(1)	3068(1)	17(1)
C(44)	9146(1)	2888(1)	2233(1)	20(1)
C(45)	9814(2)	2267(1)	2127(2)	25(1)
C(46)	10794(2)	2158(1)	2863(2)	26(1)
C(47)	11088(2)	2657(1)	3714(2)	27(1)
C(48)	10414(1)	3280(1)	3815(1)	22(1)
C(49)	7549(1)	3662(1)	3547(1)	19(1)
C(50)	7688(2)	2853(1)	3851(1)	25(1)
C(51)	6900(2)	2444(1)	4132(2)	31(1)
C(52)	5971(2)	2837(1)	4117(2)	32(1)
C(53)	5836(2)	3642(1)	3841(2)	28(1)
C(54)	6624(1)	4054(1)	3567(1)	22(1)
C(55)	9265(1)	4760(1)	4301(1)	18(1)
C(56)	8894(1)	4827(1)	5145(1)	21(1)
C(57)	9472(2)	5252(1)	6015(1)	29(1)
C(58)	10439(2)	5601(1)	6073(2)	31(1)
C(59)	10822(2)	5531(1)	5254(2)	30(1)
C(60)	10241(1)	5118(1)	4374(1)	24(1)
C(61)	6381(2)	7106(1)	-2061(2)	32(1)
C(1P)	7480(4)	3626(4)	6826(4)	74(1)
C(2P)	6517(3)	4206(3)	6514(3)	74(1)
C(3P)	5487(3)	3734(3)	6401(4)	74(1)
C(4P)	4583(3)	4373(3)	6013(3)	74(1)
C(5P)	3604(4)	3819(3)	5725(3)	74(1)
C(1Q)	7251(10)	3918(10)	6872(10)	74(1)
C(2Q)	6036(9)	3473(8)	6705(9)	74(1)

C(3Q)	5625(9)	4207(9)	6348(9)	74(1)
C(4Q)	4351(9)	3696(8)	6064(8)	74(1)
C(5Q)	3722(9)	4355(9)	6178(8)	74(1)

Table A.19 Bond Lengths [Å] for $(PPh_3)Ni[(PPh_2CH_2)_3CMe]$.

Ni(1)-P(1)	2.2073(5)	C(4)-C(5)	1.384(3)
Ni(1)-P(2)	2.2120(5)	C(4)-H(4)	0.9500
Ni(1)-P(3)	2.2170(5)	C(5)-C(6)	1.391(3)
Ni(1)-P(4)	2.2342(5)	C(5)-H(5)	0.9500
P(1)-C(13)	1.8504(17)	C(6)-H(6)	0.9500
P(1)-C(7)	1.8552(17)	C(7)-C(12)	1.378(2)
P(1)-C(1)	1.8554(18)	C(7)-C(8)	1.399(2)
P(2)-C(27)	1.8479(18)	C(8)-C(9)	1.389(2)
P(2)-C(21)	1.8479(17)	C(8)-H(8)	0.9500
P(2)-C(15)	1.8566(17)	C(9)-C(10)	1.380(3)
P(3)-C(35)	1.8411(18)	C(9)-H(9)	0.9500
P(3)-C(41)	1.8499(18)	C(10)-C(11)	1.382(3)
P(3)-C(29)	1.8575(17)	C(10)-H(10)	0.9500
P(4)-C(49)	1.8497(17)	C(11)-C(12)	1.392(2)
P(4)-C(55)	1.8507(17)	C(11)-H(11)	0.9500
P(4)-C(43)	1.8528(17)	C(12)-H(12)	0.9500
Si(1)-C(42)	1.8755(19)	C(13)-C(14)	1.536(3)
Si(1)-C(28)	1.8775(18)	C(13)-H(13A)	0.9900
Si(1)-C(61)	1.880(2)	C(13)-H(13B)	0.9900
Si(1)-C(14)	1.8860(19)	C(14)-H(14A)	0.9900
C(1)-C(6)	1.390(3)	C(14)-H(14B)	0.9900
C(1)-C(2)	1.390(2)	C(15)-C(20)	1.393(3)
C(2)-C(3)	1.394(3)	C(15)-C(16)	1.395(3)
C(2)-H(2)	0.9500	C(16)-C(17)	1.385(3)
C(3)-C(4)	1.380(3)	C(16)-H(16)	0.9500
C(3)-H(3)	0.9500	C(17)-C(18)	1.387(3)

C(17)-H(17)	0.9500	C(35)-C(40)	1.387(3)
C(18)-C(19)	1.375(3)	C(35)-C(36)	1.389(3)
C(18)-H(18)	0.9500	C(36)-C(37)	1.394(3)
C(19)-C(20)	1.400(3)	C(36)-H(36)	0.9500
C(19)-H(19)	0.9500	C(37)-C(38)	1.364(4)
C(20)-H(20)	0.9500	C(37)-H(37)	0.9500
C(21)-C(22)	1.389(3)	C(38)-C(39)	1.383(4)
C(21)-C(26)	1.404(2)	C(38)-H(38)	0.9500
C(22)-C(23)	1.389(3)	C(39)-C(40)	1.395(3)
C(22)-H(22)	0.9500	C(39)-H(39)	0.9500
C(23)-C(24)	1.386(3)	C(40)-H(40)	0.9500
C(23)-H(23)	0.9500	C(41)-C(42)	1.536(3)
C(24)-C(25)	1.386(3)	C(41)-H(41A)	0.9900
C(24)-H(24)	0.9500	C(41)-H(41B)	0.9900
C(25)-C(26)	1.378(3)	C(42)-H(42A)	0.9900
C(25)-H(25)	0.9500	C(42)-H(42B)	0.9900
C(26)-H(26)	0.9500	C(43)-C(48)	1.390(2)
C(27)-C(28)	1.540(2)	C(43)-C(44)	1.394(2)
C(27)-H(27A)	0.9900	C(44)-C(45)	1.387(2)
C(27)-H(27B)	0.9900	C(44)-H(44)	0.9500
C(28)-H(28A)	0.9900	C(45)-C(46)	1.386(3)
C(28)-H(28B)	0.9900	C(45)-H(45)	0.9500
C(29)-C(34)	1.393(2)	C(46)-C(47)	1.383(3)
C(29)-C(30)	1.399(2)	C(46)-H(46)	0.9500
C(30)-C(31)	1.390(2)	C(47)-C(48)	1.394(3)
C(30)-H(30)	0.9500	C(47)-H(47)	0.9500
C(31)-C(32)	1.388(3)	C(48)-H(48)	0.9500
C(31)-H(31)	0.9500	C(49)-C(54)	1.391(2)
C(32)-C(33)	1.376(3)	C(49)-C(50)	1.391(3)
C(32)-H(32)	0.9500	C(50)-C(51)	1.392(3)
C(33)-C(34)	1.391(3)	C(50)-H(50)	0.9500
C(33)-H(33)	0.9500	C(51)-C(52)	1.383(3)
C(34)-H(34)	0.9500	C(51)-H(51)	0.9500

C(52)-C(53)	1.375(3)	C(3P)-H(3PA)	0.9900
C(52)-H(52)	0.9500	C(3P)-H(3PB)	0.9900
C(53)-C(54)	1.390(2)	C(4P)-C(5P)	1.531(3)
C(53)-H(53)	0.9500	C(4P)-H(4PA)	0.9900
C(54)-H(54)	0.9500	C(4P)-H(4PB)	0.9900
C(55)-C(60)	1.395(2)	C(5P)-H(5PA)	0.9800
C(55)-C(56)	1.398(2)	C(5P)-H(5PB)	0.9800
C(56)-C(57)	1.392(3)	C(5P)-H(5PC)	0.9800
C(56)-H(56)	0.9500	C(1Q)-C(2Q)	1.714(14)
C(57)-C(58)	1.381(3)	C(1Q)-H(1QA)	0.9800
C(57)-H(57)	0.9500	C(1Q)-H(1QB)	0.9800
C(58)-C(59)	1.375(3)	C(1Q)-H(1QC)	0.9800
C(58)-H(58)	0.9500	C(2Q)-C(3Q)	1.353(14)
C(59)-C(60)	1.391(3)	C(2Q)-H(2QA)	0.9900
C(59)-H(59)	0.9500	C(2Q)-H(2QB)	0.9900
C(60)-H(60)	0.9500	C(3Q)-C(4Q)	1.814(14)
C(61)-H(61A)	0.9800	C(3Q)-H(3QA)	0.9900
C(61)-H(61B)	0.9800	C(3Q)-H(3QB)	0.9900
C(61)-H(61C)	0.9800	C(4Q)-C(5Q)	1.405(14)
C(1P)-C(2P)	1.543(3)	C(4Q)-H(4QA)	0.9900
C(1P)-H(1PA)	0.9800	C(4Q)-H(4QB)	0.9900
C(1P)-H(1PB)	0.9800	C(5Q)-H(5QA)	0.9800
C(1P)-H(1PC)	0.9800	C(5Q)-H(5QB)	0.9800
C(2P)-C(3P)	1.534(3)	C(5Q)-H(5QC)	0.9800
C(2P)-H(2PA)	0.9900		
C(2P)-H(2PB)	0.9900		
C(3P)-C(4P)	1.557(3)		

Table A.20 Angles [°] for $(PPh_3)Ni[(PPh_2CH_2)_3CMe]$.

P(1)-Ni(1)-P(2)	107.133(18)	P(2)-Ni(1)-P(3)	108.461(18)
P(1)-Ni(1)-P(3)	107.421(17)	P(1)-Ni(1)-P(4)	112.928(18)

P(2)-Ni(1)-P(4)	109.353(17)	C(6)-C(1)-P(1)	117.81(13)
P(3)-Ni(1)-P(4)	111.364(18)	C(2)-C(1)-P(1)	123.93(14)
C(13)-P(1)-C(7)	99.64(8)	C(1)-C(2)-C(3)	120.88(18)
C(13)-P(1)-C(1)	100.63(8)	C(1)-C(2)-H(2)	119.6
C(7)-P(1)-C(1)	94.93(7)	C(3)-C(2)-H(2)	119.6
C(13)-P(1)-Ni(1)	115.74(6)	C(4)-C(3)-C(2)	120.22(19)
C(7)-P(1)-Ni(1)	122.45(6)	C(4)-C(3)-H(3)	119.9
C(1)-P(1)-Ni(1)	119.07(6)	C(2)-C(3)-H(3)	119.9
C(27)-P(2)-C(21)	99.52(8)	C(3)-C(4)-C(5)	119.51(18)
C(27)-P(2)-C(15)	99.33(8)	C(3)-C(4)-H(4)	120.2
C(21)-P(2)-C(15)	94.59(8)	C(5)-C(4)-H(4)	120.2
C(27)-P(2)-Ni(1)	117.33(6)	C(4)-C(5)-C(6)	120.14(18)
C(21)-P(2)-Ni(1)	122.89(6)	C(4)-C(5)-H(5)	119.9
C(15)-P(2)-Ni(1)	118.31(5)	C(6)-C(5)-H(5)	119.9
C(35)-P(3)-C(41)	101.06(8)	C(1)-C(6)-C(5)	121.02(17)
C(35)-P(3)-C(29)	94.03(8)	C(1)-C(6)-H(6)	119.5
C(41)-P(3)-C(29)	98.41(8)	C(5)-C(6)-H(6)	119.5
C(35)-P(3)-Ni(1)	118.84(6)	C(12)-C(7)-C(8)	118.08(16)
C(41)-P(3)-Ni(1)	118.99(6)	C(12)-C(7)-P(1)	118.82(13)
C(29)-P(3)-Ni(1)	120.61(6)	C(8)-C(7)-P(1)	122.89(13)
C(49)-P(4)-C(55)	99.90(8)	C(9)-C(8)-C(7)	120.27(17)
C(49)-P(4)-C(43)	98.85(8)	C(9)-C(8)-H(8)	119.9
C(55)-P(4)-C(43)	100.27(8)	C(7)-C(8)-H(8)	119.9
C(49)-P(4)-Ni(1)	117.85(6)	C(10)-C(9)-C(8)	120.81(18)
C(55)-P(4)-Ni(1)	118.35(6)	C(10)-C(9)-H(9)	119.6
C(43)-P(4)-Ni(1)	117.97(5)	C(8)-C(9)-H(9)	119.6
C(42)-Si(1)-C(28)	111.94(9)	C(9)-C(10)-C(11)	119.41(17)
C(42)-Si(1)-C(61)	105.48(9)	C(9)-C(10)-H(10)	120.3
C(28)-Si(1)-C(61)	103.80(9)	C(11)-C(10)-H(10)	120.3
C(42)-Si(1)-C(14)	113.90(9)	C(10)-C(11)-C(12)	119.59(18)
C(28)-Si(1)-C(14)	115.56(9)	C(10)-C(11)-H(11)	120.2
C(61)-Si(1)-C(14)	104.79(9)	C(12)-C(11)-H(11)	120.2
C(6)-C(1)-C(2)	118.21(16)	C(7)-C(12)-C(11)	121.81(17)

C(7)-C(12)-H(12)	119.1	C(22)-C(21)-P(2)	118.55(13)
C(11)-C(12)-H(12)	119.1	C(26)-C(21)-P(2)	123.60(14)
C(14)-C(13)-P(1)	114.62(12)	C(21)-C(22)-C(23)	121.44(17)
C(14)-C(13)-H(13A)	108.6	C(21)-C(22)-H(22)	119.3
P(1)-C(13)-H(13A)	108.6	C(23)-C(22)-H(22)	119.3
C(14)-C(13)-H(13B)	108.6	C(24)-C(23)-C(22)	120.0(2)
P(1)-C(13)-H(13B)	108.6	C(24)-C(23)-H(23)	120.0
H(13A)-C(13)-H(13B)	107.6	C(22)-C(23)-H(23)	120.0
C(13)-C(14)-Si(1)	122.83(12)	C(25)-C(24)-C(23)	119.26(18)
C(13)-C(14)-H(14A)	106.6	C(25)-C(24)-H(24)	120.4
Si(1)-C(14)-H(14A)	106.6	C(23)-C(24)-H(24)	120.4
C(13)-C(14)-H(14B)	106.6	C(26)-C(25)-C(24)	120.64(17)
Si(1)-C(14)-H(14B)	106.6	C(26)-C(25)-H(25)	119.7
H(14A)-C(14)-H(14B)	106.6	C(24)-C(25)-H(25)	119.7
C(20)-C(15)-C(16)	118.37(16)	C(25)-C(26)-C(21)	120.96(18)
C(20)-C(15)-P(2)	122.11(14)	C(25)-C(26)-H(26)	119.5
C(16)-C(15)-P(2)	119.42(13)	C(21)-C(26)-H(26)	119.5
C(17)-C(16)-C(15)	120.91(19)	C(28)-C(27)-P(2)	115.47(13)
C(17)-C(16)-H(16)	119.5	C(28)-C(27)-H(27A)	108.4
C(15)-C(16)-H(16)	119.5	P(2)-C(27)-H(27A)	108.4
C(16)-C(17)-C(18)	120.2(2)	C(28)-C(27)-H(27B)	108.4
C(16)-C(17)-H(17)	119.9	P(2)-C(27)-H(27B)	108.4
C(18)-C(17)-H(17)	119.9	H(27A)-C(27)-H(27B)	107.5
C(19)-C(18)-C(17)	119.79(18)	C(27)-C(28)-Si(1)	121.51(12)
C(19)-C(18)-H(18)	120.1	C(27)-C(28)-H(28A)	106.9
C(17)-C(18)-H(18)	120.1	Si(1)-C(28)-H(28A)	106.9
C(18)-C(19)-C(20)	120.2(2)	C(27)-C(28)-H(28B)	106.9
C(18)-C(19)-H(19)	119.9	Si(1)-C(28)-H(28B)	106.9
C(20)-C(19)-H(19)	119.9	H(28A)-C(28)-H(28B)	106.7
C(15)-C(20)-C(19)	120.45(19)	C(34)-C(29)-C(30)	117.54(16)
C(15)-C(20)-H(20)	119.8	C(34)-C(29)-P(3)	123.76(14)
C(19)-C(20)-H(20)	119.8	C(30)-C(29)-P(3)	118.70(12)
C(22)-C(21)-C(26)	117.64(16)	C(31)-C(30)-C(29)	121.38(16)

C(31)-C(30)-H(30)	119.3	C(42)-C(41)-H(41A)	108.4
C(29)-C(30)-H(30)	119.3	P(3)-C(41)-H(41A)	108.4
C(32)-C(31)-C(30)	119.98(18)	C(42)-C(41)-H(41B)	108.4
C(32)-C(31)-H(31)	120.0	P(3)-C(41)-H(41B)	108.4
C(30)-C(31)-H(31)	120.0	H(41A)-C(41)-H(41B)	107.5
C(33)-C(32)-C(31)	119.31(17)	C(41)-C(42)-Si(1)	120.94(13)
C(33)-C(32)-H(32)	120.3	C(41)-C(42)-H(42A)	107.1
C(31)-C(32)-H(32)	120.3	Si(1)-C(42)-H(42A)	107.1
C(32)-C(33)-C(34)	120.77(18)	C(41)-C(42)-H(42B)	107.1
C(32)-C(33)-H(33)	119.6	Si(1)-C(42)-H(42B)	107.1
C(34)-C(33)-H(33)	119.6	H(42A)-C(42)-H(42B)	106.8
C(33)-C(34)-C(29)	120.97(18)	C(48)-C(43)-C(44)	117.97(16)
C(33)-C(34)-H(34)	119.5	C(48)-C(43)-P(4)	124.82(14)
C(29)-C(34)-H(34)	119.5	C(44)-C(43)-P(4)	117.21(13)
C(40)-C(35)-C(36)	118.41(17)	C(45)-C(44)-C(43)	121.21(17)
C(40)-C(35)-P(3)	123.76(15)	C(45)-C(44)-H(44)	119.4
C(36)-C(35)-P(3)	117.34(14)	C(43)-C(44)-H(44)	119.4
C(35)-C(36)-C(37)	121.0(2)	C(46)-C(45)-C(44)	120.02(18)
C(35)-C(36)-H(36)	119.5	C(46)-C(45)-H(45)	120.0
C(37)-C(36)-H(36)	119.5	C(44)-C(45)-H(45)	120.0
C(38)-C(37)-C(36)	120.0(2)	C(47)-C(46)-C(45)	119.61(17)
C(38)-C(37)-H(37)	120.0	C(47)-C(46)-H(46)	120.2
C(36)-C(37)-H(37)	120.0	C(45)-C(46)-H(46)	120.2
C(37)-C(38)-C(39)	120.1(2)	C(46)-C(47)-C(48)	120.03(17)
C(37)-C(38)-H(38)	119.9	C(46)-C(47)-H(47)	120.0
C(39)-C(38)-H(38)	119.9	C(48)-C(47)-H(47)	120.0
C(38)-C(39)-C(40)	120.0(2)	C(43)-C(48)-C(47)	121.09(17)
C(38)-C(39)-H(39)	120.0	C(43)-C(48)-H(48)	119.5
C(40)-C(39)-H(39)	120.0	C(47)-C(48)-H(48)	119.5
C(35)-C(40)-C(39)	120.5(2)	C(54)-C(49)-C(50)	118.26(16)
C(35)-C(40)-H(40)	119.8	C(54)-C(49)-P(4)	117.77(13)
C(39)-C(40)-H(40)	119.8	C(50)-C(49)-P(4)	123.97(14)
C(42)-C(41)-P(3)	115.56(12)	C(49)-C(50)-C(51)	120.35(18)

C(49)-C(50)-H(50)	119.8	Si(1)-C(61)-H(61B)	109.5
C(51)-C(50)-H(50)	119.8	H(61A)-C(61)-H(61B)	109.5
C(52)-C(51)-C(50)	120.59(19)	Si(1)-C(61)-H(61C)	109.5
C(52)-C(51)-H(51)	119.7	H(61A)-C(61)-H(61C)	109.5
C(50)-C(51)-H(51)	119.7	H(61B)-C(61)-H(61C)	109.5
C(53)-C(52)-C(51)	119.55(18)	C(3P)-C(2P)-C(1P)	110.2(4)
C(53)-C(52)-H(52)	120.2	C(3P)-C(2P)-H(2PA)	109.6
C(51)-C(52)-H(52)	120.2	C(1P)-C(2P)-H(2PA)	109.6
C(52)-C(53)-C(54)	120.04(19)	C(3P)-C(2P)-H(2PB)	109.6
C(52)-C(53)-H(53)	120.0	C(1P)-C(2P)-H(2PB)	109.6
C(54)-C(53)-H(53)	120.0	H(2PA)-C(2P)-H(2PB)	108.1
C(53)-C(54)-C(49)	121.17(18)	C(2P)-C(3P)-C(4P)	104.8(4)
C(53)-C(54)-H(54)	119.4	C(2P)-C(3P)-H(3PA)	110.8
C(49)-C(54)-H(54)	119.4	C(4P)-C(3P)-H(3PA)	110.8
C(60)-C(55)-C(56)	117.54(16)	C(2P)-C(3P)-H(3PB)	110.8
C(60)-C(55)-P(4)	119.16(13)	C(4P)-C(3P)-H(3PB)	110.8
C(56)-C(55)-P(4)	123.28(14)	H(3PA)-C(3P)-H(3PB)	108.9
C(57)-C(56)-C(55)	120.86(17)	C(5P)-C(4P)-C(3P)	100.6(4)
C(57)-C(56)-H(56)	119.6	C(5P)-C(4P)-H(4PA)	111.6
C(55)-C(56)-H(56)	119.6	C(3P)-C(4P)-H(4PA)	111.6
C(58)-C(57)-C(56)	120.61(18)	C(5P)-C(4P)-H(4PB)	111.6
C(58)-C(57)-H(57)	119.7	C(3P)-C(4P)-H(4PB)	111.6
C(56)-C(57)-H(57)	119.7	H(4PA)-C(4P)-H(4PB)	109.4
C(59)-C(58)-C(57)	119.24(18)	C(2Q)-C(1Q)-H(1QA)	109.5
C(59)-C(58)-H(58)	120.4	C(2Q)-C(1Q)-H(1QB)	109.5
C(57)-C(58)-H(58)	120.4	H(1QA)-C(1Q)-H(1QB)	109.5
C(58)-C(59)-C(60)	120.58(19)	C(2Q)-C(1Q)-H(1QC)	109.5
C(58)-C(59)-H(59)	119.7	H(1QA)-C(1Q)-H(1QC)	109.5
C(60)-C(59)-H(59)	119.7	H(1QB)-C(1Q)-H(1QC)	109.5
C(59)-C(60)-C(55)	121.17(17)	C(3Q)-C(2Q)-C(1Q)	85.5(9)
C(59)-C(60)-H(60)	119.4	C(3Q)-C(2Q)-H(2QA)	114.4
C(55)-C(60)-H(60)	119.4	C(1Q)-C(2Q)-H(2QA)	114.4
Si(1)-C(61)-H(61A)	109.5	C(3Q)-C(2Q)-H(2QB)	114.4

C(1Q)-C(2Q)-H(2QB)	114.4	C(3Q)-C(4Q)-H(4QA)	111.9
H(2QA)-C(2Q)-H(2QB)	111.5	C(5Q)-C(4Q)-H(4QB)	111.9
C(2Q)-C(3Q)-C(4Q)	84.6(9)	C(3Q)-C(4Q)-H(4QB)	111.9
C(2Q)-C(3Q)-H(3QA)	114.5	H(4QA)-C(4Q)-H(4QB)	109.6
C(4Q)-C(3Q)-H(3QA)	114.5	C(4Q)-C(5Q)-H(5QA)	109.5
C(2Q)-C(3Q)-H(3QB)	114.5	C(4Q)-C(5Q)-H(5QB)	109.5
C(4Q)-C(3Q)-H(3QB)	114.5	H(5QA)-C(5Q)-H(5QB)	109.5
H(3QA)-C(3Q)-H(3QB)	111.7	C(4Q)-C(5Q)-H(5QC)	109.5
C(5Q)-C(4Q)-C(3Q)	99.3(10)	H(5QA)-C(5Q)-H(5QC)	109.5
C(5Q)-C(4Q)-H(4QA)	111.9	H(5QB)-C(5Q)-H(5QC)	109.5

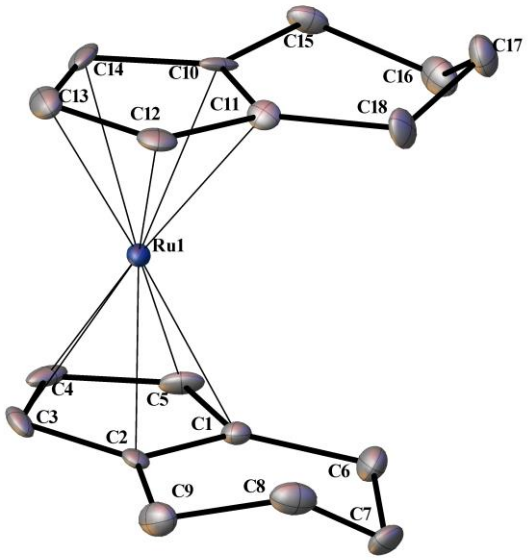

Figure A.6 X-ray structure of $Ru(C_9H_{11})_2$

Table A.21 Crystal data and structure refinement for $Ru(C_9H_{11})_2$.

Identification code	adi8

Empirical formula	C18 H22 Ru
Formula weight	339.42
Temperature	110(2) K
Wavelength	1.54178 Å
Crystal system	Monoclinic
Space group	P 1 c 1
Unit cell dimensions	a = 12.3717(14) Å □= 90°.
	b = 6.5709(7) Å □= 96.262(6)°.
	c = 17.5678(19) Å □ = 90°.
Volume	1419.6(3) $Å^3$
Z	4
Density (calculated)	1.588 Mg/m^3
Absorption coefficient	8.772 mm^{-1}
F(000)	696
Crystal size	0.10 x 0.08 x 0.04 mm^3
Theta range for data collection	3.594 to 61.056°.
Index ranges	-14<=h<=14, -7<=k<=7, -19<=l<=19
Reflections collected	29166
Independent reflections	4278 [R(int) = 0.0544]
Completeness to theta = 67.679°	83.9 %
Absorption correction	Semi-empirical from equivalents
Max. and min. transmission	0.7519 and 0.4831
Refinement method	Full-matrix least-squares on F^2
Data / restraints / parameters	4278 / 2 / 345
Goodness-of-fit on F^2	1.120
Final R indices [I>2sigma(I)]	R1 = 0.0209, wR2 = 0.0514
R indices (all data)	R1 = 0.0210, wR2 = 0.0514
Absolute structure parameter	0.496(10)
Extinction coefficient	0.0037(2)
Largest diff. peak and hole	0.565 and -0.682 $e.Å^{-3}$

Table A.22 Atomic coordinates (x 10^4) and equivalent isotropic displacement parameters ($Å^2$ x 10^3) for $Ru(C_9H_{11})_2$. U(eq) is defined as one third of the trace of the orthogonalized U^{ij} tensor.

	x	y	z	U(eq)
Ru(1)	4030(1)	6599(1)	1679(1)	9(1)
Ru(2)	9967(1)	2172(1)	4983(1)	8(1)
C(1)	5647(5)	8016(8)	1719(3)	10(1)
C(2)	5632(5)	6234(9)	1255(3)	9(1)
C(3)	4807(6)	6480(8)	627(4)	14(2)
C(4)	4318(5)	8431(9)	685(3)	17(1)
C(5)	4842(4)	9376(8)	1365(3)	14(1)
C(6)	6439(5)	8327(9)	2419(3)	17(1)
C(7)	7305(4)	6644(9)	2507(3)	18(1)
C(8)	6854(4)	4540(9)	2270(3)	19(1)
C(9)	6421(4)	4511(8)	1431(3)	17(1)
C(10)	2848(5)	7114(10)	2515(3)	12(1)
C(11)	3630(5)	5638(8)	2823(3)	11(1)
C(12)	3572(4)	3933(9)	2315(3)	14(1)
C(13)	2744(4)	4344(9)	1698(3)	19(1)
C(14)	2302(5)	6299(10)	1816(4)	18(2)
C(15)	2647(4)	9037(8)	2938(3)	14(1)
C(16)	3602(4)	9500(8)	3543(3)	18(1)
C(17)	3880(5)	7627(9)	4041(3)	18(1)
C(18)	4310(4)	5890(9)	3584(3)	16(1)
C(19)	11018(5)	2464(9)	4051(4)	10(1)
C(20)	10396(4)	632(8)	3941(3)	11(1)
C(21)	10679(4)	-626(8)	4595(3)	12(1)
C(22)	11466(4)	415(9)	5108(3)	17(1)
C(23)	11671(5)	2324(9)	4778(4)	11(1)
C(24)	10982(4)	4131(8)	3462(3)	16(1)
C(25)	9942(5)	3943(10)	2914(3)	22(1)
C(26)	9812(5)	1772(9)	2605(3)	21(1)

C(27)	9654(4)	213(9)	3223(3)	17(1)
C(28)	8226(5)	3078(8)	4906(3)	11(1)
C(29)	8464(5)	1670(9)	5528(3)	12(1)
C(30)	9285(5)	2568(10)	6064(4)	13(1)
C(31)	9561(4)	4493(8)	5785(3)	14(1)
C(32)	8919(4)	4816(8)	5062(3)	14(1)
C(33)	7359(5)	2760(9)	4254(3)	16(1)
C(34)	6604(4)	1025(9)	4430(3)	19(1)
C(35)	7250(4)	-806(9)	4781(3)	19(1)
C(36)	7836(4)	-284(8)	5559(3)	15(1)

Table A.23 Bond Lengths [Å] for $Ru(C_9H_{11})_2$.

Ru(1)-C(1)	2.200(6)	Ru(2)-C(32)	2.181(5)
Ru(1)-C(2)	2.205(6)	C(1)-C(2)	1.426(8)
Ru(1)-C(3)	2.175(6)	C(1)-C(5)	1.429(8)
Ru(1)-C(4)	2.182(5)	C(1)-C(6)	1.500(8)
Ru(1)-C(5)	2.182(5)	C(2)-C(3)	1.428(9)
Ru(1)-C(10)	2.210(6)	C(2)-C(9)	1.504(8)
Ru(1)-C(11)	2.214(5)	C(3)-H(3)	0.9500
Ru(1)-C(12)	2.186(5)	C(3)-C(4)	1.425(8)
Ru(1)-C(13)	2.177(5)	C(4)-H(4)	0.9500
Ru(1)-C(14)	2.186(6)	C(4)-C(5)	1.438(8)
Ru(2)-C(19)	2.207(6)	C(5)-H(5)	0.9500
Ru(2)-C(20)	2.207(5)	C(6)-H(6A)	0.9900
Ru(2)-C(21)	2.180(5)	C(6)-H(6B)	0.9900
Ru(2)-C(22)	2.175(5)	C(6)-C(7)	1.536(8)
Ru(2)-C(23)	2.179(6)	C(7)-H(7A)	0.9900
Ru(2)-C(28)	2.224(6)	C(7)-H(7B)	0.9900
Ru(2)-C(29)	2.207(6)	C(7)-C(8)	1.531(8)
Ru(2)-C(30)	2.177(6)	C(8)-H(8A)	0.9900
Ru(2)-C(31)	2.172(5)	C(8)-H(8B)	0.9900

C(8)-C(9)	1.514(8)	C(23)-H(23)	0.9500
C(9)-H(9A)	0.9900	C(24)-H(24A)	0.9900
C(9)-H(9B)	0.9900	C(24)-H(24B)	0.9900
C(10)-C(11)	1.433(8)	C(24)-C(25)	1.526(8)
C(10)-C(14)	1.438(9)	C(25)-H(25A)	0.9900
C(10)-C(15)	1.501(9)	C(25)-H(25B)	0.9900
C(11)-C(12)	1.430(7)	C(25)-C(26)	1.529(9)
C(11)-C(18)	1.508(7)	C(26)-H(26A)	0.9900
C(12)-H(12)	0.9500	C(26)-H(26B)	0.9900
C(12)-C(13)	1.433(7)	C(26)-C(27)	1.521(8)
C(13)-H(13)	0.9500	C(27)-H(27A)	0.9900
C(13)-C(14)	1.420(9)	C(27)-H(27B)	0.9900
C(14)-H(14)	0.9500	C(28)-C(29)	1.438(8)
C(15)-H(15A)	0.9900	C(28)-C(32)	1.436(8)
C(15)-H(15B)	0.9900	C(28)-C(33)	1.496(8)
C(15)-C(16)	1.531(7)	C(29)-C(30)	1.434(9)
C(16)-H(16A)	0.9900	C(29)-C(36)	1.505(8)
C(16)-H(16B)	0.9900	C(30)-H(30)	0.9500
C(16)-C(17)	1.528(8)	C(30)-C(31)	1.412(9)
C(17)-H(17A)	0.9900	C(31)-H(31)	0.9500
C(17)-H(17B)	0.9900	C(31)-C(32)	1.438(7)
C(17)-C(18)	1.525(8)	C(32)-H(32)	0.9500
C(18)-H(18A)	0.9900	C(33)-H(33A)	0.9900
C(18)-H(18B)	0.9900	C(33)-H(33B)	0.9900
C(19)-C(20)	1.430(8)	C(33)-C(34)	1.526(8)
C(19)-C(23)	1.437(9)	C(34)-H(34A)	0.9900
C(19)-C(24)	1.505(8)	C(34)-H(34B)	0.9900
C(20)-C(21)	1.428(8)	C(34)-C(35)	1.535(8)
C(20)-C(27)	1.501(7)	C(35)-H(35A)	0.9900
C(21)-H(21)	0.9500	C(35)-H(35B)	0.9900
C(21)-C(22)	1.428(7)	C(35)-C(36)	1.516(7)
C(22)-H(22)	0.9500	C(36)-H(36A)	0.9900
C(22)-C(23)	1.416(8)	C(36)-H(36B)	0.9900

Table A.24 Angles [°] for $Ru(C_9H_{11})_2$.

C(1)-Ru(1)-C(2)	37.8(2)	C(12)-Ru(1)-C(10)	63.6(2)
C(1)-Ru(1)-C(10)	125.4(2)	C(12)-Ru(1)-C(11)	37.92(19)
C(1)-Ru(1)-C(11)	112.6(2)	C(12)-Ru(1)-C(14)	63.9(2)
C(2)-Ru(1)-C(10)	157.8(2)	C(13)-Ru(1)-C(1)	162.0(2)
C(2)-Ru(1)-C(11)	125.0(2)	C(13)-Ru(1)-C(2)	128.1(2)
C(3)-Ru(1)-C(1)	63.8(2)	C(13)-Ru(1)-C(4)	124.8(2)
C(3)-Ru(1)-C(2)	38.0(2)	C(13)-Ru(1)-C(5)	158.5(2)
C(3)-Ru(1)-C(4)	38.2(2)	C(13)-Ru(1)-C(10)	63.6(2)
C(3)-Ru(1)-C(5)	63.8(2)	C(13)-Ru(1)-C(11)	63.6(2)
C(3)-Ru(1)-C(10)	163.0(2)	C(13)-Ru(1)-C(12)	38.34(19)
C(3)-Ru(1)-C(11)	157.6(2)	C(13)-Ru(1)-C(14)	38.0(2)
C(3)-Ru(1)-C(12)	124.7(2)	C(14)-Ru(1)-C(1)	158.6(2)
C(3)-Ru(1)-C(13)	112.3(2)	C(14)-Ru(1)-C(2)	162.4(2)
C(3)-Ru(1)-C(14)	128.2(3)	C(14)-Ru(1)-C(10)	38.2(2)
C(4)-Ru(1)-C(1)	64.2(2)	C(14)-Ru(1)-C(11)	63.6(2)
C(4)-Ru(1)-C(2)	63.8(2)	C(19)-Ru(2)-C(20)	37.8(2)
C(4)-Ru(1)-C(5)	38.5(2)	C(19)-Ru(2)-C(28)	125.2(2)
C(4)-Ru(1)-C(10)	128.7(2)	C(19)-Ru(2)-C(29)	158.0(2)
C(4)-Ru(1)-C(11)	162.98(19)	C(20)-Ru(2)-C(28)	113.0(2)
C(4)-Ru(1)-C(12)	157.7(2)	C(20)-Ru(2)-C(29)	125.6(2)
C(4)-Ru(1)-C(14)	112.6(2)	C(21)-Ru(2)-C(19)	63.3(2)
C(5)-Ru(1)-C(1)	38.1(2)	C(21)-Ru(2)-C(20)	38.0(2)
C(5)-Ru(1)-C(2)	63.3(2)	C(21)-Ru(2)-C(28)	128.9(2)
C(5)-Ru(1)-C(10)	113.3(2)	C(21)-Ru(2)-C(29)	113.4(2)
C(5)-Ru(1)-C(11)	128.47(19)	C(21)-Ru(2)-C(32)	162.70(18)
C(5)-Ru(1)-C(12)	162.07(19)	C(22)-Ru(2)-C(19)	63.7(2)
C(5)-Ru(1)-C(14)	125.8(2)	C(22)-Ru(2)-C(20)	63.9(2)
C(10)-Ru(1)-C(11)	37.8(2)	C(22)-Ru(2)-C(21)	38.3(2)
C(12)-Ru(1)-C(1)	127.5(2)	C(22)-Ru(2)-C(23)	38.0(2)
C(12)-Ru(1)-C(2)	112.2(2)	C(22)-Ru(2)-C(28)	163.2(2)

C(22)-Ru(2)-C(29)	128.8(2)	C(5)-C(1)-Ru(1)	70.3(3)
C(22)-Ru(2)-C(30)	112.5(2)	C(5)-C(1)-C(6)	129.3(5)
C(22)-Ru(2)-C(32)	157.3(2)	C(6)-C(1)-Ru(1)	126.5(4)
C(23)-Ru(2)-C(19)	38.2(2)	C(1)-C(2)-Ru(1)	70.9(3)
C(23)-Ru(2)-C(20)	63.8(2)	C(1)-C(2)-C(3)	108.2(5)
C(23)-Ru(2)-C(21)	63.6(2)	C(1)-C(2)-C(9)	122.2(5)
C(23)-Ru(2)-C(28)	157.7(2)	C(3)-C(2)-Ru(1)	69.8(3)
C(23)-Ru(2)-C(29)	162.6(2)	C(3)-C(2)-C(9)	129.6(5)
C(23)-Ru(2)-C(32)	124.5(2)	C(9)-C(2)-Ru(1)	126.8(4)
C(29)-Ru(2)-C(28)	37.9(2)	Ru(1)-C(3)-H(3)	122.7
C(30)-Ru(2)-C(19)	162.3(2)	C(2)-C(3)-Ru(1)	72.1(3)
C(30)-Ru(2)-C(20)	158.4(2)	C(2)-C(3)-H(3)	125.7
C(30)-Ru(2)-C(21)	125.6(2)	C(4)-C(3)-Ru(1)	71.2(3)
C(30)-Ru(2)-C(23)	127.8(3)	C(4)-C(3)-C(2)	108.7(5)
C(30)-Ru(2)-C(28)	63.7(2)	C(4)-C(3)-H(3)	125.7
C(30)-Ru(2)-C(29)	38.2(2)	Ru(1)-C(4)-H(4)	123.7
C(30)-Ru(2)-C(32)	63.9(2)	C(3)-C(4)-Ru(1)	70.6(3)
C(31)-Ru(2)-C(19)	128.1(2)	C(3)-C(4)-H(4)	126.5
C(31)-Ru(2)-C(20)	162.5(2)	C(3)-C(4)-C(5)	107.0(5)
C(31)-Ru(2)-C(21)	157.68(19)	C(5)-C(4)-Ru(1)	70.8(3)
C(31)-Ru(2)-C(22)	124.2(2)	C(5)-C(4)-H(4)	126.5
C(31)-Ru(2)-C(23)	111.8(2)	Ru(1)-C(5)-H(5)	123.6
C(31)-Ru(2)-C(28)	63.9(2)	C(1)-C(5)-Ru(1)	71.7(3)
C(31)-Ru(2)-C(29)	63.8(2)	C(1)-C(5)-C(4)	108.7(5)
C(31)-Ru(2)-C(30)	37.9(2)	C(1)-C(5)-H(5)	125.6
C(31)-Ru(2)-C(32)	38.59(19)	C(4)-C(5)-Ru(1)	70.8(3)
C(32)-Ru(2)-C(19)	112.4(2)	C(4)-C(5)-H(5)	125.6
C(32)-Ru(2)-C(20)	128.1(2)	C(1)-C(6)-H(6A)	109.3
C(32)-Ru(2)-C(28)	38.04(19)	C(1)-C(6)-H(6B)	109.3
C(32)-Ru(2)-C(29)	63.7(2)	C(1)-C(6)-C(7)	111.8(5)
C(2)-C(1)-Ru(1)	71.3(3)	H(6A)-C(6)-H(6B)	107.9
C(2)-C(1)-C(5)	107.5(5)	C(7)-C(6)-H(6A)	109.3
C(2)-C(1)-C(6)	123.2(5)	C(7)-C(6)-H(6B)	109.3

C(6)-C(7)-H(7A)	108.9	C(11)-C(12)-C(13)	107.9(5)
C(6)-C(7)-H(7B)	108.9	C(13)-C(12)-Ru(1)	70.5(3)
H(7A)-C(7)-H(7B)	107.8	C(13)-C(12)-H(12)	126.0
C(8)-C(7)-C(6)	113.1(4)	Ru(1)-C(13)-H(13)	123.3
C(8)-C(7)-H(7A)	108.9	C(12)-C(13)-Ru(1)	71.2(3)
C(8)-C(7)-H(7B)	108.9	C(12)-C(13)-H(13)	125.8
C(7)-C(8)-H(8A)	109.5	C(14)-C(13)-Ru(1)	71.4(3)
C(7)-C(8)-H(8B)	109.5	C(14)-C(13)-C(12)	108.4(5)
H(8A)-C(8)-H(8B)	108.1	C(14)-C(13)-H(13)	125.8
C(9)-C(8)-C(7)	110.9(5)	Ru(1)-C(14)-H(14)	123.2
C(9)-C(8)-H(8A)	109.5	C(10)-C(14)-Ru(1)	71.8(3)
C(9)-C(8)-H(8B)	109.5	C(10)-C(14)-H(14)	126.0
C(2)-C(9)-C(8)	110.1(5)	C(13)-C(14)-Ru(1)	70.7(3)
C(2)-C(9)-H(9A)	109.6	C(13)-C(14)-C(10)	108.0(5)
C(2)-C(9)-H(9B)	109.6	C(13)-C(14)-H(14)	126.0
C(8)-C(9)-H(9A)	109.6	C(10)-C(15)-H(15A)	109.5
C(8)-C(9)-H(9B)	109.6	C(10)-C(15)-H(15B)	109.5
H(9A)-C(9)-H(9B)	108.2	C(10)-C(15)-C(16)	110.7(4)
C(11)-C(10)-Ru(1)	71.3(3)	H(15A)-C(15)-H(15B)	108.1
C(11)-C(10)-C(14)	107.8(5)	C(16)-C(15)-H(15A)	109.5
C(11)-C(10)-C(15)	121.6(5)	C(16)-C(15)-H(15B)	109.5
C(14)-C(10)-Ru(1)	70.0(4)	C(15)-C(16)-H(16A)	109.6
C(14)-C(10)-C(15)	130.4(6)	C(15)-C(16)-H(16B)	109.6
C(15)-C(10)-Ru(1)	128.0(4)	H(16A)-C(16)-H(16B)	108.1
C(10)-C(11)-Ru(1)	70.9(3)	C(17)-C(16)-C(15)	110.2(5)
C(10)-C(11)-C(18)	123.2(5)	C(17)-C(16)-H(16A)	109.6
C(12)-C(11)-Ru(1)	70.0(3)	C(17)-C(16)-H(16B)	109.6
C(12)-C(11)-C(10)	108.0(5)	C(16)-C(17)-H(17A)	109.3
C(12)-C(11)-C(18)	128.7(5)	C(16)-C(17)-H(17B)	109.3
C(18)-C(11)-Ru(1)	127.9(4)	H(17A)-C(17)-H(17B)	107.9
Ru(1)-C(12)-H(12)	123.0	C(18)-C(17)-C(16)	111.7(5)
C(11)-C(12)-Ru(1)	72.1(3)	C(18)-C(17)-H(17A)	109.3
C(11)-C(12)-H(12)	126.0	C(18)-C(17)-H(17B)	109.3

C(11)-C(18)-C(17)	110.9(4)	C(22)-C(23)-Ru(2)	70.8(3)
C(11)-C(18)-H(18A)	109.5	C(22)-C(23)-C(19)	108.2(5)
C(11)-C(18)-H(18B)	109.5	C(22)-C(23)-H(23)	125.9
C(17)-C(18)-H(18A)	109.5	C(19)-C(24)-H(24A)	109.8
C(17)-C(18)-H(18B)	109.5	C(19)-C(24)-H(24B)	109.8
H(18A)-C(18)-H(18B)	108.1	C(19)-C(24)-C(25)	109.6(5)
C(20)-C(19)-Ru(2)	71.1(3)	H(24A)-C(24)-H(24B)	108.2
C(20)-C(19)-C(23)	108.0(5)	C(25)-C(24)-H(24A)	109.8
C(20)-C(19)-C(24)	123.0(5)	C(25)-C(24)-H(24B)	109.8
C(23)-C(19)-Ru(2)	69.8(3)	C(24)-C(25)-H(25A)	109.6
C(23)-C(19)-C(24)	129.0(5)	C(24)-C(25)-H(25B)	109.6
C(24)-C(19)-Ru(2)	126.7(4)	C(24)-C(25)-C(26)	110.3(5)
C(19)-C(20)-Ru(2)	71.1(3)	H(25A)-C(25)-H(25B)	108.1
C(19)-C(20)-C(27)	122.6(5)	C(26)-C(25)-H(25A)	109.6
C(21)-C(20)-Ru(2)	70.0(3)	C(26)-C(25)-H(25B)	109.6
C(21)-C(20)-C(19)	107.3(5)	C(25)-C(26)-H(26A)	109.0
C(21)-C(20)-C(27)	130.0(5)	C(25)-C(26)-H(26B)	109.0
C(27)-C(20)-Ru(2)	126.9(4)	H(26A)-C(26)-H(26B)	107.8
Ru(2)-C(21)-H(21)	123.3	C(27)-C(26)-C(25)	113.0(5)
C(20)-C(21)-Ru(2)	72.0(3)	C(27)-C(26)-H(26A)	109.0
C(20)-C(21)-H(21)	125.6	C(27)-C(26)-H(26B)	109.0
C(22)-C(21)-Ru(2)	70.7(3)	C(20)-C(27)-C(26)	111.2(5)
C(22)-C(21)-C(20)	108.7(5)	C(20)-C(27)-H(27A)	109.4
C(22)-C(21)-H(21)	125.6	C(20)-C(27)-H(27B)	109.4
Ru(2)-C(22)-H(22)	123.3	C(26)-C(27)-H(27A)	109.4
C(21)-C(22)-Ru(2)	71.1(3)	C(26)-C(27)-H(27B)	109.4
C(21)-C(22)-H(22)	126.1	H(27A)-C(27)-H(27B)	108.0
C(23)-C(22)-Ru(2)	71.2(3)	C(29)-C(28)-Ru(2)	70.4(3)
C(23)-C(22)-C(21)	107.8(5)	C(29)-C(28)-C(33)	124.2(5)
C(23)-C(22)-H(22)	126.1	C(32)-C(28)-Ru(2)	69.4(3)
Ru(2)-C(23)-H(23)	123.0	C(32)-C(28)-C(29)	107.3(5)
C(19)-C(23)-Ru(2)	71.9(4)	C(32)-C(28)-C(33)	128.4(5)
C(19)-C(23)-H(23)	125.9	C(33)-C(28)-Ru(2)	128.2(4)

C(28)-C(29)-Ru(2)	71.7(3)	C(28)-C(33)-H(33A)	109.5
C(28)-C(29)-C(36)	120.8(5)	C(28)-C(33)-H(33B)	109.5
C(30)-C(29)-Ru(2)	69.8(3)	C(28)-C(33)-C(34)	110.7(5)
C(30)-C(29)-C(28)	107.8(5)	H(33A)-C(33)-H(33B)	108.1
C(30)-C(29)-C(36)	131.2(6)	C(34)-C(33)-H(33A)	109.5
C(36)-C(29)-Ru(2)	127.3(4)	C(34)-C(33)-H(33B)	109.5
Ru(2)-C(30)-H(30)	123.1	C(33)-C(34)-H(34A)	109.4
C(29)-C(30)-Ru(2)	72.1(3)	C(33)-C(34)-H(34B)	109.4
C(29)-C(30)-H(30)	125.6	C(33)-C(34)-C(35)	111.3(4)
C(31)-C(30)-Ru(2)	70.9(3)	H(34A)-C(34)-H(34B)	108.0
C(31)-C(30)-C(29)	108.7(5)	C(35)-C(34)-H(34A)	109.4
C(31)-C(30)-H(30)	125.6	C(35)-C(34)-H(34B)	109.4
Ru(2)-C(31)-H(31)	123.3	C(34)-C(35)-H(35A)	109.4
C(30)-C(31)-Ru(2)	71.2(3)	C(34)-C(35)-H(35B)	109.4
C(30)-C(31)-H(31)	126.0	H(35A)-C(35)-H(35B)	108.0
C(30)-C(31)-C(32)	107.9(5)	C(36)-C(35)-C(34)	111.2(5)
C(32)-C(31)-Ru(2)	71.0(3)	C(36)-C(35)-H(35A)	109.4
C(32)-C(31)-H(31)	126.0	C(36)-C(35)-H(35B)	109.4
Ru(2)-C(32)-H(32)	122.8	C(29)-C(36)-C(35)	111.0(5)
C(28)-C(32)-Ru(2)	72.6(3)	C(29)-C(36)-H(36A)	109.4
C(28)-C(32)-C(31)	108.2(5)	C(29)-C(36)-H(36B)	109.4
C(28)-C(32)-H(32)	125.9	C(35)-C(36)-H(36A)	109.4
C(31)-C(32)-Ru(2)	70.4(3)	C(35)-C(36)-H(36B)	109.4
C(31)-C(32)-H(32)	125.9	H(36A)-C(36)-H(36B)	108.0

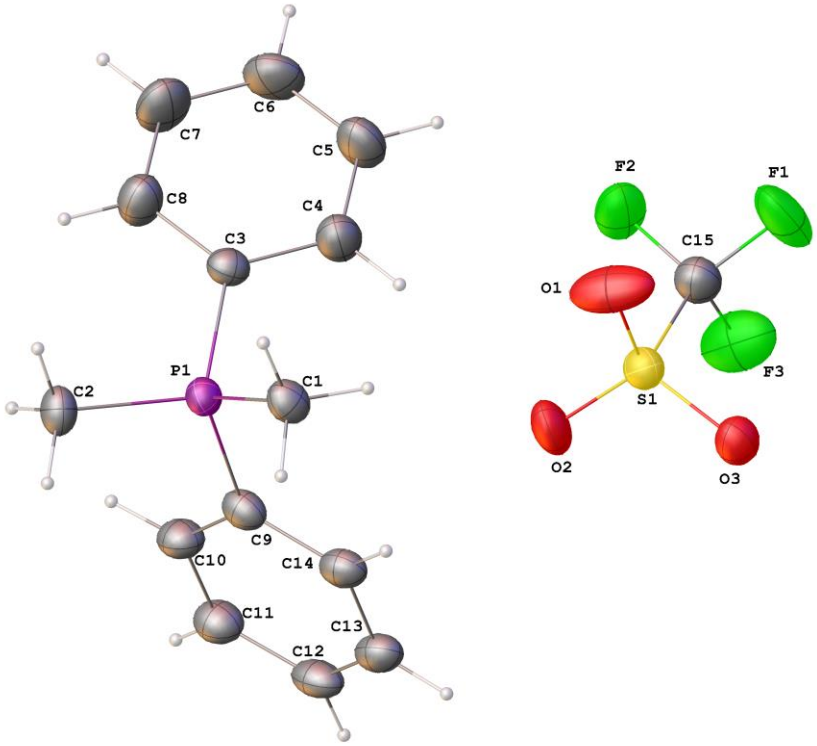

Figure A.7 X-ray structure of $[Ph_2Me_2P][O_3SCF_3]$.

Table A.25 Crystal data and structure refinement for $[Ph_2Me_2P][O_3SCF_3]$.

Identification code	p21_c	
Empirical formula	C15 H16 F3 O3 P S	
Formula weight	364.31	
Temperature	110(2) K	
Wavelength	1.54178 Å	
Crystal system	Monoclinic	
Space group	P2(1)/c	
Unit cell dimensions	a = 12.0810(9) Å	□= 90°.
	b = 13.5081(11) Å	□= 105.831(4)°.
	c = 10.5159(8) Å	□ = 90°.
Volume	1651.0(2) Å3	

Z	4
Density (calculated)	1.466 Mg/m^3
Absorption coefficient	3.056 mm^{-1}
F(000)	752
Crystal size	0.14 x 0.04 x 0.01 mm^3
Theta range for data collection	3.80 to 59.98°.
Index ranges	-13<=h<=13, -15<=k<=15, -10<=l<=11
Reflections collected	25208
Independent reflections	2446 [R(int) = 0.0546]
Completeness to theta = 59.98°	99.7 %
Absorption correction	Semi-empirical from equivalents
Max. and min. transmission	0.9701 and 0.6743
Refinement method	Full-matrix least-squares on F^2
Data / restraints / parameters	2446 / 181 / 229
Goodness-of-fit on F^2	1.044
Final R indices [I>2sigma(I)]	R1 = 0.0350, wR2 = 0.0835
R indices (all data)	R1 = 0.0531, wR2 = 0.0899
Largest diff. peak and hole	0.316 and -0.274 $e.Å^{-3}$

Table A.26 Atomic coordinates (x 10^4) and equivalent isotropic displacement parameters ($Å^2$ x 10^3) for $[Ph_2Me_2P][O_3SCF_3]$. U(eq) is defined as one third of the trace of the orthogonalized U^{ij} tensor.

	x	y	z	U(eq)
P(1)	8299(1)	5939(1)	7107(1)	22(1)
C(1)	9152(2)	6377(2)	6090(2)	28(1)
C(2)	8855(2)	6419(2)	8735(2)	29(1)
C(3)	6830(2)	6296(2)	6420(2)	25(1)
C(4)	6302(2)	6060(2)	5112(3)	37(1)
C(5)	5150(2)	6266(2)	4565(3)	42(1)
C(6)	4524(2)	6694(2)	5323(3)	47(1)
C(7)	5035(3)	6923(2)	6633(3)	52(1)

C(8)	6195(2)	6732(2)	7182(3)	39(1)
C(9)	8360(40)	4616(3)	7160(30)	27(1)
C(10)	7914(10)	4069(5)	8028(13)	31(1)
C(11)	7891(8)	3048(6)	7960(8)	34(2)
C(12)	8320(7)	2557(5)	7051(9)	34(2)
C(13)	8788(7)	3098(6)	6204(9)	31(1)
C(14)	8802(14)	4131(6)	6240(13)	29(1)
C(9A)	8280(50)	4617(3)	7190(40)	27(1)
C(10A)	7729(14)	4251(7)	8098(17)	31(1)
C(11A)	7668(10)	3243(8)	8268(11)	34(2)
C(12A)	8129(8)	2602(7)	7534(12)	34(2)
C(13A)	8638(10)	2956(8)	6593(10)	31(1)
C(14A)	8734(18)	3975(8)	6433(17)	29(1)
C(15)	6598(2)	5228(2)	1238(3)	36(1)
F(1)	6332(1)	5623(2)	32(2)	63(1)
F(2)	5912(1)	5634(1)	1877(2)	49(1)
F(3)	6343(2)	4276(1)	1076(2)	63(1)
S(1)	8114(1)	5424(1)	2070(1)	28(1)
O(1)	8240(2)	6468(2)	2067(2)	61(1)
O(2)	8236(2)	4985(2)	3353(2)	46(1)
O(3)	8697(2)	4881(1)	1275(2)	37(1)

Table A.27 Bond Lengths [Å] for $[Ph_2Me_2P][O_3SCF_3]$.

P(1)-C(1)	1.777(2)	C(2)-H(2A)	0.9800
P(1)-C(2)	1.782(2)	C(2)-H(2B)	0.9800
P(1)-C(9A)	1.788(4)	C(2)-H(2C)	0.9800
P(1)-C(9)	1.788(3)	C(3)-C(8)	1.383(4)
P(1)-C(3)	1.790(2)	C(3)-C(4)	1.387(4)
C(1)-H(1A)	0.9800	C(4)-C(5)	1.382(4)
C(1)-H(1B)	0.9800	C(4)-H(4)	0.9500
C(1)-H(1C)	0.9800	C(5)-C(6)	1.368(4)

C(5)-H(5)	0.9500	C(10A)-C(11A)	1.379(5)
C(6)-C(7)	1.381(4)	C(10A)-H(10A)	0.9500
C(6)-H(6)	0.9500	C(11A)-C(12A)	1.374(6)
C(7)-C(8)	1.387(4)	C(11A)-H(11A)	0.9500
C(7)-H(7)	0.9500	C(12A)-C(13A)	1.385(6)
C(8)-H(8)	0.9500	C(12A)-H(12A)	0.9500
C(9)-C(14)	1.389(5)	C(13A)-C(14A)	1.395(5)
C(9)-C(10)	1.394(5)	C(13A)-H(13A)	0.9500
C(10)-C(11)	1.381(5)	C(14A)-H(14A)	0.9500
C(10)-H(10)	0.9500	C(15)-F(2)	1.321(3)
C(11)-C(12)	1.375(6)	C(15)-F(3)	1.323(3)
C(11)-H(11)	0.9500	C(15)-F(1)	1.332(3)
C(12)-C(13)	1.387(6)	C(15)-S(1)	1.820(3)
C(12)-H(12)	0.9500	S(1)-O(1)	1.418(2)
C(13)-C(14)	1.395(5)	S(1)-O(3)	1.4332(19)
C(13)-H(13)	0.9500	S(1)-O(2)	1.4442(19)
C(14)-H(14)	0.9500		
C(9A)-C(14A)	1.389(5)		
C(9A)-C(10A)	1.394(5)		

Table A.28 Angles [°] for $[Ph_2Me_2P][O_3SCF_3]$.

C(1)-P(1)-C(2)	109.20(12)	P(1)-C(1)-H(1A)	109.5
C(1)-P(1)-C(9A)	112.4(6)	P(1)-C(1)-H(1B)	109.5
C(2)-P(1)-C(9A)	108.9(15)	H(1A)-C(1)-H(1B)	109.5
C(1)-P(1)-C(9)	109.0(5)	P(1)-C(1)-H(1C)	109.5
C(2)-P(1)-C(9)	109.4(12)	H(1A)-C(1)-H(1C)	109.5
C(9A)-P(1)-C(9)	4(2)	H(1B)-C(1)-H(1C)	109.5
C(1)-P(1)-C(3)	109.92(12)	P(1)-C(2)-H(2A)	109.5
C(2)-P(1)-C(3)	111.19(12)	P(1)-C(2)-H(2B)	109.5
C(9A)-P(1)-C(3)	105.2(18)	H(2A)-C(2)-H(2B)	109.5
C(9)-P(1)-C(3)	108.1(14)	P(1)-C(2)-H(2C)	109.5

H(2A)-C(2)-H(2C)	109.5	C(12)-C(13)-H(13)	119.5
H(2B)-C(2)-H(2C)	109.5	C(14)-C(13)-H(13)	119.6
C(8)-C(3)-C(4)	119.7(2)	C(9)-C(14)-C(13)	119.2(6)
C(8)-C(3)-P(1)	121.78(19)	C(9)-C(14)-H(14)	120.4
C(4)-C(3)-P(1)	118.4(2)	C(13)-C(14)-H(14)	120.4
C(5)-C(4)-C(3)	120.3(3)	C(14A)-C(9A)-C(10A)	120.6(6)
C(5)-C(4)-H(4)	119.8	C(14A)-C(9A)-P(1)	125.7(9)
C(3)-C(4)-H(4)	119.8	C(10A)-C(9A)-P(1)	113.8(8)
C(6)-C(5)-C(4)	119.8(3)	C(11A)-C(10A)-C(9A)	119.4(8)
C(6)-C(5)-H(5)	120.1	C(11A)-C(10A)-H(10A)	120.3
C(4)-C(5)-H(5)	120.1	C(9A)-C(10A)-H(10A)	120.3
C(5)-C(6)-C(7)	120.5(3)	C(12A)-C(11A)-C(10A)	120.4(9)
C(5)-C(6)-H(6)	119.7	C(12A)-C(11A)-H(11A)	119.8
C(7)-C(6)-H(6)	119.7	C(10A)-C(11A)-H(11A)	119.8
C(6)-C(7)-C(8)	120.0(3)	C(11A)-C(12A)-C(13A)	120.8(8)
C(6)-C(7)-H(7)	120.0	C(11A)-C(12A)-H(12A)	119.6
C(8)-C(7)-H(7)	120.0	C(13A)-C(12A)-H(12A)	119.6
C(3)-C(8)-C(7)	119.7(3)	C(12A)-C(13A)-C(14A)	119.6(9)
C(3)-C(8)-H(8)	120.2	C(12A)-C(13A)-H(13A)	120.3
C(7)-C(8)-H(8)	120.2	C(14A)-C(13A)-H(13A)	120.2
C(14)-C(9)-C(10)	119.7(5)	C(9A)-C(14A)-C(13A)	119.3(8)
C(14)-C(9)-P(1)	118.1(7)	C(9A)-C(14A)-H(14A)	120.3
C(10)-C(9)-P(1)	122.0(6)	C(13A)-C(14A)-H(14A)	120.4
C(11)-C(10)-C(9)	120.2(7)	F(2)-C(15)-F(3)	108.2(2)
C(11)-C(10)-H(10)	120.0	F(2)-C(15)-F(1)	107.2(2)
C(9)-C(10)-H(10)	119.8	F(3)-C(15)-F(1)	106.2(2)
C(12)-C(11)-C(10)	120.8(6)	F(2)-C(15)-S(1)	112.57(18)
C(12)-C(11)-H(11)	119.6	F(3)-C(15)-S(1)	111.83(18)
C(10)-C(11)-H(11)	119.6	F(1)-C(15)-S(1)	110.45(19)
C(11)-C(12)-C(13)	119.2(6)	O(1)-S(1)-O(3)	115.95(13)
C(11)-C(12)-H(12)	120.4	O(1)-S(1)-O(2)	115.24(14)
C(13)-C(12)-H(12)	120.4	O(3)-S(1)-O(2)	113.15(12)
C(12)-C(13)-C(14)	120.9(6)	O(1)-S(1)-C(15)	103.77(13)

O(3)-S(1)-C(15)	103.62(12)	O(2)-S(1)-C(15)	102.86(12)

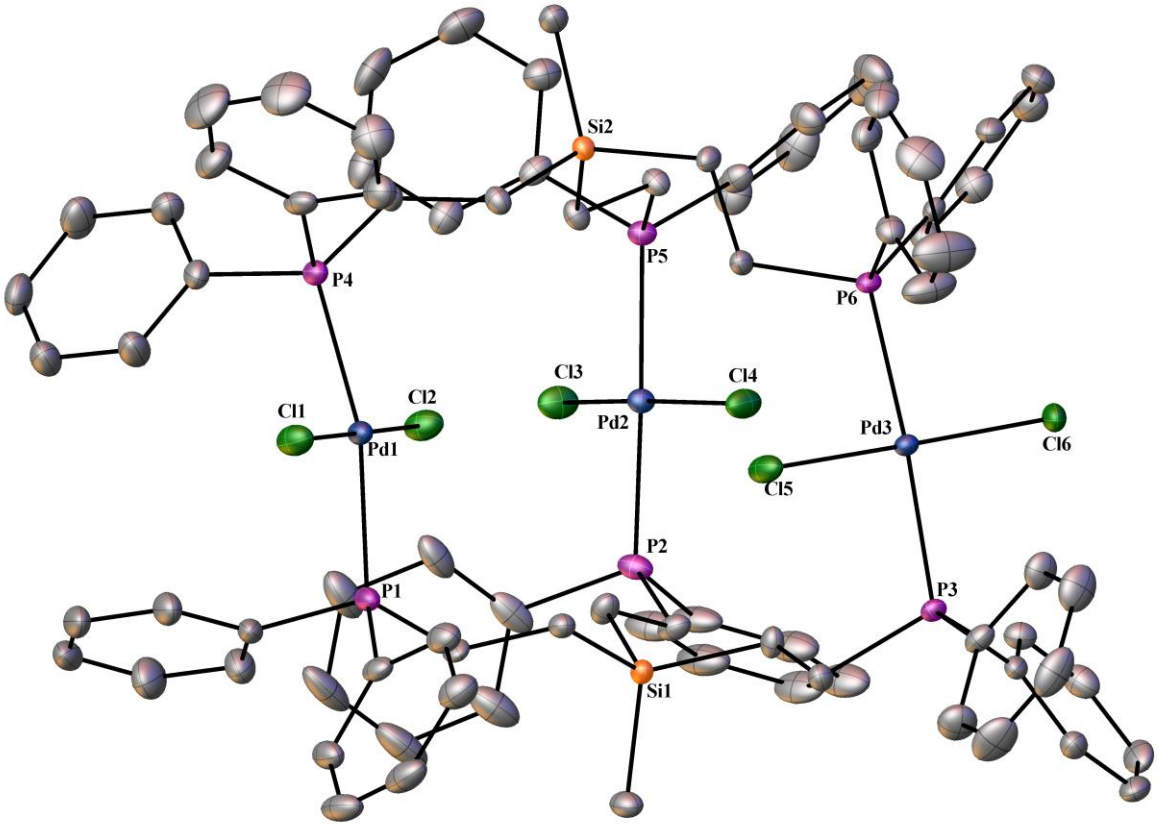

Figure A.8 X-ray structure of $(Cl_2Pd)_3[(PPh_2CH_2CH_2)_3SiMe]_2$.

Table A.29 Crystal data for for $(Cl_2Pd)_3[(PPh_2CH_2CH_2)_3SiMe]_2$.

Identification code	b2p47
Empirical formula	C91.40 H100.80 Cl16.80 P6 Pd3 Si2
Formula weight	2356.07
Temperature	110.15 K
Wavelength	0.71073 Å

Crystal system	Triclinic	
Space group	P-1	
Unit cell dimensions	a = 16.840(3) Å	α= 105.01(3)°.
	b = 17.518(4) Å	β= 91.64(3)°.
	c = 20.586(4) Å	γ = 117.01(3)°.
Volume	5150(2) $Å^3$	
Z	2	
Density (calculated)	1.519 Mg/m^3	
Absorption coefficient	1.113 mm^{-1}	
F(000)	2382	
Crystal size	0.56 x 0.51 x 0.26 mm^3	
Theta range for data collection	1.377 to 27.535°.	
Index ranges	-21<=h<=21, -22<=k<=22, -26<=l<=26	
Reflections collected	60110	
Independent reflections	23264 [R(int) = 0.0402]	
Completeness to theta = 25.242°	99.6 %	
Absorption correction	Semi-empirical from equivalents	
Max. and min. transmission	0.7456 and 0.4361	
Refinement method	Full-matrix least-squares on F^2	
Data / restraints / parameters	23264 / 497 / 1153	
Goodness-of-fit on F^2	1.019	
Final R indices [I>2sigma(I)]	R1 = 0.0497, wR2 = 0.1221	
R indices (all data)	R1 = 0.0688, wR2 = 0.1351	
Extinction coefficient	n/a	
Largest diff. peak and hole	2.730 and -1.935 e.$Å^{-3}$	

Table A.30 Atomic coordinates (x 10^4) and equivalent isotropic displacement parameters ($Å^2$ x 10^3) for $(Cl_2Pd)_3[(PPh_2CH_2CH_2)_3SiMe]_2$. U(eq) is defined as one third of the trace of the orthogonalized U^{ij} tensor.

	x	y	z	U(eq)
Pd(1)	-602(1)	2213(1)	7806(1)	16(1)

Pd(2)	3079(1)	5504(1)	6414(1)	13(1)
Pd(3)	3895(1)	2343(1)	7293(1)	12(1)
Cl(1)	-1578(1)	1153(1)	8266(1)	25(1)
Cl(2)	362(1)	3277(1)	7347(1)	25(1)
Cl(3)	2799(1)	6474(1)	6002(1)	24(1)
Cl(4)	3534(1)	4585(1)	6747(1)	23(1)
Cl(5)	2430(1)	1643(1)	7480(1)	25(1)
Cl(6)	5381(1)	2947(1)	7178(1)	20(1)
P(1)	-1154(1)	1204(1)	6723(1)	18(1)
P(2)	2412(1)	4468(1)	5350(1)	18(1)
P(3)	3458(1)	1205(1)	6265(1)	12(1)
P(4)	-317(1)	3345(1)	8800(1)	16(1)
P(5)	3708(1)	6537(1)	7496(1)	14(1)
P(6)	4216(1)	3411(1)	8336(1)	12(1)
Si(1)	1218(1)	1727(1)	5634(1)	13(1)
Si(2)	2707(1)	5021(1)	9019(1)	12(1)
C(1)	-407(3)	1404(3)	6097(2)	18(1)
C(2)	474(3)	1373(3)	6275(2)	17(1)
C(3)	1474(3)	2904(3)	5702(2)	19(1)
C(4)	2193(3)	3333(3)	5285(2)	19(1)
C(5)	2334(3)	1768(3)	5810(2)	17(1)
C(6)	2334(3)	906(3)	5849(2)	16(1)
C(7)	631(3)	982(3)	4755(2)	22(1)
C(8)	795(3)	4335(3)	8991(2)	16(1)
C(9)	1567(3)	4094(3)	9014(2)	16(1)
C(10)	2722(3)	5385(3)	8236(2)	16(1)
C(11)	3682(3)	6049(3)	8186(2)	15(1)
C(12)	3535(3)	4581(3)	9044(2)	15(1)
C(13)	3358(3)	3793(3)	8422(2)	15(1)
C(14)	3019(3)	6012(3)	9783(2)	20(1)
C(15)	-2078(3)	1370(3)	6421(2)	24(1)
C(16)	-2810(3)	1173(4)	6770(3)	32(1)
C(17)	-3476(3)	1383(4)	6607(3)	36(1)

C(18)	-3425(3)	1788(4)	6114(3)	39(1)
C(19)	-2709(4)	1984(4)	5764(3)	41(1)
C(20)	-2039(3)	1769(4)	5918(3)	33(1)
C(21)	-1640(3)	9(3)	6615(2)	21(1)
C(22)	-2405(3)	-624(3)	6139(2)	27(1)
C(23)	-2726(3)	-1534(3)	6059(3)	34(1)
C(24)	-2279(3)	-1804(3)	6438(3)	35(1)
C(25)	-1500(3)	-1184(3)	6905(3)	31(1)
C(26)	-1182(3)	-272(3)	6992(2)	27(1)
C(27)	1279(3)	4295(7)	5083(4)	28(2)
C(28)	784(4)	4432(6)	5587(4)	30(2)
C(29)	-125(4)	4174(5)	5410(4)	38(2)
C(30)	-539(3)	3779(5)	4730(5)	43(2)
C(31)	-44(4)	3641(5)	4225(4)	47(2)
C(32)	865(5)	3899(6)	4402(4)	38(2)
C(27A)	1315(9)	4206(17)	4987(10)	32(3)
C(28A)	720(12)	4375(15)	5378(8)	31(3)
C(29A)	-161(10)	4077(12)	5076(10)	38(3)
C(30A)	-445(8)	3611(11)	4384(10)	41(3)
C(31A)	150(11)	3442(12)	3993(8)	43(3)
C(32A)	1030(11)	3739(15)	4295(10)	36(3)
C(33)	2992(16)	4799(19)	4672(11)	34(3)
C(34)	2850(14)	5366(18)	4378(11)	37(3)
C(35)	3354(13)	5672(13)	3890(10)	40(4)
C(36)	4000(12)	5412(12)	3696(8)	38(3)
C(37)	4143(12)	4845(13)	3991(9)	39(3)
C(38)	3639(15)	4538(16)	4479(10)	38(3)
C(33A)	3137(6)	4759(7)	4718(4)	28(2)
C(34A)	3081(5)	5312(6)	4362(4)	34(2)
C(35A)	3656(5)	5560(5)	3896(4)	39(2)
C(36A)	4288(5)	5256(5)	3788(3)	41(2)
C(37A)	4344(5)	4704(5)	4144(4)	41(2)
C(38A)	3769(6)	4455(6)	4610(4)	38(2)

C(39)	3395(3)	216(3)	6430(2)	17(1)
C(40)	2757(3)	-652(3)	6064(3)	28(1)
C(41)	2743(4)	-1384(3)	6221(3)	36(1)
C(42)	3360(4)	-1248(3)	6745(3)	34(1)
C(43)	3999(4)	-391(4)	7114(3)	33(1)
C(44)	4021(3)	342(3)	6963(2)	23(1)
C(45)	4136(3)	1383(3)	5600(2)	15(1)
C(46)	4230(3)	683(3)	5166(2)	19(1)
C(47)	4739(3)	833(3)	4651(2)	24(1)
C(48)	5152(3)	1672(3)	4563(2)	26(1)
C(49)	5054(3)	2362(3)	4979(2)	24(1)
C(50)	4556(3)	2229(3)	5502(2)	18(1)
C(51)	-1130(3)	3731(3)	8680(2)	20(1)
C(52)	-923(3)	4623(3)	8900(2)	27(1)
C(53)	-1556(4)	4884(4)	8749(3)	36(1)
C(54)	-2393(3)	4248(4)	8370(3)	32(1)
C(55)	-2616(3)	3352(4)	8168(3)	35(1)
C(56)	-1986(3)	3099(4)	8315(3)	34(1)
C(57)	-474(3)	3054(3)	9591(2)	21(1)
C(58)	40(3)	2703(3)	9806(2)	25(1)
C(59)	-36(4)	2504(4)	10413(3)	35(1)
C(60)	-634(4)	2645(4)	10804(3)	42(1)
C(61)	-1160(4)	2967(4)	10587(3)	43(1)
C(62)	-1081(3)	3184(3)	9983(3)	31(1)
C(63)	3205(3)	7254(3)	7813(2)	18(1)
C(64)	3708(3)	8071(3)	8325(2)	26(1)
C(65)	3322(4)	8606(4)	8581(3)	36(1)
C(66)	2442(4)	8343(4)	8332(3)	36(1)
C(67)	1934(4)	7543(4)	7828(3)	30(1)
C(68)	2315(3)	6991(3)	7567(2)	23(1)
C(69)	4885(3)	7358(3)	7566(2)	18(1)
C(70)	5580(3)	7470(3)	8024(2)	26(1)
C(71)	6448(3)	8158(4)	8090(3)	36(1)

C(72)	6624(3)	8740(3)	7712(3)	37(1)
C(73)	5939(4)	8624(4)	7251(3)	39(1)
C(74)	5068(3)	7930(3)	7170(3)	29(1)
C(75)	5264(3)	4453(3)	8494(2)	14(1)
C(76)	5957(3)	4791(3)	9038(2)	19(1)
C(77)	6732(3)	5593(3)	9116(2)	26(1)
C(78)	6828(3)	6063(3)	8659(2)	27(1)
C(79)	6141(3)	5727(3)	8111(2)	25(1)
C(80)	5364(3)	4938(3)	8030(2)	19(1)
C(81)	4265(3)	2950(3)	9025(2)	18(1)
C(82)	4163(4)	2094(4)	8861(3)	39(1)
C(83)	4163(5)	1699(4)	9362(3)	49(2)
C(84)	4267(4)	2158(4)	10033(3)	37(1)
C(85)	4373(3)	3018(4)	10208(2)	29(1)
C(86)	4376(3)	3412(3)	9711(2)	25(1)
Cl(1M)	2000(1)	2248(1)	9746(1)	62(1)
Cl(2M)	698(1)	1327(1)	8500(1)	52(1)
C(10S)	1587(4)	1361(4)	8989(3)	38(1)
Cl(1P)	5836(2)	-3(2)	9498(1)	96(1)
Cl(2P)	6087(2)	1160(3)	8642(3)	199(2)
C(13S)	6565(6)	679(7)	9052(5)	92(3)
Cl(3M)	-938(2)	-773(2)	9023(2)	108(1)
Cl(4M)	-1939(2)	-46(2)	9858(1)	86(1)
C(11S)	-1034(6)	174(6)	9436(5)	74(2)
Cl(5M)	791(2)	-940(2)	8000(1)	70(1)
Cl(6M)	643(1)	-1125(2)	6574(1)	109(1)
C(12S)	1363(5)	-721(5)	7325(4)	56(2)
Cl(7M)	156(2)	5283(2)	7401(2)	102(1)
Cl(8M)	-1649(2)	4445(3)	6663(2)	152(2)
C(14S)	-858(6)	4308(7)	7104(5)	79(3)
Cl(3P)	969(5)	3478(7)	2108(6)	159(4)
Cl(4P)	2159(4)	3186(5)	2780(3)	99(2)
C(15S)	1818(13)	3847(12)	2634(8)	57(4)

Table A.31 Bond Lengths [Å] for $(Cl_2Pd)_3[(PPh_2CH_2CH_2)_3SiMe]_2$.

Pd(1)-Cl(1)	2.2979(14)	P(6)-C(75)	1.814(4)
Pd(1)-Cl(2)	2.2918(14)	P(6)-C(81)	1.822(4)
Pd(1)-P(1)	2.3033(16)	Si(1)-C(2)	1.873(4)
Pd(1)-P(4)	2.3087(15)	Si(1)-C(3)	1.871(4)
Pd(2)-Cl(3)	2.2997(12)	Si(1)-C(5)	1.868(4)
Pd(2)-Cl(4)	2.3030(11)	Si(1)-C(7)	1.859(4)
Pd(2)-P(2)	2.3013(16)	Si(2)-C(9)	1.866(4)
Pd(2)-P(5)	2.3232(16)	Si(2)-C(10)	1.878(4)
Pd(3)-Cl(5)	2.2990(13)	Si(2)-C(12)	1.879(4)
Pd(3)-Cl(6)	2.2797(12)	Si(2)-C(14)	1.864(4)
Pd(3)-P(3)	2.3203(15)	C(1)-H(1A)	0.9900
Pd(3)-P(6)	2.3099(14)	C(1)-H(1B)	0.9900
P(1)-C(1)	1.814(4)	C(1)-C(2)	1.545(6)
P(1)-C(15)	1.825(5)	C(2)-H(2A)	0.9900
P(1)-C(21)	1.815(5)	C(2)-H(2B)	0.9900
P(2)-C(4)	1.817(4)	C(3)-H(3A)	0.9900
P(2)-C(27)	1.834(4)	C(3)-H(3B)	0.9900
P(2)-C(27A)	1.776(10)	C(3)-C(4)	1.527(6)
P(2)-C(33)	1.795(11)	C(4)-H(4A)	0.9900
P(2)-C(33A)	1.820(4)	C(4)-H(4B)	0.9900
P(3)-C(6)	1.834(4)	C(5)-H(5A)	0.9900
P(3)-C(39)	1.809(4)	C(5)-H(5B)	0.9900
P(3)-C(45)	1.807(4)	C(5)-C(6)	1.533(6)
P(4)-C(8)	1.823(4)	C(6)-H(6A)	0.9900
P(4)-C(51)	1.818(4)	C(6)-H(6B)	0.9900
P(4)-C(57)	1.819(5)	C(7)-H(7A)	0.9800
P(5)-C(11)	1.830(4)	C(7)-H(7B)	0.9800
P(5)-C(63)	1.815(4)	C(7)-H(7C)	0.9800
P(5)-C(69)	1.817(4)	C(8)-H(8A)	0.9900
P(6)-C(13)	1.843(4)	C(8)-H(8B)	0.9900

C(8)-C(9)	1.541(5)	C(24)-H(24)	0.9500
C(9)-H(9A)	0.9900	C(24)-C(25)	1.385(7)
C(9)-H(9B)	0.9900	C(25)-H(25)	0.9500
C(10)-H(10A)	0.9900	C(25)-C(26)	1.392(7)
C(10)-H(10B)	0.9900	C(26)-H(26)	0.9500
C(10)-C(11)	1.529(5)	C(27)-C(28)	1.3900
C(11)-H(11A)	0.9900	C(27)-C(32)	1.3900
C(11)-H(11B)	0.9900	C(28)-H(28)	0.9500
C(12)-H(12A)	0.9900	C(28)-C(29)	1.3900
C(12)-H(12B)	0.9900	C(29)-H(29)	0.9500
C(12)-C(13)	1.523(5)	C(29)-C(30)	1.3900
C(13)-H(13A)	0.9900	C(30)-H(30)	0.9500
C(13)-H(13B)	0.9900	C(30)-C(31)	1.3900
C(14)-H(14A)	0.9800	C(31)-H(31)	0.9500
C(14)-H(14B)	0.9800	C(31)-C(32)	1.3900
C(14)-H(14C)	0.9800	C(32)-H(32)	0.9500
C(15)-C(16)	1.395(6)	C(27A)-C(28A)	1.3900
C(15)-C(20)	1.381(7)	C(27A)-C(32A)	1.3900
C(16)-H(16)	0.9500	C(28A)-H(28A)	0.9500
C(16)-C(17)	1.388(7)	C(28A)-C(29A)	1.3900
C(17)-H(17)	0.9500	C(29A)-H(29A)	0.9500
C(17)-C(18)	1.366(8)	C(29A)-C(30A)	1.3900
C(18)-H(18)	0.9500	C(30A)-H(30A)	0.9500
C(18)-C(19)	1.376(8)	C(30A)-C(31A)	1.3900
C(19)-H(19)	0.9500	C(31A)-H(31A)	0.9500
C(19)-C(20)	1.393(7)	C(31A)-C(32A)	1.3900
C(20)-H(20)	0.9500	C(32A)-H(32A)	0.9500
C(21)-C(22)	1.385(6)	C(33)-C(34)	1.3900
C(21)-C(26)	1.396(7)	C(33)-C(38)	1.3900
C(22)-H(22)	0.9500	C(34)-H(34)	0.9500
C(22)-C(23)	1.392(7)	C(34)-C(35)	1.3900
C(23)-H(23)	0.9500	C(35)-H(35)	0.9500
C(23)-C(24)	1.371(8)	C(35)-C(36)	1.3900

C(36)-H(36)	0.9500	C(48)-H(48)	0.9500
C(36)-C(37)	1.3900	C(48)-C(49)	1.369(7)
C(37)-H(37)	0.9500	C(49)-H(49)	0.9500
C(37)-C(38)	1.3900	C(49)-C(50)	1.385(6)
C(38)-H(38)	0.9500	C(50)-H(50)	0.9500
C(33A)-C(34A)	1.3900	C(51)-C(52)	1.377(6)
C(33A)-C(38A)	1.3900	C(51)-C(56)	1.388(6)
C(34A)-H(34A)	0.9500	C(52)-H(52)	0.9500
C(34A)-C(35A)	1.3900	C(52)-C(53)	1.393(7)
C(35A)-H(35A)	0.9500	C(53)-H(53)	0.9500
C(35A)-C(36A)	1.3900	C(53)-C(54)	1.378(7)
C(36A)-H(36A)	0.9500	C(54)-H(54)	0.9500
C(36A)-C(37A)	1.3900	C(54)-C(55)	1.376(7)
C(37A)-H(37A)	0.9500	C(55)-H(55)	0.9500
C(37A)-C(38A)	1.3900	C(55)-C(56)	1.375(7)
C(38A)-H(38A)	0.9500	C(56)-H(56)	0.9500
C(39)-C(40)	1.382(6)	C(57)-C(58)	1.387(7)
C(39)-C(44)	1.399(6)	C(57)-C(62)	1.384(6)
C(40)-H(40)	0.9500	C(58)-H(58)	0.9500
C(40)-C(41)	1.393(7)	C(58)-C(59)	1.377(7)
C(41)-H(41)	0.9500	C(59)-H(59)	0.9500
C(41)-C(42)	1.369(8)	C(59)-C(60)	1.376(8)
C(42)-H(42)	0.9500	C(60)-H(60)	0.9500
C(42)-C(43)	1.373(8)	C(60)-C(61)	1.365(9)
C(43)-H(43)	0.9500	C(61)-H(61)	0.9500
C(43)-C(44)	1.383(6)	C(61)-C(62)	1.385(7)
C(44)-H(44)	0.9500	C(62)-H(62)	0.9500
C(45)-C(46)	1.394(6)	C(63)-C(64)	1.394(6)
C(45)-C(50)	1.396(6)	C(63)-C(68)	1.388(6)
C(46)-H(46)	0.9500	C(64)-H(64)	0.9500
C(46)-C(47)	1.386(6)	C(64)-C(65)	1.376(7)
C(47)-H(47)	0.9500	C(65)-H(65)	0.9500
C(47)-C(48)	1.377(7)	C(65)-C(66)	1.373(8)

C(66)-H(66)	0.9500	C(83)-H(83)	0.9500
C(66)-C(67)	1.371(8)	C(83)-C(84)	1.367(8)
C(67)-H(67)	0.9500	C(84)-H(84)	0.9500
C(67)-C(68)	1.395(6)	C(84)-C(85)	1.378(7)
C(68)-H(68)	0.9500	C(85)-H(85)	0.9500
C(69)-C(70)	1.390(6)	C(85)-C(86)	1.374(6)
C(69)-C(74)	1.386(6)	C(86)-H(86)	0.9500
C(70)-H(70)	0.9500	Cl(1M)-C(10S)	1.741(6)
C(70)-C(71)	1.383(7)	Cl(2M)-C(10S)	1.749(6)
C(71)-H(71)	0.9500	C(10S)-H(10C)	0.9900
C(71)-C(72)	1.372(8)	C(10S)-H(10D)	0.9900
C(72)-H(72)	0.9500	Cl(1P)-C(13S)	1.756(9)
C(72)-C(73)	1.377(8)	Cl(2P)-C(13S)	1.736(11)
C(73)-H(73)	0.9500	C(13S)-H(13C)	0.9900
C(73)-C(74)	1.384(7)	C(13S)-H(13D)	0.9900
C(74)-H(74)	0.9500	Cl(3M)-C(11S)	1.739(9)
C(75)-C(76)	1.385(6)	Cl(4M)-C(11S)	1.715(8)
C(75)-C(80)	1.400(6)	C(11S)-H(11C)	0.9900
C(76)-H(76)	0.9500	C(11S)-H(11D)	0.9900
C(76)-C(77)	1.382(6)	Cl(5M)-C(12S)	1.739(7)
C(77)-H(77)	0.9500	Cl(6M)-C(12S)	1.706(8)
C(77)-C(78)	1.371(7)	C(12S)-H(12C)	0.9900
C(78)-H(78)	0.9500	C(12S)-H(12D)	0.9900
C(78)-C(79)	1.386(7)	Cl(7M)-C(14S)	1.719(10)
C(79)-H(79)	0.9500	Cl(8M)-C(14S)	1.729(8)
C(79)-C(80)	1.370(6)	C(14S)-H(14D)	0.9900
C(80)-H(80)	0.9500	C(14S)-H(14E)	0.9900
C(81)-C(82)	1.375(7)	Cl(3P)-C(15S)	1.53(2)
C(81)-C(86)	1.393(6)	Cl(4P)-C(15S)	1.59(2)
C(82)-H(82)	0.9500	C(15S)-H(15A)	0.9900
C(82)-C(83)	1.384(7)	C(15S)-H(15B)	0.9900

Table A.32 Angles [°] for $(Cl_2Pd)_3[(PPh_2CH_2CH_2)_3SiMe]_2$.

Cl(1)-Pd(1)-P(1)	91.35(5)	C(27A)-P(2)-C(33A)	106.8(8)
Cl(1)-Pd(1)-P(4)	90.67(5)	C(33)-P(2)-Pd(2)	114.2(10)
Cl(2)-Pd(1)-Cl(1)	179.42(4)	C(33)-P(2)-C(4)	108.9(9)
Cl(2)-Pd(1)-P(1)	88.76(5)	C(33)-P(2)-C(27)	102.7(9)
Cl(2)-Pd(1)-P(4)	89.07(5)	C(33A)-P(2)-Pd(2)	111.4(4)
P(1)-Pd(1)-P(4)	164.56(4)	C(6)-P(3)-Pd(3)	110.65(14)
Cl(3)-Pd(2)-Cl(4)	171.85(4)	C(39)-P(3)-Pd(3)	108.94(14)
Cl(3)-Pd(2)-P(2)	86.88(5)	C(39)-P(3)-C(6)	107.9(2)
Cl(3)-Pd(2)-P(5)	92.88(4)	C(45)-P(3)-Pd(3)	119.70(14)
Cl(4)-Pd(2)-P(5)	88.84(4)	C(45)-P(3)-C(6)	103.54(19)
P(2)-Pd(2)-Cl(4)	91.65(5)	C(45)-P(3)-C(39)	105.43(19)
P(2)-Pd(2)-P(5)	178.22(4)	C(8)-P(4)-Pd(1)	115.93(14)
Cl(5)-Pd(3)-P(3)	87.97(5)	C(51)-P(4)-Pd(1)	105.38(15)
Cl(5)-Pd(3)-P(6)	87.43(6)	C(51)-P(4)-C(8)	106.0(2)
Cl(6)-Pd(3)-Cl(5)	173.44(4)	C(51)-P(4)-C(57)	105.4(2)
Cl(6)-Pd(3)-P(3)	92.47(6)	C(57)-P(4)-Pd(1)	118.01(14)
Cl(6)-Pd(3)-P(6)	92.04(6)	C(57)-P(4)-C(8)	105.1(2)
P(6)-Pd(3)-P(3)	175.37(4)	C(11)-P(5)-Pd(2)	115.12(14)
C(1)-P(1)-Pd(1)	117.03(15)	C(63)-P(5)-Pd(2)	117.16(15)
C(1)-P(1)-C(15)	105.0(2)	C(63)-P(5)-C(11)	102.10(19)
C(1)-P(1)-C(21)	104.9(2)	C(63)-P(5)-C(69)	101.8(2)
C(15)-P(1)-Pd(1)	103.18(15)	C(69)-P(5)-Pd(2)	113.36(15)
C(21)-P(1)-Pd(1)	119.30(15)	C(69)-P(5)-C(11)	105.61(19)
C(21)-P(1)-C(15)	106.0(2)	C(13)-P(6)-Pd(3)	111.29(13)
C(4)-P(2)-Pd(2)	115.15(15)	C(75)-P(6)-Pd(3)	115.97(13)
C(4)-P(2)-C(27)	102.1(4)	C(75)-P(6)-C(13)	102.80(18)
C(4)-P(2)-C(33A)	103.4(4)	C(75)-P(6)-C(81)	106.96(19)
C(27)-P(2)-Pd(2)	112.3(3)	C(81)-P(6)-Pd(3)	110.02(14)
C(27A)-P(2)-Pd(2)	119.9(7)	C(81)-P(6)-C(13)	109.42(19)
C(27A)-P(2)-C(4)	98.3(9)	C(3)-Si(1)-C(2)	107.11(19)

C(5)-Si(1)-C(2)	113.18(19)	C(3)-C(4)-H(4B)	109.3
C(5)-Si(1)-C(3)	106.16(19)	H(4A)-C(4)-H(4B)	107.9
C(7)-Si(1)-C(2)	110.7(2)	Si(1)-C(5)-H(5A)	107.8
C(7)-Si(1)-C(3)	109.3(2)	Si(1)-C(5)-H(5B)	107.8
C(7)-Si(1)-C(5)	110.2(2)	H(5A)-C(5)-H(5B)	107.1
C(9)-Si(2)-C(10)	111.03(19)	C(6)-C(5)-Si(1)	118.0(3)
C(9)-Si(2)-C(12)	107.35(19)	C(6)-C(5)-H(5A)	107.8
C(10)-Si(2)-C(12)	109.87(18)	C(6)-C(5)-H(5B)	107.8
C(14)-Si(2)-C(9)	110.0(2)	P(3)-C(6)-H(6A)	110.0
C(14)-Si(2)-C(10)	108.3(2)	P(3)-C(6)-H(6B)	110.0
C(14)-Si(2)-C(12)	110.26(19)	C(5)-C(6)-P(3)	108.6(3)
P(1)-C(1)-H(1A)	108.6	C(5)-C(6)-H(6A)	110.0
P(1)-C(1)-H(1B)	108.6	C(5)-C(6)-H(6B)	110.0
H(1A)-C(1)-H(1B)	107.6	H(6A)-C(6)-H(6B)	108.4
C(2)-C(1)-P(1)	114.5(3)	Si(1)-C(7)-H(7A)	109.5
C(2)-C(1)-H(1A)	108.6	Si(1)-C(7)-H(7B)	109.5
C(2)-C(1)-H(1B)	108.6	Si(1)-C(7)-H(7C)	109.5
Si(1)-C(2)-H(2A)	110.0	H(7A)-C(7)-H(7B)	109.5
Si(1)-C(2)-H(2B)	110.0	H(7A)-C(7)-H(7C)	109.5
C(1)-C(2)-Si(1)	108.6(3)	H(7B)-C(7)-H(7C)	109.5
C(1)-C(2)-H(2A)	110.0	P(4)-C(8)-H(8A)	109.2
C(1)-C(2)-H(2B)	110.0	P(4)-C(8)-H(8B)	109.2
H(2A)-C(2)-H(2B)	108.3	H(8A)-C(8)-H(8B)	107.9
Si(1)-C(3)-H(3A)	109.0	C(9)-C(8)-P(4)	112.1(3)
Si(1)-C(3)-H(3B)	109.0	C(9)-C(8)-H(8A)	109.2
H(3A)-C(3)-H(3B)	107.8	C(9)-C(8)-H(8B)	109.2
C(4)-C(3)-Si(1)	112.8(3)	Si(2)-C(9)-H(9A)	108.6
C(4)-C(3)-H(3A)	109.0	Si(2)-C(9)-H(9B)	108.6
C(4)-C(3)-H(3B)	109.0	C(8)-C(9)-Si(2)	114.6(3)
P(2)-C(4)-H(4A)	109.3	C(8)-C(9)-H(9A)	108.6
P(2)-C(4)-H(4B)	109.3	C(8)-C(9)-H(9B)	108.6
C(3)-C(4)-P(2)	111.7(3)	H(9A)-C(9)-H(9B)	107.6
C(3)-C(4)-H(4A)	109.3	Si(2)-C(10)-H(10A)	109.4

Si(2)-C(10)-H(10B)	109.4	C(17)-C(16)-C(15)	119.7(5)
H(10A)-C(10)-H(10B)	108.0	C(17)-C(16)-H(16)	120.1
C(11)-C(10)-Si(2)	111.3(3)	C(16)-C(17)-H(17)	119.4
C(11)-C(10)-H(10A)	109.4	C(18)-C(17)-C(16)	121.1(5)
C(11)-C(10)-H(10B)	109.4	C(18)-C(17)-H(17)	119.4
P(5)-C(11)-H(11A)	109.1	C(17)-C(18)-H(18)	120.1
P(5)-C(11)-H(11B)	109.1	C(17)-C(18)-C(19)	119.8(5)
C(10)-C(11)-P(5)	112.6(3)	C(19)-C(18)-H(18)	120.1
C(10)-C(11)-H(11A)	109.1	C(18)-C(19)-H(19)	120.2
C(10)-C(11)-H(11B)	109.1	C(18)-C(19)-C(20)	119.7(6)
H(11A)-C(11)-H(11B)	107.8	C(20)-C(19)-H(19)	120.2
Si(2)-C(12)-H(12A)	108.7	C(15)-C(20)-C(19)	121.0(5)
Si(2)-C(12)-H(12B)	108.7	C(15)-C(20)-H(20)	119.5
H(12A)-C(12)-H(12B)	107.6	C(19)-C(20)-H(20)	119.5
C(13)-C(12)-Si(2)	114.1(3)	C(22)-C(21)-P(1)	121.9(4)
C(13)-C(12)-H(12A)	108.7	C(22)-C(21)-C(26)	119.8(4)
C(13)-C(12)-H(12B)	108.7	C(26)-C(21)-P(1)	118.1(3)
P(6)-C(13)-H(13A)	107.9	C(21)-C(22)-H(22)	120.3
P(6)-C(13)-H(13B)	107.9	C(21)-C(22)-C(23)	119.4(5)
C(12)-C(13)-P(6)	117.7(3)	C(23)-C(22)-H(22)	120.3
C(12)-C(13)-H(13A)	107.9	C(22)-C(23)-H(23)	119.8
C(12)-C(13)-H(13B)	107.9	C(24)-C(23)-C(22)	120.4(5)
H(13A)-C(13)-H(13B)	107.2	C(24)-C(23)-H(23)	119.8
Si(2)-C(14)-H(14A)	109.5	C(23)-C(24)-H(24)	119.4
Si(2)-C(14)-H(14B)	109.5	C(23)-C(24)-C(25)	121.1(5)
Si(2)-C(14)-H(14C)	109.5	C(25)-C(24)-H(24)	119.4
H(14A)-C(14)-H(14B)	109.5	C(24)-C(25)-H(25)	120.7
H(14A)-C(14)-H(14C)	109.5	C(24)-C(25)-C(26)	118.7(5)
H(14B)-C(14)-H(14C)	109.5	C(26)-C(25)-H(25)	120.7
C(16)-C(15)-P(1)	117.9(4)	C(21)-C(26)-H(26)	119.7
C(20)-C(15)-P(1)	123.1(4)	C(25)-C(26)-C(21)	120.6(4)
C(20)-C(15)-C(16)	118.6(4)	C(25)-C(26)-H(26)	119.7
C(15)-C(16)-H(16)	120.1	C(28)-C(27)-P(2)	118.0(4)

C(28)-C(27)-C(32)	120.0	C(31A)-C(32A)-C(27A)	120.0
C(32)-C(27)-P(2)	121.2(4)	C(31A)-C(32A)-H(32A)	120.0
C(27)-C(28)-H(28)	120.0	C(34)-C(33)-P(2)	120.6(13)
C(27)-C(28)-C(29)	120.0	C(34)-C(33)-C(38)	120.0
C(29)-C(28)-H(28)	120.0	C(38)-C(33)-P(2)	119.3(13)
C(28)-C(29)-H(29)	120.0	C(33)-C(34)-H(34)	120.0
C(30)-C(29)-C(28)	120.0	C(33)-C(34)-C(35)	120.0
C(30)-C(29)-H(29)	120.0	C(35)-C(34)-H(34)	120.0
C(29)-C(30)-H(30)	120.0	C(34)-C(35)-H(35)	120.0
C(29)-C(30)-C(31)	120.0	C(36)-C(35)-C(34)	120.0
C(31)-C(30)-H(30)	120.0	C(36)-C(35)-H(35)	120.0
C(30)-C(31)-H(31)	120.0	C(35)-C(36)-H(36)	120.0
C(32)-C(31)-C(30)	120.0	C(37)-C(36)-C(35)	120.0
C(32)-C(31)-H(31)	120.0	C(37)-C(36)-H(36)	120.0
C(27)-C(32)-H(32)	120.0	C(36)-C(37)-H(37)	120.0
C(31)-C(32)-C(27)	120.0	C(36)-C(37)-C(38)	120.0
C(31)-C(32)-H(32)	120.0	C(38)-C(37)-H(37)	120.0
C(28A)-C(27A)-P(2)	122.6(12)	C(33)-C(38)-H(38)	120.0
C(28A)-C(27A)-C(32A)	120.0	C(37)-C(38)-C(33)	120.0
C(32A)-C(27A)-P(2)	117.2(12)	C(37)-C(38)-H(38)	120.0
C(27A)-C(28A)-H(28A)	120.0	C(34A)-C(33A)-P(2)	120.0(5)
C(29A)-C(28A)-C(27A)	120.0	C(34A)-C(33A)-C(38A)	120.0
C(29A)-C(28A)-H(28A)	120.0	C(38A)-C(33A)-P(2)	120.0(5)
C(28A)-C(29A)-H(29A)	120.0	C(33A)-C(34A)-H(34A)	120.0
C(30A)-C(29A)-C(28A)	120.0	C(35A)-C(34A)-C(33A)	120.0
C(30A)-C(29A)-H(29A)	120.0	C(35A)-C(34A)-H(34A)	120.0
C(29A)-C(30A)-H(30A)	120.0	C(34A)-C(35A)-H(35A)	120.0
C(29A)-C(30A)-C(31A)	120.0	C(34A)-C(35A)-C(36A)	120.0
C(31A)-C(30A)-H(30A)	120.0	C(36A)-C(35A)-H(35A)	120.0
C(30A)-C(31A)-H(31A)	120.0	C(35A)-C(36A)-H(36A)	120.0
C(30A)-C(31A)-C(32A)	120.0	C(35A)-C(36A)-C(37A)	120.0
C(32A)-C(31A)-H(31A)	120.0	C(37A)-C(36A)-H(36A)	120.0
C(27A)-C(32A)-H(32A)	120.0	C(36A)-C(37A)-H(37A)	120.0

C(38A)-C(37A)-C(36A)	120.0	C(49)-C(48)-C(47)	120.2(4)
C(38A)-C(37A)-H(37A)	120.0	C(49)-C(48)-H(48)	119.9
C(33A)-C(38A)-H(38A)	120.0	C(48)-C(49)-H(49)	119.8
C(37A)-C(38A)-C(33A)	120.0	C(48)-C(49)-C(50)	120.4(4)
C(37A)-C(38A)-H(38A)	120.0	C(50)-C(49)-H(49)	119.8
C(40)-C(39)-P(3)	123.4(4)	C(45)-C(50)-H(50)	120.0
C(40)-C(39)-C(44)	118.7(4)	C(49)-C(50)-C(45)	120.0(4)
C(44)-C(39)-P(3)	117.9(3)	C(49)-C(50)-H(50)	120.0
C(39)-C(40)-H(40)	119.8	C(52)-C(51)-P(4)	123.3(3)
C(39)-C(40)-C(41)	120.4(5)	C(52)-C(51)-C(56)	118.6(4)
C(41)-C(40)-H(40)	119.8	C(56)-C(51)-P(4)	118.1(4)
C(40)-C(41)-H(41)	120.0	C(51)-C(52)-H(52)	119.7
C(42)-C(41)-C(40)	120.1(5)	C(51)-C(52)-C(53)	120.5(5)
C(42)-C(41)-H(41)	120.0	C(53)-C(52)-H(52)	119.7
C(41)-C(42)-H(42)	119.8	C(52)-C(53)-H(53)	120.1
C(41)-C(42)-C(43)	120.3(5)	C(54)-C(53)-C(52)	119.9(5)
C(43)-C(42)-H(42)	119.8	C(54)-C(53)-H(53)	120.1
C(42)-C(43)-H(43)	119.9	C(53)-C(54)-H(54)	120.0
C(42)-C(43)-C(44)	120.2(5)	C(55)-C(54)-C(53)	119.9(5)
C(44)-C(43)-H(43)	119.9	C(55)-C(54)-H(54)	120.0
C(39)-C(44)-H(44)	119.8	C(54)-C(55)-H(55)	120.1
C(43)-C(44)-C(39)	120.3(5)	C(56)-C(55)-C(54)	119.9(5)
C(43)-C(44)-H(44)	119.8	C(56)-C(55)-H(55)	120.1
C(46)-C(45)-P(3)	121.2(3)	C(51)-C(56)-H(56)	119.4
C(46)-C(45)-C(50)	118.9(4)	C(55)-C(56)-C(51)	121.2(5)
C(50)-C(45)-P(3)	119.8(3)	C(55)-C(56)-H(56)	119.4
C(45)-C(46)-H(46)	119.9	C(58)-C(57)-P(4)	118.7(3)
C(47)-C(46)-C(45)	120.1(4)	C(62)-C(57)-P(4)	121.7(4)
C(47)-C(46)-H(46)	119.9	C(62)-C(57)-C(58)	119.6(4)
C(46)-C(47)-H(47)	119.9	C(57)-C(58)-H(58)	119.8
C(48)-C(47)-C(46)	120.2(4)	C(59)-C(58)-C(57)	120.5(4)
C(48)-C(47)-H(47)	119.9	C(59)-C(58)-H(58)	119.8
C(47)-C(48)-H(48)	119.9	C(58)-C(59)-H(59)	120.2

C(60)-C(59)-C(58)	119.6(5)	C(71)-C(70)-C(69)	119.9(5)
C(60)-C(59)-H(59)	120.2	C(71)-C(70)-H(70)	120.1
C(59)-C(60)-H(60)	119.8	C(70)-C(71)-H(71)	119.8
C(61)-C(60)-C(59)	120.3(5)	C(72)-C(71)-C(70)	120.3(5)
C(61)-C(60)-H(60)	119.8	C(72)-C(71)-H(71)	119.8
C(60)-C(61)-H(61)	119.6	C(71)-C(72)-H(72)	120.1
C(60)-C(61)-C(62)	120.8(5)	C(71)-C(72)-C(73)	119.9(5)
C(62)-C(61)-H(61)	119.6	C(73)-C(72)-H(72)	120.1
C(57)-C(62)-C(61)	119.2(5)	C(72)-C(73)-H(73)	119.6
C(57)-C(62)-H(62)	120.4	C(72)-C(73)-C(74)	120.7(5)
C(61)-C(62)-H(62)	120.4	C(74)-C(73)-H(73)	119.6
C(64)-C(63)-P(5)	119.9(3)	C(69)-C(74)-H(74)	120.3
C(68)-C(63)-P(5)	121.1(3)	C(73)-C(74)-C(69)	119.4(5)
C(68)-C(63)-C(64)	119.0(4)	C(73)-C(74)-H(74)	120.3
C(63)-C(64)-H(64)	119.9	C(76)-C(75)-P(6)	124.3(3)
C(65)-C(64)-C(63)	120.2(5)	C(76)-C(75)-C(80)	118.9(4)
C(65)-C(64)-H(64)	119.9	C(80)-C(75)-P(6)	116.8(3)
C(64)-C(65)-H(65)	119.8	C(75)-C(76)-H(76)	119.9
C(66)-C(65)-C(64)	120.4(5)	C(77)-C(76)-C(75)	120.1(4)
C(66)-C(65)-H(65)	119.8	C(77)-C(76)-H(76)	119.9
C(65)-C(66)-H(66)	119.7	C(76)-C(77)-H(77)	119.6
C(67)-C(66)-C(65)	120.5(5)	C(78)-C(77)-C(76)	120.7(4)
C(67)-C(66)-H(66)	119.7	C(78)-C(77)-H(77)	119.6
C(66)-C(67)-H(67)	120.2	C(77)-C(78)-H(78)	120.2
C(66)-C(67)-C(68)	119.7(5)	C(77)-C(78)-C(79)	119.5(4)
C(68)-C(67)-H(67)	120.2	C(79)-C(78)-H(78)	120.2
C(63)-C(68)-C(67)	120.2(5)	C(78)-C(79)-H(79)	119.8
C(63)-C(68)-H(68)	119.9	C(80)-C(79)-C(78)	120.5(4)
C(67)-C(68)-H(68)	119.9	C(80)-C(79)-H(79)	119.8
C(70)-C(69)-P(5)	123.1(3)	C(75)-C(80)-H(80)	119.9
C(74)-C(69)-P(5)	117.0(3)	C(79)-C(80)-C(75)	120.2(4)
C(74)-C(69)-C(70)	119.8(4)	C(79)-C(80)-H(80)	119.9
C(69)-C(70)-H(70)	120.1	C(82)-C(81)-P(6)	118.6(3)

C(82)-C(81)-C(86)	118.2(4)	Cl(2P)-C(13S)-H(13D)	108.8
C(86)-C(81)-P(6)	123.2(3)	H(13C)-C(13S)-H(13D)	107.7
C(81)-C(82)-H(82)	119.5	Cl(3M)-C(11S)-H(11C)	108.7
C(81)-C(82)-C(83)	121.0(5)	Cl(3M)-C(11S)-H(11D)	108.7
C(83)-C(82)-H(82)	119.5	Cl(4M)-C(11S)-Cl(3M)	114.1(5)
C(82)-C(83)-H(83)	119.9	Cl(4M)-C(11S)-H(11C)	108.7
C(84)-C(83)-C(82)	120.1(5)	Cl(4M)-C(11S)-H(11D)	108.7
C(84)-C(83)-H(83)	119.9	H(11C)-C(11S)-H(11D)	107.6
C(83)-C(84)-H(84)	120.2	Cl(5M)-C(12S)-H(12C)	109.2
C(83)-C(84)-C(85)	119.7(5)	Cl(5M)-C(12S)-H(12D)	109.2
C(85)-C(84)-H(84)	120.2	Cl(6M)-C(12S)-Cl(5M)	112.2(4)
C(84)-C(85)-H(85)	119.9	Cl(6M)-C(12S)-H(12C)	109.2
C(86)-C(85)-C(84)	120.2(5)	Cl(6M)-C(12S)-H(12D)	109.2
C(86)-C(85)-H(85)	119.9	H(12C)-C(12S)-H(12D)	107.9
C(81)-C(86)-H(86)	119.7	Cl(7M)-C(14S)-Cl(8M)	112.6(5)
C(85)-C(86)-C(81)	120.7(4)	Cl(7M)-C(14S)-H(14D)	109.1
C(85)-C(86)-H(86)	119.7	Cl(7M)-C(14S)-H(14E)	109.1
Cl(1M)-C(10S)-Cl(2M)	111.5(3)	Cl(8M)-C(14S)-H(14D)	109.1
Cl(1M)-C(10S)-H(10C)	109.3	Cl(8M)-C(14S)-H(14E)	109.1
Cl(1M)-C(10S)-H(10D)	109.3	H(14D)-C(14S)-H(14E)	107.8
Cl(2M)-C(10S)-H(10C)	109.3	Cl(3P)-C(15S)-Cl(4P)	120.2(12)
Cl(2M)-C(10S)-H(10D)	109.3	Cl(3P)-C(15S)-H(15A)	107.3
H(10C)-C(10S)-H(10D)	108.0	Cl(3P)-C(15S)-H(15B)	107.3
Cl(1P)-C(13S)-H(13C)	108.8	Cl(4P)-C(15S)-H(15A)	107.3
Cl(1P)-C(13S)-H(13D)	108.8	Cl(4P)-C(15S)-H(15B)	107.3
Cl(2P)-C(13S)-Cl(1P)	113.8(5)	H(15A)-C(15S)-H(15B)	106.9
Cl(2P)-C(13S)-H(13C)	108.8		

APPENDIX B

ADDITIONAL TEM DATA

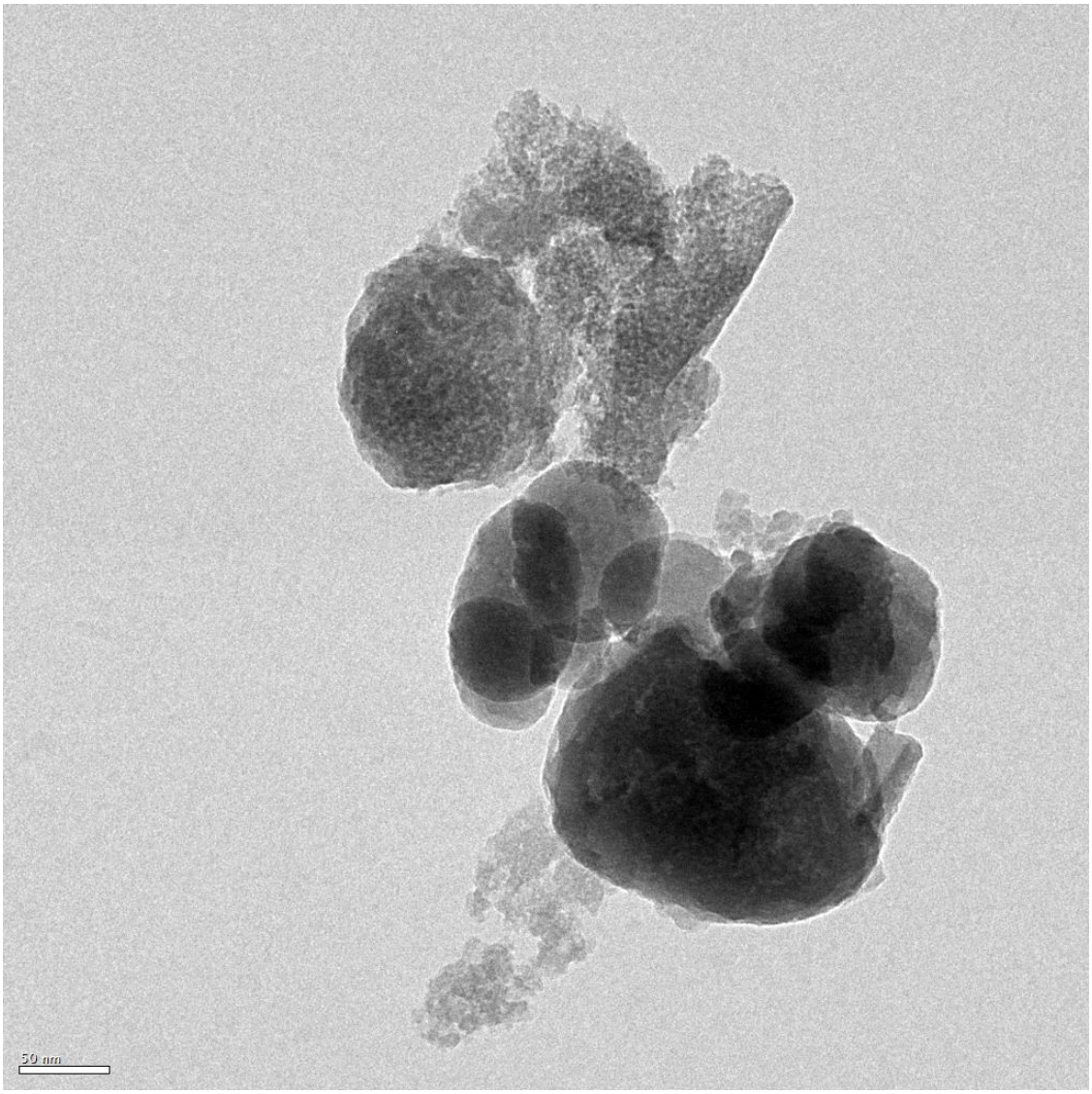

Figure B.1 TEM image (area 4) of a nickel catalyst prepared by the adsorption and decomposition of nickelocene on silica gel.

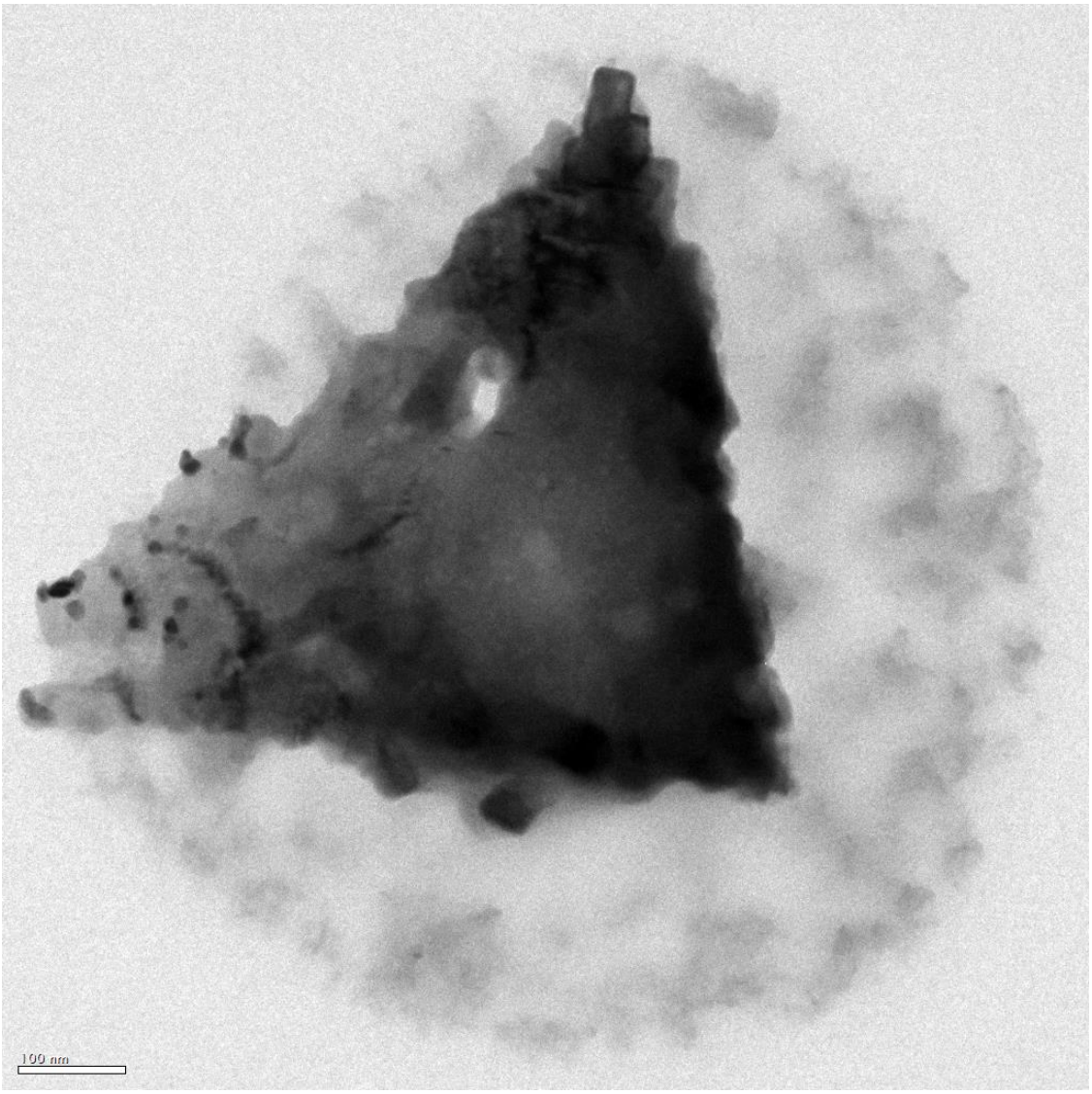

Figure B.2 TEM image (area 1) of a nickel catalyst prepared by the adsorption and decomposition of nickelocene on silica gel.

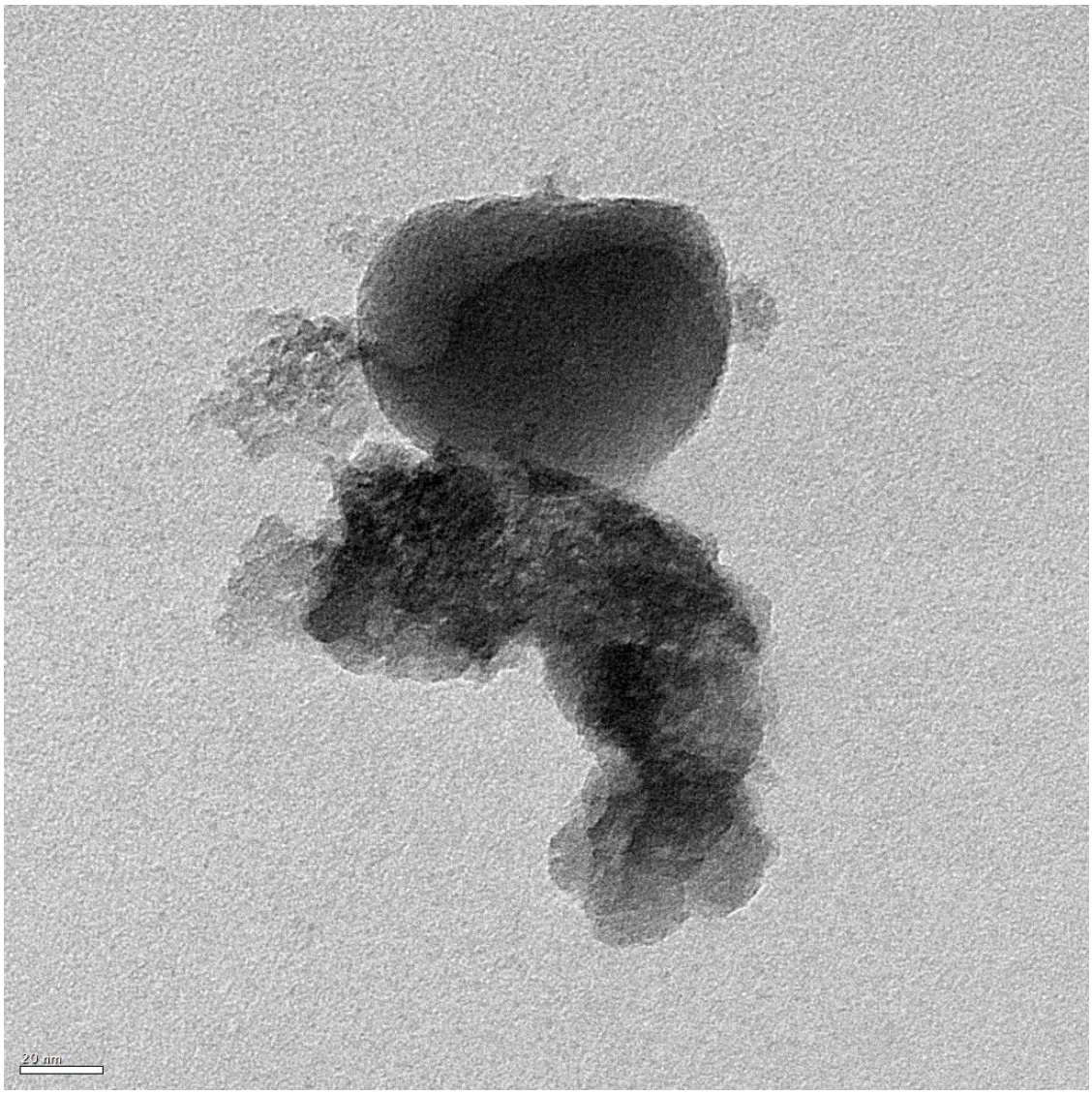

Figure B.3 TEM image (area 3) of a nickel catalyst prepared by the adsorption and decomposition of nickelocene on silica gel.

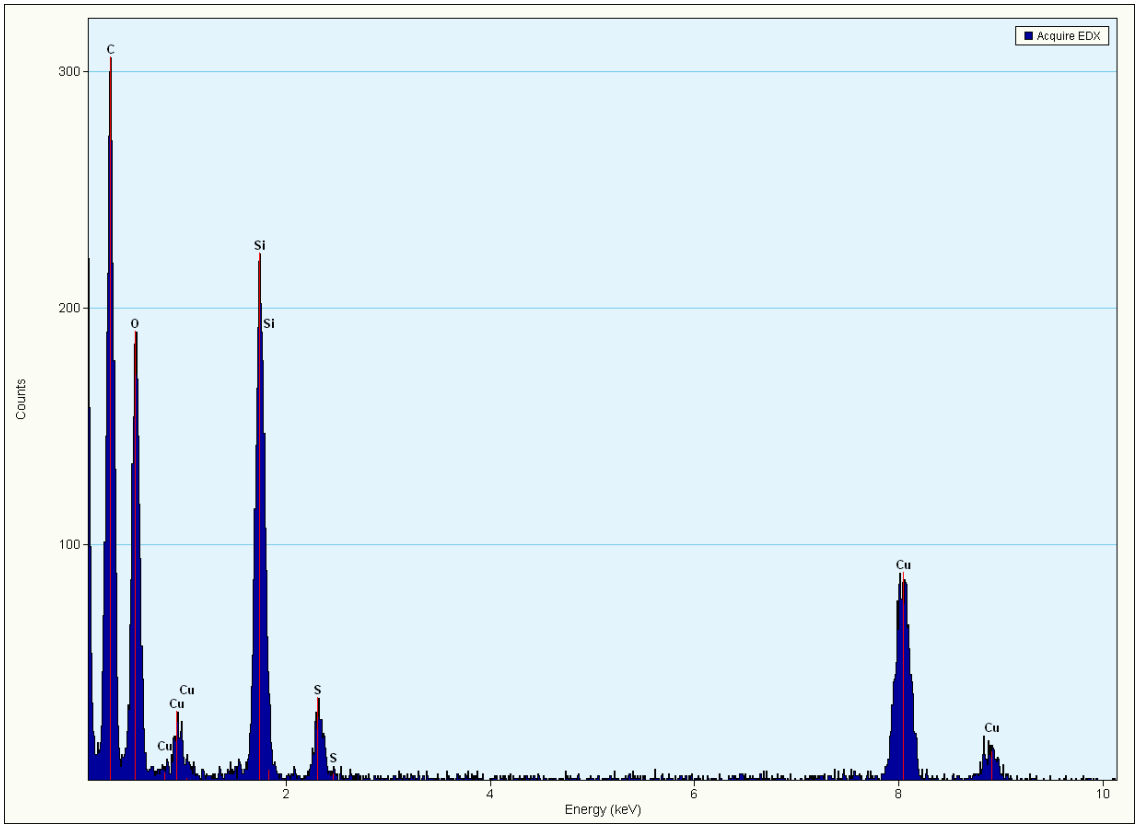

Figure B.4 Representative EDS spectrum (area 3) of a nickel catalyst prepared by the adsorption and decomposition of nickelocene on silica gel.

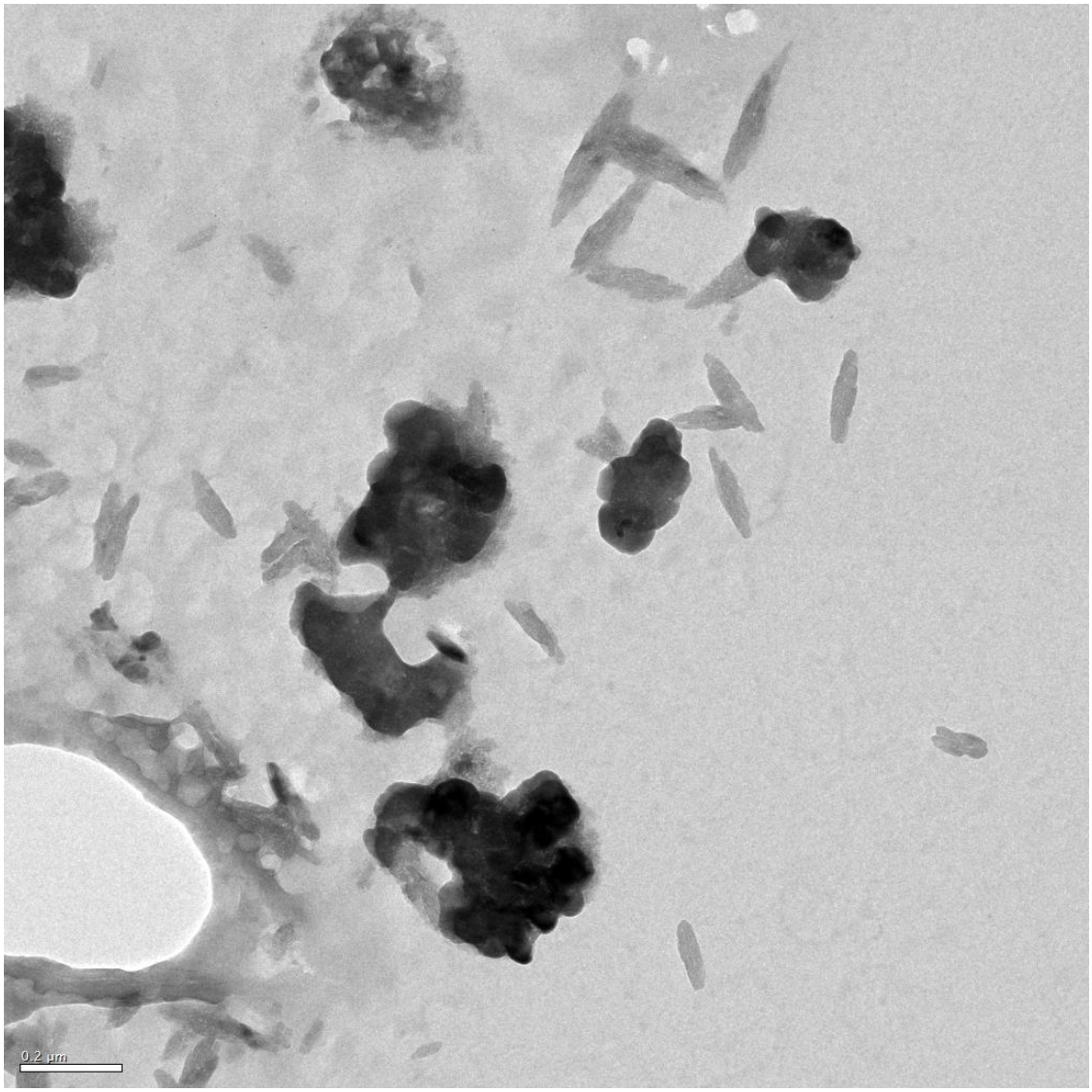

Figure B.5 TEM image (area 4) of a nickel catalyst prepared by the adsorption of nickelocene on silica gel and the subsequent decomposition after it has been used in one catalytic cycle.

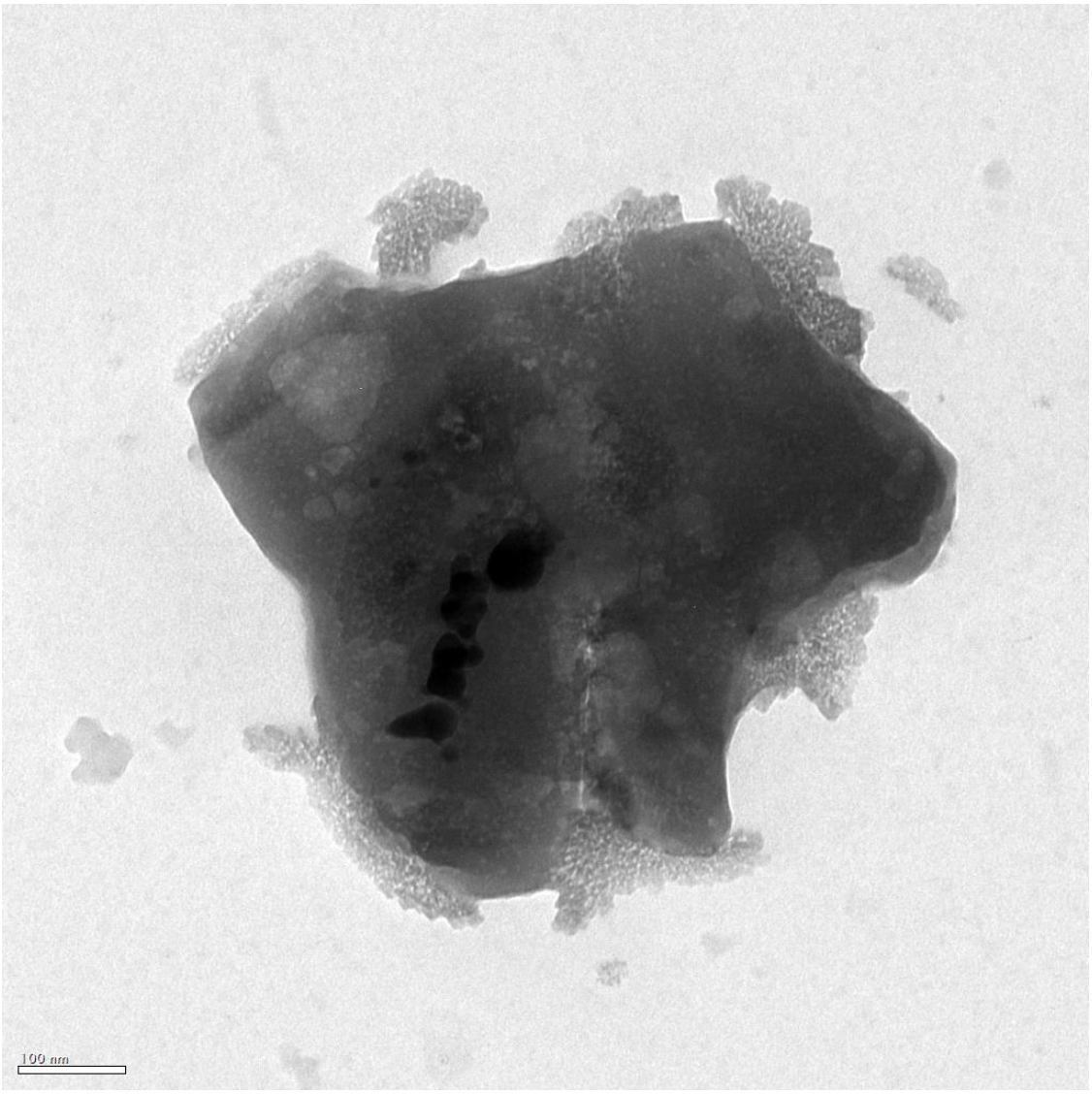

Figure B.6 TEM image (area 1) of a nickel catalyst prepared by the adsorption of nickelocene on silica gel and the subsequent decomposition after it has been used in one catalytic cycle.

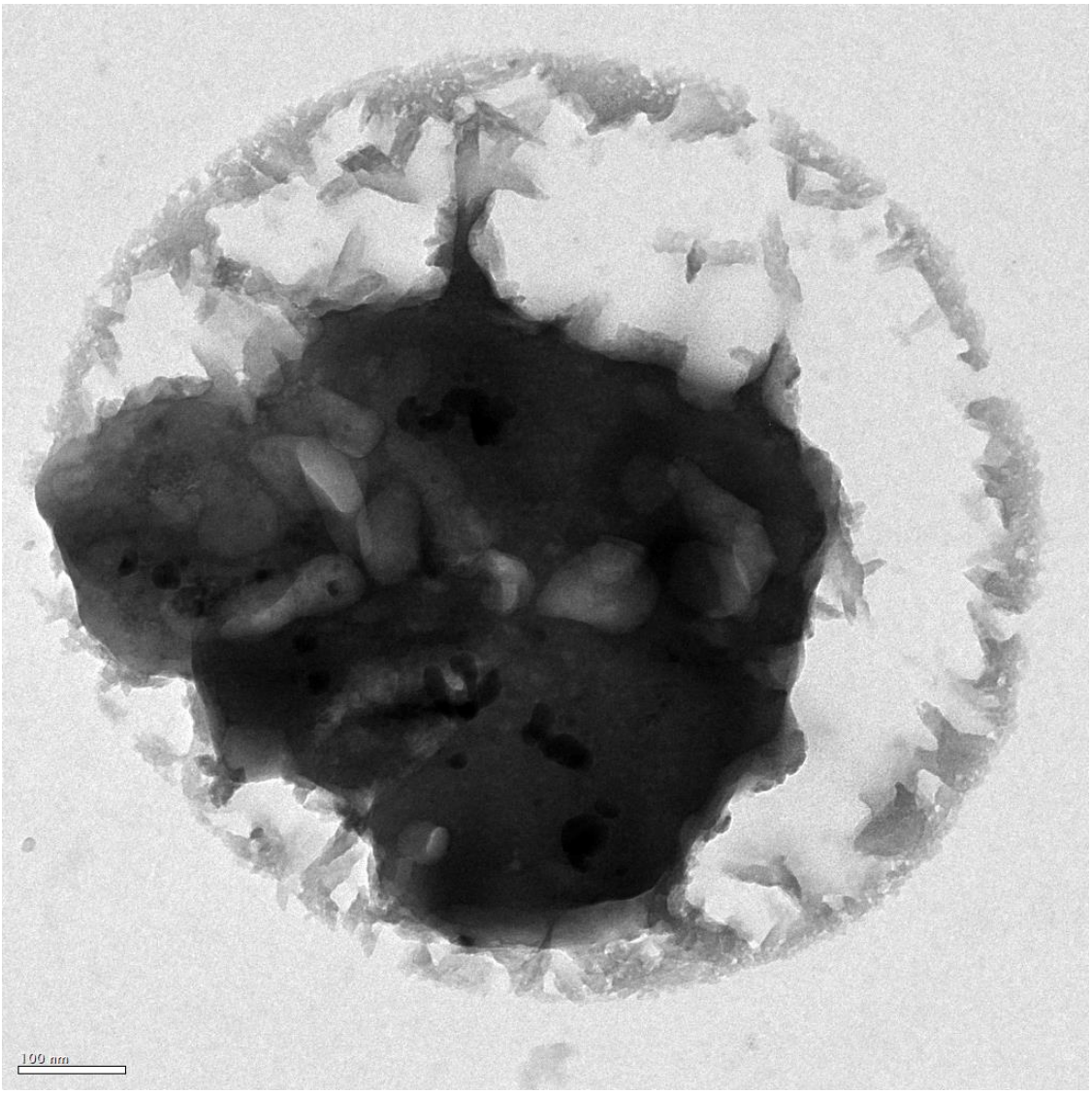

Figure B.7 TEM image (area 2) of a nickel catalyst prepared by the adsorption of nickelocene on silica gel and the subsequent decomposition after it has been used in one catalytic cycle.

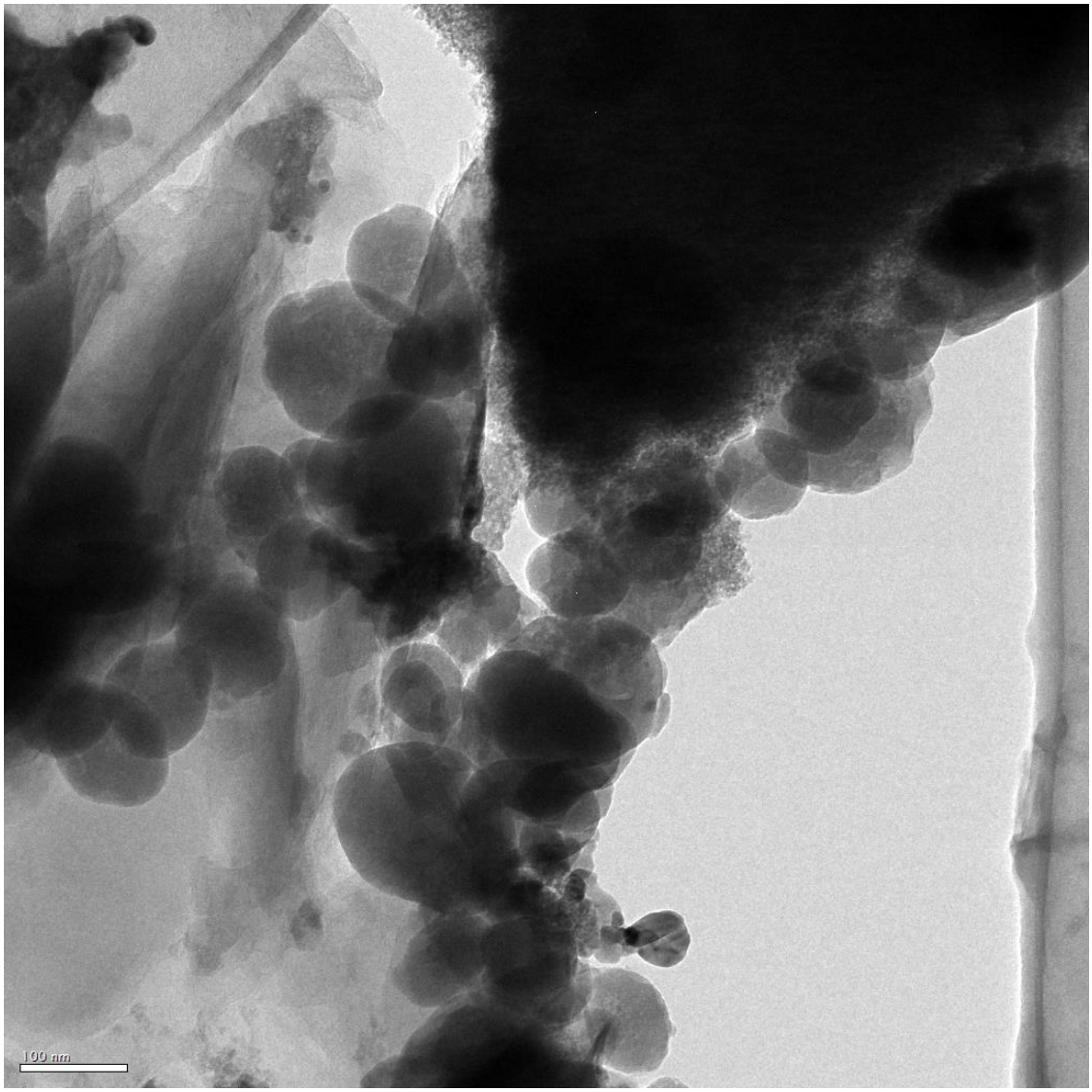

Figure B.8 TEM image (area 3-2) of a nickel catalyst prepared by the adsorption of nickelocene on silica gel and the subsequent decomposition after it has been used in one catalytic cycle.

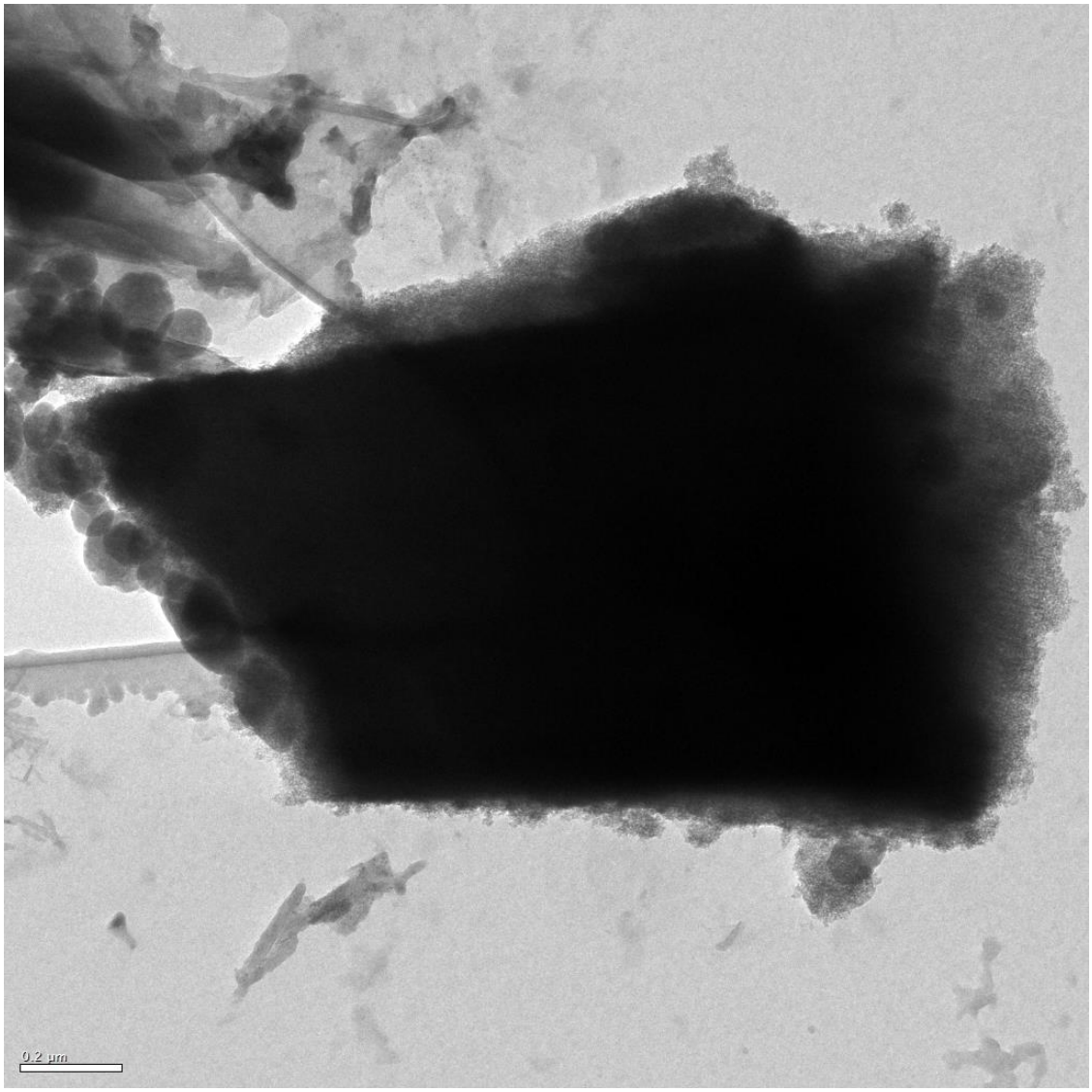

Figure B.9 TEM image (area 3) of a nickel catalyst prepared by the adsorption of nickelocene on silica gel and the subsequent decomposition after it has been used in one catalytic cycle.

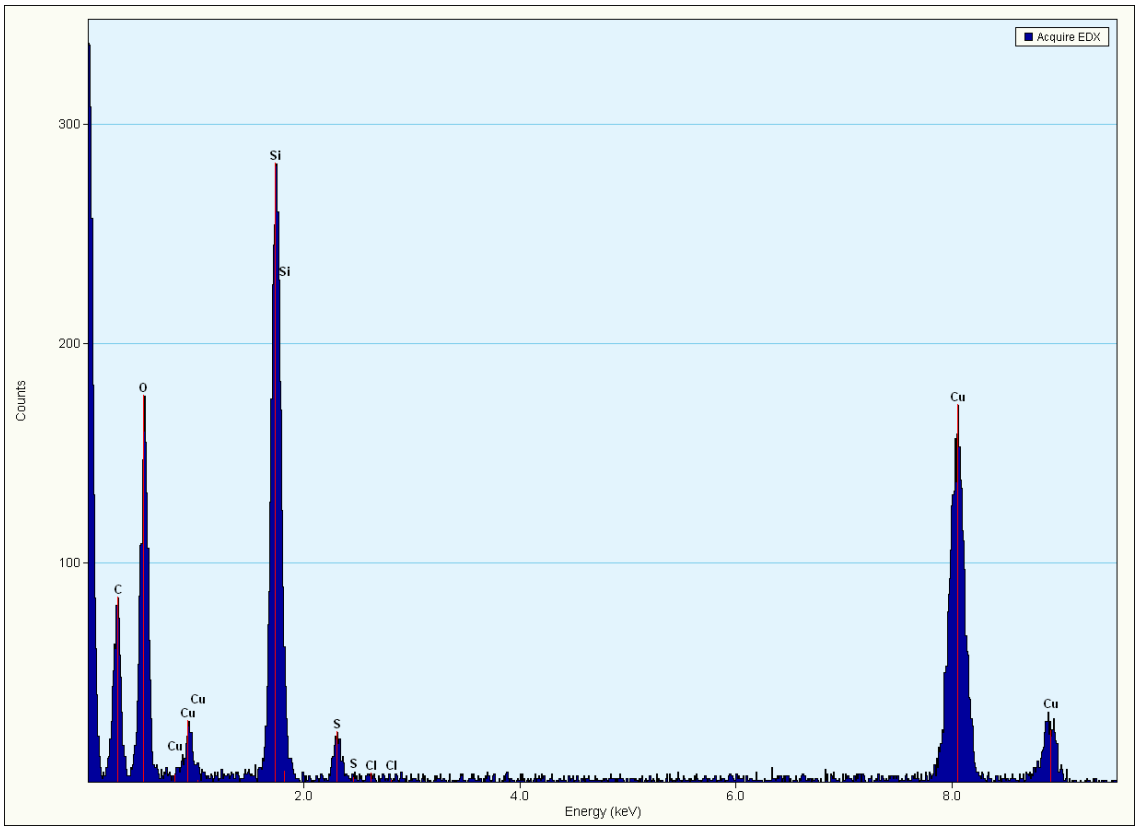

Figure B.10 Representative EDS spectrum (area 3) of a nickel catalyst prepared by the adsorption of nickelocene on silica gel and the subsequent decomposition after it has been used in one catalytic cycle.

APPENDIX C

NMR SPECTRA

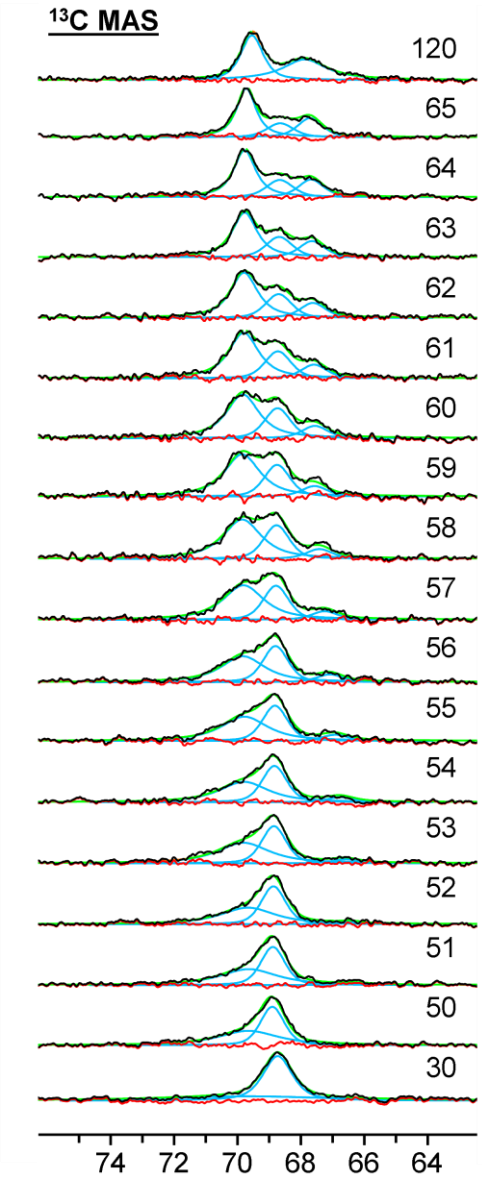

Figure C.1 Full range of ^{13}C MAS spectra of **10a**, recorded with 2 kHz MAS rotational frequency using various values for the decoupling power level pl12 (listed on the right). A pl12 of 120 corresponds to zero decoupling power and 1.5 is the maximum power level tolerated by the 7 mm probe.

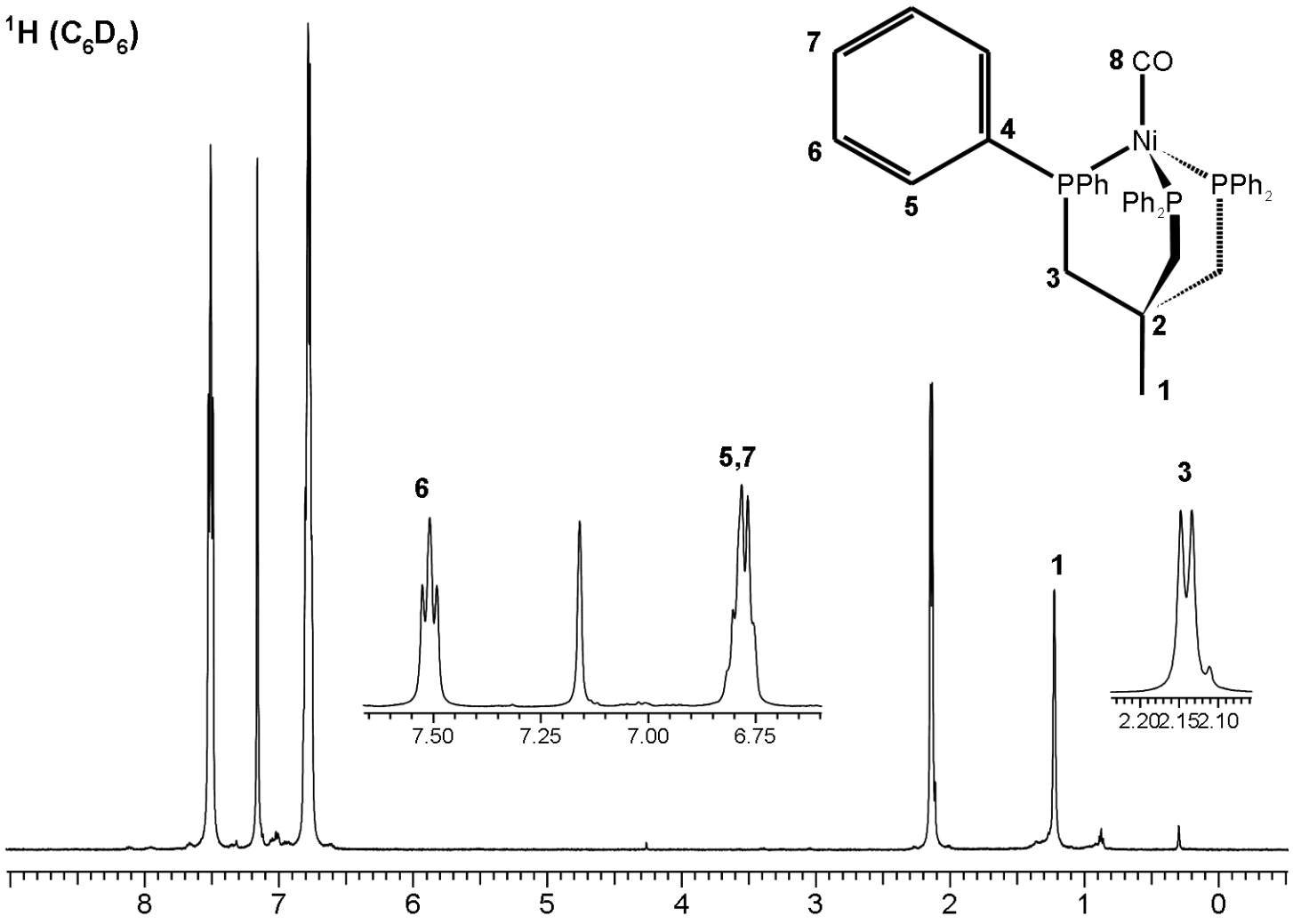

Figure C.2 ^{1}NMR of Ni(CO)Triphos.

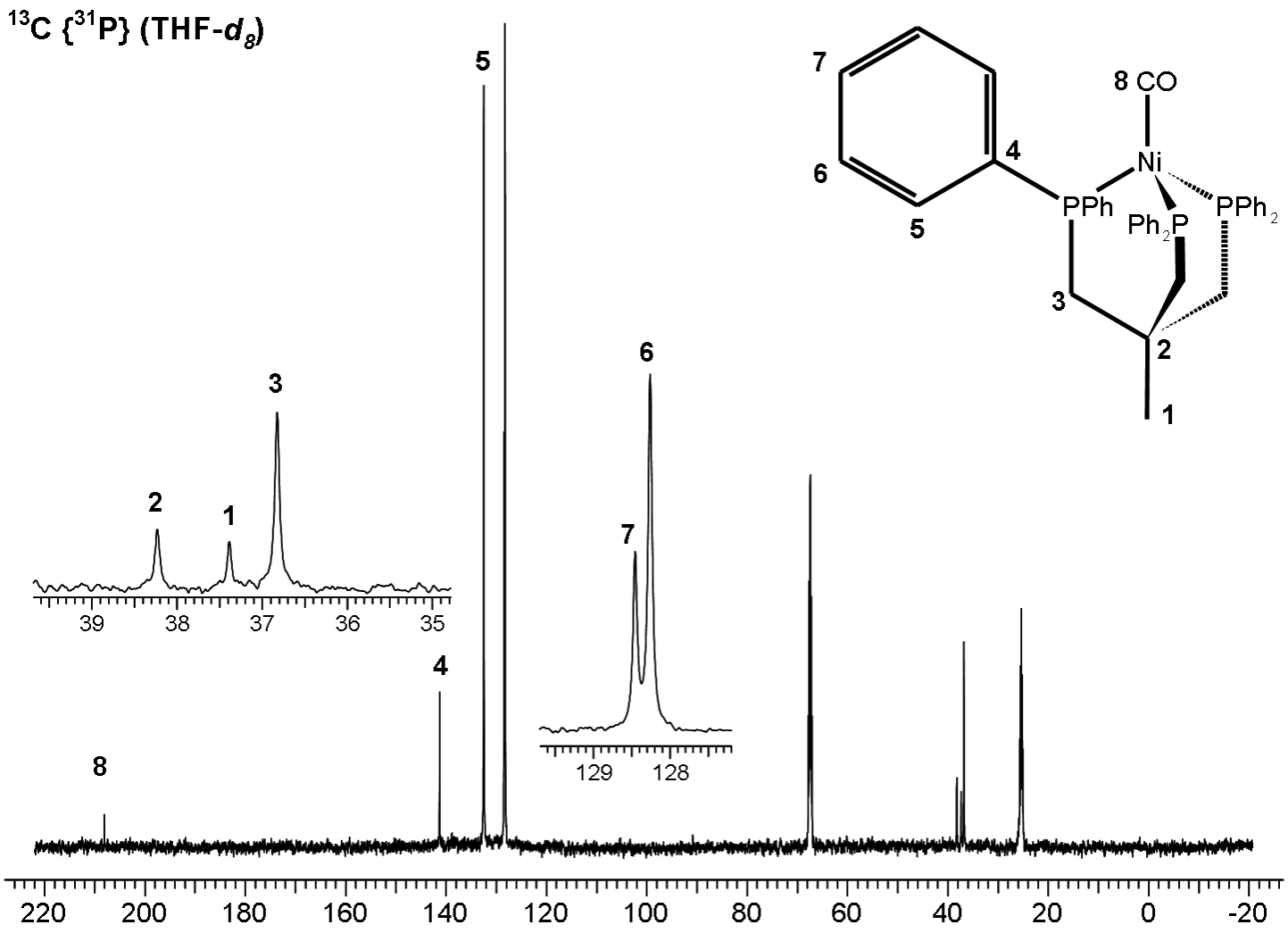

Figure C.3 $^{13}C\{^{31}P\}$ NMR of Ni(CO)Triphos.

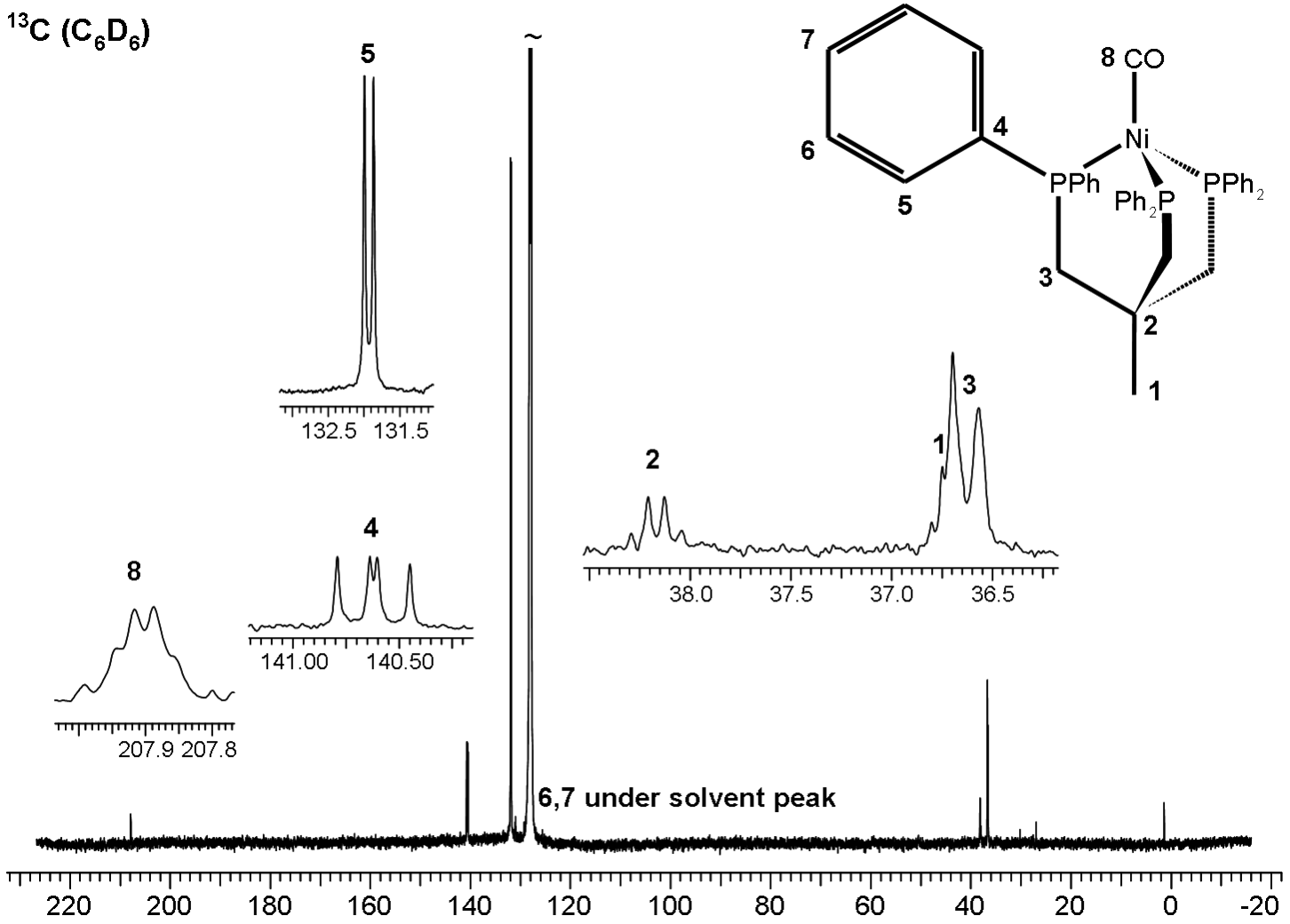

Figure C.4 ^{13}C NMR spectrum of Ni(CO)Triphos.

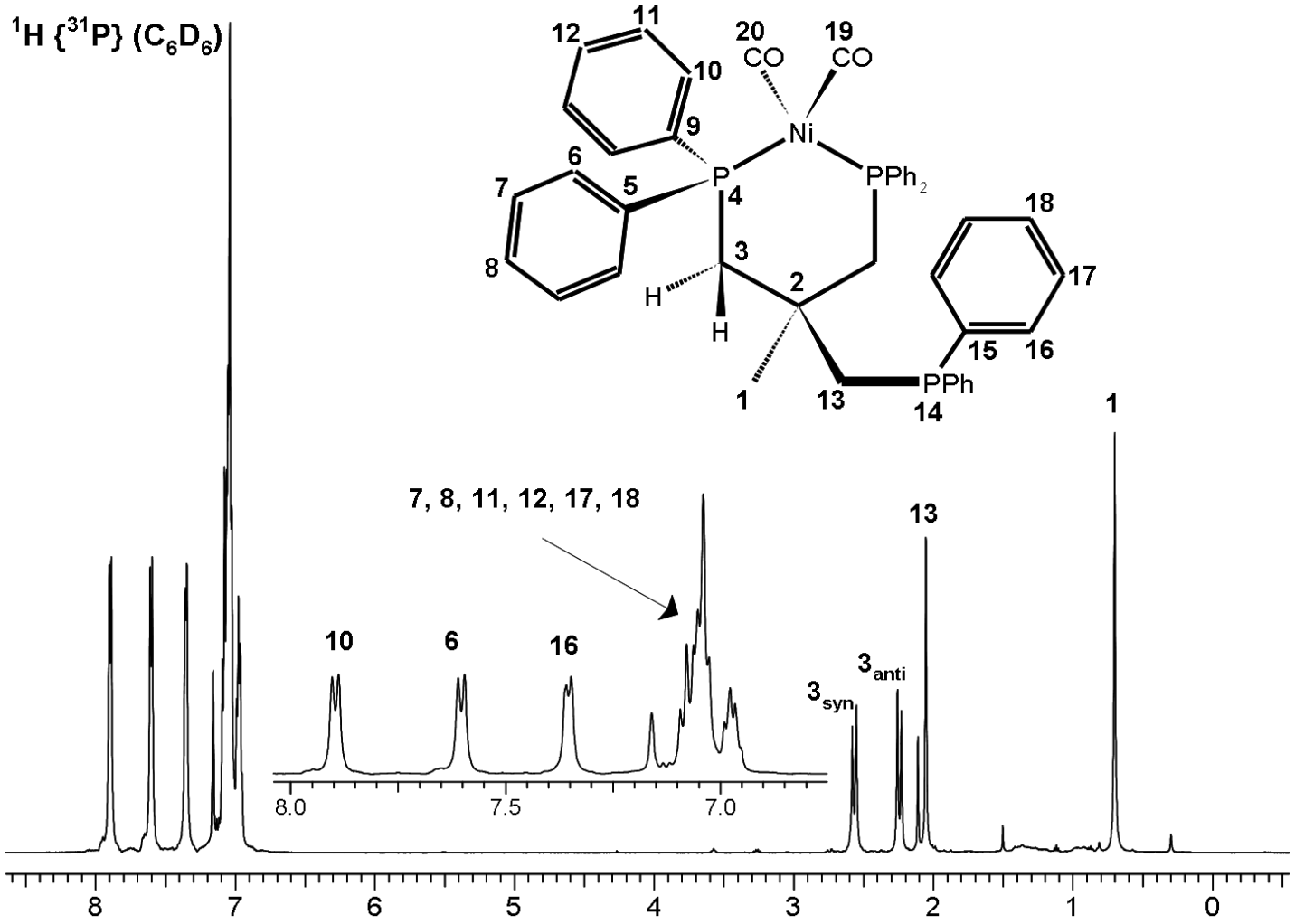

Figure C.5 ^{1}H{^{31}P} NMR of Ni(CO)$_2$Triphos.

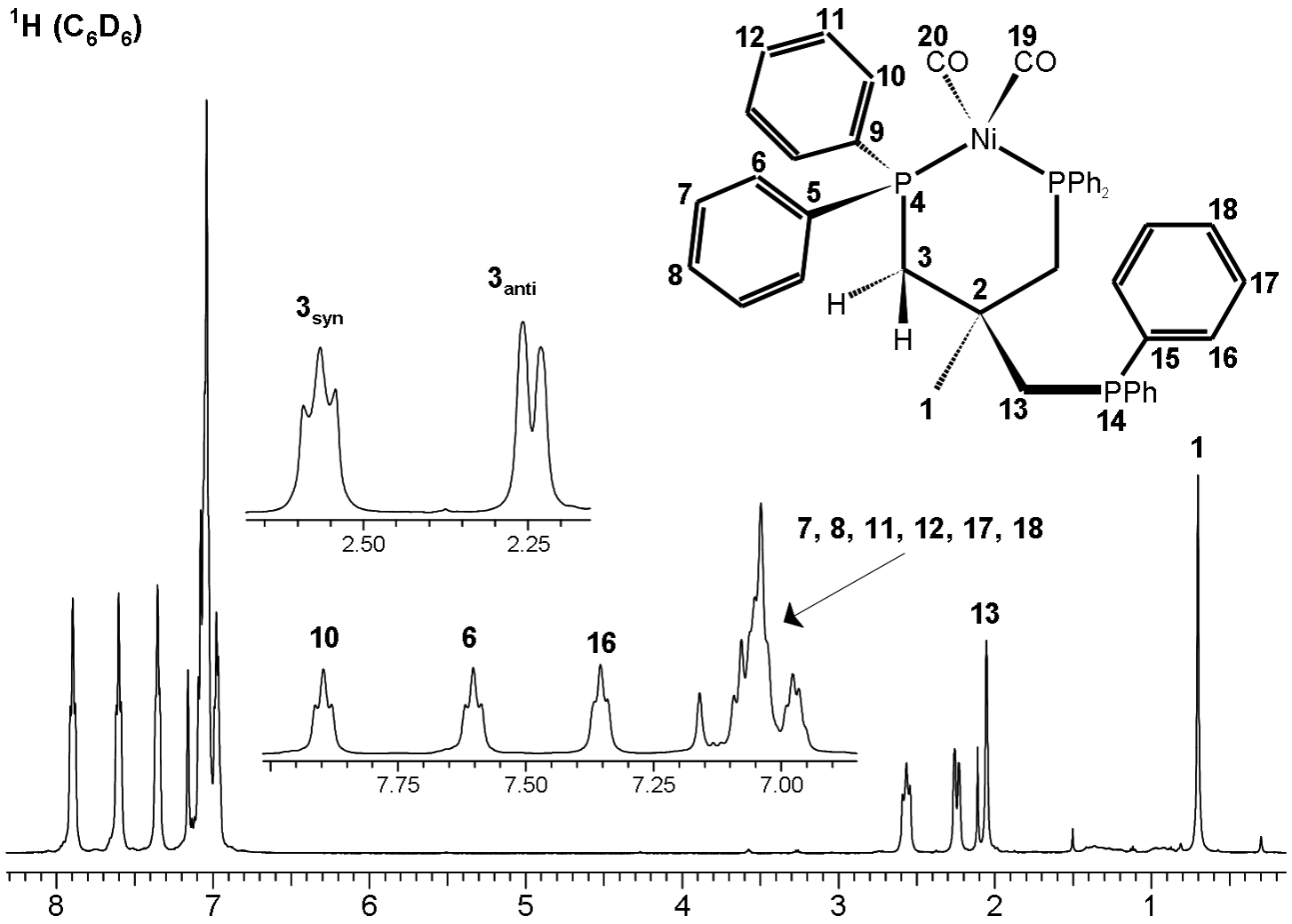

Figure C.6 ^{1}H NMR of $Ni(CO)_2$Triphos.

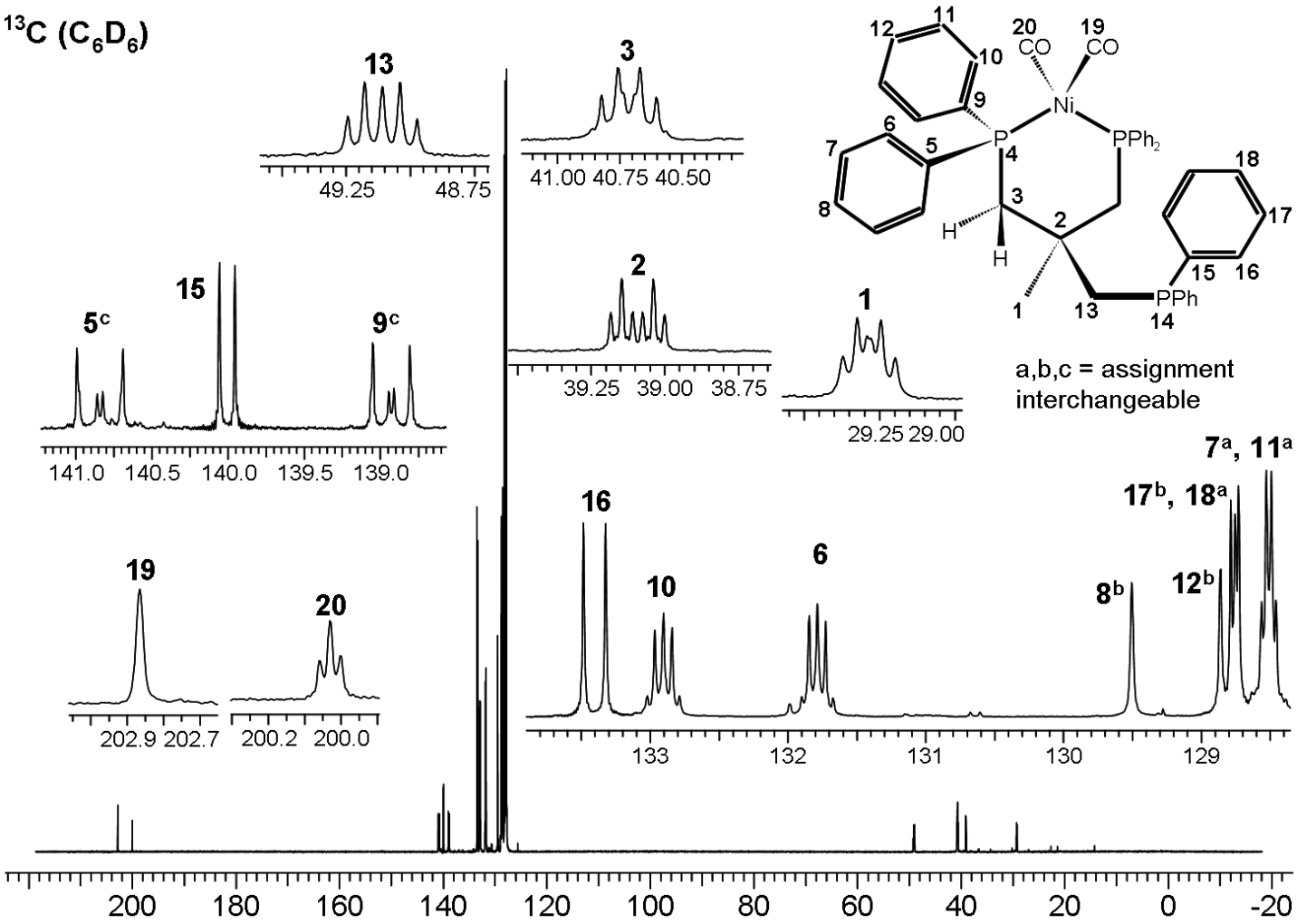

Figure C.7 ^{13}C NMR of $Ni(CO)_2$Triphos.

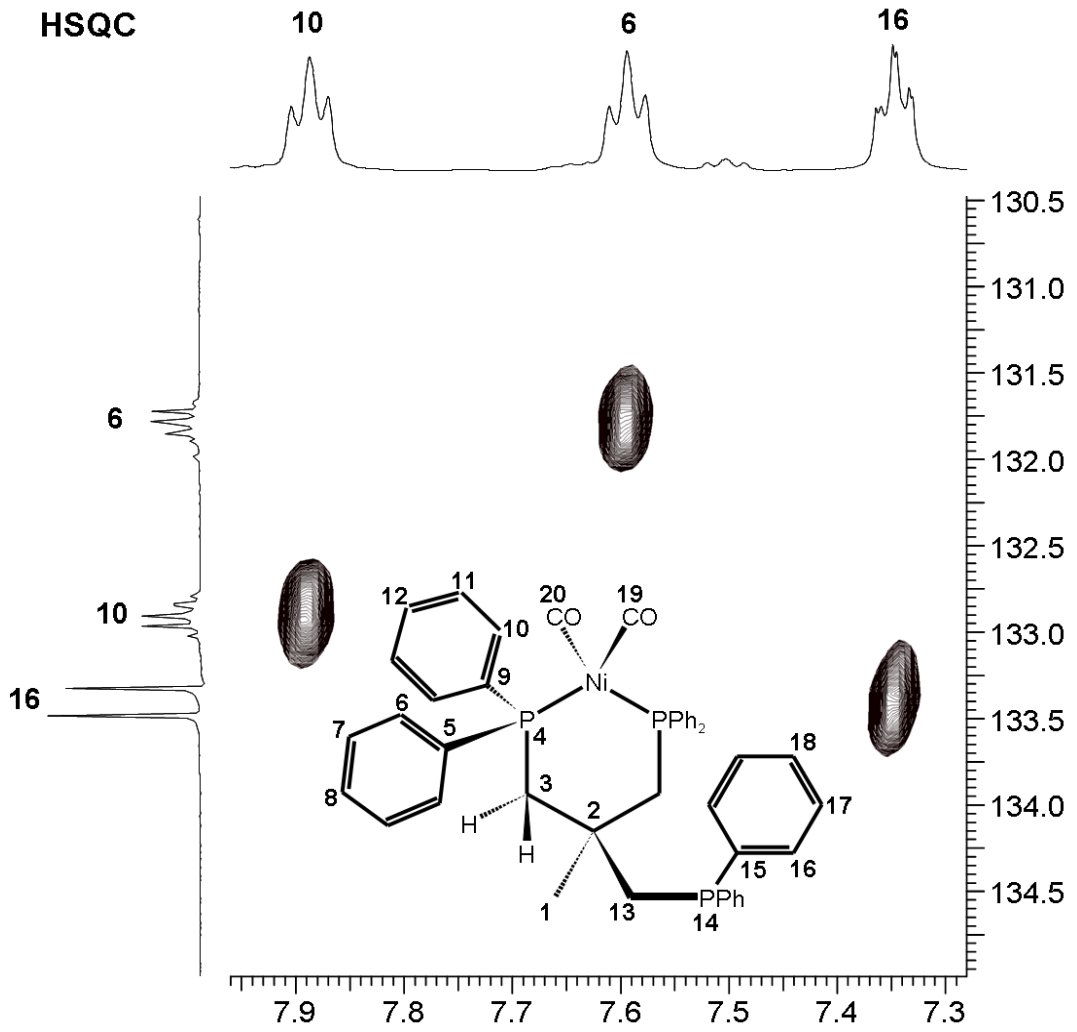

Figure C.8 HSQC of $Ni(CO)_2$Triphos.

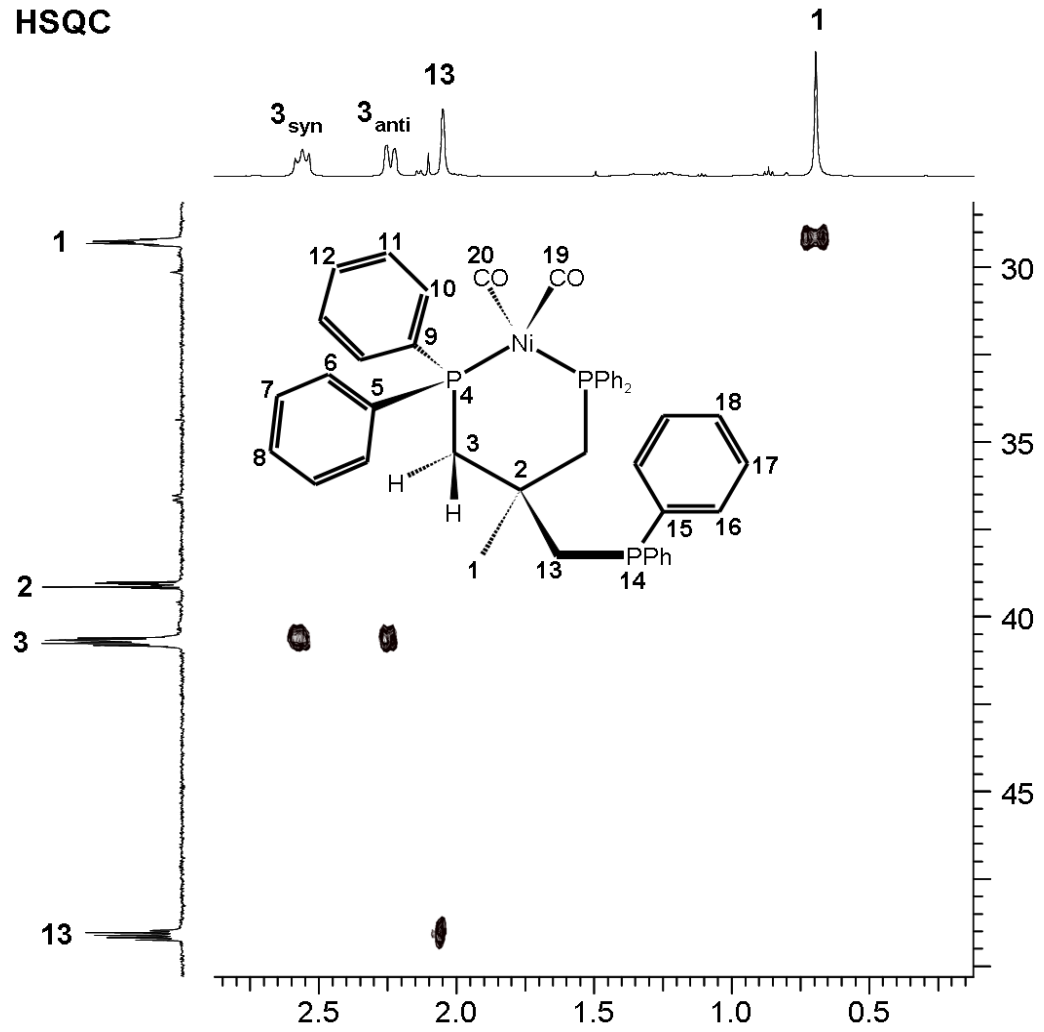

Figure C.9 HSQC of $Ni(CO)_2$Triphos.

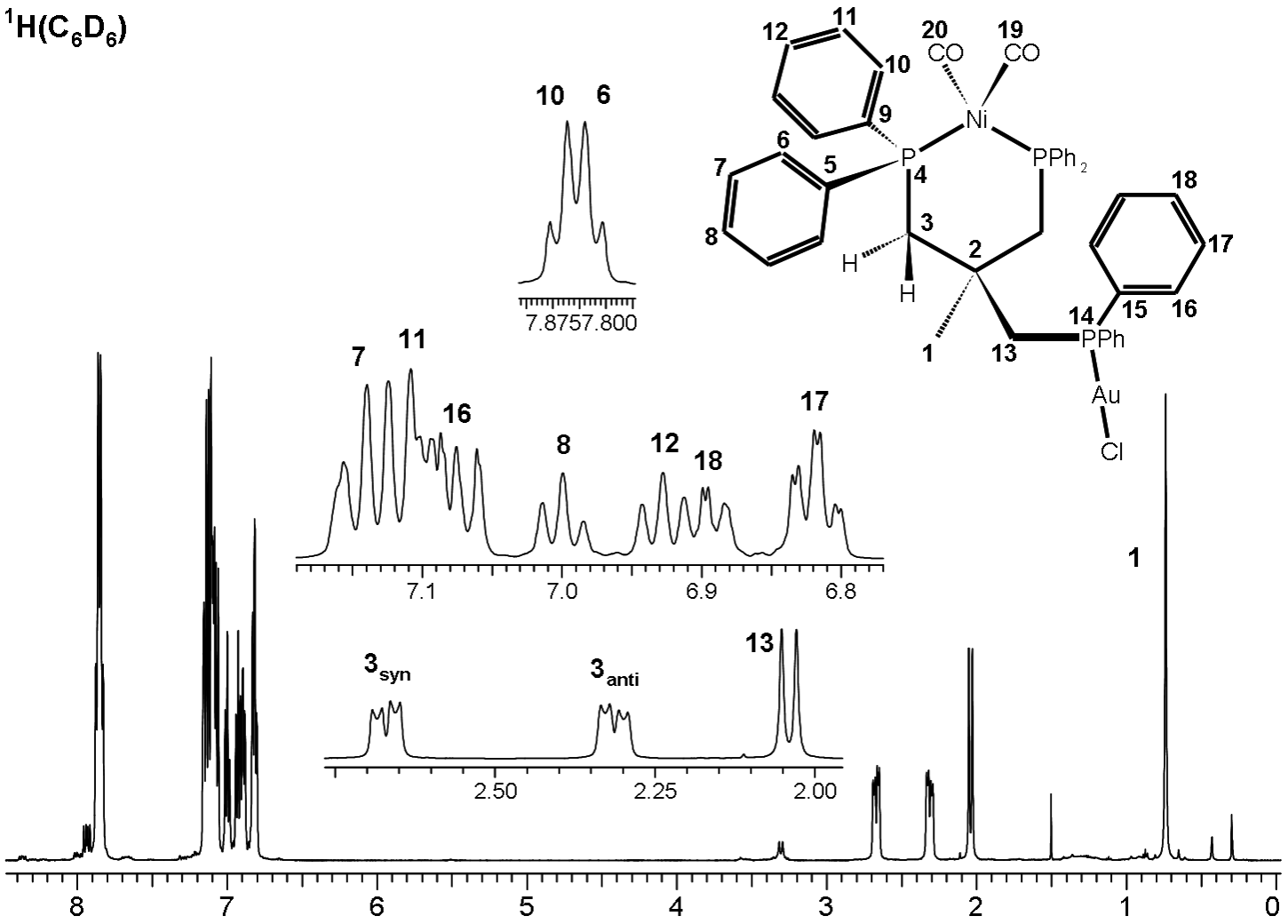

Figure C.10 ^1H NMR of $Ni(CO)_2$TriphosAuCl.

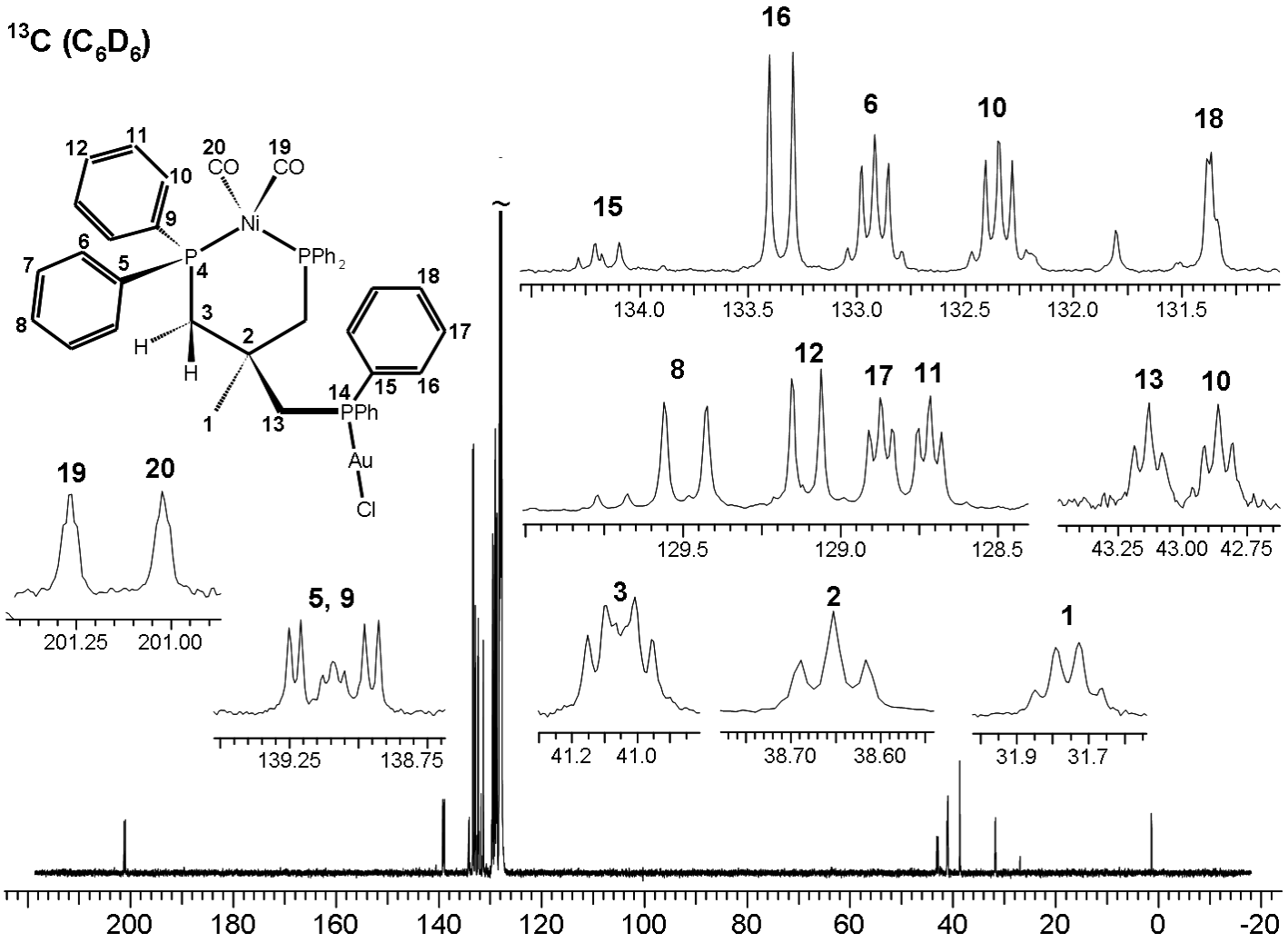

Figure C.11 ^{13}C NMR spectrum of $Ni(CO)_2$TriphosAuCl.

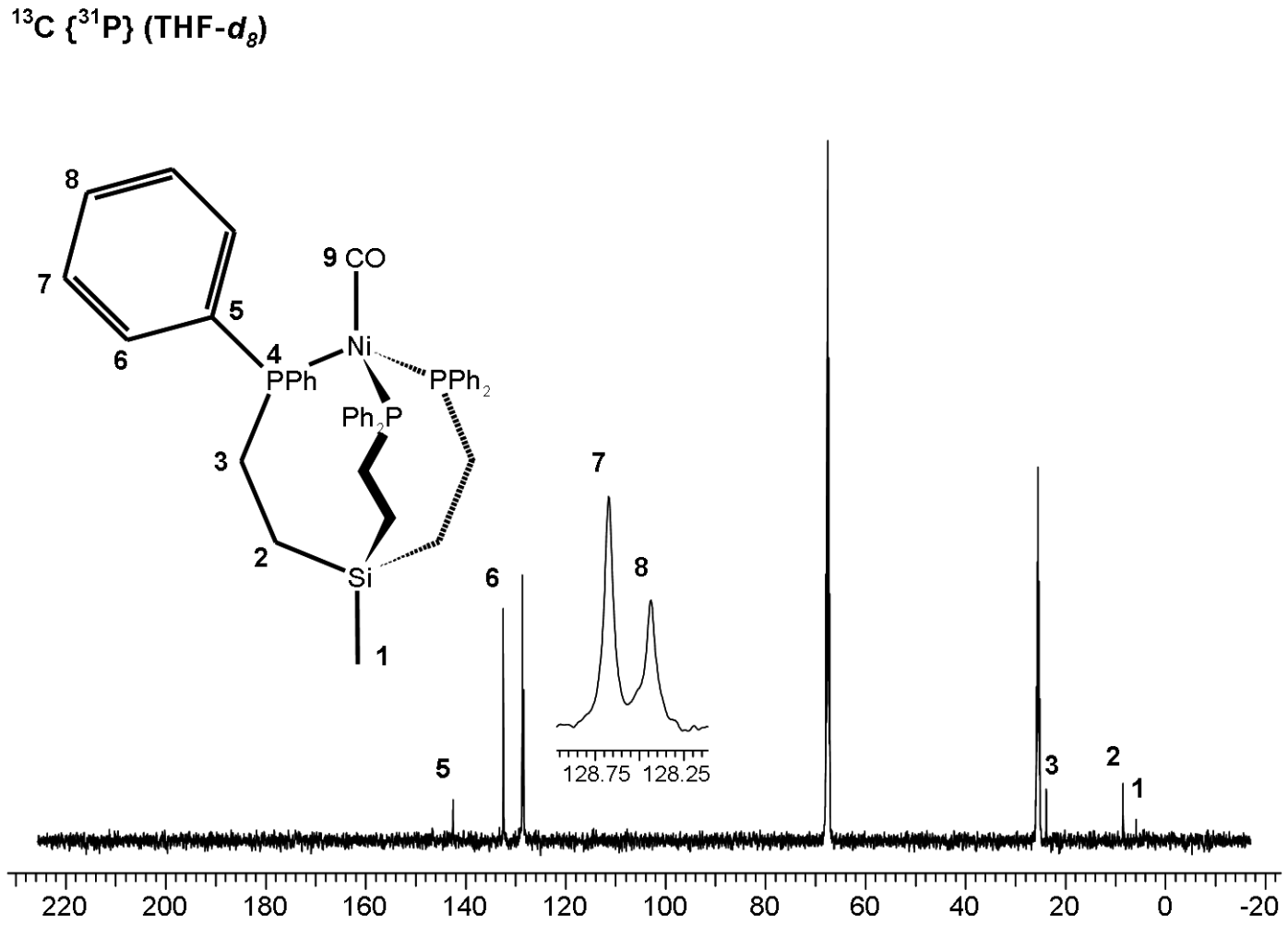

Figure C.12 $^{13}C\{^{31}P\}$ NMR of (CO)Ni[$(PPh_2CH_2CH_2)_3SiMe$].

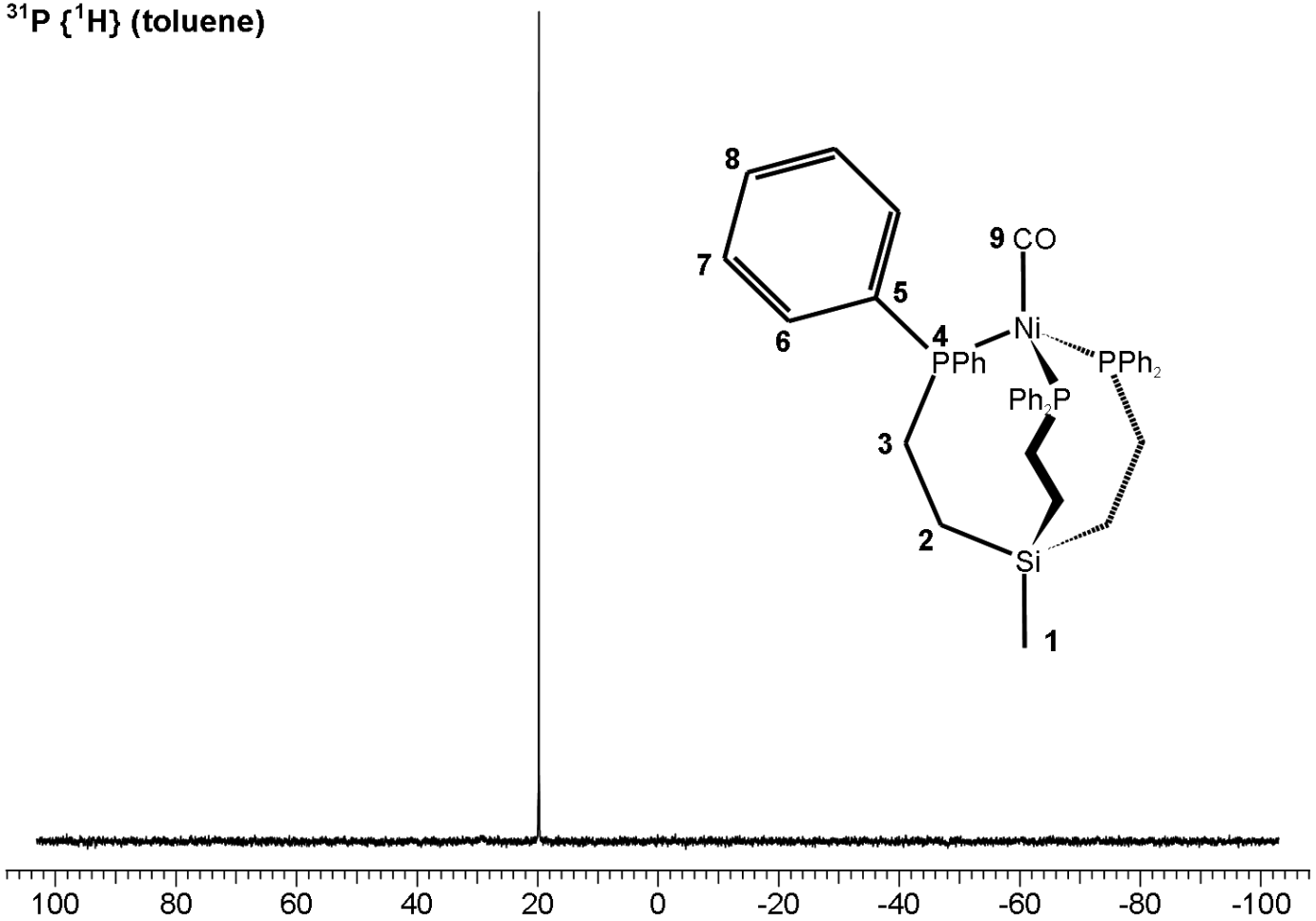

Figure C.13 $^{31}P\{^{1}H\}$ NMR spectrum of (CO)Ni[$(PPh_2CH_2CH_2)_3SiMe$].

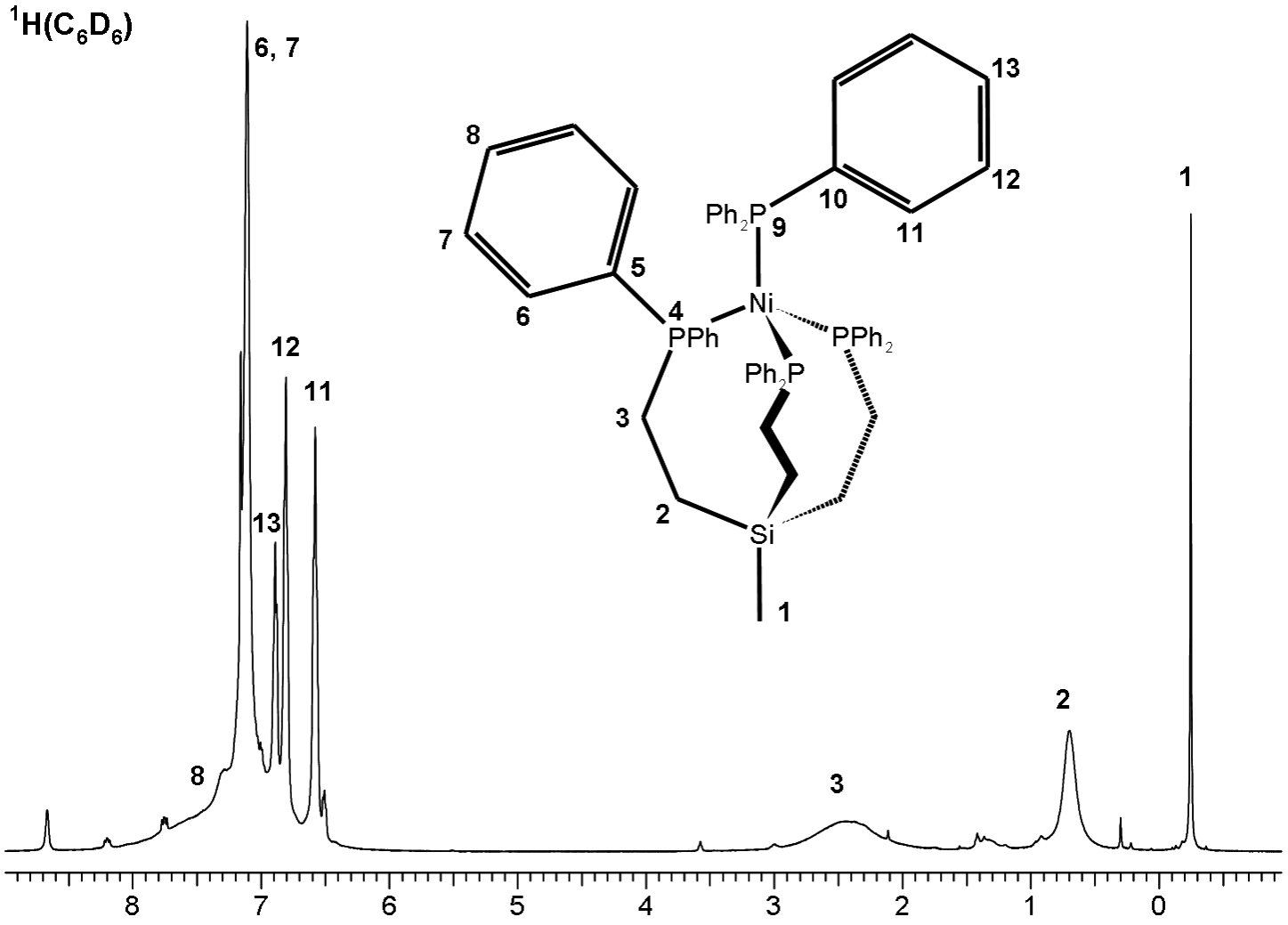

Figure C.14 ^{1}H NMR spectrum of $(Ph_3P)Ni[(PPh_2CH_2CH_2)_3SiMe]$.

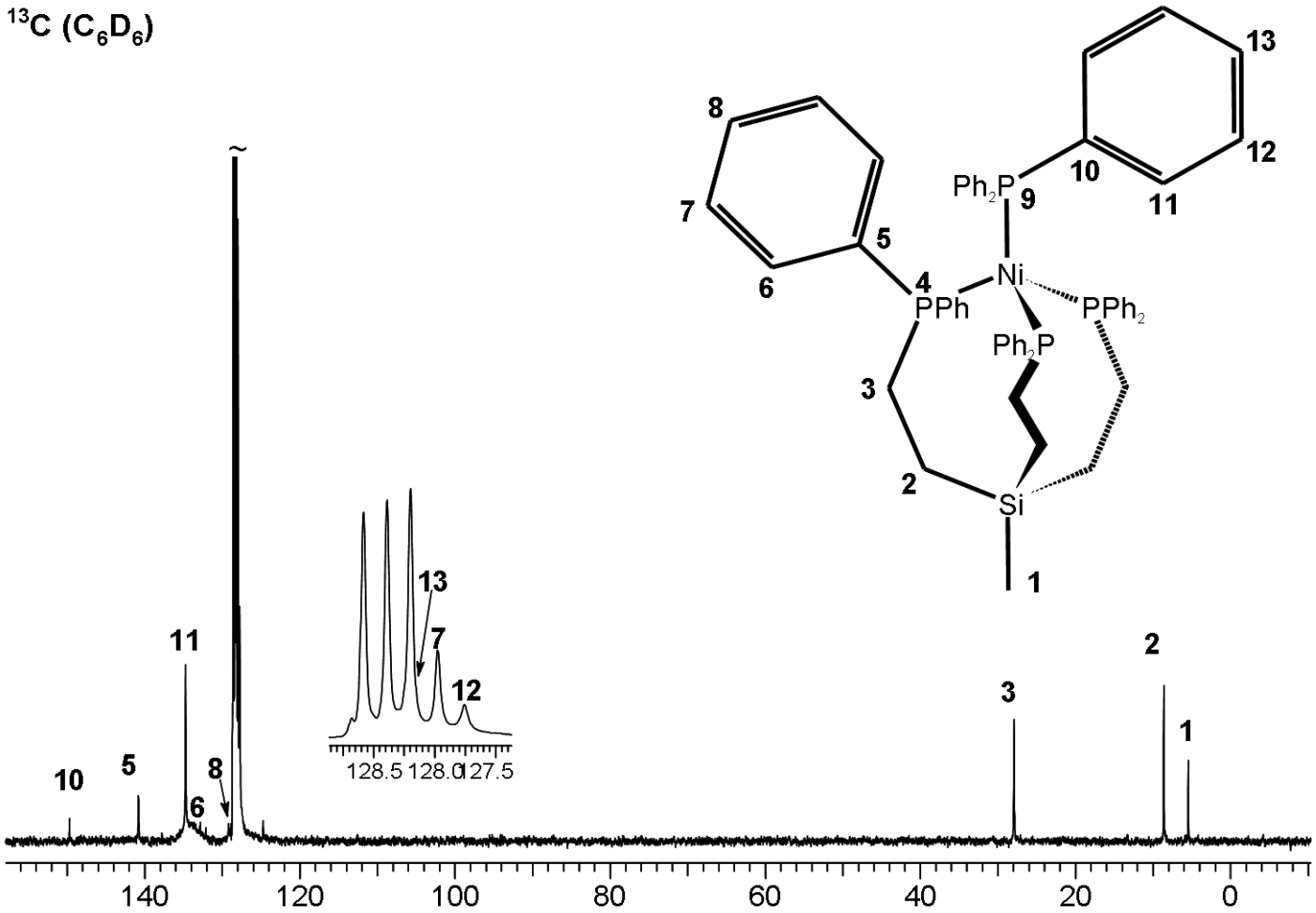

Figure C.15 $^{13}C\{^{31}P\}$ NMR spectrum of $(Ph_3P)Ni[(PPh_2CH_2CH_2)_3SiMe]$.

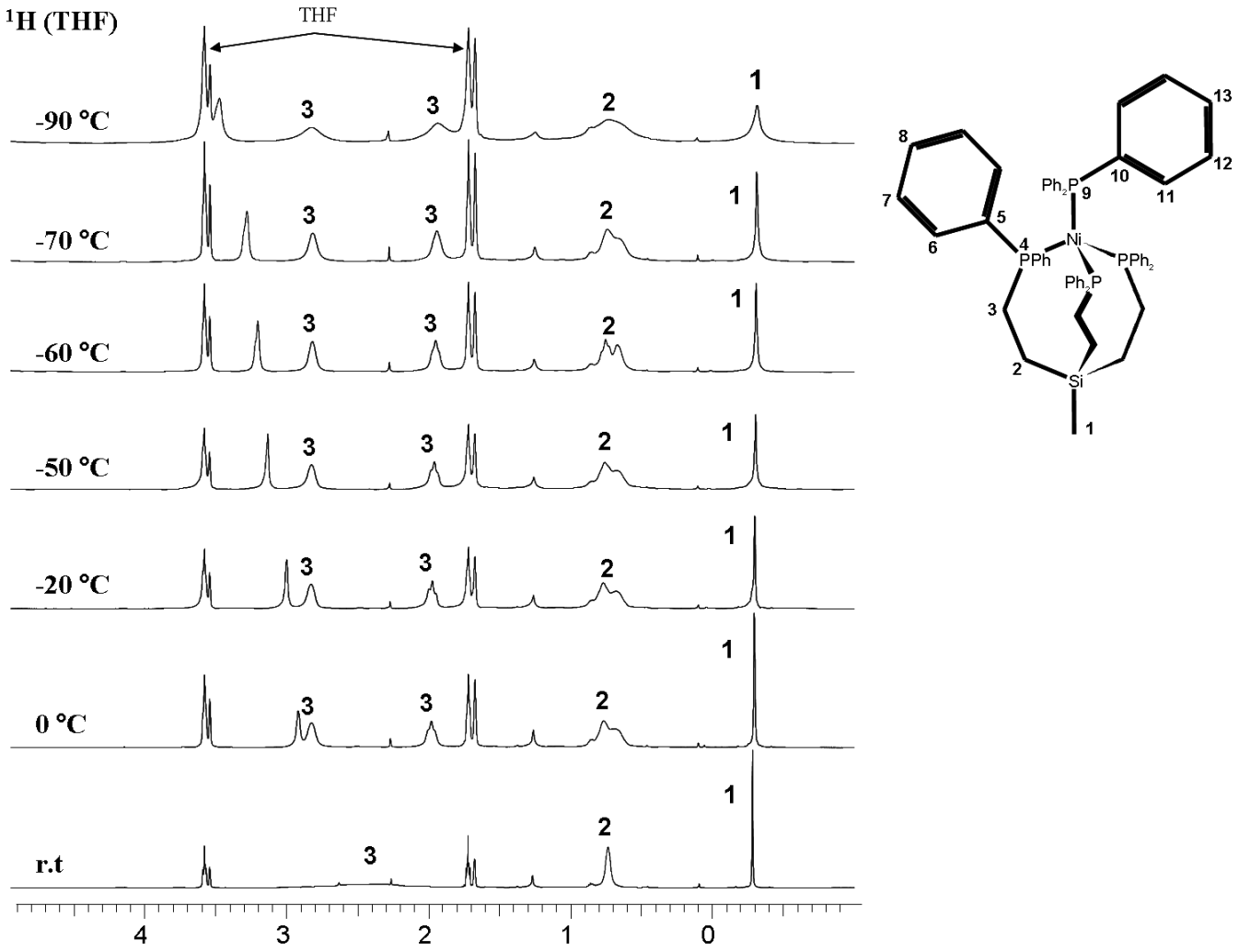

Figure C.16 Variable temperature ^{1}H NMR spectra of $(Ph_3P)Ni[(PPh_2CH_2CH_2)_3SiMe]$ showing that signal 3 splits in two.

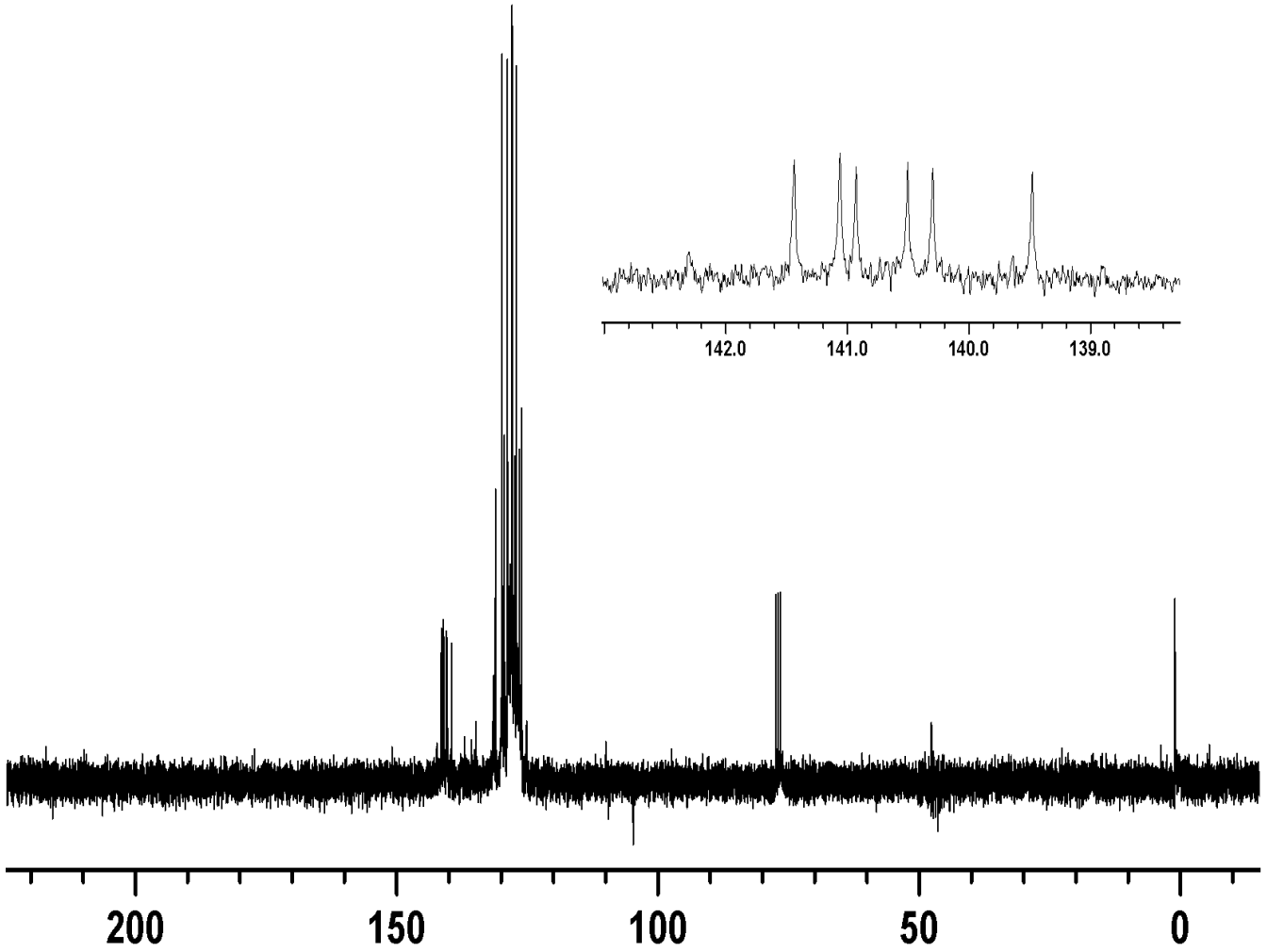

Figure C.17 ^{13}C NMR of the products of a Ni catalyzed cyclotrimerization of Ph-C≡C (mainly 1,4,5-triphenylbenzene).

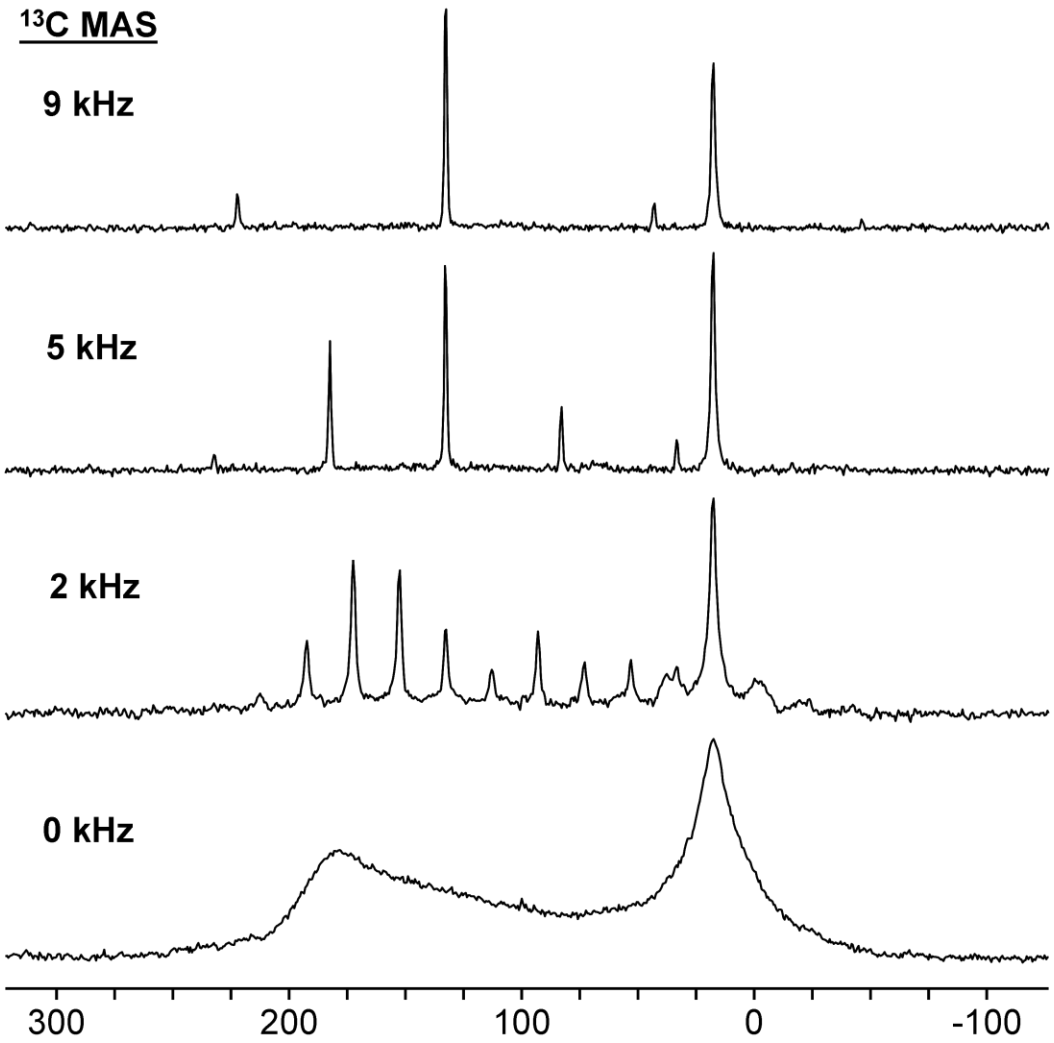

Figure C.18 ^{13}C MAS NMR spectra (recorded without decoupling or cross polarization) of hexamethyl benzene.

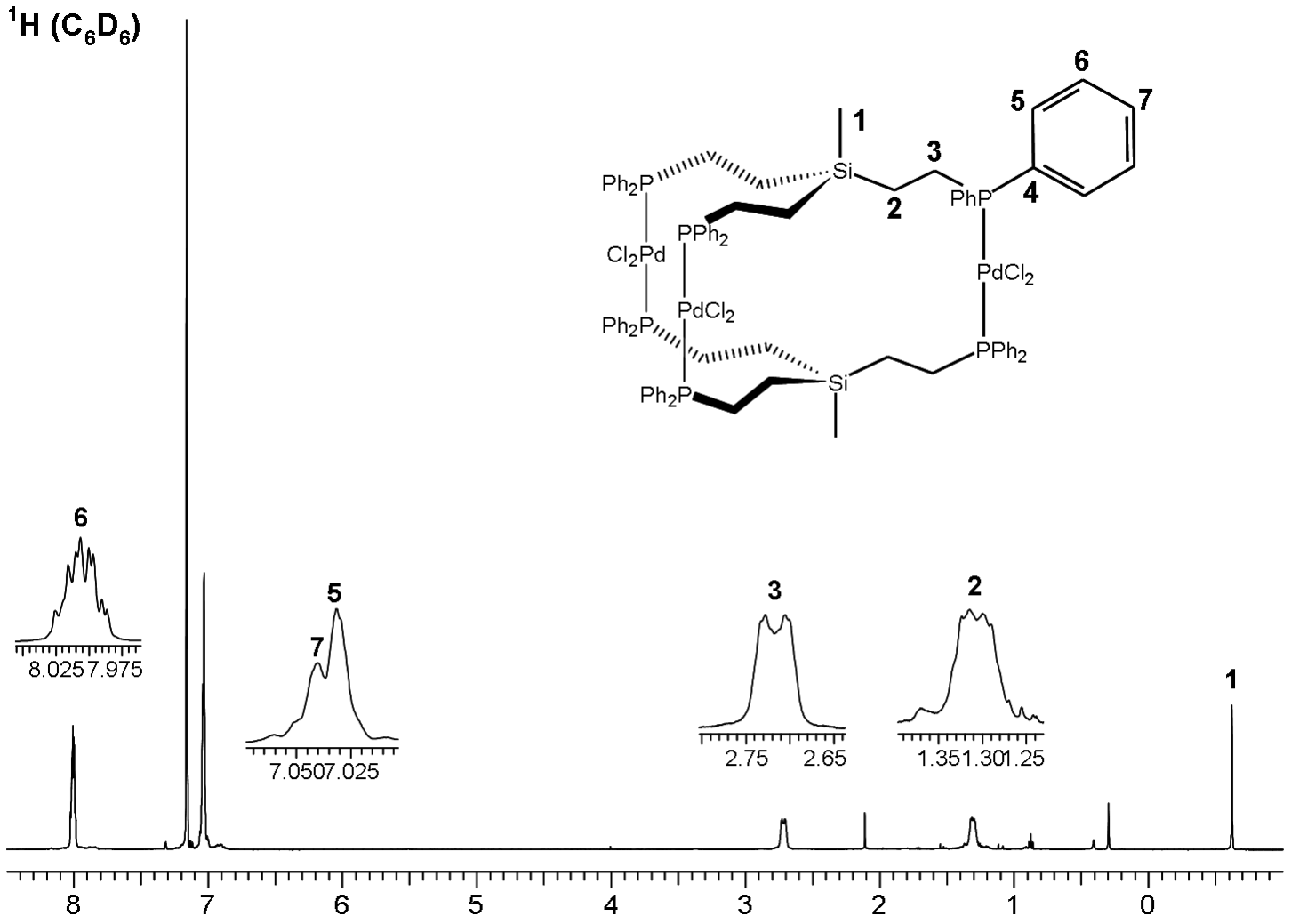

Figure C.19 ^{1}H NMR of $(Cl_2Pd)_3[(PPh_2CH_2CH_2)_3SiMe]_2$.

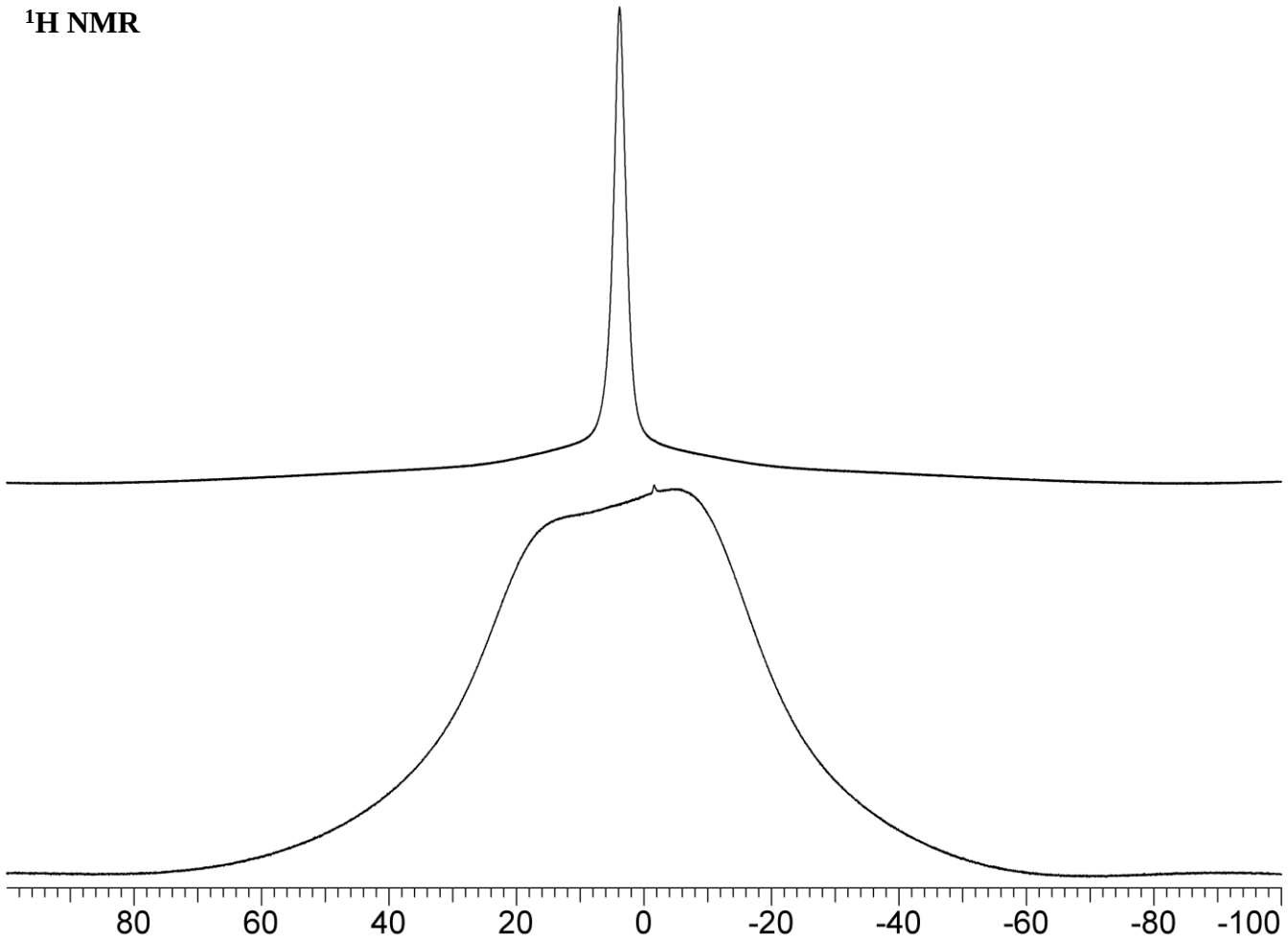

Figure C.20 ^{1}H NMR of **10** (bottom) and **10a** (top) recorded on a 500 MHz solution state NMR spectrometer by filling the powder into a standard 5 mm glass sample tube.

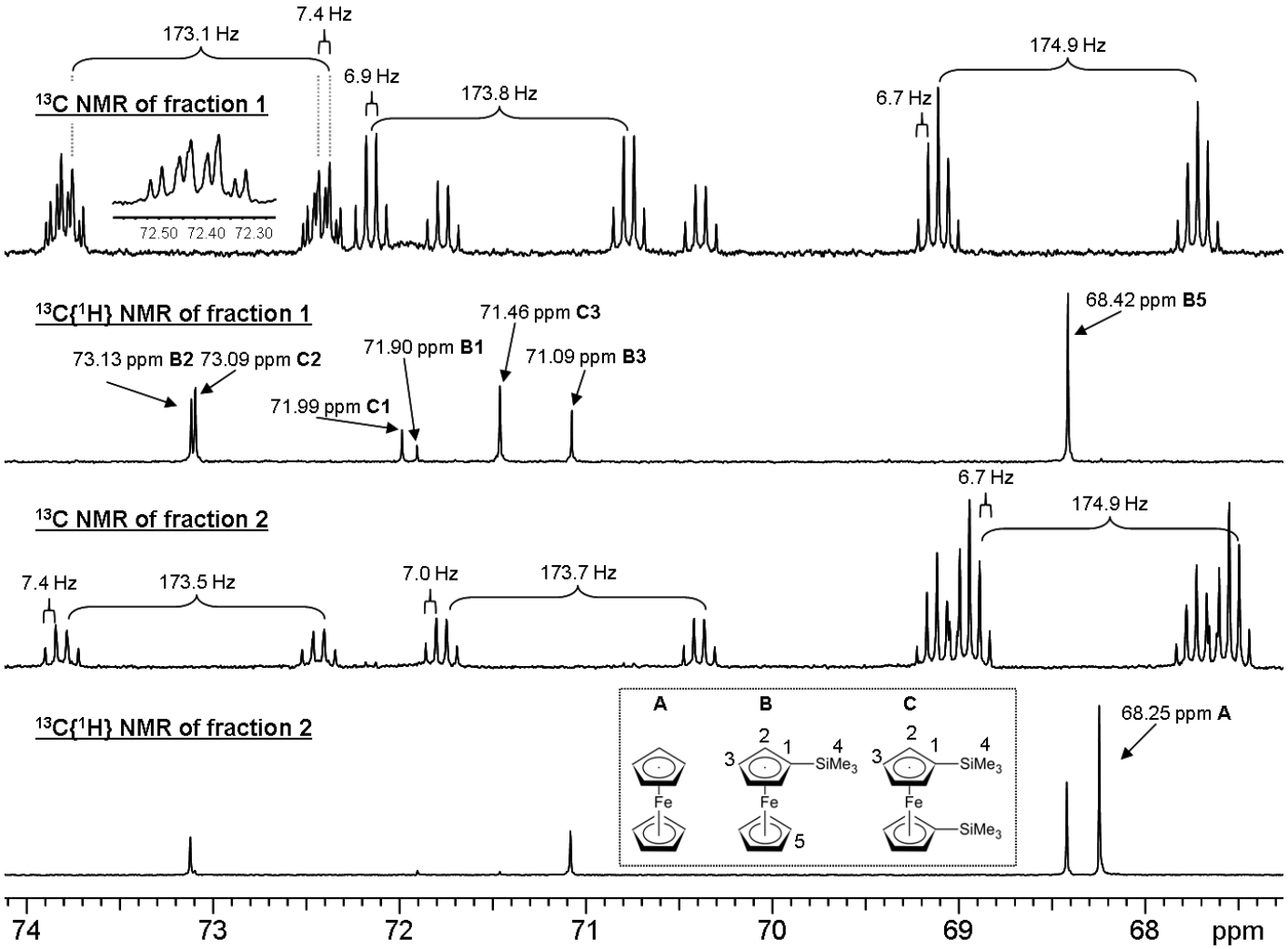

Figure C.21 ^{13}C NMR spectra of two different fractions obtained during the chromatography of TMS-substituted ferrocene.

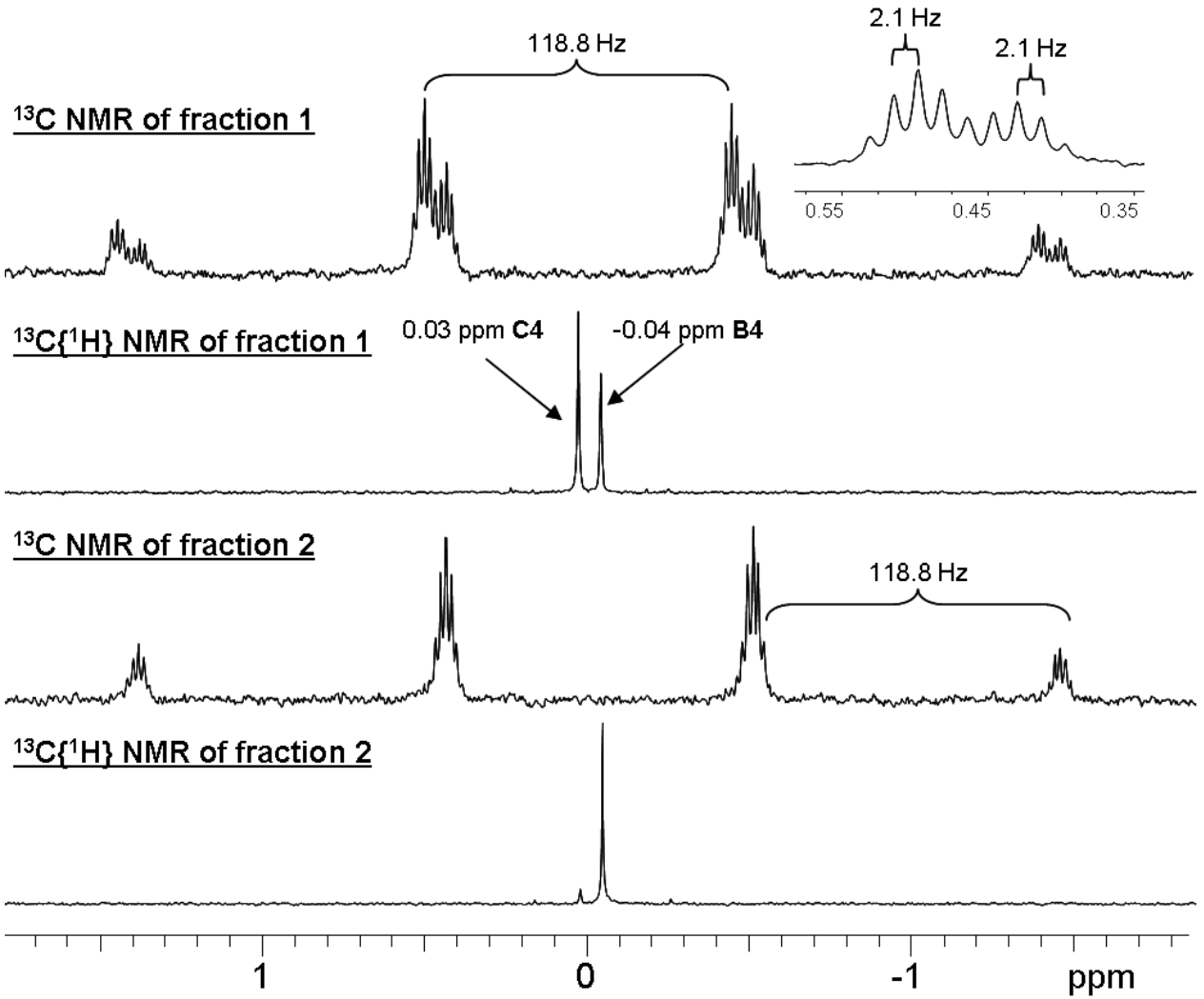

Figure C.22 ^{13}C NMR spectra of the methyl region of two different fractions obtained during the chromatography of TMS-substituted ferrocene.